



HAL
open science

Large eddy simulation of evaporating sprays in complex geometries using Eulerian and Lagrangian methods

Félix Jaegle

► **To cite this version:**

Félix Jaegle. Large eddy simulation of evaporating sprays in complex geometries using Eulerian and Lagrangian methods. Fluids mechanics [physics.class-ph]. Institut National Polytechnique de Toulouse - INPT, 2009. English. NNT : 2009INPT067H . tel-04285015

HAL Id: tel-04285015

<https://theses.hal.science/tel-04285015v1>

Submitted on 14 Nov 2023

HAL is a multi-disciplinary open access archive for the deposit and dissemination of scientific research documents, whether they are published or not. The documents may come from teaching and research institutions in France or abroad, or from public or private research centers.

L'archive ouverte pluridisciplinaire **HAL**, est destinée au dépôt et à la diffusion de documents scientifiques de niveau recherche, publiés ou non, émanant des établissements d'enseignement et de recherche français ou étrangers, des laboratoires publics ou privés.



THESE

En vue de l'obtention du

DOCTORAT DE L'UNIVERSITÉ DE TOULOUSE

Délivré par Institut National Polytechnique de Toulouse
Discipline ou spécialité : Dynamique des Fluides

Présentée et soutenue par Felix JAEGLE
Le 14 décembre 2009

Titre :
**Large eddy simulation of evaporating sprays in complex geometries
using Eulerian and Lagrangian methods**

JURY

Michael Breuer Rapporteur
William P. Jones Rapporteur
Bénédicte Cuenot Directeur de thèse
Carmen Jiménez Examineur
Gérard Lavergne Examineur
Matthieu Rullaud Examineur

Ecole doctorale : Mécanique, Energétique, Génie civil, Procédés
Unité de recherche : CERFACS
Directeur(s) de Thèse : Bénédicte Cuenot, Olivier Vermorel
Rapporteurs : William P. Jones, Michael Breuer

To Katrin
To my parents

Betrachte, wie in Abendsonne-Glut
Die grünumgebenen Hütten schimmern.
Sie rückt und weicht, der Tag ist überlebt,
Dort eilt sie hin und fördert neues Leben.
O daß kein Flügel mich vom Boden hebt
Ihr nach und immer nach zu streben!
Ich sah im ewigen Abendstrahl
Die stille Welt zu meinen Füßen,
Entzündet alle Höhn beruhigt jedes Tal,
Den Silberbach in goldne Ströme fließen.
Nicht hemmte dann den göttergleichen Lauf
Der wilde Berg mit allen seinen Schluchten;
Schon tut das Meer sich mit erwärmten Buchten
Vor den erstaunten Augen auf.
Doch scheint die Göttin endlich wegzusinken;
Allein der neue Trieb erwacht,
Ich eile fort, ihr ew'ges Licht zu trinken,
Vor mir den Tag und hinter mir die Nacht,
Den Himmel über mir und unter mir die Wellen.
Ein schöner Traum, indessen sie entweicht.
Ach! zu des Geistes Flügeln wird so leicht
Kein körperlicher Flügel sich gesellen.
Doch ist es jedem eingeboren
Daß sein Gefühl hinauf und vorwärts dringt,
Wenn über uns, im blauen Raum verloren,
Ihr schmetternd Lied die Lerche singt;
Wenn über schroffen Fichtenhöhen
Der Adler ausgebreitet schwebt,
Und über Flächen, über Seen
Der Kranich nach der Heimat strebt.

Goethe, on jet-powered flight

Contents

Résumé / Abstract	15
Acknowledgements	17
List of symbols	19
I The industrial context	25
1 General introduction	27
1.1 Propulsion technology for aeronautical applications	27
1.1.1 Historical development	27
1.2 Lean combustion	29
1.2.1 Injector design philosophies	30
1.3 Simulation tools for research and combustor design	33
1.3.1 Turbulence and unsteady phenomena	33
1.3.2 Liquid phase modelization	34
1.3.3 Combustion	35
1.3.4 Parallel computing	35
1.4 Scope of the present work	36
1.5 Organization of this thesis	37
II Governing equations	39
2 Governing equations for the gaseous phase	41
2.1 Introduction	41
2.2 The governing equations	41
2.2.1 The equation of state	43

2.2.2	Conservation of Mass: Species diffusion flux	43
2.2.3	Viscous stress tensor	44
2.2.4	Heat flux vector	44
2.2.5	Transport coefficients	45
2.3	The LES Concept	46
2.4	The Governing Equations for LES	47
2.4.1	The filtered viscous terms	48
2.4.2	Subgrid-scale turbulent terms for LES	48
2.5	Models for the subgrid stress tensor	49
2.5.1	Smagorinsky model	49
2.5.2	WALE model	50
2.5.3	Filtered Smagorinsky model	50
2.5.4	Dynamic Smagorinsky model	50
3	Governing equations for the dispersed, liquid phase	51
3.1	Introduction	51
3.2	The Eulerian-Lagrangian approach	52
3.2.1	Coupling between phases	52
3.3	The mesoscopic Eulerian-Eulerian approach	53
3.3.1	Two-phase eulerian closure models	59
3.3.2	LES equations for the dispersed phase	60
3.3.3	Sub-grid scale models for the dispersed phase	61
3.4	Definition of characteristic diameters in a spray	62
4	Modeling of the exchanges between phases	63
4.1	Introduction	63
4.2	Drag	63
4.2.1	Two-way coupling terms for drag	64
4.3	Evaporation model	65
4.3.1	Mass transfer	67
4.3.2	Two-way coupling terms for mass transfer	69
4.3.3	Heat transfer	69
4.3.4	Coupling terms for heat transfer	78

4.3.5	Treatment of droplet boiling	79
4.3.6	Vanishing droplets in EL	79
4.4	Summary of the liquid phase governing equations	81
5	The numerical approach	83
5.1	Introduction	83
5.2	The cell-vertex approach	84
5.3	The convection schemes for the gaseous phase	85
5.3.1	The Lax-Wendroff scheme	86
5.3.2	The TTGC scheme	86
5.4	The convection schemes for the dispersed phase	86
5.4.1	The PSI scheme	87
5.5	The diffusion scheme	90
5.6	Calculation of the timestep	90
5.6.1	Liquid phase timestep	90
5.7	Artificial viscosity models for the gaseous phase	91
5.7.1	Introduction	91
5.7.2	The sensors	92
5.7.3	The operators	93
5.7.4	The sensors for the Eulerian dispersed phase	93
5.8	Boundary conditions	94
5.9	Numerical aspects of the Euler-Lagrange solver	95
5.9.1	Time integration	95
5.9.2	Interpolation methods	95
5.9.3	Two-way coupling terms	95
5.10	Wall interaction of Lagrangian particles	96
III	Preliminary studies	99
6	Wall modeling	101
6.1	Introduction	101
6.1.1	The turbulent boundary layer	102
6.2	Wall-function implementation methods	106

6.2.1	The cell-vertex approach for wall-boundaries	106
6.2.2	The use of wall functions in LES solvers	108
6.2.3	Implementation with slip velocity at the wall	109
6.2.4	Corner problem	110
6.2.5	Implementation without slip velocity at the wall	111
6.2.6	Limitations of the no-slip approach	112
6.3	Applications and Results	113
6.3.1	Turbulent channel flow	114
6.3.2	Flow over a sudden expansion	116
6.3.3	Injector for aero-engines (TLC configuration)	118
6.4	Analysis of limits of wall function approaches	123
6.4.1	Implementation method	123
6.4.2	Grid dependency	125
6.4.3	The influence of the subgrid-scale viscosity model	125
6.5	Conclusion	131
6.6	Summary of the elements applied on the TLC configuration	132
7	Pressure drop in LES of complex geometries	133
7.1	Pressure drop in complex geometries	133
7.1.1	Pressure drop definitions	134
7.2	Sources of error on pressure drop	135
7.2.1	Convergence study of a single passage of a swirler	135
7.2.2	Analytical study of the error due to near-wall discretization	139
7.3	A method for very small scale geometric details (PPSG)	144
7.3.1	The numerical test case of a single perforation	147
7.4	Application of the PPSG method to the TLC configuration	148
7.5	Conclusion	149
8	Injection for multipoint systems	153
8.1	Introduction	153
8.1.1	Atomization of liquid jets in a crossflow	154
8.2	Injection methods	156
8.2.1	Modeling of the injection near-field	156

8.2.2	Implementation of the model for Euler-Lagrange	159
8.2.3	Implementation of the model for Euler-Euler	160
8.3	The experimental setup	163
8.3.1	Computational domain	163
8.4	Gaseous flow field	164
8.5	Euler-Euler numerical scheme	165
8.6	Test cases	167
8.7	Results	168
8.7.1	Flow and spray topology	169
8.7.2	Comparison of averaged results	173
8.8	Computational cost	176
8.9	Conclusion	176
8.10	Tables	178
IV	Application to an aeronautical multipoint injector	181
9	Description of the TLC configuration	183
9.1	Introduction	183
9.2	The SNECMA staged premixing swirler	183
9.2.1	Geometry	183
9.2.2	Injection of liquid fuel	185
9.3	The ONERA non-reacting test bench	185
9.3.1	Measurement methods	186
9.4	The numerical setup	187
9.4.1	Modifications of the original geometry	187
9.4.2	The computational grid	188
10	Gaseous flow results of the TLC configuration	191
10.1	Introduction	191
10.2	Computational setup	191
10.3	Results	193
10.3.1	Instantaneous flow topology	193
10.3.2	Time-averaged results	197

10.3.3	Comparison with experimental data / LES quality	201
11	Two-phase flow results of the TLC configuration	207
11.1	Introduction	207
11.2	Computational setup	208
11.2.1	Euler-Euler computational setup	209
11.2.2	Euler-Lagrange computational setup	210
11.3	Results	210
11.3.1	Instantaneous two-phase flow topology	210
11.3.2	Evaporation phenomena	214
11.3.3	Time-averaged results, comparison with experimental data	225
11.4	Computational cost	232
11.5	Conclusion	233
11.6	Tables	234
V	Appendices	247
A	Validation of the evaporation model	249
A.1	Introduction	249
A.1.1	One-dimensional evaporation of a monodisperse droplet stream	249
A.1.2	Simulation parameters	250
A.1.3	The analytical solution	250
A.1.4	Results	253
B	One-dimensional spray flames	257
B.1	Introduction	257
B.2	Anchored spray flame	258
B.2.1	Chemistry	258
B.2.2	Spray properties	258
B.2.3	Analytical solution	258
B.2.4	Simulation parameters	259
B.2.5	Results	259
B.3	Saturated spray flame	263
B.3.1	Chemistry	263

B.3.2	Spray properties	263
B.3.3	Simulation parameters	263
B.3.4	Results	264
B.4	Conclusion of the one-dimensional test cases	266

Résumé / Abstract

Résumé

Dû aux efforts apportés à la réduction des émissions de NO_x dans des chambres de combustion aéronautiques il y a une tendance récente vers des systèmes à combustion pauvre. Cela résulte dans l'apparition de nouveaux types d'injecteur qui sont caractérisés par une complexité géométrique accrue et par des nouvelles stratégies pour l'injection du carburant liquide, comme des systèmes multi-point. Les deux éléments créent des exigences supplémentaires pour des outils de simulation numériques.

La simulation à grandes échelles (SGE ou LES en anglais) est aujourd'hui considérée comme la méthode la plus prometteuse pour capturer les phénomènes d'écoulement complexes qui apparaissent dans une telle application. Dans le présent travail, deux sujets principaux sont abordés: Le premier est le traitement de la paroi ce qui nécessite une modélisation qui reste délicate en SGE, en particulier dans des géométries complexes. Une nouvelle méthode d'implémentation pour des lois de paroi est proposée. Une étude dans une géométrie réaliste démontre que la nouvelle formulation donne de meilleurs résultats comparé à l'implémentation classique. Ensuite, la capacité d'une approche SGE typique (utilisant des lois de paroi) de prédire la perte de charge dans une géométrie représentative est analysée et des sources d'erreur sont identifiées.

Le deuxième sujet est la simulation du carburant liquide dans une chambre de combustion. Avec des méthodes Euleriennes et Lagrangiennes, deux approches sont disponibles pour cette tâche. La méthode Eulerienne considère un spray de gouttelettes comme un milieu continu pour lequel on peut écrire des équations de transport. Dans la formulation Lagrangienne, des gouttes individuelles sont suivies ce qui mène à des équations simples. D'autre part, sur le plan numérique, le grand nombre de gouttes à traiter peut s'avérer délicat. La comparaison des deux méthodes sous conditions identiques (solveur gazeux, modèles physiques) est un aspect central du présent travail. Les phénomènes les plus importants dans ce contexte sont l'évaporation ainsi que le problème d'injection d'un jet liquide dans un écoulement gazeux transverse ce qui correspond à une version simplifiée d'un système multi-point.

Le cas d'application final est la configuration d'un seul injecteur aéronautique, monté dans un banc d'essai expérimental. Ceci permet d'appliquer de manière simultanée tous les développements préliminaires de ce travail. L'écoulement considéré est non-réactif mais à part cela il correspond au régime ralenti d'un moteur d'avion. Dû aux conditions préchauffées, le spray issu du système d'injection multi-point s'évapore dans la chambre. Cet écoulement est simulé utilisant les approches Euleriennes et Lagrangiennes et les résultats sont comparés aux données expérimentales.

Mots clés: *LES, turbulence, modèle de paroi, loi de paroi, écoulement diphasique, spray, Euler-Euler, Euler-Lagrange, injection, évaporation, moteur d'avion, chambre de combustion*

Abstract

Due to efforts to reduce NO_x emissions of aeronautical combustors, there is a recent trend towards lean combustion technologies. This results in novel injector designs, which are characterized by increased geometrical complexity and new injection strategies for the liquid fuel, such as multipoint systems. Both elements create additional challenges for numerical simulation tools.

Large-Eddy simulation (LES) is regarded as the most promising method to capture complex flow phenomena in such an application. In the present work, two main areas of interest are considered: The first is wall modeling, which remains a challenging field in LES, in particular for complex geometries. A new implementation method for wall functions that uses a no-slip condition at the wall is proposed. It is shown that in a realistic burner geometry the new formulation yields improved results compared to a classical implementation. Furthermore, the capability of a typical LES with wall models to predict the pressure drop in a representative geometry is assessed and sources of error are identified.

The second topic is the simulation of liquid fuel in a combustor. With Eulerian and Lagrangian methods, two different approaches are available for this task. The Eulerian approach considers a droplet spray as a continuum for which transport equations can be formulated. In the Lagrangian formulation, individual droplets are tracked, which leads to a simple formulation but can be challenging in terms of numerics due to the large number of particles to be treated. The comparison of these methods under identical conditions (gaseous flow solver, physical models) is a central aspect of the present work. The most important phenomena that are studied in view of the final application are evaporation and the problem of transverse liquid jets in a gaseous crossflow as a simplified representation of a multipoint system.

The final application case is the configuration of a single aeronautical injector mounted in an experimental test bench. It allows to simultaneously apply all preliminary developments. The flow considered is non-reactive but otherwise corresponds to a partial load regime in an aero-engine. Due to the pre-heated conditions, the spray issued by the multi-point injection undergoes evaporation. This flow is simulated using Eulerian and Lagrangian methods and the results are compared to experimental data.

Keywords: *LES, turbulence, wall model, wall function, two-phase flow, spray, Euler-Euler, Euler-Lagrange, injection, evaporation, aero-engine, combustor*

Acknowledgements

[Remerciements/Danksagung]

Although a thesis like this ultimately has to be written and defended by one single person, there are many who help, contribute and support during the years that lead to its completion. It is to all these people that I would like to express my gratitude.

Tout d'abord à Bénédicte Cuenot et Thierry Poinot qui ont encadré ma thèse, donné de l'aide et de nouvelles idées, qui ont lu et amélioré les piles de papier de différentes tailles que j'ai déposées sur leurs bureaux, et qui m'ont donné la possibilité de partir et élargir mes horizons scientifiques lors d'écoles d'été ou de conférences. Muchas gracias también a Carmen Jiménez por el tiempo tan agradable e interesante pasado en Madrid. Esta visita me ha permitido no sólo aprender un poco de español, sino también descubrir nuevos caminos para el desarrollo de mi tesis.

I also want to thank the entire committee of the defence for having taken the time to read and comment on my manuscript and finally travel to Toulouse during a very busy period.

Et bien sûr, je remercie aussi tous mes collègues et amis, responsables pour le mélange unique de bonne ambiance et compétence qui a marqué mes trois ans au CERFACS. Ce sont en particulier mes collègues de bureau, Thomas Schmitt et ces derniers temps Marlène Sanjosé, collègue diphasique du côté Eulérien de la force. Bien sûr aussi les deux 'Lagrangiens', Marta García et Jean-Mathieu Senoner (qui m'a aussi initié au vélo de route et avec qui j'ai partagé deux 'Alb Extrem' et de nombreux cols dans les Pyrénées). Et naturellement aussi Olivier Cabrit, toujours prêt pour une discussion enrichissante sur des lois de paroi ou la photographie. Un grand merci aussi à mon 'fan club' (j'étais vraiment épaté par cette action après la soutenance!): Benedetta Franzelli, Matthias Kraushaar, Jorge Amaya, Elsa Gullaude, Camilo Silva, Patricia Sierra, Victor Granet, Thomas Pedot, Kerstin Wiczorek, Benoit Enaux, Matthieu Leyko, Matthieu Boileau, Guilhem Lacaze, Eléonore Riber, les 'Eccomet guys', Dirk Wunsch, Bernhard Wagner, Zafer Zeren, Davide Zuzio, Marco Maglio, Virginel Bodoc, Vital Gutierrez, mes collègues au Ciemat (et après), Jerome Dombard et Ignacio Hernandez (cités dans un ordre complètement aléatoire).

Merci beaucoup aussi à l'équipe CSG pour son aide et sa patience avec mes divers ordinateurs portables peu fiables! Un grand merci également à Michèle Campassens, Marie Labadens et Nicole Boutet qui ont beaucoup aidé à résoudre tous les petits et grands problèmes administratifs. La quasi non-existence de bureaucratie qui marque le CERFACS est grâce à votre travail génial!

Ausserdem möchte ich mich bei meinen Eltern und meiner Familie für ihre Unterstützung in jeder erdenklichen Form in diesen drei Jahren aber auch lange davor bedanken. Und schliesslich gilt mein größter Dank natürlich Katrin (meiner Lieblingsmathematikerin, der ich selbst als Doktor nur mit Mühe das Wasser reichen kann) für drei Jahre, in denen sie mir zwar geographisch fern war, auf ihre unvergleichliche Art aber zu meiner Ausgeglichenheit und damit zum Gelingen dieser Arbeit entscheidend beigetragen hat.

List of symbols

Roman characters

Symbol	Description	Unit
c	Propagation velocity	$[m/s]$
c_d	Discharge coefficient	$[-]$
C	Constant of the logarithmic law	$[-]$
C_c	Constant of the law of the wake	$[-]$
C_{ab}	Liquid column breakup coefficient	$[-]$
C^{blend}	Constant of a blending function	$[-]$
C_D	Average drag coefficient in the liquid column region	$[-]$
C_s	Smagorinsky constant	$[-]$
C_{sF}	Filtered Smagorinsky constant	$[-]$
C_w	WALE model constant	$[-]$
$C_{s,l}$	Smagorinsky constant for the dispersed phase	$[-]$
$C_{V,l}$	Yoshizawa constant for the dispersed phase	$[-]$
C_v	Heat capacity at constant volume	$[J/(kgK)]$
C_p	Heat capacity at constant pressure	$[J/(kgK)]$
d_0	Orifice diameter	$[m]$
d_{col}	Liquid column diameter	$[m]$
d_p	Diameter of a Lagrangian particle	$[m]$
D_{32}	Sauter mean diameter (SMD) of a droplet size distribution	$[m]$
D_{10}	Mean diameter of a droplet size distribution	$[m]$
D_k	Diffusion coefficient of species k	$[-]$
D_{inj}	Diameter of the jet injection orifice	$[m]$
E	Gaseous total energy per unit mass	$[J/kg]$
$F_{d,i}$	Volumetric force vector of particle drag	$[N/m^3]$
$F_{p,i}$	Drag force vector of a Lagrangian particle	$[N]$
h_s	Sensible enthalpy	$[J/kg]$
$J_{j,k}$	Diffusive flux vector of species k	$[kg/(m^2s)]$
$J_{j,k}$	Turbulent diffusive flux vector of species k	$[kg/(m^2s)]$
k	Von Kármán constant	$[-]$
l_m	Mixing length	$[m]$
l_{col}	Liquid column length	$[m]$
L_v	Latent heat of evaporation	$[J/kg]$
m_p	Mass of a Lagrangian particle	$[kg]$
\dot{m}_p	Rate of change of droplet mass	$[kg/s]$
\dot{m}_p	Mass flux of gaseous fuel from a droplet	$[kg/s]$
\dot{m}	Mass flux	$[kg/s]$

Symbol	Description	Unit
n_s	Number of perforations	[-]
n_{bin}	Number of diameter classes (or bins)	[-]
P	Pressure	$[N/m^2]$
P	Probability density function	[-]
q	Momentum flux ratio	[-]
q_i	Heat flux vector	$[J/(m^2s)]$
q_i^t	Turbulent heat flux vector	$[J/(m^2s)]$
Q	Q-criterion	$[1/s^2]$
Q_{ij}	vorticity tensor	$[1/s]$
$\bar{q}_{\Theta,i}^t$	Subgrid flux of uncorrelated energy in the dispersed phase	$[J/(m^2s)]$
$\bar{q}_{h,i}^t$	Subgrid flux of sensible enthalpy in the dispersed phase	$[J/(m^2s)]$
r	Mixture gas constant	$[J/(kgK)]$
R	Universal gas constant (mass)	$[J/(kgK)]$
s_l	Vector of source terms in the Euler-Euler framework	
S	Cross-section surface	$[m^2]$
S_E	Energy source term	$[J/(m^3s)]$
S_{ij}	Boussinesq tensor (rate of strain tensor)	$[m/s^2]$
S_k	Species source term	$[kg/(m^3s)]$
$S_{M,i}^{l-g}$	Vector of momentum source terms	$[N/m^3]$
t	Time	$[s]$
T	Gaseous temperature	$[K]$
T_p	Temperature of a Lagrangian particle	$[K]$
T_{wb}	Wet bulb temperature	$[K]$
u_i	Gaseous velocity vector	$[m/s]$
u_l	Eulerian liquid phase velocity	$[m/s]$
$u_{p,i}$	Velocity vector of a Lagrangian particle	$[m/s]$
V_i	Species diffusion velocity vector	$[m/s]$
V_j	Control volume of a node j in the cell-vertex framework	$[m^3]$
w	Interpolation function in the Euler-Lagr. approach	[-]
W	Molecular weight	$[kg/mol]$
W_{Θ}	Uncorrelated energy variation due to drag	$[J/(m^3s)]$
x_i	Spatial coordinate (vector)	$[m]$
x	Spatial coordinate	$[m]$
$x_{p,i}$	Position vector of a Lagrangian particle	$[m]$
x_b, y_b, z_b	Coordinates of the point of liquid column breakup	$[m]$
X_k	Molar fraction of species k	[-]
y	Spatial coordinate	$[m]$
Y_k	Mass fraction of species k	[-]
z	Spatial coordinate	$[m]$

Greek characters

Symbol	Description	Unit
α	Term in the Barenblatt law	[—]
α_l	Liquid volume fraction	[—]
β	Term in the Barenblatt law	[—]
γ	Adiabatic exponent	[—]
Γ_l	Rate of change per unit volume of the liquid phase mass	$[kg/(sm^3)]$
Γ	Rate of mass change per unit vol. in the gas phase by evap.	$[kg/(sm^3)]$
$\Gamma_{u,i}$	Momentum exchange through mass exchange	$[kg/(s^2m^2)]$
Γ_Θ	Uncorrelated energy variation due to mass transfer	$[J/(m^3s)]$
δ_c	Channel half-width	$[m]$
δ	Constant of the Colin sensor for artificial viscosity	[—]
δ_{ij}	Kronecker symbol	[—]
$\delta\tilde{R}_{l,ij}$	Uncorrelated velocity tensor	$[m^2/s^2]$
$\delta\tilde{\Theta}_l$	Uncorrelated Energy	$[m^2/s^2]$
Δ	Characteristic length scale of a grid cell	$[m]$
Δp	Pressure drop	$[N/m^2]$
ϵ_1	Constant of the Colin sensor for artificial viscosity	[—]
ϵ_2	Constant of the Colin sensor for artificial viscosity	[—]
ϵ_3	Constant of the Colin sensor for artificial viscosity	[—]
ζ_e	Artificial viscosity sensor	[—]
Θ	Distribution function in the Euler-Lagrange approach	[—]
$\kappa_{l,t}$	Yoshizawa turbulent viscosity of the dispersed phase	$[m^2/s]$
λ	Heat conduction coefficient	$[J/(mKs)]$
μ	Molecular viscosity	$[Ns/m^2]$
μ_t	Turbulent viscosity	$[Ns/m^2]$
μ_{sgs}	Subgrid-scale viscosity	$[Ns/m^2]$
ν	Kinematic viscosity	$[m^2/s]$
ν_t	Turbulent kinematic viscosity	$[m^2/s]$
$\nu_{l,t}$	Smagorinsky turbulent viscosity of the dispersed phase	$[m^2/s]$
Ξ	Term of the Colin sensor for artificial viscosity	[—]
Π_g	Sensible enth. rate of ch. per unit vol. in the gas phase by evap.	$[J/(m^3s)]$
Π_l	Sensible enth. rate of ch. per unit vol. in the liq. phase by evap.	$[J/(m^3s)]$
ρ	Gaseous density	$[kg/m^3]$
ρ_k	Density of the gaseous species k	$[kg/m^3]$
ρ_l	Liquid phase density	$[kg/m^3]$
τ_{ij}	Stress tensor	$[N/m^2]$
τ_{ij}^t	Turbulent tress tensor	$[N/m^2]$
τ_p	Particle relaxation timescale	$[s]$
τ_p'	Stokes drag particle relaxation timescale	$[s]$
τ_L	Characteristic timescale of a gaseous flow	$[s]$
τ_{ab}	Liquid column breakup timescale	$[s]$
$\bar{\tau}_{l,ij}^t$	Subgrid stress tensor of the dispersed phase	$[N/m^2]$

Symbol	Description	Unit
Φ_g^c	Sensible enth. rate of change in the gas due to conduction	$[J/s]$
Φ_g^{ev}	Sensible enth. rate of change in the gas due to evaporation	$[J/s]$
Φ_l^{ev}	Sensible enth. rate of change in the liq. due to evaporation	$[J/s]$
Φ_l^c	Sensible enth. rate of change in the liq. due to conduction	$[J/s]$
Φ_l	Liquid volume flux	$[m^3/(sm^2)]$
Ψ	Spray function	
$\dot{\omega}_k$	Chemical source term of species k	$[kg/(m^3s)]$

Special characters

Symbol	Description	Unit
\mathbf{C}	Collisional term in the Euler-Euler framework	
$\mathbf{D}_{j,e}$	Residual distribution matrix	
\mathbf{F}_l	Flux tensor in the Euler-Euler framework	
$\vec{\mathcal{F}}$	Flux tensor of the conservative variables	
$\vec{\mathcal{F}}^C$	Convective part of the flux tensor of the conservative variables	
$\vec{\mathcal{F}}^V$	Viscous part of the flux tensor of the conservative variables	
\mathcal{H}_f	Gaseous flow realization	
\mathcal{R}	Universal gas constant (molar)	$[J/(molK)]$
\mathbf{S}	Vector of source terms	
\vec{S}_f	Normal vector of an element face	
\vec{S}_k	Normal vector of an element vertex	
$\vec{S}_{j,e}$	Normal vector of an element e associated with a node j	
$\vec{S}_{j,e}^{ff}$	Normal vector of a boundary face	
\mathbf{T}	Uncorrelated flux operator in the Euler-Euler framework	
\mathbf{U}_Θ	Term describing effects of $\delta\tilde{R}_{l,ij}$ on $\delta\tilde{\Theta}_l$	
\mathbf{U}	Vector of conservative flow variables	

Dimensionless numbers

Symbol	Description
B_M	Spalding number for mass transfer
B_T	Spalding number for heat transfer
Le	Lewis number
Nu	Nusselt number
Pr	Prandtl number
Pr_t	Turbulent Prandtl number
Re_p	Particle Reynolds number
$Re_{\tau\omega}$	Friction Reynolds number
Re_b	Bulk Reynolds number
Sc	Schmidt number
Sh	Sherwood number
St	Stokes number
We	Weber number

Indices and superscripts

Symbol	Description
+	Superscript of quantities written in wall units
BL	Index of quantities in the liquid column boundary layer
e	Element (or grid cell) in the cell-vertex framework
g	Index of a gaseous phase quantity
inj	Index of quantities located at the jet injection point
j	Index of a grid node
k	Index of an element vertex
l	Index of a liquid phase quantity
w	Index of a variable located at the wall
we	Index of quantities associated with a near-wall element

Part I

The industrial context

Chapter 1

General introduction

Contents

1.1 Propulsion technology for aeronautical applications	27
1.1.1 Historical development	27
1.2 Lean combustion	29
1.2.1 Injector design philosophies	30
1.3 Simulation tools for research and combustor design	33
1.3.1 Turbulence and unsteady phenomena	33
1.3.2 Liquid phase modelization	34
1.3.3 Combustion	35
1.3.4 Parallel computing	35
1.4 Scope of the present work	36
1.5 Organization of this thesis	37

1.1 Propulsion technology for aeronautical applications

1.1.1 Historical development

Aeronautical propulsion has relied heavily on combustion technology from its very beginnings, with battery, fuel-cell, solar or even nuclear-powered electric propulsion limited to small-scale unmanned or proof-of-concept research applications (see figure 1.1 for illustrative examples).

The vast majority of combustion-based propulsion systems uses liquid hydrocarbons, mostly kerosene as a fuel, which is mainly due to three aspects: The first is high specific energy content, which is an important factor because relationship between the necessary propulsive force and system weight is quadratic for all heavier-than-air aeronautical applications. The second is (volumetric) energy density, because high storage volumes quickly translates into a drag penalty. The third is security, where the risk of accidental ignition (during handling, storage or in the aftermath of crashes) must be minimized. It is primarily for the latter two requirements that gaseous fuels (such as hydrogen, even when stored in liquefied form) have not seen extensive use in commercial flight. Figure 1.2 shows an overview of the specific versus the volumetric energy content of different storage/conversion technologies.

In roughly the first half of the timeline of powered flight, internal combustion engines based on the Otto cycle (less widespread also the Diesel cycle) in conjunction with airscrews dominated



Figure 1.1: Examples for non-combustion based aeronautical concepts. Left: Icaré solar aircraft (photo Universität Stuttgart). Center: Boeing phantom works fuel cell demonstrator (Photo: Boeing). Right: Convair NB-36H nuclear testbed (Photo: Wikipedia).

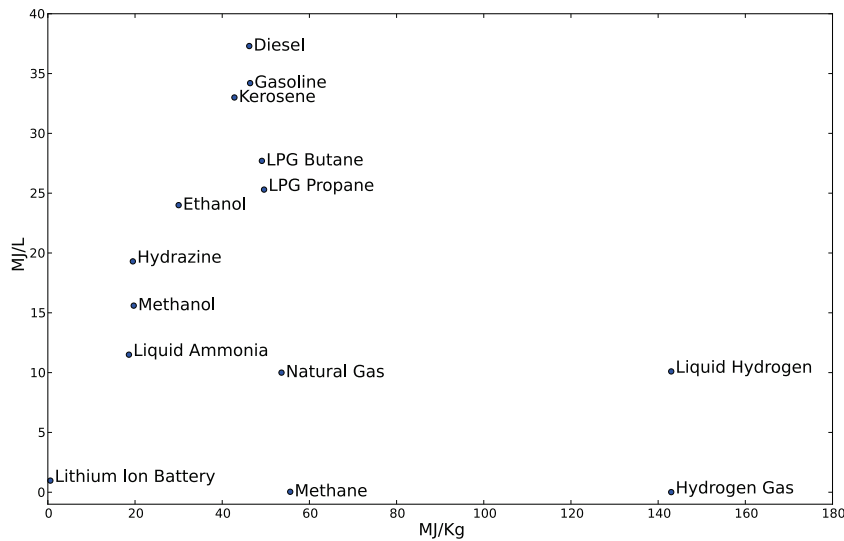


Figure 1.2: Specific energy versus energy density of different storage/conversion technologies.

propulsion technology. It was mainly the inherent limitation of those systems in terms of flight speed (due to blade tip losses when they become sonic) that spurred research of alternative technologies for military applications. This research, led mainly by Sir Frank Whittle and Dr. von Ohain resulted in the first applications of the jet engine during the second world war. This type of engine is based on a continuous thermodynamical cycle, where a rotating compressor is mechanically linked to a turbine. The thermodynamical potential created in the combustion chamber is used in part in the turbine to power the compressor, the surplus (after losses) is subsequently converted into a high momentum jet using a nozzle. A simplified version of this process is given by the Joule cycle (also known as the Brayton cycle), that is schematized in figure 1.3.

This technology quickly saw commercial use because the increased speeds were an important argument, especially for transcontinental travel in the USA but also for intercontinental travel worldwide. While military development focused mainly on technical feasibility and the increase of thrust to weight ratio, it was mainly the civil use that created the need to increase engine performance on mainly three other sectors. The first is specific fuel consumption, the second is engine noise and the third emission reduction. The demand for more efficient engines with lowered environmental impact gave rise to a series of new technologies. Specific fuel consumption and noise are significantly reduced by changing the overall layout of the system. Here, the introduction of high bypass turbofan engines and double/triple spool concepts (more recently also

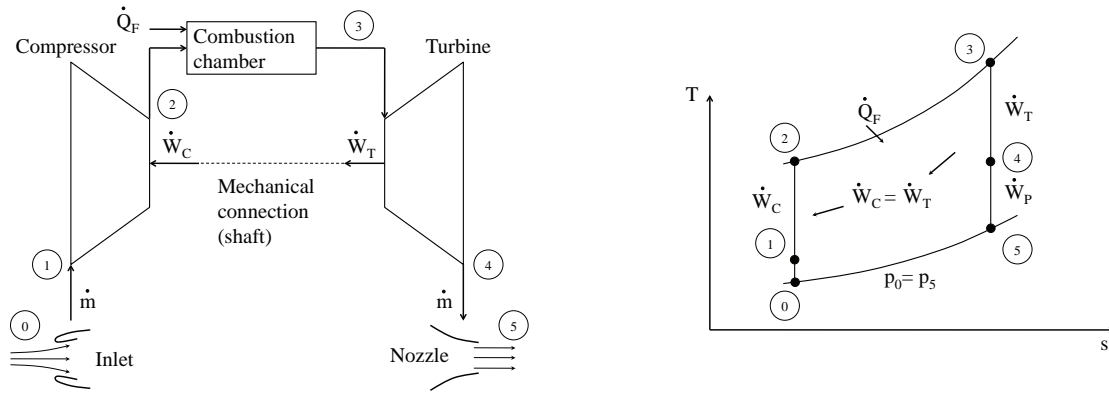


Figure 1.3: Schematic of a simplified jet engine (left) and the associated thermodynamic cycle (right). Q_F is the heat generated by combustion, W_C the work applied to the combustor and W_T the work generated in the turbine. The remaining work, noted W_P is available for propulsion after acceleration in a nozzle. The Joule (or Brayton-) cycle displayed here neglects all losses that occur during compression, expansion and combustion.

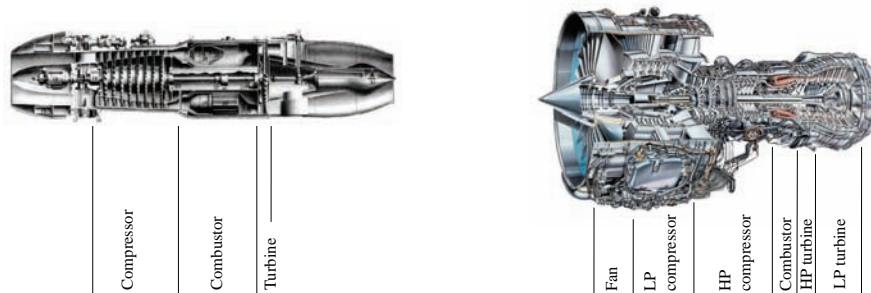


Figure 1.4: Comparison of one of the earliest operational jet engines (Jumo 004) with a current generation, high-bypass, twin-spool design (IAE V2500). In this layout, the high pressure (HP) compressor and turbine are connected by one shaft, while the low pressure (LP) compressor, the fan and the LP turbine are mounted on another one. This way, each group of components turns at its optimal rotation speed.

the geared fan) can be mentioned as key innovations. As an illustration, figure 1.4 compares the configuration of an early example and a current generation engine. Furthermore, the efficiency of thermodynamic cycle itself can be optimized by increasing the overall pressure ratio of the engine, which is helped by improved compressor designs and turbine blade cooling technologies.

The field of emission reduction is influenced by two tendencies. The emission of CO_2 is closely linked to overall fuel consumption and therefore influenced by the beforementioned means to increase engine efficiency. Other emissions like NO_x , CO , unburned hydrocarbons or particle emissions like soot are primarily influenced by combustor design.

1.2 Lean combustion

Lean combustion is a key technology in modern aero-engines. The initial push towards lean combustion technologies has been initiated in the 1980s, as a controversy arose in the US about the negative impact of the then to be developed supersonic aircraft programme (HSCT) on the ozone layer [33] [39]. This resulted in political pressure on engine manufacturers to reduce pollutant emission, with a focus on NO_x . Today, more and more stringent emission reduction

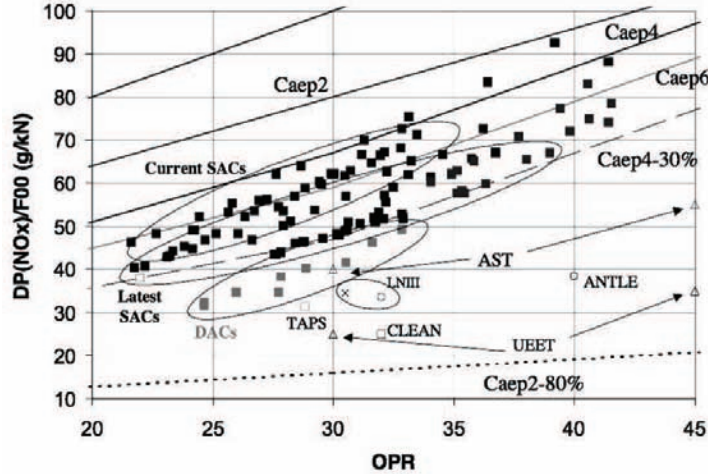


Figure 1.5: Mass of NO_x emitted divided by engine thrust versus the overall engine pressure ratio (OPR). Comparison of in-service combustor concepts and current research and development programs. Included are ICAO regulation levels (Caep). DAC stands for Double Annular combustor, while SAC denotes Single Annular combustor designs. TAPS and ANTLE are research combustors that both use fuel staging inside the injector. Source ICAO database and CAEP6 results. Diagram: public documentation of the TLC project.

goals for commercial aviation in general lead to increased efforts, in particular in the EU to develop lean combustion technologies and all associated measurement and simulation tools. In this context, the EU research projects LOPOCOTEP and TLC can be mentioned, with the latter forming the larger framework for the present study.

The design challenges for lean combustion systems are numerous, only the most important mechanisms shall be explained in the following, along the lines of the flow diagram in figure 1.6. The main conflict of design objectives arises from high safety requirements. Here, lean and completely premixed combustion (without locally rich burning zones) increases the risk of flame blowoff at partial load regimes and also the risk of instabilities from interaction of acoustics and flame dynamics [23]. Furthermore, premixing creates a risk of flame flashback into the premixing system, which can lead to the failure of the concerned parts of the combustor. The cited safety concerns are generally less and less easily addressed with increasing overall pressure ratio.

Other tradeoffs have to be made concerning the premixing that often relies on the generation of high turbulence intensities and therefore can increase the pressure drop of a combustor, reducing the overall efficiency of the engine. An effect created by increased overall pressure (and temperature) ratios is the increased need for air to dilute the combustion products, which is counter-productive in decreasing the equivalence ratio in the primary zone.

1.2.1 Injector design philosophies

There is a number of injector design philosophies that are aimed at lean combustion. There are different terminologies, which often depend on the manufacturer, but in principle they can be grouped in the following subtypes [39].

The most extreme one is the so-called Lean Premixed Pre-evaporated approach (LPP). It is mostly aimed at small engines with low overall pressure ratio, where instabilities and flashback risk are relatively well-controlled. It is, however being studied for higher pressure ratio applications, as it represents the ideal solution in terms of NO_x reduction [16]. An example for a LPP module is pictured in figure 1.7, which also shows LES results of evaporated fuel to visualize the premixing process.

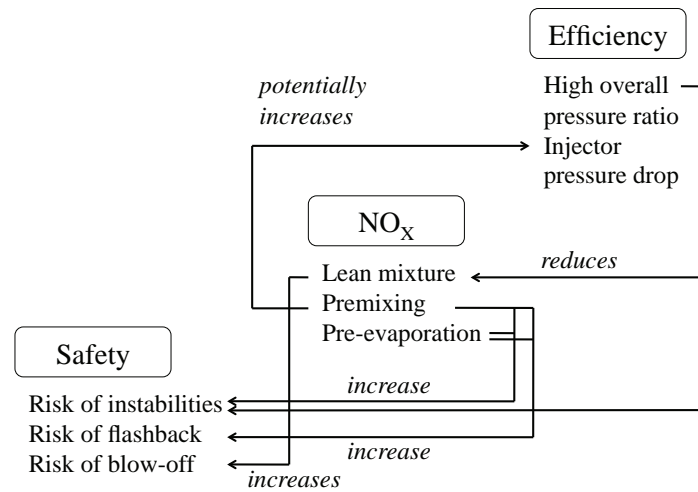


Figure 1.6: Tradeoffs in combustor design when reducing emissions and increasing efficiency.

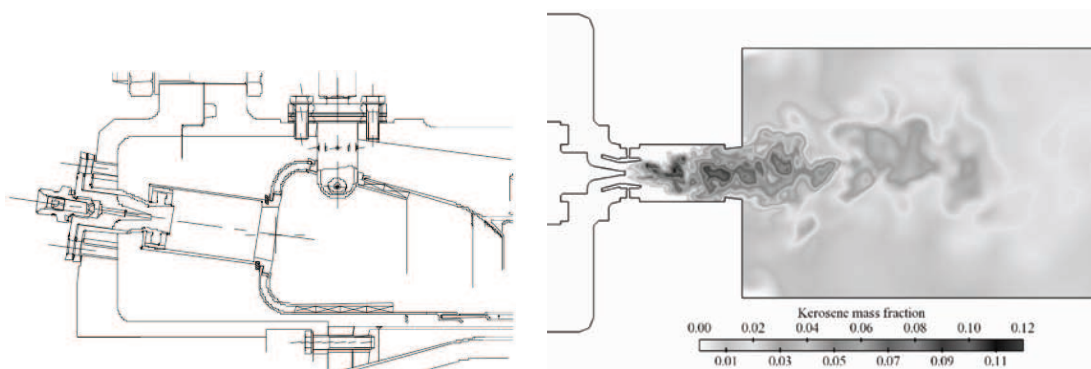


Figure 1.7: Example for a LPP (for Lean, Premixed, Pre-evaporated) injector of a helicopter engine. The fuel is injected into a central, high speed airstream for quick atomization and mixes with a swirled, outer flow inside the injector tube. The mass fraction of evaporated fuel (right) shows the premixing process. Sources: schematic from public documentation of the TLC project (left), simulation result by Felix Jaegle, CERFACS (right).

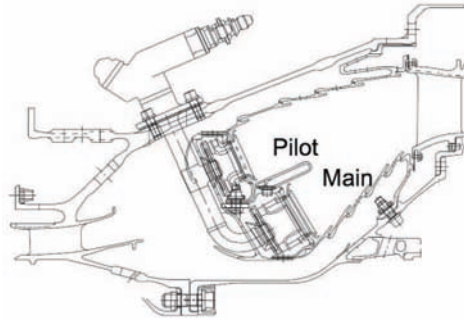


Figure 1.8: Example for a double annular combustor (DAC). Cross-section through the ring of a CFM 56 5B combustion chamber. Source: public documentation of the TLC project.

A less problematic version of this injection concept is the so-called LP (for Lean Premixed, sometimes also referred to as PERM (for Partially Evaporation & Rapid Mixing) approach, which relies on pre-mixing primary air with the liquid fuel, whereas evaporation remains incomplete at the entry into the chamber. This method mitigates certain problems related to flashback and instabilities.

The third class is often referred to as LDI for Lean Direct Injection, which uses sophisticated fuel injection methods that allow a very homogeneous spray distribution through direct injection, which is often achieved by multipoint systems.

All injection strategies for lean combustion mentioned above are characterized by a narrow operating range. In particular, lean burning zones are prone to becoming unstable or being blown off for reduced power settings. In contrast, conventional burners with a rich primary zone remain stable even in reduced power regimes. To overcome this problem, staged combustion systems have been introduced, which allow to safely decrease power output by additionally changing the fuel flow ratio between stages or by deactivating the burner partially. This so-called fuel staging can be achieved in different ways. The first is to separate the entire annular combustor into two rings (DAC concept for Double Annular Combustor), which is shown in figure 1.8 at the example of the CFM 56 5B combustor. This technology allows to significantly reduce NO_X emissions compared to SAC designs (see figure 1.5). The downsides to this concept are increased emissions of unburned hydrocarbons and CO , added weight and complexity as well as difficult cooling and related lifetime issues.

For these reasons, an alternative fuel staging method allowing for a single annular combustor (SAC) design is being pursued by numerous engine manufacturers, notably General Electric, Rolls Royce and SNECMA. The concept consists in dividing each individual injector in two separate stages. Figure 1.9 shows two examples for this approach, one is the TAPS (for Twin Annular Premixing Swirler) by GE, which will see commercial application in the latest generation GENx engine. The other one is the SNECMA multipoint injector, which is studied experimentally in the TLC project and represents the main application case of the present work. Although the manufacturer does not use this terminology, it can be considered an example for the LDI design philosophy. It is composed of a pilot stage in the center with a hollow-cone type atomizer, while the annular main stage, which is arranged around the pilot injector, uses a multi-point injection system. This injector will be described in more detail in chapter 9.

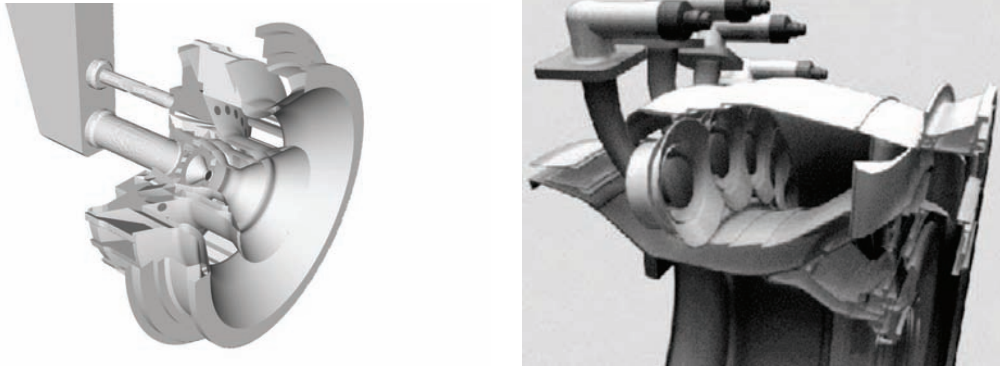


Figure 1.9: *Examples for fuel staging inside the injector. Left: SNECMA multi-point injector. Right GE TAPS concept for the GENx engine (source Dodds [37]).*

1.3 Simulation tools for research and combustor design

Numerical simulation has become an important tool for combustion research but increasingly also for combustor design. It is widely used in industry for dimensioning of combustor designs. Here, well-proven RANS methods are widely used. Advances in computing resources but also in simulation methods allow sophisticated LES simulations to reach truly industrial-scale, as demonstrated by the work of Boileau for the ignition of an entire helicopter chamber [20].

1.3.1 Turbulence and unsteady phenomena

The simulation of the gaseous flow in a combustor is a challenging task, because it conditions and interacts with all parts of the physics involved.

- **Turbulence:** the flow inside a combustor is always strongly turbulent by design as it promotes atomization, mixing (of spray and evaporated fuel) and burning at high energy densities. As all turbulent scales cannot be resolved in most realistic flows, turbulence models are of great importance.
- **Wall interaction** is very important as combustion chambers are confined flows by their very nature. The challenges associated differ, for instance, from airfoil design, where a very detailed understanding of phenomena like boundary layer separation and re-attachment is needed. In combustion chambers, the difficulty lies more in the complexity of the geometry and the unsteady flow. The prediction of pressure drop is associated to wall-interaction and necessitates great attention. As turbulent boundary layers cannot be resolved in the majority of applications, modeling of these zones is an important aspect in numerical simulations.
- **Swirled flows** are systematically encountered in combustion chambers as they allow to create central recirculation zones with free stagnation points, which allows to stabilize a flame without a mechanical flameholder (a device that is still found in afterburners, with very limited lifetime). This is achieved either by provoking vortex breakdown or forced by the shape of the swirler exit (the boundary between the two method being not clearly defined).
- **Acoustics** are an important link in the feedback loop that creates combustion instabilities. Together with unsteady flow phenomena, acoustics influence the unsteady heat release rate of the flame, which in turn acts as an acoustic source. The three mechanisms combined

can lead to the excitation of instabilities. Acoustics, but also unsteady flow in general necessitate special boundary conditions that take reflective or non-reflective behaviour at walls or inlets/outlets respectively.

The three major simulation strategies for the gaseous phase are the direct numerical simulation (DNS), large eddy simulation (LES) and the solution of the Reynolds averaged Navier Stokes equations (RANS). Only DNS and LES are adapted to properly simulate unsteady phenomena, which is a major advantage over RANS in view of the unsteady nature of a great number of flows. Furthermore, transient cases like ignition cannot be tackled with RANS. On the other hand, RANS facilitates the modeling of steady turbulent boundary layers and is thus well-adapted for instance for the prediction of pressure drop.

DNS due to its high computational cost is currently limited to academic cases, where it greatly contributes to the understanding and related modeling efforts of many different types of flows. LES is the method of choice if unsteady phenomena are to be considered in cases of industrial scale. Additionally, it yields results superior to RANS simulations, even for statistically steady flows, due to the lower modeling content related to turbulence. The main challenge associated with this method is the treatment of boundary layers due to the high cost of resolving these zones. Substantial efforts are therefore undertaken to develop wall-modeling approaches that are adapted to LES or to create hybrid RANS/LES approaches.

1.3.2 Liquid phase modelization

Phenomena related to the presence of liquid fuel play an important role in combustion applications. The following list outlines the most important ones and names the associated challenges for numerical simulation or modeling approaches.

- Heat and mass exchange between phases are important for combustion as evaporation of fuel influences many aspects of flame structure and dynamics. A wide range of models with varying degree of detail is available.
- Droplet dynamics determine the distribution and mixing processes of a spray. Modeling approaches for spherical droplets are widely available.
- Breakup mechanisms, in applications where their role is determinant (e.g. at injection). One distinguishes between primary and secondary breakup. Primary breakup is the disintegration of large, coherent liquid phase structures such as jets or sheets. They are mainly governed by the gas-liquid interface (influenced by surface tension, densities and viscosities) and its interaction with flow and turbulence on either side. Secondary breakup mechanisms apply to approximately spherical liquid structures or droplets. For this particular case of breakup in a spray, models can be formulated based on statistical considerations.
- Droplet-wall interaction is often encountered in combustion applications. It is a very complex process with many different outcomes such as film forming, re-bounce, splashing etc. Modeling approaches have therefore often very limited domains of validity.
- Droplet-droplet interaction occurs in dense spray regions and is equally complex. Depending on impact energy, angle, offset and size ratio of collision partners, a multitude of liquid structures like ligaments, satellite drops, rings, fingers etc is observed. Modeling is therefore a complex task.

Three major classes of methods for the simulation a two-phase flow can be distinguished. The first is the direct simulation of the gas-liquid interface using level-set [147], volume of fluid

(VOF) [54], ghost fluid methods [42] or a method coupling all three approaches [91]. This method allows in particular to simulate primary breakup processes. In terms of computational cost, it is, however, out of reach for industrial-scale applications.

The second, very popular approach is limited to the representation of a dispersed phase, i.e. a set of droplets, which are tracked individually. This representation of a spray is combined with a classical Eulerian approach for the gaseous phase, which includes the exchange of coupling terms in both directions. Due to the Lagrangian point of view that is taken in the modeling of individual droplets, this method is referred to as the Eulerian-Lagrangian approach.

The third method assumes that the dispersed phase can be viewed as a continuum, for which transport equations can be formulated and solved numerically similarly to the ones of the gaseous phase. As the Eulerian point of view is taken for both phases, it is known as the Eulerian-Eulerian approach.

1.3.3 Combustion

The simulation of turbulent flames is naturally an essential discipline for the simulation of combustion chambers. It interacts very closely with turbulence, the liquid phase and acoustics, but also wall-interaction can be cited as a phenomenon that must be taken into account.

- Chemistry of kerosene flames involves typically hundreds of species and reactions. In order to make the numerical simulation of realistic cases feasible, this very complex system has to be simplified and broken down to the most important mechanisms.
- As typical LES meshes cannot resolve a flame front, additional methodologies are needed. This can be achieved by artificially thickening the flame front [115] or by tracking a surface that corresponds to the flame (G-equation [107] [108]) to name two examples. Furthermore, models for the wrinkling due to subgrid-scale turbulence are necessary.
- In two-phase flow, there is a complex interaction between the flame front and droplets. This includes the burning of individual droplets, group combustion or external sheath combustion of a spray (see figure 1.10). Here, it is the combination of the description for the liquid phase and the way the flame is represented numerically that makes it possible or impossible to take into account certain phenomena. For instance, a thickened flame will not reproduce combustion of individual droplets, even if the Lagrangian approach would allow it in principle. Inversely, a Euler-Euler formulation for the spray cannot simulate individual droplet burning, even if the flame front was entirely resolved. More information on spray combustion regimes can be found in the work of Reveillon [123].

1.3.4 Parallel computing

Large-scale applications in computational fluid mechanics are generally very demanding in terms of computational resources. Today, this need is more and more addressed by parallel machines, which means that numerical solvers have to be conceived with parallelization in mind. The AVBP code in its baseline version (the gaseous, reactive solver) has proven to perform very well on massively parallel architectures [143] [144].

The development of extensions for the simulation of two-phase flows has been focused on the aspect of parallel implementation from the beginning, which is also one of the reasons the Euler-Euler formulation has been favoured for early development. The reason for this lies in the structure of the spray solver that is identical to the gaseous one and therefore adds no additional complexity in terms of parallelization. Consequently, the Euler-Euler solver has proven

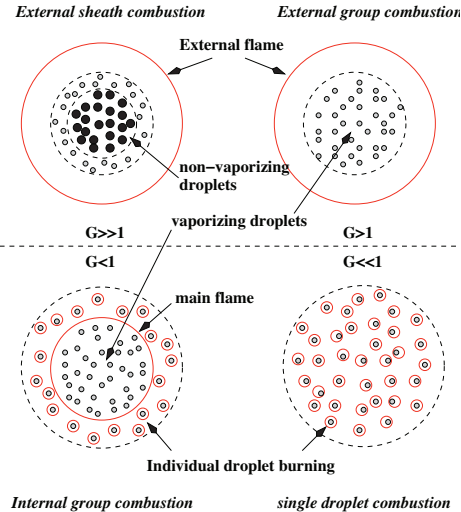


Figure 1.10: Schematic of different spray combustion regimes, from Reveillon and Vervisch [123].

to be capable of tackling very large problems [20].

Some difficulties in the development of a Eulerian-Lagrangian solver lie in the parallel implementation. Here, two basic approaches exist that shall be outlined briefly:

The first is to keep the Lagrangian solver separate from the gaseous one and run both parts on dedicated processors. This method is the easiest to implement but it quickly reaches its limits for large numbers of particles. In this case, the coupling terms between gaseous and liquid phase that have to be channeled through the network between processors become the limiting factor of the approach.

The second method is to run the Lagrangian particles and the gaseous solver simultaneously on each processor. Ideally, the mesh is divided between processors in such a way that particles that are *spatially* inside the partition associated to a given processor are also *numerically* treated by the same processor. This is quite challenging to implement for several reasons: at the initialization of a computation, the partitioning of the mesh has to take into account the spatial distribution of Lagrangian particles as an additional constraint. Furthermore, as the particle field can evolve over time, this partitioning ideally is of a dynamical type that adapts to changes in particle distribution. In its present form, the AVBP Lagrangian code runs the gas phase and the particles simultaneously but does not yet have neither a multi-constrain load balancing nor a dynamical procedure. Detailed information on numerical aspects of the Lagrangian version of AVBP can be found in the work of García [49].

1.4 Scope of the present work

The first objective of this thesis is to provide a contribution to the understanding of spray simulations in a typical future generation aeronautical combustor and to identify determining factors for the quality of such a simulation. The injector to be considered is distinguished by two main characteristics that have not been encountered very frequently in LES simulations in the past. The first is the high degree of geometrical complexity, which translates to an increased focus on wall-modeling. Furthermore, as there are multiple flow paths through the injector, the subject of pressure drop prediction gains in importance compared to past simulations, because mass flux imbalances between different flow paths (here: injector stages) significantly reduce the accuracy of the result.

The second characteristic is the multi-point injection system that has made its appearance in LES simulations only recently. The present study aims at the development of procedures and models to include such an injection in a LES.

The second main objective is to compare different numerical approaches to simulate the liquid phase on cases of increasing complexity up to the simulation of evaporating spray in the industrial-scale TLC configuration. CERFACS is in the unique position to have developed a code that is at the same time capable of performing industrial-scale LES, while combining the gaseous solver with both, an Euler-Euler and an Euler-Lagrange version of a solver for the liquid phase. This allows for the first time to perform direct comparisons between both approaches on large LES cases in an iso-code, iso-mesh and iso-model environment. All parts of this work that are related to two-phase flows are conceived with this direct comparison in mind.

1.5 Organization of this thesis

In the first part of this manuscript, the governing equations for the gaseous and the liquid phase are detailed. The description of the Eulerian and the Lagrangian formulations is followed by a part dedicated to all closure models that are common to both approaches. A particular focus is put on the evaporation model, as the implementation and validation into the Lagrangian code has been an important part in the early stages of the present work. It is followed by a description of the numerical methods involved in the different methods.

The second part is dedicated to preliminary studies and developments that are necessary steps to prepare the final, applicative simulations. This part includes the development of an alternative implementation of wall functions in a cell-vertex numerical solver, which addresses a certain number of issues that have been identified during early stages of this work. The assessment of the wall-modeling approach also includes the analysis of the error on pressure drop in complex geometries. This part also describes methods of practical interest for management of this error in cases it cannot be avoided.

Development concerning two-phase flows is dedicated to the multipoint injection system. Here, the case of a plain, liquid jet in a gaseous crossflow has been identified as an ideal test case for this type of injection. Simple models for the liquid jet region are laid out in detail and the particular aspects of implementation into Eulerian and Lagrangian simulations are detailed.

The subject of the final part is the application of all previously described developments on the final application, the so-called TLC configuration that consists in the SNECMA multi-point injector (see section 1.2.1) mounted in a pressurized test bench. First, the purely gaseous flow is considered. The discussion of the results includes a comparison to experimental data. In a second step, the results of non-reactive two-phase flow inside the TLC configuration are discussed for Eulerian and Lagrangian results with a comparison to the experiment.

Although spray combustion (being a subject of its own) is not inside the scope of this thesis, one-dimensional flame simulations that serve mainly as validation cases for rapid evaporation processes are included as appendices.

Part II

Governing equations

Chapter 2

Governing equations for the gaseous phase

Contents

2.1	Introduction	41
2.2	The governing equations	41
2.2.1	The equation of state	43
2.2.2	Conservation of Mass: Species diffusion flux	43
2.2.3	Viscous stress tensor	44
2.2.4	Heat flux vector	44
2.2.5	Transport coefficients	45
2.3	The LES Concept	46
2.4	The Governing Equations for LES	47
2.4.1	The filtered viscous terms	48
2.4.2	Subgrid-scale turbulent terms for LES	48
2.5	Models for the subgrid stress tensor	49
2.5.1	Smagorinsky model	49
2.5.2	WALE model	50
2.5.3	Filtered Smagorinsky model	50
2.5.4	Dynamic Smagorinsky model	50

2.1 Introduction

This chapter presents the equations for the gas phase that are implemented in the numerical solver AVBP used throughout the present work. The equations shown here are limited to those actually used in the scope of this thesis and therefore not an exhaustive description of AVBP. For more detail, the reader is referred to the official handbook of the AVBP code on which this chapter is based.

2.2 The governing equations

Throughout this part, the index notation (Einstein's rule of summation) is adopted for the description of the governing equations. Note however that index k is reserved to refer to the k^{th}

species and will not follow the summation rule unless specifically mentioned or implied by the \sum sign.

The set of conservation equations describing the evolution of a compressible flow with chemical reactions of thermodynamically active scalars reads,

$$\frac{\partial \rho u_i}{\partial t} + \frac{\partial}{\partial x_j}(\rho u_i u_j) = - \frac{\partial}{\partial x_j}[P \delta_{ij} - \tau_{ij}] + S_{M,i}^{l-g}, \quad (2.1)$$

$$\frac{\partial \rho E}{\partial t} + \frac{\partial}{\partial x_j}(\rho E u_j) = - \frac{\partial}{\partial x_j}[u_i (P \delta_{ij} - \tau_{ij}) + q_j] + S_E, \quad (2.2)$$

$$\frac{\partial \rho_k}{\partial t} + \frac{\partial}{\partial x_j}(\rho_k u_j) = - \frac{\partial}{\partial x_j}[J_{j,k}] + S_k. \quad (2.3)$$

In equations 2.1 to 2.3, which respectively correspond to the conservation laws for momentum, total energy and species, the following symbols (ρ , u_i , E , ρ_k) denote the density, the velocity vector, the total energy per unit mass and the density of the chemical species k : $\rho_k = \rho Y_k$ for $k = 1$ to N (where N is the total number of species). Furthermore, P denotes the pressure, τ_{ij} the stress tensor, q_i the heat flux vector and $J_{j,k}$ the vector of the diffusive flux of species k . There are several source terms: $S_{M,i}^{l-g}$ is the vector of momentum source terms and accounts for the coupling from the dispersed phase to the gas. The source term in the total energy equation (eq. 2.2) can be decomposed into a chemical source term and heat transfer due to droplet evaporation: $S_E = \dot{\omega}_T + S_E^{l-g}$. The source term in the species transport equations (eq. 2.3) contains contributions from chemical production or consumption of species, $\dot{\omega}_k$, as well as the evaporated droplet mass transfer S_F^{l-g} , that is applied to the equation of the evaporating (or fuel-) species F : $S_k = \dot{\omega}_k + S_F^{l-g}$. The term S_F^{l-g} is zero for all other species $k \neq F$.

It is common to distinguish between inviscid and a viscous terms. They are respectively noted for the three conservation equations:

Inviscid terms:

$$\begin{pmatrix} \rho u_i u_j + P \delta_{ij} \\ (\rho E + P \delta_{ij}) u_j \\ \rho_k u_j \end{pmatrix} \quad (2.4)$$

where the pressure P is given by the equation of state for a perfect gas (eq. 2.6).

Viscous terms:

The components of the viscous flux tensor take the form:

$$\begin{pmatrix} -\tau_{ij} \\ -(u_i \tau_{ij}) + q_j \\ J_{j,k} \end{pmatrix} \quad (2.5)$$

J_k is the diffusive flux of species k and is presented in section 2.2.2 (eq. 2.16). The stress tensor τ_{ij} is explicited in section 2.2.3 (eq. 2.17). Finally, section 2.2.4 details the heat flux vector q_j (eq. 2.20).

2.2.1 The equation of state

The equation of state for an ideal gas mixture writes:

$$P = \rho r T \quad (2.6)$$

where r is the gas constant of the mixture dependant on time and space: $r = \frac{R}{W}$ where W is the mean molecular weight of the mixture:

$$\frac{1}{W} = \sum_{k=1}^N \frac{Y_k}{W_k} \quad (2.7)$$

The gas constant r and the heat capacities of the gas mixture depend on the local gas composition as:

$$r = \frac{R}{W} = \sum_{k=1}^N \frac{Y_k}{W_k} \mathcal{R} = \sum_{k=1}^N Y_k r_k \quad (2.8)$$

$$C_p = \sum_{k=1}^N Y_k C_{p,k} \quad (2.9)$$

$$C_v = \sum_{k=1}^N Y_k C_{v,k} \quad (2.10)$$

where $\mathcal{R} = 8.3143 \text{ J/mol.K}$ is the universal gas constant. The adiabatic exponent for the mixture is given by $\gamma = C_p/C_v$. Thus, the gas constant, the heat capacities and the adiabatic exponent are no longer constant. They depend on the local gas composition as expressed by the local mass fractions $Y_k(x, t)$:

$$r = r(x, t), \quad C_p = C_p(x, t), \quad C_v = C_v(x, t), \quad \text{and} \quad \gamma = \gamma(x, t) \quad (2.11)$$

2.2.2 Conservation of Mass: Species diffusion flux

In multi-species flows the total mass conservation implies that:

$$\sum_{k=1}^N Y_k V_i^k = 0 \quad (2.12)$$

where V_i^k are the components in directions ($i=1,2,3$) of the diffusion velocity of species k . They are often expressed as a function of the species gradients using the Hirschfelder Curtis approximation:

$$X_k V_i^k = -D_k \frac{\partial X_k}{\partial x_i}, \quad (2.13)$$

where X_k is the molar fraction of species k : $X_k = Y_k W/W_k$. In terms of mass fraction, the approximation 2.13 may be expressed as:

$$Y_k V_i^k = -D_k \frac{W_k}{W} \frac{\partial X_k}{\partial x_i}, \quad (2.14)$$

Summing equation 2.14 over all k 's shows that the approximation 2.14 does not necessarily comply with equation 2.12 that expresses mass conservation. In order to achieve this, a correction diffusion velocity \vec{V}^c is added to the convection velocity to ensure global mass conservation (see [115]) as:

$$V_i^c = \sum_{k=1}^N D_k \frac{W_k}{W} \frac{\partial X_k}{\partial x_i}, \quad (2.15)$$

and computing the diffusive species flux for each species k as:

$$J_{i,k} = -\rho \left(D_k \frac{W_k}{W} \frac{\partial X_k}{\partial x_i} - Y_k V_i^c \right), \quad (2.16)$$

Here, D_k are the diffusion coefficients for each species k in the mixture (see section 2.2.5). Using equation 2.16 to determine the diffusive species flux implicitly verifies equation 2.12.

2.2.3 Viscous stress tensor

The stress tensor τ_{ij} is given by:

$$\tau_{ij} = 2\mu \left(S_{ij} - \frac{1}{3} \delta_{ij} S_{ll} \right) \quad (2.17)$$

where S_{ij} is the rate of strain tensor

$$S_{ij} = \frac{1}{2} \left(\frac{\partial u_j}{\partial x_i} + \frac{\partial u_i}{\partial x_j} \right) \quad (2.18)$$

Equation 2.17 may also be written:

$$\begin{aligned} \tau_{xx} &= \frac{2\mu}{3} \left(2 \frac{\partial u}{\partial x} - \frac{\partial v}{\partial y} - \frac{\partial w}{\partial z} \right), & \tau_{xy} &= \mu \left(\frac{\partial u}{\partial y} + \frac{\partial v}{\partial x} \right) \\ \tau_{yy} &= \frac{2\mu}{3} \left(2 \frac{\partial v}{\partial y} - \frac{\partial u}{\partial x} - \frac{\partial w}{\partial z} \right), & \tau_{xz} &= \mu \left(\frac{\partial u}{\partial z} + \frac{\partial w}{\partial x} \right) \\ \tau_{zz} &= \frac{2\mu}{3} \left(2 \frac{\partial z}{\partial w} - \frac{\partial u}{\partial x} - \frac{\partial v}{\partial y} \right), & \tau_{yz} &= \mu \left(\frac{\partial v}{\partial z} + \frac{\partial w}{\partial y} \right) \end{aligned} \quad (2.19)$$

where μ is the shear viscosity (see section 2.2.5).

2.2.4 Heat flux vector

For multi-species flows, an additional heat flux term appears in the diffusive heat flux. This term is due to heat transport by species diffusion. The total heat flux vector then takes the form:

$$q_i = \underbrace{-\lambda \frac{\partial T}{\partial x_i}}_{\text{Heat conduction}} - \underbrace{\rho \sum_{k=1}^N \left(D_k \frac{W_k}{W} \frac{\partial X_k}{\partial x_i} - Y_k V_i^c \right) h_{s,k}}_{\text{Heat flux through species diffusion}} = -\lambda \frac{\partial T}{\partial x_i} + \sum_{k=1}^N J_{i,k} h_{s,k} \quad (2.20)$$

where λ is the heat conduction coefficient of the mixture (see section 2.2.5) and $h_{s,k}$ the sensible enthalpy of the species k .

2.2.5 Transport coefficients

In CFD codes for multi-species flows the molecular viscosity μ is often assumed to be independent of the gas composition and close to that of air so that the classical Sutherland law can be used. The same assumption for a multi-species gas yields:

$$\mu = c_1 \frac{T^{3/2}}{T + c_2} \frac{T_{ref} + c_2}{T_{ref}^{3/2}} \quad (2.21)$$

where c_1 and c_2 must be determined so as to fit the real viscosity of the mixture. For air at $T_{ref} = 273$ K, $c_1 = 1.71e-5$ kg/m.s and $c_2 = 110.4$ K (see [155]). A second law is available, called Power law:

$$\mu = c_1 \left(\frac{T}{T_{ref}} \right)^b \quad (2.22)$$

with b typically ranging between 0.5 and 1.0. For example $b = 0.76$ for air.

The heat conduction coefficient of the gas mixture can then be computed by introducing the molecular Prandtl number of the mixture as:

$$\lambda = \frac{\mu C_p}{P_r} \quad (2.23)$$

with P_r supposed constant in time and space.

The computation of the species diffusion coefficients D_k is a specific issue. These coefficients should be expressed as a function of the binary coefficients D_{ij} obtained from kinetic theory (Hirschfelder et al. [64]). The mixture diffusion coefficient for species k , D_k , is computed as (Bird et al. [15]):

$$D_k = \frac{1 - Y_k}{\sum_{j \neq k}^N X_j / D_{jk}} \quad (2.24)$$

The D_{ij} are complex functions of collision integrals and thermodynamic variables. For a simulation involving complex chemistry, using equation 2.24 makes sense. If a simplified chemical scheme is used, modeling diffusivity in a precise way is not needed so that this approach is much less attractive. Therefore, a simplified approximation is used in AVBP for D_k . The Schmidt numbers $S_{c,k}$ of the species are supposed to be constant so that the binary diffusion coefficient for each species is computed as:

$$D_k = \frac{\mu}{\rho S_{c,k}} \quad (2.25)$$

2.3 The LES Concept

Large Eddy Simulation (LES) [128, 116] is nowadays recognized as an intermediate approach in comparison to the more classical Reynolds Averaged Navier-Stokes (RANS) methodologies. Although conceptually very different these two approaches aim at providing new systems of governing equations to mimic the characteristics of turbulent flows.

The derivation of the new governing equations is obtained by introducing operators to be applied to the set of compressible Navier-Stokes equations. Unclosed terms arise from these manipulations and models need to be supplied for the problem to be solved. The major differences between RANS and LES come from the operator employed in the derivation. In RANS the operation consists of a temporal or ensemble average over a set of realizations of the studied flow [116, 26]. The unclosed terms are representative of the physics taking place over the entire range of frequencies present in the ensemble of realizations under consideration. In LES, the operator is a spatially localized time independent filter of given size, Δ , to be applied to a single realization of the studied flow. Resulting from this spatial filtering is a separation between the large (greater than the filter size) and small (smaller than the filter size) scales. The unclosed terms in LES represent the physics associated with the small structures (with high frequencies) present in the flow. Figure 2.1 illustrates the conceptual differences between (a) RANS and (b) LES when applied to a homogeneous isotropic turbulent field.

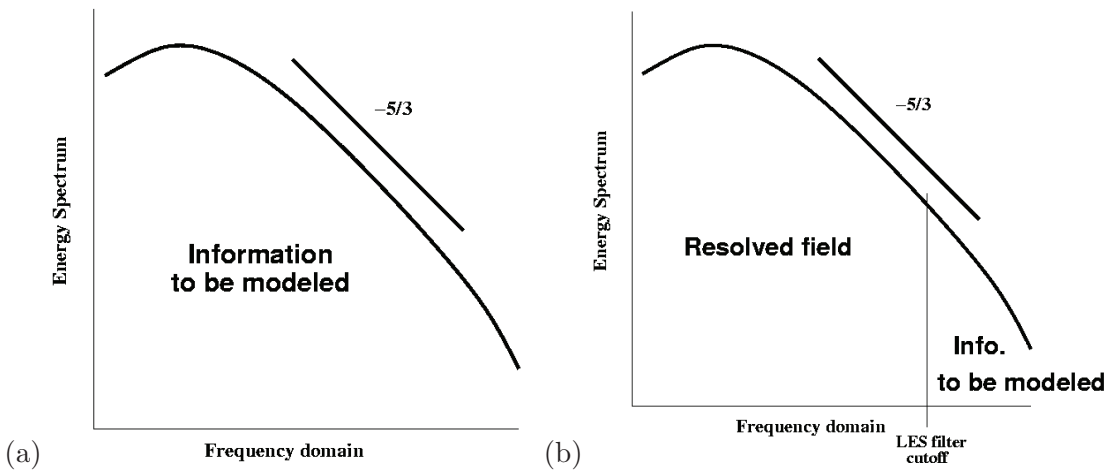


Figure 2.1: Conceptual representation of (a) RANS and (b) LES applied to a homogeneous isotropic turbulent field.

Due to the filtering approach, LES allows a dynamic representation of the large scale motions whose contributions are critical in complex geometries. The LES predictions of complex turbulent flows are therefore closer to the physics since large scale phenomena such as large vortex shedding and acoustic waves are embedded in the set of governing equations [115].

For the reasons presented above, LES has a clear potential in predicting turbulent flows encountered in industrial applications. Such possibilities are however restricted by the hypothesis introduced while constructing LES models.

This chapter describes the equation solved for LES of non-reacting multi-species flows in AVBP. Section 2.5 presents the models used for turbulent viscosity.

2.4 The Governing Equations for LES

The filtered quantity \bar{f} is resolved in the numerical simulation whereas $f' = f - \bar{f}$ is the subgrid scale part (the unresolved motion of the flow). For variable density ρ , a mass-weighted Favre filtering is introduced such as:

$$\bar{\rho} \tilde{f} = \overline{\rho f} \quad (2.26)$$

The conservation equations for large eddy simulation are obtained by filtering the instantaneous equations 2.1, 2.2 and 2.3:

$$\frac{\partial \bar{\rho} \tilde{u}_i}{\partial t} + \frac{\partial}{\partial x_j} (\bar{\rho} \tilde{u}_i \tilde{u}_j) = - \frac{\partial}{\partial x_j} [\bar{P} \delta_{ij} - \overline{\tau_{ij}} - \overline{\tau_{ij}^t}] + \bar{S}_{M,i}^{l-g} \quad (2.27)$$

$$\frac{\partial \bar{\rho} \tilde{E}}{\partial t} + \frac{\partial}{\partial x_j} (\bar{\rho} \tilde{E} \tilde{u}_j) = - \frac{\partial}{\partial x_j} [\overline{u_i (P \delta_{ij} - \tau_{ij})} + \bar{q}_j + \bar{q}_j^t] + \bar{S}_E \quad (2.28)$$

$$\frac{\partial \bar{\rho} \tilde{Y}_k}{\partial t} + \frac{\partial}{\partial x_j} (\bar{\rho} \tilde{Y}_k \tilde{u}_j) = - \frac{\partial}{\partial x_j} [\bar{J}_{j,k} + \bar{J}_{j,k}^t] + \bar{S}_k \quad (2.29)$$

In equations 2.27, 2.28 and 2.29, there are now three types of terms to be distinguished: the inviscid terms, the viscous terms and the subgrid scale terms.

Inviscid terms:

These terms are equivalent to the unfiltered equations except that they now contain filtered quantities:

$$\begin{pmatrix} \bar{\rho} \tilde{u}_i \tilde{u}_j + \bar{P} \delta_{ij} \\ \bar{\rho} \tilde{E} \tilde{u}_j + \bar{P} u_j \delta_{ij} \\ \bar{\rho}_k \tilde{u}_j \end{pmatrix} \quad (2.30)$$

Viscous terms:

The viscous terms take the form:

$$\begin{pmatrix} -\overline{\tau_{ij}} \\ -(u_i \overline{\tau_{ij}}) + \bar{q}_j \\ \bar{J}_{j,k} \end{pmatrix} \quad (2.31)$$

Filtering the balance equations leads to unclosed quantities, which need to be modeled, as presented in sections 2.4.1 and 2.4.2.

Subgrid scale turbulent terms:

The subgrid scale terms are:

$$\begin{pmatrix} -\overline{\tau_{ij}^t} \\ \bar{q}_j^t \\ \bar{J}_{j,k}^t \end{pmatrix} \quad (2.32)$$

2.4.1 The filtered viscous terms

The filtered diffusion terms are (see T. Poinso and D. Veynante, Chapter 4 [115]): the laminar filtered stress tensor $\overline{\tau_{ij}}$, which is given by the following relations:

$$\begin{aligned}\overline{\tau_{ij}} &= \overline{2\mu(S_{ij} - \frac{1}{3}\delta_{ij}S_{ll})}, \\ &\approx 2\overline{\mu}(\tilde{S}_{ij} - \frac{1}{3}\delta_{ij}\tilde{S}_{ll}),\end{aligned}\quad (2.33)$$

and

$$\tilde{S}_{ij} = \frac{1}{2}\left(\frac{\partial\tilde{u}_j}{\partial x_i} + \frac{\partial\tilde{u}_i}{\partial x_j}\right),\quad (2.34)$$

Equation 2.33 may also be written:

$$\begin{aligned}\overline{\tau_{xx}} &\approx \frac{2\overline{\mu}}{3}\left(2\frac{\partial\tilde{u}}{\partial x} - \frac{\partial\tilde{v}}{\partial y} - \frac{\partial\tilde{w}}{\partial z}\right), & \overline{\tau_{xy}} &\approx \overline{\mu}\left(\frac{\partial\tilde{u}}{\partial y} + \frac{\partial\tilde{v}}{\partial x}\right) \\ \overline{\tau_{yy}} &\approx \frac{2\overline{\mu}}{3}\left(2\frac{\partial\tilde{v}}{\partial y} - \frac{\partial\tilde{u}}{\partial x} - \frac{\partial\tilde{w}}{\partial z}\right), & \overline{\tau_{xz}} &\approx \overline{\mu}\left(\frac{\partial\tilde{u}}{\partial z} + \frac{\partial\tilde{w}}{\partial x}\right) \\ \overline{\tau_{zz}} &\approx \frac{2\overline{\mu}}{3}\left(2\frac{\partial\tilde{w}}{\partial z} - \frac{\partial\tilde{u}}{\partial x} - \frac{\partial\tilde{v}}{\partial y}\right), & \overline{\tau_{yz}} &\approx \overline{\mu}\left(\frac{\partial\tilde{v}}{\partial z} + \frac{\partial\tilde{w}}{\partial y}\right)\end{aligned}\quad (2.35)$$

The filtered diffusive species flux vector for non-reactive flows is:

$$\begin{aligned}\overline{J_{i,k}} &= -\rho\left(D_k\frac{W_k}{W}\frac{\partial X_k}{\partial x_i} - Y_k V_i^c\right) \\ &\approx -\overline{\rho}\left(\overline{D}_k\frac{W_k}{W}\frac{\partial \tilde{X}_k}{\partial x_i} - \tilde{Y}_k \tilde{V}_i^c\right),\end{aligned}\quad (2.36)$$

where higher order correlations between the different variables of the expression are assumed negligible.

The filtered heat flux is :

$$\begin{aligned}\overline{q_i} &= -\lambda\frac{\partial T}{\partial x_i} + \sum_{k=1}^N \overline{J_{i,k} h_{s,k}} \\ &\approx -\overline{\lambda}\frac{\partial T}{\partial x_i} + \sum_{k=1}^N \overline{J_{i,k}} \tilde{h}_{s,k}\end{aligned}\quad (2.37)$$

These forms assume that the spatial variations of molecular diffusion fluxes are negligible and can be modelled through simple gradient assumptions.

2.4.2 Subgrid-scale turbulent terms for LES

As highlighted above, filtering the transport equations yields a closure problem evidenced by the so called ‘‘subgrid-scale’’ (sgs) turbulent fluxes (see eq. 2.4). For the system to be solved numerically, closures need to be supplied.

The Reynolds tensor is :

$$\overline{\tau_{ij}^t} = -\overline{\rho}(u_i u_j - \tilde{u}_i \tilde{u}_j)\quad (2.38)$$

$\overline{\tau_{ij}^t}$ is modeled as:

$$\overline{\tau_{ij}^t} = 2\overline{\rho}\nu_t\left(\tilde{S}_{ij} - \frac{1}{3}\delta_{ij}\tilde{S}_{ll}\right),\quad (2.39)$$

This relation is known as the Boussinesq approximation. It relates the subgrid stresses to a quantity that takes the form of a viscosity and is therefore called subgrid-scale turbulent viscosity, ν_t . Models for this term are explained in section 2.5.

The subgrid scale diffusive species flux vector is:

$$\overline{J_{i,k}^t} = \overline{\rho}\left(u_i \tilde{Y}_k - \tilde{u}_i \tilde{Y}_k\right),\quad (2.40)$$

$\overline{J_{i,k}^t}$ is modeled as:

$$\overline{J_{i,k}^t} = -\bar{\rho} \left(D_k^t \frac{W_k}{W} \frac{\partial \tilde{X}_k}{\partial x_i} - \tilde{Y}_k \tilde{V}_i^{c,t} \right), \quad (2.41)$$

with

$$D_k^t = \frac{\nu_t}{S_{c,k}^t} \quad (2.42)$$

The turbulent Schmidt number $S_{c,k}^t = 0.6$ is the same for all species. Note also that having one turbulent Schmidt number for all the species does not imply, $\tilde{V}^{c,t} = 0$ because of the W_k/W term in equation 2.41.

The subgrid scale heat flux vector is:

$$\overline{q_i^t} = \bar{\rho} (\widetilde{u_i E} - \tilde{u}_i \tilde{E}), \quad (2.43)$$

where E is the total energy. In the source code, the modelisation for \tilde{q}^t is written :

$$\overline{q_i^t} = -\lambda_t \frac{\partial \tilde{T}}{\partial x_i} + \sum_{k=1}^N \overline{J_{i,k}^t} \tilde{h}_{s,k}, \quad (2.44)$$

with

$$\lambda_t = \frac{\mu_t \overline{C_p}}{P_r^t}. \quad (2.45)$$

The turbulent Prandtl number is fixed at $P_r^t = 0.6$.

The correction diffusion velocities are then obtained from:

$$\tilde{V}_i^c + \tilde{V}_i^{c,t} = \sum_{k=1}^N \left(\frac{\bar{\mu}}{\bar{\rho} S_{c,k}} + \frac{\mu_t}{\bar{\rho} S_{c,k}^t} \right) \frac{W_k}{W} \frac{\partial \tilde{X}_k}{\partial x_i}, \quad (2.46)$$

and where Eqs. 2.25 and 2.42 are used.

2.5 Models for the subgrid stress tensor

Models for the subgrid-scale turbulent viscosity ν_t are an essential part of a LES. The sgs turbulence models are derived on the theoretical ground that the LES filter is spatially and temporally invariant. Variations in the filter size due to non-uniform meshes are not directly accounted for in the LES models. Change of cell topology is only accounted for through the use of the local cell volume, that is $\Delta = V_{cell}^{1/3}$.

2.5.1 Smagorinsky model

In the Smagorinsky model, the sgs viscosity ν_t is obtained from

$$\nu_t = (C_S \Delta)^2 \sqrt{2 \tilde{S}_{ij} \tilde{S}_{ij}} \quad (2.47)$$

where Δ denotes the characteristic filter width (cube-root of the cell volume), C_S is the model constant set to 0.18 but can vary between 0.1 and 0.18 depending on the flow configuration. The Smagorinsky model [140] was developed in the 1960s and heavily tested for multiple flow

configurations. This closure is characterized by its globally correct prediction of kinetic energy dissipation in homogeneous isotropic turbulence. However, it predicts non-zero turbulent viscosity levels in flow regions of pure shear, which makes it unsuitable for many wall-bounded flows [104]. This also means that its behaviour is too dissipative in transitioning flows [128].

2.5.2 WALE model

In the WALE model, the expression for ν_t takes the form

$$\nu_t = (C_w \Delta)^2 \frac{(s_{ij}^d s_{ij}^d)^{3/2}}{(\tilde{S}_{ij} \tilde{S}_{ij})^{5/2} + (s_{ij}^d s_{ij}^d)^{5/4}} \quad (2.48)$$

with

$$s_{ij}^d = \frac{1}{2} (\tilde{g}_{ij}^2 + \tilde{g}_{ji}^2) - \frac{1}{3} \tilde{g}_{kk}^2 \delta_{ij} \quad (2.49)$$

Δ denotes again the characteristic filter width (cube-root of the cell volume), $C_w = 0.4929$ is the model constant and \tilde{g}_{ij} denotes the resolved velocity gradient. The WALE model [104] was developed for wall bounded flows and allows to obtain correct scaling laws near the wall.

2.5.3 Filtered Smagorinsky model

$$\nu_t = (C_{SF} \Delta)^2 \sqrt{2 \text{HP}(\tilde{S}_{ij}) \text{HP}(\tilde{S}_{ij})} \quad (2.50)$$

with Δ being the filter with, $C_{SF} = 0.37$ is the model constant and $\text{HP}(\tilde{S}_{ij})$ denotes the resolved strain rate tensor obtained from a high-pass filtered velocity field. This model was developed in order to allow a better representation of local phenomena typical of complex turbulent flows [38]. With the Filtered Smagorinsky model, near-wall flows and transition are better predicted than with the standard formulation.

2.5.4 Dynamic Smagorinsky model

$$\nu_t = (C_{SD} \Delta)^2 \sqrt{2 \tilde{S}_{ij} \tilde{S}_{ij}} \quad (2.51)$$

where Δ denotes the filter characteristic length (cube-root of the cell volume). The difference compared to the expression obtained for the conventional Smagorinsky model 2.47 comes from the evaluation of the closure coefficient C_{SD} . In the Dynamic Smagorinsky approach proposed by Germano *et al.* [50], that coefficient is obtained within the simulation and is no more a user defined variable. The expression from which C_{SD} is obtained stems from the Germano inequality and follows Lilly's procedure [87]:

$$C_{SD}^2 = \frac{1}{2} \frac{M_{ij} M_{ij}}{L_{ij} L_{ij}} \quad (2.52)$$

In the previous expression, the following tensors are defined by,

$$M_{ij} = \hat{\Delta}^2 \sqrt{2 \langle \tilde{S}_{ij} \rangle \langle \tilde{S}_{ij} \rangle} \langle \tilde{S}_{ij} \rangle \quad L_{ij} = \langle \tilde{u}_i \rangle \langle \tilde{u}_j \rangle - \langle \tilde{u}_i \tilde{u}_j \rangle, \quad (2.53)$$

and introduce the notion of "test" filter of characteristic length $\hat{\Delta}$ equal to the cubic root of the volume defined by all the cells surrounding the cell of interest. Note that clipping and smoothing ensures none negative values for C_{SD} .

Chapter 3

Governing equations for the dispersed, liquid phase

Contents

3.1	Introduction	51
3.2	The Eulerian-Lagrangian approach	52
3.2.1	Coupling between phases	52
3.3	The mesoscopic Eulerian-Eulerian approach	53
3.3.1	Two-phase eulerian closure models	59
3.3.2	LES equations for the dispersed phase	60
3.3.3	Sub-grid scale models for the dispersed phase	61
3.4	Definition of characteristic diameters in a spray	62

3.1 Introduction

In contrast to newtonian fluid flow descriptions that are mainly based on continuum mechanics with an eulerian point of view, spray dynamics may be described with different theoretical approaches. In the Lagrangian approach (denoted EL), the dispersed phase is considered as a set of discrete particles on which point mechanics apply. In the Eulerian approach (denoted EE), the spray is viewed as a continuum (similar to the Navier-Stokes equations being the continuum description of many molecules) with local mean properties that correspond to the considered set of particles.

Both approaches are implemented in different modules of the AVBP solver that can be coupled with the gaseous part described in chapter 2. As the physical models that appear in EE and EL are identical, their detailed description is centralized in chapter 4.

Assumptions

- (i) The particles are spherical non-deformable droplets, and thus not subject to breakup mechanisms.
- (ii) The density ratio between the liquid and the gas allows to limit the interacting forces to drag.

- (iii) The temperature (and thus the sensible enthalpy) is uniform inside the droplets, which corresponds to the assumption of infinite liquid phase conductivity.
- (iv) The dispersed phase is diluted (the liquid volume fraction $\alpha_l < 0.01$) and the gaseous volume fraction is $1 - \alpha_l \equiv 1$.
- (v) Droplet-droplet interactions (such as collisions) are negligible.

3.2 The Eulerian-Lagrangian approach

In the Lagrangian approach, each droplet is considered individually. This results in a compact set of equations. A purely kinematic relation can be stated for the position $x_{p,i}$ and the velocity $u_{p,i}$ of a given particle:

$$\frac{dx_{p,i}}{dt} = u_{p,i} \quad (3.1)$$

The second relation is the conservation of momentum given by Newton's second law:

$$\frac{du_{p,i}}{dt} = \frac{F_{d,i}}{m_p} \quad (3.2)$$

where $F_{d,i}$ is the vector of the force exerted on the particle. An expression for $F_{d,i}$ is detailed in section 4.2. Note that the direct effect of subgrid-scale fluctuations on the particle motion is neglected. This effect becomes significant when the droplet Stokes number based on the Kolmogorov time scale τ_η approaches unity [41, 96]. However, Apte et al. [6] showed that it is small for swirling flows with subgrid scale energy contents much smaller than those of the resolved scales. The relation governing the evolution of droplet mass is given by:

$$\frac{dm_p}{dt} = -\pi d_p Sh [\rho D_F] \ln(1 + B_M) \quad (3.3)$$

where d_p is the droplet diameter, Sh the Sherwood number and B_M the Spalding number for mass transfer. Details on the derivation of this expression are given in section 4.3.1. The evolution of the temperature of a particle is:

$$\frac{dT_p}{dt} = \frac{1}{m_p C_{p,l}} \Phi_l^c \quad (3.4)$$

where Φ_l^c is the conductive heat transfer inside the droplet and $C_{p,l}$ the liquid phase heat capacity at constant pressure.

3.2.1 Coupling between phases

The right-hand side terms of equations 3.2 to 3.4 depend on variables of the gas phase. To effect this direct coupling, gaseous quantities have to be interpolated from the Eulerian grid to the particle position. The value of an arbitrary gaseous variable $f_{g@p}$ at the particle p is obtained from

$$f_{g@p} = \sum_{j \in K_e} w(x_{p,i}, x_{j,i}) \bar{f}_{g,j} \quad (3.5)$$

In the grid cell e considered, the value is summed over all nodes j located at the vertices K_e of the cell. Each contribution is weighted by $w(x_{p,i}, x_{j,i})$ that is given by an interpolation function. Note that the values transferred to the particles in a LES are always the resolved (or filtered) ones. More information on the interpolation schemes can be found in section 5.9.2 where numerical aspects of the Lagrangian solver are described.

Additional coupling terms appear at the transfer from the liquid to the gas phase, the so-called two-way coupling (or inverse coupling). In the Lagrangian solver, a generic two-way coupling term, noted S_p , generated at a particle k that is located inside the grid cell e is transferred to the Eulerian grid in the following way: the contribution received by a given grid node j is obtained by the summation of all weighted contributions from all particles inside \mathcal{D}_j , the set of cells having a vertex coinciding with j (see figure 3.1 for a schematic):

$$S_j = \frac{1}{V_j} \sum_{k \in \mathcal{D}_j} \Theta_{j,e}^{(k)} S_p^{(k)} \quad (3.6)$$

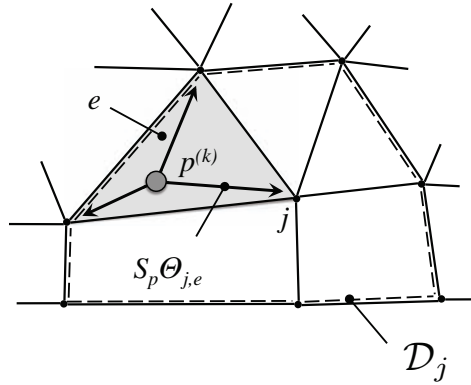


Figure 3.1: Distribution of the source terms generated by a Lagrangian particle k to the Eulerian grid.

As the source terms in the gaseous equations are quantities measured per unit volume, the sum is divided by V_j , the nodal control volume or the median dual cell. The weights $\Theta_{j,e}^{(k)}$ are given by a distribution function that is detailed in section 5.9.3. Details on the actual source terms can be found in chapter 4, where models for the transfer terms between phases are presented.

3.3 The mesoscopic Eulerian-Eulerain approach

In the Euler-Euler approach, the description of the history of each particle is replaced by the description of their mean properties, regarding the spray as a continuous fluid. The averaging procedure – volumic or statistical – leads in principle to two different formulations that differ by their respective assumptions, the definition of the mean properties and the models used to close the transport equations. However the resulting sets of equations are very similar. In AVBP the statistical average is used as described below.

Statistical average

The Euler-Euler equations are obtained from the statistical average applied to the flow description issued from the kinetic theory of gases [25, 74, 102]. The main steps are summarized here as follows:

1. a number density function is defined, conditioned by one realisation of the carrying flow
2. a transport equation is written to describe the evolution of this function
3. a local statistical average operator is defined from this function
4. the product of the transport equation by any spray function Ψ (droplet number, density, temperature), and the statistical averaging lead to the general Enskog equation
5. replacing Ψ with appropriate quantities, a system of conservation equations is established for the mean spray dynamics, named *mesoscopic*
6. models are developed to close the terms linked to the uncorrelated motion and the exchange terms between the two phases that appear in the equations

Note that this procedure does not include any averaging due to LES filtering, which is presented in section 3.3.2.

Due to the description of the spray in mesoscopic quantities, additional assumptions are necessary:

- (vi) The low impact of the diluted liquid phase on the carrying phase allows to condition the statistics on one realisation only of the carrying phase.
- (vii) The spray is locally monodisperse.
- (viii) Droplets have locally the same temperature (mono-temperature spray).

Definitions

Mass Statistical Average

Similarly to the Favre average introduced for compressible gaseous flows with density variation, it is useful to define a mass-weighted average for the particles:

$$\check{\Psi} = \langle \Psi \rangle_l = \frac{1}{\rho_l \check{\alpha}_l} \int m_p \Psi(u_p, T_p, m_p) f_p(u_p, T_p, m_p | \mathcal{H}_f) du_p dT_p dm_p \quad (3.7)$$

Here, $f_p(u_p, T_p, m_p | \mathcal{H}_f)$ is a probability function of the particle density, conditioned on a flow realization \mathcal{H}_f . ρ_l is the liquid density and $\check{\alpha}_l$ is the volume fraction of the dispersed phase defined by:

$$\rho_l \check{\alpha}_l = \int \mu_p f_p(u_p, T_p, m_p | \mathcal{H}_f) du_p dT_p dm_p \quad (3.8)$$

Mesoscopic and uncorrelated motions

Replacing Ψ with the particle velocity \mathbf{u}_p gives the local instantaneous mean velocity of the liquid spray, conditioned on the gaseous flow realization \mathcal{H}_f :

$$\check{\mathbf{u}}_l(\mathbf{x}, t | \mathcal{H}_f) = \langle \mathbf{u}_p \rangle_l \quad (3.9)$$

where $\check{\mathbf{u}}_l$ is a mean eulerian velocity called *mesoscopic velocity*. Each individual particle located at \mathbf{x} at time t has its own velocity \mathbf{u}_p that is the summation of the *mesoscopic velocity* and a residual velocity \mathbf{u}_p'' called *uncorrelated velocity*:

$$\mathbf{u}_p = \check{\mathbf{u}}_l + \mathbf{u}_p'' \quad \text{with} \quad \langle \mathbf{u}_p'' \rangle_l = 0 \quad (3.10)$$

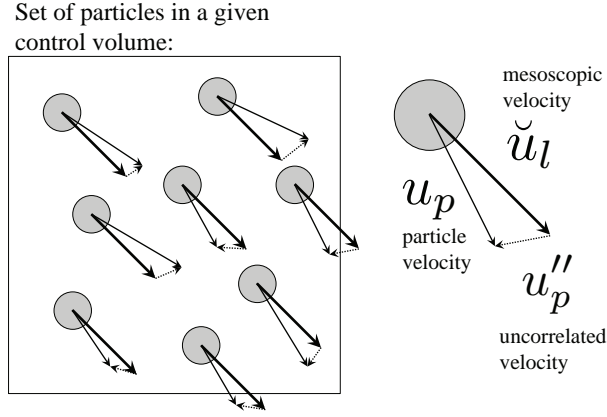


Figure 3.2: Decomposition of the lagrangian particle velocity \mathbf{u}_p into a mesoscopic part $\check{\mathbf{u}}_l$ and an uncorrelated part \mathbf{u}_p''

This velocity decomposition allows to see the spray as a set of particles with the same *mesoscopic motion* while each particle has its own motion at the *uncorrelated velocity* (cf. Fig. 3.2).

The modelling of the uncorrelated motion introduces a number of quantities such as the uncorrelated velocity tensor $\delta\check{R}_l$:

$$\delta\check{R}_{l,ij}(\mathbf{x}, t|\mathcal{H}_f) = \langle u_{p,i}'' u_{p,j}'' \rangle_l \quad (3.11)$$

and the uncorrelated energy $\delta\check{\theta}_l$:

$$\delta\check{\theta}_l = \frac{1}{2} \langle u_{p,i}'' u_{p,i}'' \rangle_l \quad (3.12)$$

$\delta\check{\theta}_l$ corresponds to the half-trace of the uncorrelated velocity tensor and obeys a transport equation. It is analogous to a “temperature” of the dispersed phase.

The deviatoric part of the uncorrelated velocity tensor $\delta\check{R}_l^*$ is:

$$\delta\check{R}_{l,ij}^* = \delta\check{R}_{l,ij} - \frac{2}{3} \delta\check{\theta}_l \delta_{ij} \quad (3.13)$$

The Enskog equation

Multiplying the Boltzmann equation with any particle function Ψ and integrating in the phase space ($\int \cdot du_p dT_p dm_p$), one obtains *the general form of the Enskog equation*:

$$\begin{aligned} \frac{\partial}{\partial t} \rho_l \check{\alpha}_l \langle \Psi \rangle_l + \frac{\partial}{\partial x_i} \rho_l \check{\alpha}_l \langle u_{p,i} \Psi \rangle_l &= \mathbf{C}(m_p \Psi) \\ &+ \rho_l \check{\alpha}_l \left\langle \frac{du_{p,j}}{dt} \frac{\partial \Psi}{\partial u_{p,j}} \right\rangle_l + \rho_l \check{\alpha}_l \left\langle \frac{dT_p}{dt} \frac{\partial \Psi}{\partial T_p} \right\rangle_l \\ &+ \rho_l \check{\alpha}_l \left\langle \frac{dm_p}{dt} \left(\frac{\partial \Psi}{\partial m_p} + \frac{\Psi}{m_p} \right) \right\rangle_l \end{aligned} \quad (3.14)$$

where $\mathbf{C}(m_p \Psi)$ is the variation of $\rho_l \check{\alpha}_l \check{\Psi}$ due to interactions between particles. Noting that

$\langle u_{p,i}\Psi \rangle_l = \langle u_{p,i} \rangle_l \langle \Psi \rangle_l + \langle u''_{p,i}\Psi \rangle_l$, Eq. 3.14 may be rewritten as:

$$\begin{aligned} \frac{\partial}{\partial t} \rho_l \check{\alpha}_l \check{\Psi} + \frac{\partial}{\partial x_i} \rho_l \check{\alpha}_l \check{u}_{l,i} \check{\Psi} &= \mathbf{T}(\Psi) + \mathbf{C}(m_p \Psi) \\ &+ \rho_l \check{\alpha}_l \left\langle \frac{du_{p,j}}{dt} \frac{\partial \Psi}{\partial u_{p,j}} \right\rangle_l + \rho_l \check{\alpha}_l \left\langle \frac{dT_p}{dt} \frac{\partial \Psi}{\partial T_p} \right\rangle_l \\ &+ \rho_l \check{\alpha}_l \left\langle \frac{dm_p}{dt} \left(\frac{\partial \Psi}{\partial m_p} + \frac{\Psi}{m_p} \right) \right\rangle_l \end{aligned} \quad (3.15)$$

where $\mathbf{T}(\Psi)$ is the uncorrelated flux operator defined as:

$$\mathbf{T}(\Psi) = -\frac{\partial}{\partial x_i} \rho_l \check{\alpha}_l \langle u''_{p,i}\Psi \rangle_l \quad (3.16)$$

When Ψ also varies in time and space (the uncorrelated energy for example, see Eq. 3.21), the following terms appear in the right hand side term of Eq. 3.14 and 3.15:

$$\rho_l \check{\alpha}_l \left\langle \frac{\partial}{\partial t} \Psi \right\rangle_l + \rho_l \check{\alpha}_l \left\langle u_{p,i} \frac{\partial}{\partial x_j} \Psi \right\rangle_l \quad (3.17)$$

Conservation equations

Number density Taking $\Psi = \frac{1}{m_p}$, one obtains:

$$\frac{\partial}{\partial t} \check{n}_l + \frac{\partial}{\partial x_i} \check{n}_l \check{u}_{l,i} = \mathbf{T}(m_p^{-1}) + \mathbf{C}(1) \quad (3.18)$$

Note that in the case of a monodisperse spray, all particles have locally the same mass ($m_p = \text{const}$) so that: $\mathbf{T}(m_p^{-1}) = -\frac{\partial}{\partial x_i} \rho_l \check{\alpha}_l \left\langle \frac{u''_{p,i}}{m_p} \right\rangle_l = 0$. The collisional term $\mathbf{C}(1)$ is set to 0 in AVBP.

Volume fraction

Taking $\Psi = 1$, one obtains:

$$\frac{\partial}{\partial t} \rho_l \check{\alpha}_l + \frac{\partial}{\partial x_i} \rho_l \check{\alpha}_l \check{u}_{l,i} = \mathbf{T}(1) + \mathbf{C}(m_p) + \Gamma_l \quad (3.19)$$

where $\mathbf{T}(1) = 0$ et $\Gamma_l = -\Gamma = \rho_l \check{\alpha}_l \left\langle \frac{1}{m_p} \frac{dm_p}{dt} \right\rangle_l$ is the rate of change of mass through phase exchange (evaporation). The collisional term $\mathbf{C}(m_p)$ is set to 0 in AVBP.

Momentum

Taking $\Psi = \mathbf{u}_p$, one obtains:

$$\frac{\partial}{\partial t} \rho_l \check{\alpha}_l \check{u}_{l,i} + \frac{\partial}{\partial x_j} \rho_l \check{\alpha}_l \check{u}_{l,i} \check{u}_{l,j} = \mathbf{T}(u''_{p,i}) + \mathbf{C}(m_p \mathbf{u}_p) + F_{d,i} + \Gamma_{u,i} \quad (3.20)$$

$\mathbf{T}(u''_{p,i})$ represents the transport of momentum by the uncorrelated motion. $\mathbf{C}(m_p \mathbf{u}_p)$ is the exchange of momentum among particles (collisions, breakup, coalescence, etc.) and is set to 0 in AVBP. $F_{d,i} = \rho_l \check{\alpha}_l \left\langle \frac{F_{p,i}}{m_p} \right\rangle_l$ is the exchange of momentum with the gaseous phase via the drag force \mathbf{F}_p exerted on each particle. $\Gamma_{u,i} = \rho_l \check{\alpha}_l \left\langle \frac{u_{p,i}}{m_p} \frac{dm_p}{dt} \right\rangle_l$ is the exchange of momentum with the gaseous phase through mass exchange. In the case of a monodisperse spray where particles have locally the same temperature (mono-temperature spray), one has: $\Gamma_{u,i} = \Gamma_l \check{u}_{l,i}$.

Uncorrelated energy

Taking $\Psi = \frac{1}{2} (u_{p,i} - \check{u}_{l,i}) (u_{p,i} - \check{u}_{l,i}) = \frac{1}{2} u''_{p,i} u''_{p,i}$ and adding the terms of Eq. 3.17 to the Enskog equation (Eq. 3.15), one obtains:

$$\frac{\partial}{\partial t} \rho_l \check{\alpha}_l \delta \check{\theta}_l + \frac{\partial}{\partial x_i} \rho_l \check{\alpha}_l \check{u}_{l,i} \delta \check{\theta}_l = \mathbf{T} \left(\frac{1}{2} u''_{p,i} u''_{p,i} \right) + \mathbf{C} \left(\frac{1}{2} m_p u''_{p,i} u''_{p,i} \right) + W_\theta + \Gamma_\theta + \mathbf{U}_\theta \quad (3.21)$$

$\mathbf{T} \left(\frac{1}{2} u''_{p,i} u''_{p,i} \right)$ represents the transport of uncorrelated energy by the uncorrelated motion. $\mathbf{C} (m_p \mathbf{u}_p)$ is the exchange of uncorrelated energy between particles. $W_\theta = \rho_l \check{\alpha}_l \left\langle u''_{p,i} \frac{F_{p,i}}{m_p} \right\rangle_l$ is the uncorrelated energy variation due to drag. $\Gamma_\theta = \rho_l \check{\alpha}_l \left\langle \frac{1}{2} \frac{u''_{p,i} u''_{p,i}}{m_p} \frac{dm_p}{dt} \right\rangle_l$ is the uncorrelated energy variation due the mass transfer between the phases. For a monodisperse and mono-temperature spray, one has: $\Gamma_\theta = \Gamma_l \delta \check{\theta}_l$. Finally, $\mathbf{U}_\theta = -\rho_l \check{\alpha}_l \delta \check{R}_{l,ij} \frac{\partial \check{u}_{l,i}}{\partial x_j}$ comes from additional terms (Eq. 3.17) and includes the effects of the uncorrelated tensor $\delta \check{R}_l$ on the uncorrelated energy.

Sensible enthalpy

Taking $\Psi = h_{s,p}$, one obtains:

$$\frac{\partial}{\partial t} \rho_l \check{\alpha}_l \check{h}_{s,l} + \frac{\partial}{\partial x_j} \rho_l \check{\alpha}_l \check{u}_{l,j} \check{h}_{s,l} = \mathbf{T} (h''_p) + \mathbf{C} (m_p h_{s,p}) + \Pi_l \quad (3.22)$$

$\mathbf{T} (h''_p)$ represents the transport of sensible enthalpy by the uncorrelated motion. $\mathbf{C} (m_p \mathbf{u}_p)$ is the exchange of sensible enthalpy between particles, assumed to be 0 in the present work. Π_l is the sensible enthalpy rate of change per unit volume due to evaporation.

Summary of conservation equations

The conservation equations for the dispersed phase are:

$$\frac{\partial}{\partial t} \check{n}_l + \frac{\partial}{\partial x_j} \check{n}_l \check{u}_{l,j} = 0 \quad (3.23)$$

$$\frac{\partial}{\partial t} \rho_l \check{\alpha}_l + \frac{\partial}{\partial x_j} \rho_l \check{\alpha}_l \check{u}_{l,j} = S_\alpha^{g-l} \quad (3.24)$$

$$\frac{\partial}{\partial t} \rho_l \check{\alpha}_l \check{u}_{l,i} + \frac{\partial}{\partial x_j} \rho_l \check{\alpha}_l \check{u}_{l,i} \check{u}_{l,j} = \mathbf{T} (u''_{p,i}) + S_{ML,i}^{g-l} \quad (3.25)$$

$$\frac{\partial}{\partial t} \rho_l \check{\alpha}_l \delta \check{\theta}_l + \frac{\partial}{\partial x_i} \rho_l \check{\alpha}_l \check{u}_{l,i} \delta \check{\theta}_l = \mathbf{T} \left(\frac{1}{2} u''_{p,i} u''_{p,i} \right) + \mathbf{U}_\theta + S_R^{g-l} \quad (3.26)$$

$$\frac{\partial}{\partial t} \rho_l \check{\alpha}_l \check{h}_{s,l} + \frac{\partial}{\partial x_i} \rho_l \check{\alpha}_l \check{u}_{l,i} \check{h}_{s,l} = S_{El}^{g-l} \quad (3.27)$$

Temporal evolution	Mesoscopic movement	Uncorrelated movement	Source terms
-----------------------	------------------------	--------------------------	-----------------

Equations. 3.23–3.27 may be rewritten in a more compact form:

$$\frac{\partial \mathbf{w}_l}{\partial t} + \nabla \cdot \mathbf{F}_l = \mathbf{s}_l \quad (3.28)$$

where $\mathbf{w}_l = (\check{n}_l, \rho_l \check{\alpha}_l, \rho_l \check{\alpha}_l \check{u}_l, \rho_l \check{\alpha}_l \check{v}_l, \rho_l \check{\alpha}_l \check{w}_l, \rho_l \check{\alpha}_l \delta \check{\theta}_l, \rho_l \check{\alpha}_l \check{h}_{s,l})^T$ is the vector of conservative mesoscopic variables of the liquid phase with \check{u}_l, \check{v}_l et \check{w}_l the three components of the liquid mesoscopic velocity: $\check{\mathbf{u}}_l = (\check{u}_l, \check{v}_l, \check{w}_l)^T$. \mathbf{F}_l is the flux tensor of the liquid phase composed of convection by mesoscopic motion \mathbf{F}_l^M and uncorrelated motion \mathbf{F}_l^U :

$$\mathbf{F}_l = \mathbf{F}_l^M(\mathbf{w}_l) + \mathbf{F}_l^U(\mathbf{u}_p'') \quad (3.29)$$

The tensors \mathbf{F}_l^M et \mathbf{F}_l^U are respectively written:

$$\mathbf{F}_l^M = (\mathbf{f}_l^M, \mathbf{g}_l^M, \mathbf{h}_l^M)^T \quad (3.30)$$

$$\mathbf{F}_l^U = (\mathbf{f}_l^U, \mathbf{g}_l^U, \mathbf{h}_l^U)^T \quad (3.31)$$

The three components $\mathbf{f}_l^M, \mathbf{g}_l^M$ et \mathbf{h}_l^M are defined as:

$$\mathbf{f}_l^M = \begin{pmatrix} \check{n}_l \check{u}_l \\ \rho_l \check{\alpha}_l \check{u}_l \\ \rho_l \check{\alpha}_l \check{u}_l^2 \\ \rho_l \check{\alpha}_l \check{u}_l \check{v}_l \\ \rho_l \check{\alpha}_l \check{u}_l \check{w}_l \\ \rho_l \check{\alpha}_l \check{u}_l \delta \check{\theta}_l \\ \rho_l \check{\alpha}_l \check{u}_l \check{h}_{s,l} \end{pmatrix}, \mathbf{g}_l^M = \begin{pmatrix} \check{n}_l \check{v}_l \\ \rho_l \check{\alpha}_l \check{v}_l \\ \rho_l \check{\alpha}_l \check{u}_l \check{v}_l \\ \rho_l \check{\alpha}_l \check{v}_l^2 \\ \rho_l \check{\alpha}_l \check{v}_l \check{w}_l \\ \rho_l \check{\alpha}_l \check{v}_l \delta \check{\theta}_l \\ \rho_l \check{\alpha}_l \check{v}_l \check{h}_{s,l} \end{pmatrix}, \mathbf{h}_l^M = \begin{pmatrix} \check{n}_l \check{w}_l \\ \rho_l \check{\alpha}_l \check{w}_l \\ \rho_l \check{\alpha}_l \check{u}_l \check{w}_l \\ \rho_l \check{\alpha}_l \check{v}_l \check{w}_l \\ \rho_l \check{\alpha}_l \check{w}_l^2 \\ \rho_l \check{\alpha}_l \check{w}_l \delta \check{\theta}_l \\ \rho_l \check{\alpha}_l \check{w}_l \check{h}_{s,l} \end{pmatrix} \quad (3.32)$$

The three components of the flux tensor associated to uncorrelated motion $\mathbf{f}_l^U, \mathbf{g}_l^U$ et \mathbf{h}_l^U are:

$$\mathbf{f}_l^U = \begin{pmatrix} 0 \\ 0 \\ \rho_l \check{\alpha}_l \delta \check{R}_{l,xx} \\ \rho_l \check{\alpha}_l \delta \check{R}_{l,xy} \\ \rho_l \check{\alpha}_l \delta \check{R}_{l,xz} \\ \rho_l \check{\alpha}_l \delta \check{S}_{l,ix} \\ 0 \end{pmatrix}, \mathbf{g}_l^U = \begin{pmatrix} 0 \\ 0 \\ \rho_l \check{\alpha}_l \delta \check{R}_{l,xy} \\ \rho_l \check{\alpha}_l \delta \check{R}_{l,yy} \\ \rho_l \check{\alpha}_l \delta \check{R}_{l,yz} \\ \rho_l \check{\alpha}_l \delta \check{S}_{l,iy} \\ 0 \end{pmatrix}, \mathbf{h}_l^U = \begin{pmatrix} 0 \\ 0 \\ \rho_l \check{\alpha}_l \delta \check{R}_{l,xz} \\ \rho_l \check{\alpha}_l \delta \check{R}_{l,yz} \\ \rho_l \check{\alpha}_l \delta \check{R}_{l,zz} \\ \rho_l \check{\alpha}_l \delta \check{S}_{l,iz} \\ 0 \end{pmatrix} \quad (3.33)$$

where \mathbf{s}_l is the source vector including the exchanges with the gas \mathbf{s}_{g-l} and the uncorrelated motion contributions \mathbf{s}_θ :

$$\mathbf{s}_l = \mathbf{s}_{g-l} + \mathbf{s}_\theta \quad (3.34)$$

The \mathbf{s}_{g-l} term contains mass, momentum and energy transfer:

$$\mathbf{s}_{g-l} = \begin{pmatrix} 0 \\ S_\alpha \\ S_{Ml,1}^{g-l} \\ S_{Ml,2}^{g-l} \\ S_{Ml,3}^{g-l} \\ S_R^{g-l} \\ S_{El}^{g-l} \end{pmatrix} = \begin{pmatrix} 0 \\ -\Gamma \\ -\Gamma \check{u}_l + F_{d,x} \\ -\Gamma \check{v}_l + F_{d,y} \\ -\Gamma \check{w}_l + F_{d,z} \\ -\Gamma \delta \check{\theta}_l + W_\theta \\ \Pi_l \end{pmatrix} \quad (3.35)$$

while \mathbf{s}_θ only contains the additional term that appears when deriving the uncorrelated energy equation:

$$\mathbf{s}_\theta = (0, 0, 0, 0, 0, \mathbf{U}_\theta, 0)^T \quad (3.36)$$

The vectors \mathbf{F}_l^U , \mathbf{s}_{g-l} and \mathbf{s}_θ require modelling, described in section 3.3.1. The corresponding source terms in the gaseous phase are:

$$\mathbf{s}_{l-g} = \begin{pmatrix} S_{M,1}^{l-g} \\ S_{M,2}^{l-g} \\ S_{M,3}^{l-g} \\ S_E^{l-g} \\ S_F^{l-g} \end{pmatrix} = \begin{pmatrix} \Gamma \check{u}_l - F_{d,x} \\ \Gamma \check{v}_l - F_{d,y} \\ \Gamma \check{w}_l - F_{d,z} \\ \Pi_g + \Gamma \frac{1}{2} \check{u}_{l,i}^2 - \check{u}_{l,i} F_{d,i} \\ \Gamma \delta_{k,F} \end{pmatrix} \quad (3.37)$$

$\Gamma \frac{1}{2} \check{u}_{l,i}^2$ and $-\check{u}_{l,i} F_{d,i}$ correspond respectively to evaporation and drag effects on the gaseous total energy. Π_g corresponds to the internal sensible energy transfer by evaporation processes (see section 4).

Note that conservation of momentum imposes that $S_{M,i}^{l-g} = S_{Ml,i}^{g-l}$ and conservation of species mass that $S_\alpha = S_F^{l-g}$. Additional terms appear for the energy phase exchange term S_E^{l-g} as the equations are written in terms of total energy on the gaseous side and in terms of sensible enthalpy for the liquid phase.

3.3.1 Two-phase eulerian closure models

The set of equations 3.23 to 3.27 contains unclosed terms. Those terms that are common to EL and EE are described in detail in chapter 4.

Random uncorrelated motion

An additional closure model that appears in the EE framework only is needed for the random uncorrelated movement (RUM). Development and evaluation of such models is still ongoing [125] [129] [150] and not in the scope of this work - the terms related to the RUM are therefore left unclosed. This has no consequence on the time-averaged results (apart from additional diffusion that would be caused by the RUM), as shown by Riber [124] in her thesis. The RUM can, however, contain a non-negligible fraction of the fluctuations. RMS levels of EE results can therefore be expected to be lower than their experimental or Lagrangian counterparts. Février et al. [45] as well as Vance et al. [149] studied homogeneous isotropic turbulence and a periodic channel flow respectively and proposed a correlation that relates the fluctuations of the mesoscopic velocities \check{u}' and the uncorrelated contribution to the fluctuations, δu_l :

$$\langle \delta u_{l,i} \delta u_{l,i} \rangle = \langle \check{u}'_{l,i} \check{u}'_{l,i} \rangle \frac{\langle \check{u}'_{l,i} \check{u}'_{l,i} \rangle \langle u'_i u'_i \rangle}{\langle u'_i \check{u}'_{l,i} \rangle^2} - \langle \check{u}'_{l,i} \check{u}'_{l,i} \rangle \quad (3.38)$$

This expression contains the correlation between gaseous and liquid velocity fluctuations, $\langle u'_i \check{u}'_{l,i} \rangle$, which can be included into the time-averaged solutions of an EE simulation. An approximation made in this context is to consider the gaseous velocity equal to the filtered velocity available in a LES, thus $u_i = \bar{u}_i$.

Even without the use of a dedicated model for the impact of RUM on the mesoscopic liquid-phase velocity field, this contribution can be added a posteriori to the fluctuation field. This method has been applied successfully by Riber [124] and also by Simson in a his EE study of the TLC configuration with hollow-cone injection [138].

In the previous section, the mesoscopic equations were presented. They must now be spatially filtered to obtain the LES equations.

3.3.2 LES equations for the dispersed phase

LES Filtering

The LES filtering is identical to the filtering procedure used for the gaseous phase equations. The Favre average for the dispersed phase is similar to the Favre average of the gaseous phase and is obtained by using the mesoscopic volume fraction $\check{\alpha}_l$ instead of the gaseous density ρ :

$$\overline{\alpha_l \hat{f}_l} = \overline{\check{\alpha}_l \check{f}_l} \quad (3.39)$$

where $\overline{\alpha}_l$ is the filtered volume fraction of the liquid. If the spray is monodisperse at the filter size, the liquid Favre average may be equivalently defined with the number density as:

$$\overline{\check{n}_l \check{f}_l} = \frac{\overline{6\check{\alpha}_l \check{f}_l}}{\pi \check{d}^3} = \frac{6}{\pi \check{d}^3} \overline{\alpha_l \hat{f}_l} = \overline{\check{n}_l \hat{f}_l} \quad (3.40)$$

where $\overline{\check{n}_l}$ is the filtered number density and \check{d} is the mesoscopic diameter for which it is supposed that $\overline{\check{d}} = \check{d}$, or: $\check{d}' = 0$.

The filtering of the conservation equations of the dispersed phase derived in the previous section gives the LES equations. Modelling of the sub-grid terms is described in section 3.3.3.

$$\frac{\partial \overline{\mathbf{w}}_l}{\partial t} + \nabla \cdot \overline{\mathbf{F}}_l = \overline{\mathbf{s}}_l \quad (3.41)$$

where $\overline{\mathbf{w}}_l = (\overline{\check{n}_l}, \rho_l \overline{\check{\alpha}_l}, \rho_l \overline{\check{\alpha}_l} \hat{u}_l, \rho_l \overline{\check{\alpha}_l} \hat{v}_l, \rho_l \overline{\check{\alpha}_l} \hat{w}_l, \rho_l \overline{\check{\alpha}_l} \hat{h}_l)^T$ is the vector of the filtered mesoscopic conservative variables of the liquid phase with \hat{u}_l , \hat{v}_l and \hat{w}_l the three velocity components: $\hat{\mathbf{u}}_l = (\hat{u}_l, \hat{v}_l, \hat{w}_l)^T$. $\overline{\mathbf{F}}_l$ is the filtered flux tensor defined by $\overline{\mathbf{F}}_l = (\overline{\mathbf{f}}_l, \overline{\mathbf{g}}_l, \overline{\mathbf{h}}_l)^T$ and $\overline{\mathbf{s}}_l$ the filtered source term. The fluxes $\overline{\mathbf{f}}_l$, $\overline{\mathbf{g}}_l$, $\overline{\mathbf{h}}_l$ are split in three contributions:

$$\begin{aligned} \overline{\mathbf{f}}_l &= \overline{\mathbf{f}}_l^M + \overline{\mathbf{f}}_l^t \\ \overline{\mathbf{g}}_l &= \overline{\mathbf{g}}_l^M + \overline{\mathbf{g}}_l^t \\ \overline{\mathbf{h}}_l &= \overline{\mathbf{h}}_l^M + \overline{\mathbf{h}}_l^t \end{aligned} \quad (3.42)$$

with:

$$\begin{aligned} \text{The resolved mesoscopic contribution:} & \quad \overline{\mathbf{f}}_l^M, \overline{\mathbf{g}}_l^M, \overline{\mathbf{h}}_l^M \\ \text{The sub-grid contribution:} & \quad \overline{\mathbf{f}}_l^t, \overline{\mathbf{g}}_l^t, \overline{\mathbf{h}}_l^t \end{aligned}$$

Resolved mesoscopic fluxes

The three components of the resolved mesoscopic flux tensor are defined as:

$$\overline{\mathbf{f}}_l^M = \begin{pmatrix} \overline{\check{n}_l} \hat{u}_l \\ \rho_l \overline{\check{\alpha}_l} \hat{u}_l \\ \rho_l \overline{\check{\alpha}_l} \hat{u}_l^2 \\ \rho_l \overline{\check{\alpha}_l} \hat{u}_l \hat{v}_l \\ \rho_l \overline{\check{\alpha}_l} \hat{u}_l \hat{w}_l \\ \rho_l \overline{\check{\alpha}_l} \hat{u}_l \hat{\delta}\theta_l \\ \rho_l \overline{\check{\alpha}_l} \hat{u}_l \hat{h}_l \end{pmatrix}, \quad \overline{\mathbf{g}}_l^M = \begin{pmatrix} \overline{\check{n}_l} \hat{v}_l \\ \rho_l \overline{\check{\alpha}_l} \hat{v}_l \\ \rho_l \overline{\check{\alpha}_l} \hat{u}_l \hat{v}_l \\ \rho_l \overline{\check{\alpha}_l} \hat{v}_l^2 \\ \rho_l \overline{\check{\alpha}_l} \hat{v}_l \hat{w}_l \\ \rho_l \overline{\check{\alpha}_l} \hat{v}_l \hat{\delta}\theta_l \\ \rho_l \overline{\check{\alpha}_l} \hat{v}_l \hat{h}_l \end{pmatrix}, \quad \overline{\mathbf{h}}_l^M = \begin{pmatrix} \overline{\check{n}_l} \hat{w}_l \\ \rho_l \overline{\check{\alpha}_l} \hat{w}_l \\ \rho_l \overline{\check{\alpha}_l} \hat{u}_l \hat{w}_l \\ \rho_l \overline{\check{\alpha}_l} \hat{v}_l \hat{w}_l \\ \rho_l \overline{\check{\alpha}_l} \hat{w}_l^2 \\ \rho_l \overline{\check{\alpha}_l} \hat{w}_l \hat{\delta}\theta_l \\ \rho_l \overline{\check{\alpha}_l} \hat{w}_l \hat{h}_l \end{pmatrix} \quad (3.43)$$

Sub-grid fluxes

The three components of the sub-grid flux tensor are written as:

$$\bar{\mathbf{f}}_l^t = \begin{pmatrix} 0 \\ 0 \\ -\bar{\tau}_{l,xx}^t \\ -\bar{\tau}_{l,xy}^t \\ -\bar{\tau}_{l,xz}^t \\ \bar{q}_{\theta,x}^t \\ \bar{q}_{h,x}^t \end{pmatrix}, \quad \bar{\mathbf{g}}_l^t = \begin{pmatrix} 0 \\ 0 \\ -\bar{\tau}_{l,xy}^t \\ -\bar{\tau}_{l,yy}^t \\ -\bar{\tau}_{l,yz}^t \\ \bar{q}_{\theta,y}^t \\ \bar{q}_{h,y}^t \end{pmatrix}, \quad \bar{\mathbf{h}}_l^t = \begin{pmatrix} 0 \\ 0 \\ -\bar{\tau}_{l,xz}^t \\ -\bar{\tau}_{l,yz}^t \\ -\bar{\tau}_{l,zz}^t \\ \bar{q}_{\theta,z}^t \\ \bar{q}_{h,z}^t \end{pmatrix} \quad (3.44)$$

$\bar{\tau}_l^t$ is the sub-grid stress tensor of the dispersed phase defined by:

$$\bar{\tau}_{l,ij}^t = -\rho_l \bar{\alpha}_l (\widehat{u_{l,i} u_{l,j}} - \widehat{u_{l,i}} \widehat{u_{l,j}}) \quad (3.45)$$

\bar{q}_θ^t is the sub-grid flux of uncorrelated energy:

$$\bar{q}_{\theta,i}^t = \rho_l \bar{\alpha}_l (\widehat{u_{l,i} \delta \theta} - \widehat{u_{l,i}} \widehat{\delta \theta}_l) \quad (3.46)$$

\bar{q}_h^t is the sub-grid flux of sensible enthalpy:

$$\bar{q}_{h,i}^t = \rho_l \bar{\alpha}_l (\widehat{u_{l,i} h_{s,l}} - \widehat{u_{l,i}} \widehat{h}_l) \quad (3.47)$$

In the present implementation, the sub-grid effects on the resolved liquid enthalpy are supposed negligible: $\bar{q}_h^t = 0$. The modelling of the terms $\bar{\tau}_l^t$ and \bar{q}_θ^t is described in section 3.3.3.

All source terms \bar{s}_l are approximated by their unfiltered form, i.e. subgrid-scale terms that would appear in a proper, filtered formulation are neglected. The terms are detailed in chapter 4. Details on this simplification can be found in the thesis of Boileau [18].

3.3.3 Sub-grid scale models for the dispersed phase

Sub-grid scale mesoscopic velocity tensor

By analogy with the LES modeling of gaseous flows, Riber *et al.* [125] propose a viscous-type model for the sub-grid scale mesoscopic velocity tensor $\bar{\tau}_l^t$. The deviatoric part is evaluated with the compressible Smagorinsky model [140] whereas the diagonal part is calculated with the Yoshizawa model [157]:

$$\bar{\tau}_{l,ij}^t = -\rho_l \bar{\alpha}_l (\widehat{u_{l,i} u_{l,j}} - \widehat{u_{l,i}} \widehat{u_{l,j}}) \quad (3.48)$$

$$\text{model: } \bar{\tau}_{l,ij}^t = 2\rho_l \bar{\alpha}_l \nu_{l,t} \left(\widehat{S}_{l,ij} - \frac{1}{3} \widehat{S}_{l,kk} \delta_{ij} \right) + 2\rho_l \bar{\alpha}_l \kappa_{l,t} \widehat{S}_{l,ij} \delta_{ij} \quad (3.49)$$

$$\text{with: } \widehat{S}_{l,ij} = \frac{1}{2} \left(\frac{\partial \widehat{u}_{l,i}}{\partial x_j} + \frac{\partial \widehat{u}_{l,j}}{\partial x_i} \right) - \frac{1}{3} \frac{\partial \widehat{u}_{l,k}}{\partial x_k} \delta_{ij} \quad (3.50)$$

$$\text{Smagorinsky model: } \nu_{l,t} = (C_{S,l} \Delta)^2 \sqrt{2 \widehat{S}_{l,ij} \widehat{S}_{l,ij}} \quad (3.51)$$

$$\text{Yoshizawa model: } \kappa_{l,t} = 2 (C_{V,l} \Delta)^2 \widehat{S}_{l,ij} \quad (3.52)$$

The model constants are fixed from *a priori* tests [101]: $C_{S,l} = 0.14$ et $C_{V,l} = 0.11$.

3.4 Definition of characteristic diameters in a spray

To analyze droplet sprays, statistics on droplet diameters are used to define global, characteristic diameters. The most common ones are the mean diameter D_{10} and the Sauter mean diameter (SMD or D_{32}). The indices of a characteristic diameter D_{mn} correspond to the exponents in an expression for a spray composed of N droplets:

$$D_{mn} = \frac{\sum_{i=1}^N d_i^m}{\sum_{i=1}^N d_i^n} \quad (3.53)$$

where d_i is the diameter of a given droplet i . Alternatively, for a sample divided into k diameter classes with N_i particles present in the class i , the definition of D_{mn} becomes:

$$D_{mn} = \frac{\sum_{i=1}^k N_i d_i^m}{\sum_{i=1}^k N_i d_i^n} \quad (3.54)$$

The mean diameter takes the form:

$$D_{10} = \sum_{i=1}^N d_i \quad (3.55)$$

The Sauter mean diameter is obtained from

$$D_{32} = \frac{\sum_{i=1}^N d_i^3}{\sum_{i=1}^N d_i^2} \quad (3.56)$$

and describes the diameter that has the same volume to surface ratio as the entire spray, which is of interest for evaporating cases.

Chapter 4

Modeling of the exchanges between phases

Contents

4.1	Introduction	63
4.2	Drag	63
4.2.1	Two-way coupling terms for drag	64
4.3	Evaporation model	65
4.3.1	Mass transfer	67
4.3.2	Two-way coupling terms for mass transfer	69
4.3.3	Heat transfer	69
4.3.4	Coupling terms for heat transfer	78
4.3.5	Treatment of droplet boiling	79
4.3.6	Vanishing droplets in EL	79
4.4	Summary of the liquid phase governing equations	81

4.1 Introduction

This chapter's purpose is to give a detailed overview of the physics behind the source terms related to the exchange between the gas and the liquid phase that appear in chapters 2 and 3. These terms are modeled in exactly the same way for both, the EL and EE formulation. For the sake of clarity, all gaseous variables are noted without associated filtering or interpolation operators. In the EL framework, a given gaseous flow variable, noted f_g in this chapter, corresponds in practice to $f_{g@p}$, which is the filtered quantity \bar{f}_g , interpolated from the grid nodes j of the cell e in which the particle is situated to the position $x_{p,i}$ of the particle (see section 5.9.2) for details on interpolation.

4.2 Drag

The drag force exerted by the gas with the velocity u on an isolated spherical particle of mass m_p and velocity u_p is obtained by a simplification of the Basset-Boussinesq-Oseen equation [29]:

$$\frac{F_{p,i}}{m_p} = \frac{1}{\tau_p} (u_i - u_{p,i}) \quad (4.1)$$

where τ_p is the relaxation time of the particle expressed as:

$$\tau_p = \frac{\tau'_p}{1 + 0.15Re_p^{0.687}} \quad \text{with} \quad \tau'_p = \frac{\rho_l d^2}{18\mu} \quad (4.2)$$

where Re_p is the Reynolds number of the particle:

$$Re_p = \frac{|u_i - u_{p,i}| d_p}{\nu} \quad (4.3)$$

Equation 4.2 includes an empirical correlation proposed by Schiller and Naumann [132] to take into account Reynolds number effects. For low particle Reynolds numbers, equation 4.2 yields $\tau_p = \tau'_p$. As τ'_p is in fact the drag coefficient proposed by Stokes [145], this correction degenerates into the original Stokes law. The influence of the Schiller-Naumann correction is shown in figure 4.1, where the initial acceleration of a typical particle in a combustion chamber ($d_p = 30 \mu m$, $\rho_g = 7.18 kg/m^3$, $\rho_l = 782 kg/m^3$) is considered. For a relative velocity between particle and surrounding gas of $10 m/s$, the acceleration according to the Schiller-Naumann law is five times the one obtained with the uncorrected Stokes drag.

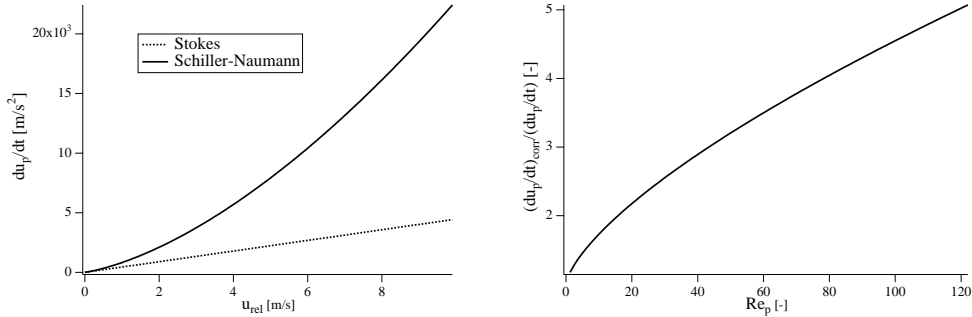


Figure 4.1: Left: initial acceleration of a droplet over the slip velocity. Right: ratio between the initial acceleration of a droplet obtained with the Schiller-Naumann correction and the uncorrected Stokes drag over the particle Reynolds number Re_p .

The effects of drag on the dispersed phase dynamics depend on the Stokes number comparing the characteristic time of the drag term τ_p to the flow characteristic time:

$$St = \frac{\tau_p}{\tau_L} \quad (4.4)$$

where $\tau_L = L/|\mathbf{u}|$ with L being a characteristic length scale of the gaseous flow. The Stokes number is an indicator of the response of the particle to the variations of the flow velocity. For $St \ll 1$, the particle behaves like a tracer of the gaseous flow. For $St \gg 1$, the particle has an inertial trajectory and is insensitive to the gaseous flow perturbations. Finally, for Stokes numbers of order unity, the effects of preferential concentration are maximum [152, 44, 43]. In the EE approach, this last regime is associated to an increased importance of the random uncorrelated motion.

4.2.1 Two-way coupling terms for drag

Two-way coupling terms model the drag forces exerted by the droplet onto the surrounding gas. Starting from the same model for drag (equation 4.1), the calculation of the source term applied at a node of the Eulerian grid of the gaseous phase differs between EL and EE.

Euler-Lagrange

For the EL approach, the drag force $F_{p,i}^{(k)}$ is obtained for each droplet (k) individually. To assemble the source term $F_{d,i}$ to be applied on the gaseous equations, a weighted distribution operation is performed. The weight $\Theta_{j,e}^{(k)}$ that is applied to the contribution of the particle (k), located inside the grid cell (or element) e to the target node j are defined in equation 5.28. The source term $F_{d,i}$ at a given grid node j is obtained by summing all weighted contributions of particles (k) located inside \mathcal{D}_j (the ensemble of all elements K_e that have a vertex coinciding with j).

$$F_{d,i} = \frac{1}{V_j} \sum_{k \in \mathcal{D}_j} \Theta_{j,e}^{(k)} F_{p,i}^{(k)} = \frac{1}{V_j} \sum_{k \in \mathcal{D}_j} \Theta_{j,e}^{(k)} \left(\frac{m_p}{\tau_p} \right)^{(k)} (u_i - u_{p,i}^{(k)}) \quad (4.5)$$

Here, V_j is the nodal control volume or the median dual cell (see section 5.2 for a definition).

Euler-Euler

In the case of EE, the source term $F_{d,i}$ that is passed to the liquid phase equations (appearing in eqs. 3.35 and 3.37) corresponds to the statistical mean of all droplets inside a given control volume.

$$F_{d,i} = \rho_l \check{\alpha}_l \left\langle \frac{F_{p,i}}{m_p} \right\rangle_l = \frac{\rho_l \check{\alpha}_l}{\tau_p} (u_i - \check{u}_{l,i}) \quad (4.6)$$

The second equality is valid for a monodisperse spray. In practice, as values for the liquid and the gaseous phase are obtained on the same grid and for the same nodal control volumes, no further transformation of the source term is needed.

4.3 Evaporation model

The evaporation model used in AVBP is an equilibrium law based on the Spalding mass-transfer model.

The following assumptions are made:

- A spherical and isolated droplet is considered, effects of interaction between droplets are neglected.
- The thermal conductivity in the liquid phase is infinite which results in a homogeneous temperature over the droplet volume.
- The droplet is assumed to be at equilibrium with the surrounding gas phase (but not at constant diameter and temperature with time).

The derivations of the evaporation model and the notation follow the outlines given by Kuo [79], Sirignano [139] and Boileau [19].

The gaseous field around a given droplet is considered non-convective, i.e. the only non-zero velocity component at any given location points in radial direction. The gas flow is also assumed

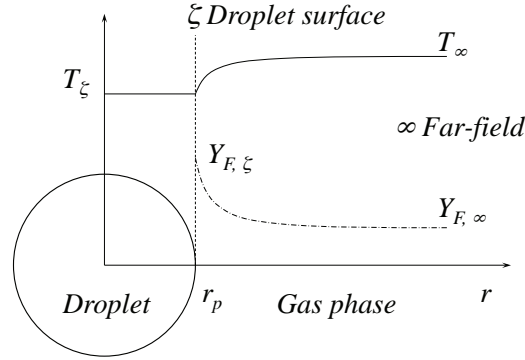


Figure 4.2: Variations of the temperature T and the fuel mass fraction Y_F over the radial distance from a spherical single droplet with constant temperature T_ζ

to be quasi steady, which means that equations are independent of time. Furthermore, the position of the liquid surface is considered constant. This reflects the fact that $\rho_l \gg \rho_g$ resulting in a velocity of the receding liquid surface that is small compared to the evaporated fuel moving away from the surface. The problem is formulated in spherical coordinates (illustrated in figure 4.2) for radii between the droplet surface (index ζ) and the far-field (index ∞). The following set of equations of the gaseous flow field for $r > r_\zeta$ is obtained:

$$\text{Mass conservation:} \quad \rho u r^2 = \text{const} = (\rho u r^2)_\zeta = \frac{\dot{m}_F}{4\pi} \quad (4.7)$$

$$\text{Fuel species conservation:} \quad \rho u r^2 \frac{dY_F}{dr} = \frac{d}{dr} \left(r^2 [\rho D_F] \frac{dY_F}{dr} \right) \quad (4.8)$$

$$\text{Energy equation:} \quad \rho u r^2 \frac{dC_P T}{dr} = \frac{d}{dr} \left(\frac{\lambda}{C_P} r^2 \frac{dC_P T}{dr} \right) \quad (4.9)$$

The expression $[\rho D_F]$ in equation 4.8 contains the diffusion coefficient of the species representing the fuel, D_F , and the density of the mixture in the gas phase, ρ . It can be expressed as a function of the gas viscosity μ and the Schmidt number of the gaseous fuel Sc_F .

$$[\rho D_F] = \frac{\mu}{Sc_F} \quad (4.10)$$

The variable λ appearing in equation 4.53 is the thermal conductivity in the gas phase.

$$\lambda = \frac{\mu \bar{C}_P}{Pr} \quad (4.11)$$

Here, \bar{C}_P is the average heat capacity at constant pressure of the gaseous mixture.

It is important to note that there are several definitions regarding the mass exchange between liquid and gaseous phase. In the equation of mass conservation (4.7), an expression for the gaseous fuel mass flux \dot{m}_F through a spherical surface at the radius r appears. Its sign is

determined by the formulation in spherical coordinates, i.e. a mass flux away from the droplet centre is positive. It is defined as:

$$\dot{m}_F = (4\pi\rho ur^2)_\zeta \quad (4.12)$$

This definition is only valid in the framework of equations 4.7 to 4.9, that is, for a steady state. On the other hand, one can define the temporal evolution of the global mass m_p of the droplet considered, which appears in a Lagrangian framework. It is defined in such form that \dot{m}_p is negative when the droplet loses mass:

$$\dot{m}_p = \frac{dm_p}{dt} \quad (4.13)$$

Combining the notion of a time-dependent system (in this case the droplet mass) with steady state equations is not admissible in the strict sense. It is, however possible to assume a quasi-steady problem, with the condition of sufficiently small rates of change in all the problem's variables. In practice, this implies restrictions on the timestep. Under this assumption, the mass flux \dot{m}_F can be directly related to the Lagrangian evolution of particle mass \dot{m}_p :

$$\dot{m}_F = 4\pi\rho ur^2 = \text{const} = (4\pi\rho ur^2)_\zeta = -\dot{m}_p \quad (4.14)$$

The derivation of the evaporation model is divided into two steps. The first one treats a model for the temporal evolution of a single droplet's mass. In a second step, two models for the droplet temperature are presented using different degrees of simplification.

4.3.1 Mass transfer

The model for the mass transfer between a single, isolated droplet and the surrounding gas is derived using the equation of species conservation (4.8). Two boundary conditions intervene, one at the droplet surface (ζ), the other at the far-field (∞).

Equation 4.8 can be integrated to give:

$$\rho ur^2 Y_F = r^2 [\rho D_F] \frac{dY_F}{dr} + c_1 \quad (4.15)$$

The constant c_1 is determined by observing that $\rho ur^2 Y_F - r^2 [\rho D_F] \frac{dY_F}{dr}$ is the fuel flux. Since only the fuel is moving, this flux is the total flux ρur^2 so that $c_1 = \rho ur^2 = \dot{m}_F/4\pi$. The equation for Y_F becomes

$$\rho ur^2 (Y_F - 1) = r^2 [\rho D_F] \frac{dY_F}{dr} \quad (4.16)$$

Assuming that $[\rho D_F]$ is constant allows to integrate (4.16) between r and ∞ :

$$\frac{\dot{m}_F}{4\pi r [\rho D_F]} = \ln \left(\frac{Y_{F,\infty} - 1}{Y_F - 1} \right) \quad (4.17)$$

Applying the boundary conditions at $r = r_\zeta$ leads to

$$\dot{m}_F = 4\pi r_\zeta [\rho D_F] \ln(B_M + 1) \quad \text{where} \quad B_M = \frac{Y_{F,\zeta} - Y_{F,\infty}}{1 - Y_{F,\zeta}} \quad (4.18)$$

This condition imposes \dot{m}_F and the speed at which the evaporated fuel leaves the droplet surface, u_ζ :

$$r_\zeta \rho_\zeta u_\zeta = \frac{\dot{m}_F}{4\pi r_\zeta} = [\rho D_F] \ln(1 + B_M) \quad (4.19)$$

Considering the evolution of the global droplet mass m_p over time, the sign changes (see definition in equation 4.14):

$$\dot{m}_p = -\pi d_p Sh [\rho D_F] \ln(1 + B_M) \quad (4.20)$$

where d_p is the particle diameter. The Sherwood number Sh can be obtained in different ways. For the case of a droplet in a quiescent atmosphere, as derived above, one obtains:

$$Sh = 2 \quad (4.21)$$

This value is not exact in the general case where droplets may have a non-zero velocity relative to the surrounding gas. This can be taken into account by correlations like the one proposed by *Ranz and Marshall* [121], which is based on the particle Reynolds number Re_p and the Schmidt number of the fuel species Sc_F .

$$Sh = 2 + 0.55 Re_p^{1/2} Sc_F^{1/3} \quad (4.22)$$

The *Spalding* number B_M uses the fuel mass fractions at the surface and the far-field, $Y_{F,\zeta}$ and $Y_{F,\infty}$. While $Y_{F,\infty}$ is interpolated from the surrounding grid nodes, an expression for $Y_{F,\zeta}$ must be obtained by stating that the flow at the droplet surface is saturated. Using the molar fraction of the fuel vapour at the surface, $X_{F,\zeta}$, the molar weight of the fuel, W_F , and $\bar{W}_{nF,\zeta}$, the molar weight of the mixture of all species *other* than the fuel, calculated at the surface, one has:

$$Y_{F,\zeta} = \frac{X_{F,\zeta} W_F}{X_{F,\zeta} W_F + (1 - X_{F,\zeta}) \bar{W}_{nF,\zeta}} \quad (4.23)$$

Assuming that this mixture does not change between the droplet surface (ζ) and the far-field (∞), $\bar{W}_{nF,\zeta}$ only depends on known variables of the far-field namely $Y_{F,\infty}$ and \bar{W} , the molar weight of the mixture of *all* species in the gas-phase.

$$\bar{W}_{nF,\zeta} = \bar{W}_{nF,\infty} = \frac{1 - Y_{F,\infty}}{1 - Y_{F,\infty} \frac{W_F}{\bar{W}}} \bar{W} \quad (4.24)$$

The fuel molar fraction, $X_{F,\zeta}$ can be written using the partial pressure of the fuel species, $P_{F,\zeta}$:

$$X_{F,\zeta} = \frac{P_{F,\zeta}}{P} \quad (4.25)$$

where $P_{F,\zeta}$ is calculated by the *Clausius-Clapeyron* law

$$P_{F,\zeta} = P_{cc} \exp \left(\frac{W_F L_v(T_{ref})}{\mathcal{R}} \left(\frac{1}{T_{cc}} - \frac{1}{T_\zeta} \right) \right) \quad (4.26)$$

where T_{cc} and p_{cc} correspond to an arbitrary reference point on the saturation curve, \mathcal{R} is the universal gas constant and $L_v(T_{ref})$ the latent heat at T_{ref} . The latent heat L_v at a given temperature T is defined as:

$$L_v(T) = h_{s,F}(T) - h_{s,p}(T) \quad (4.27)$$

4.3.2 Two-way coupling terms for mass transfer

Euler-Lagrange

While $\dot{m}_p = -\dot{m}_F$ (equation 4.18) describes the temporal evolution of a single droplet's mass, Γ_g is the mass transfer per unit volume and represents the source term that is passed to the gaseous solver. The distribution scheme for this source term is described in section 4.2.1. The expression for the weights $\Theta_{j,e}^{(k)}$ are given in equation 5.28.

$$\Gamma = -\frac{1}{V_j} \sum_{k \in \mathcal{D}_j} \Theta_{j,e}^{(k)} \left(\frac{dm_p}{dt} \right)^{(k)} = \frac{1}{V_j} \sum_{k \in \mathcal{D}_j} \Theta_{j,e}^{(k)} \dot{m}_F^{(k)} \quad (4.28)$$

Euler-Euler

In the EE framework, there are two source terms, Γ that is applied on the gaseous equations, and Γ_l that is applied on the liquid phase equations and, per definition, has the negative value of its gaseous counterpart.

$$\begin{aligned} \Gamma &= -\rho_l \check{\alpha}_l \left\langle \frac{1}{m_p} \frac{dm_p}{dt} \right\rangle_l = -\Gamma_l \\ &= \rho_l \check{\alpha}_l \dot{m}_F \end{aligned} \quad (4.29)$$

4.3.3 Heat transfer

The previous section described the evaluation of the fuel mass flux from a droplet. It must be combined with a model for the heat exchange between a droplet and its surroundings. This subject is presented in two steps. In the first, the different contributions to the enthalpy balance are defined and analytical relations are derived in a general way. Next, it is explained how these contributions can be combined to form models for droplet heat transfer, each taking a different degree of physical detail into account.

Enthalpy conservation at the gas/liquid interface

The derivation of a law for the temporal evolution of a droplet's temperature involves the enthalpy conservation equation (4.9) with boundary conditions at the far-field (∞) and the

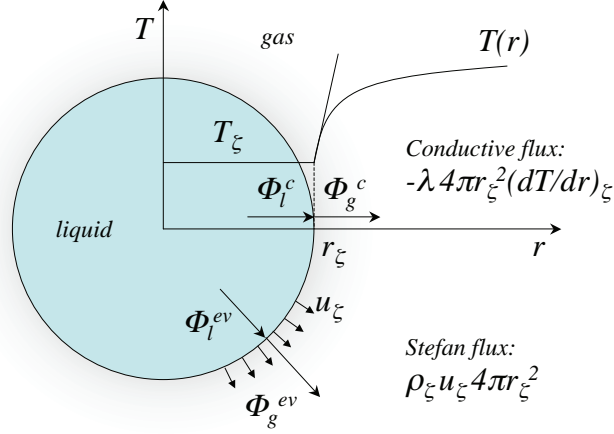


Figure 4.3: Contributions to the enthalpy balance at the liquid-gaseous interface

droplet surface (ζ). Furthermore, for the enthalpy fluxes at the interface, a conservation law at the liquid/gas interface can be stated. Figure 4.3 gives an overview of the four contributions:

$$\Phi_l^{ev} + \Phi_l^c + \Phi_g^{ev} + \Phi_g^c = 0 \quad (4.30)$$

On the gaseous side, there is a convective part, denoted Φ_g^{ev} , which represents the sensible enthalpy of the fuel species $h_{s,F}$ that is transported by the *Stefan* flux \dot{m}_F , i.e. the evaporated mass moving away from the surface at the velocity u_ζ . Φ_g^{ev} is defined as follows:

$$\Phi_g^{ev} = \dot{m}_F h_{s,F}(T_\zeta) \quad (4.31)$$

The other contribution on the gaseous side is the conductive heat transfer Φ_g^c which is proportional to the temperature gradient at the surface.

$$\Phi_g^c = \left(-4\pi r^2 \lambda \frac{dT}{dr} \right)_\zeta \quad (4.32)$$

Similarly, there also is a convective and a conductive contribution on the liquid side. Mass conservation at the interface (equation 4.7, resp. equation 4.14) states that the mass flux in the liquid and gas phase is the same, namely $\dot{m}_F = -\dot{m}_p$. On the liquid side however, this mass flux is transporting the sensible enthalpy of the liquid $h_{s,p}(T_\zeta)$. The liquid convective flux Φ_l^{ev} is thus defined as:

$$\Phi_l^{ev} = -\dot{m}_F h_{s,p}(T_\zeta) \quad (4.33)$$

The liquid conductive flux Φ_l^c depends on the temperature gradient at the surface inside the droplet:

$$\Phi_l^c = \left(4\pi r^2 \lambda_l \frac{dT_l}{dr} \right)_\zeta \quad (4.34)$$

However, as the droplet temperature is assumed constant in space, this expression can not be evaluated directly. Evaporation models that are presented in the following either neglect Φ_l^c or substitute it when necessary. Equation 4.30 can now be rewritten in a more detailed form:

$$\underbrace{-\dot{m}_F h_{s,p}(T_\zeta)}_{\text{liquid conv. flux}} + \underbrace{\Phi_l^c}_{\text{liquid cond. flux}} + \underbrace{\dot{m}_F h_{s,F}(T_\zeta)}_{\text{gaseous conv. flux}} + \underbrace{\left(-4\pi r^2 \lambda \frac{dT}{dr} \right)_\zeta}_{\text{gaseous cond. flux}} = 0 \quad (4.35)$$

Using the definition of the latent heat L_v (equation 4.27) yields the following form:

$$\dot{m}_F L_v(T_\zeta) + \Phi_l^c + \Phi_g^c = 0 \quad (4.36)$$

where $L_v(T_\zeta)$ is the heat of evaporation $h_{s,f}(T_\zeta) - h_{s,p}(T_\zeta)$ at the temperature T_ζ . Note that, while L_v is a constant in the Clausius-Clapeyron law, (equation 4.26), it changes with T_ζ in the context of equation 4.36. $L_v(T_{l,ref})$ is provided by literature at the reference temperature $T_{l,ref}$ for the liquid phase enthalpy $h_{s,p}$. To compute $L_v(T_\zeta)$, the definition of $L_v(T)$ (eq. 4.27) must be recast as:

$$L_v(T_\zeta) = h_{s,F}(T_\zeta) - h_{s,p}(T_\zeta) - h_{s,corr} \quad (4.37)$$

where $h_{s,corr}$ is a correction enthalpy that, if necessary, accounts for different reference temperatures for the gaseous and the liquid enthalpy. In AVBP, the reference temperature for the gaseous enthalpy $h_{s,F}$ is defined as $T_0 = 0K$ whereas the liquid reference temperature $T_{l,ref}$ may vary from species to species. The correction enthalpy $h_{s,corr}$ is determined by evaluating the gaseous enthalpy $h_{s,F}$ at the reference temperature of the liquid phase:

$$L_v(T_{l,ref}) = h_{s,F}(T_{l,ref}) - \underbrace{h_{s,p}(T_{l,ref})}_0 - h_{s,corr} \quad (4.38)$$

As $L_v(T_{ref})$ and $h_{s,p}(T_{l,ref}) = 0$ are known, and $h_{s,F}(T_{l,ref})$ is evaluated using the thermodynamic tables of AVBP, $h_{s,corr}$ can be obtained from:

$$h_{s,corr} = h_{s,F}(T_{l,ref}) - L_v(T_{l,ref}) \quad (4.39)$$

A typical curve of $L_v(T_\zeta)$ vs T_ζ is shown in figure 4.4 for n-heptane.

The remaining term in equation 4.36 to be evaluated is the gaseous conductive enthalpy flux Φ_g^c . Differences between early models in literature mainly concern how this term is derived. In any case, the derivations presented in the following are only valid in the case of a quiescent atmosphere (i.e. $u_p - u_g = 0$), which makes corrections necessary if cases with a slip velocity are considered.

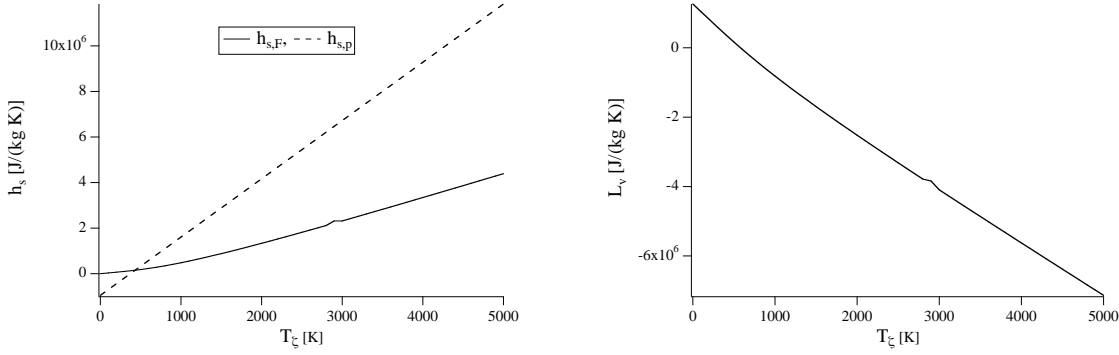


Figure 4.4: Example of *n*-heptane. Left: evolutions of the gaseous fuel sensible enthalpy $h_{s,F}$ and the liquid phase sensible enthalpy $h_{s,p}$ over the droplet surface temperature T_{ζ} . Right: evolution of the fuel species latent heat L_v over T_{ζ}

The d^2 -law

The simplest form of an evaporation law was originally introduced by Spalding [142] and Godsave [51] in 1953 and is commonly known as Spalding law or d^2 -law. It considers only effects on the gaseous side of the droplet surface while neglecting all effects on the liquid side. Consequently, the unknown term for the liquid conductive heat transfer Φ_l^c that contributes to the energy balance (4.36) is neglected. Equation 4.36 then reduces to

$$\dot{m}_F L_v(T_{\zeta}) = -\Phi_g^c \quad (4.40)$$

It will be shown in the following that this equality corresponds to a state in which the droplet attained a state equilibrium that is characterized by the so-called equilibrium- or “wet bulb temperature”, T_{wb} . This temperature is a function of the gaseous conditions near the droplet. Its value has no influence on the droplet itself but in certain implementations it may be needed to obtain two-way coupling terms. Combining equations 4.40 and 4.64 yields:

$$B_T = \frac{(T_{\infty} - T_{\zeta}) C_P}{L_v(T_{\zeta})} \quad (4.41)$$

This simplified form of the temperature Spalding number B_T , combined with the mass transfer number B_M (4.19) and the Clausius-Clapeyron relation (4.26) also allows to iteratively obtain the wet bulb temperature for given ambient conditions.

The infinite conductivity model

This model is the most commonly used for spray simulations. It meets the concerns raised by studies like Law [83] or Hubbart et al. [68] that transient droplet heating cannot be neglected in combustion applications. As it assumes a uniform droplet temperature, which corresponds to the hypothetical case of infinitely fast liquid phase heat transfer, it is often referred to as the infinite conductivity model (Aggarwal et al. [4]).

We recall that the derivations of droplet mass transfer are based on the assumption of quasi-steadyness, i.e. a rate of change of global droplet quantities that is sufficiently low to consider

the system as stationary at a given instant in time. The same reasoning shall now be applied for the droplet heat transfer. In this case, the enthalpy fluxes are evaluated for a steady state while the droplet temperature is allowed to vary over time. Again, quasi-steadyness translates to a condition of a timestep sufficiently short to keep variation of global quantities negligibly small.

If one considers the temporal evolution of the *global* enthalpy $m_p h_{s,p}(T_p)$ of a given droplet (index p), only the heat fluxes on the liquid side contribute to the equation.

$$\frac{d}{dt} (m_p h_{s,p}(T_p)) = \Phi_l^{ev} + \Phi_l^c \quad (4.42)$$

Splitting up the temporal derivative on the left hand side and substituting Φ_l^{ev} according to equation 4.33 gives:

$$\frac{d m_p}{dt} h_{s,p}(T_p) + \frac{d (h_{s,p}(T_p))}{dt} m_p = -\dot{m}_F h_{s,p}(T_\zeta) + \Phi_l^c \quad (4.43)$$

The droplet temperature is constant over r , so T_ζ equals T_p . Furthermore, under the assumption of quasi-steadyness, the gaseous fuel mass flux \dot{m}_F can be substituted by the evolution of the droplet mass \dot{m}_p (using equation 4.14) which results in the terms describing the enthalpy transport by the *Stefan* flux on both sides of equation 4.43 becoming identical:

$$\frac{d m_p}{dt} h_{s,p}(T_p) = \dot{m}_p h_{s,p}(T_\zeta) \quad (4.44)$$

Moreover, the variation of the liquid sensible enthalpy, $d(h_{s,p}(T_p))$, can be expressed as:

$$d(h_{s,p}(T_p)) = C_{p,l} dT_p \quad (4.45)$$

Injecting equations 4.45 and 4.44 into equation 4.43 finally yields a law for the Lagrangian temporal derivative of the droplet temperature:

$$\frac{dT_p}{dt} = \frac{1}{m_p C_{p,l}} \Phi_l^c \quad (4.46)$$

Using equations 4.36 and 4.14, Φ_l^c can be substituted and one obtains:

$$\frac{dT_p}{dt} = \frac{1}{m_p C_{p,l}} (-\Phi_g^c + \dot{m}_p L_v(T_\zeta)) \quad (4.47)$$

Note that the evolution of the droplet temperature given by equation 4.46 depends on the liquid conductive heat exchange Φ_l^c which, in most cases, only plays a role during the droplet heatup phase at the onset of evaporation. At later phases in the evaporaton process, the terms $-\Phi_g^c$ and $\dot{m}_p L_v(T_\zeta)$ will balance each other so that Φ_l^c becomes negligible. This corresponds to the steady state considered by the d^2 -law with equation 4.40 being satisfied. With $dT_p / dt \rightarrow 0$ for $\Phi_l^c \rightarrow 0$, the droplet temperature tends towards the wet bulb condition of a constant temperature T_{wb} .

In equation 4.47, the remaining unknown is Φ_g^c for which analytical expressions using two different approaches as derived in the following sections (equations 4.54 and 4.67).

Heat transfer of a solid sphere (No Stefan flux)

This approach is based on the assumption that the *Stefan* flux $\dot{m}_F = 4\pi\rho ur^2$ which appears on the left hand side of the enthalpy conservation in the gas phase (equation 4.9), can be neglected. This corresponds to the behaviour of a solid, spherical particle. Note that this simplification is limited to equation 4.9 and that the *Stefan* flux \dot{m}_F is still taken into account for mass transfer and the enthalpy balance at the interface (equation 4.30). The thermal conductivity in the gas, $\lambda = \mu \bar{C}_P / Pr$, is considered constant over the radial distance r . Equation 4.9 then takes the form:

$$0 = \frac{d}{dr} \left(\lambda r^2 \frac{dT}{dr} \right) \quad (4.48)$$

Integrating the expression gives

$$\lambda r^2 \frac{dT}{dr} = c_1 \quad (4.49)$$

with an integration constant c_1 that can be determined by applying the boundary conditions at the surface ζ .

$$c_1 = \lambda r_\zeta^2 \left[\frac{dT}{dr} \right]_\zeta \quad (4.50)$$

After separating the variables r and T and another integration, one obtains

$$T = -\frac{1}{r} \left(r_\zeta^2 \left[\frac{dT}{dr} \right]_\zeta \right) + c_2 \quad (4.51)$$

where the value of the constant c_2 follows from the application of the boundary conditions at the far-field ∞ .

$$\left[\frac{dT}{dr} \right]_\zeta = \frac{1}{r_\zeta} (T_\infty - T_\zeta) \quad (4.52)$$

This is an explicit expression for the temperature gradient at the droplet surface which allows to write Φ_g^c in the following way:

$$\Phi_g^c = -4\pi r_\zeta^2 \lambda \left[\frac{dT}{dr} \right]_\zeta = 2\pi d_p \lambda (T_\zeta - T_\infty) \quad (4.53)$$

The factor 2 appearing in this equation corresponds to the *Nusselt* number Nu which is constant under the assumption of a quiescent atmosphere. When droplets encounter a relative velocity with respect to the gas phase, the Nusselt number Nu , just as the Sherwood number Sh in the case of the mass transfer, has to be corrected. This is done using the *Ranz-Marshall* [121] correlation based on the particle Reynolds number Re_p and the Prandtl number Pr . Equation 4.53 then reads:

$$\Phi_g^c = \pi d_p Nu \lambda (T_\zeta - T_\infty) \quad (4.54)$$

with

$$Nu = 2 + 0.55 Re_p^{1/2} Pr^{1/3} \quad (4.55)$$

Heat transfer of an evaporating droplet (Stefan flux non zero)

An alternative way to derive Φ_g^c is based on equation 4.9 without simplification, i.e. without neglecting enthalpy transported by the *Stefan* flux $\dot{m}_F = 4\pi r^2 \rho u$. The thermal conductivity λ is again assumed to be constant over the radial distance r . Mass conservation (equation 4.7) allows to replace $r^2 \rho u$ on the left hand side by $r_\zeta^2 \rho_\zeta u_\zeta = \dot{m}_F / 4\pi$, where \dot{m}_F is the *Stefan* flux at the droplet surface.

$$\dot{m}_F C_P \frac{dT}{dr} = 4\pi \frac{d}{dr} \left(\lambda r^2 \frac{dT}{dr} \right) \quad (4.56)$$

Integration of this equation yields:

$$\dot{m}_F C_P T = 4\pi r^2 \lambda \frac{dT}{dr} + c_1 \quad (4.57)$$

where c_1 is a constant determined by applying the boundary condition at the surface ζ .

$$\dot{m}_F C_P T_\zeta = 4\pi r_\zeta^2 \lambda \left[\frac{dT}{dr} \right]_\zeta + c_1 \quad (4.58)$$

The term $4\pi r_\zeta^2 \lambda \left[\frac{dT}{dr} \right]_\zeta$ can directly be replaced using equation 4.32 and taking into account that the thermal conductivity λ has been assumed to be constant.

$$4\pi r_\zeta^2 \lambda \left[\frac{dT}{dr} \right]_\zeta = -\Phi_g^c \quad (4.59)$$

Injecting this expression in the integrated conservation law (4.57) via c_1 , one obtains:

$$\dot{m}_F \left(C_P T - C_P T_\zeta - \frac{\Phi_g^c}{\dot{m}_F} \right) = 4\pi r^2 \lambda \frac{dT}{dr} \quad (4.60)$$

The separation of the variables r and T and a second integration gives

$$-\frac{1}{r} = \frac{4\pi\lambda}{\dot{m}_F C_P} \ln \left(T - T_\zeta - \frac{\Phi_g^c}{\dot{m}_F C_P} \right) + c_2 \quad (4.61)$$

Applying the far-field boundary condition ∞ allows to determine c_2 . One finally obtains:

$$\frac{1}{r} = \frac{4\pi\lambda}{\dot{m}_F C_P} \ln \left(\frac{T_\infty - T_\zeta - \frac{\Phi_g^c}{\dot{m}_F C_P}}{T - T_\zeta - \frac{\Phi_g^c}{\dot{m}_F C_P}} \right) \quad (4.62)$$

This is a relation between the gaseous temperature as a function of the radial distance and the conductive enthalpy flux at the liquid side. It does not directly contain the desired information

on Φ_g^c . However, if evaluated at the surface, it provides an expression for the mass flux \dot{m}_F that is different from equation 4.20

$$\dot{m}_F = \frac{4\pi\lambda r_\zeta}{C_P} \ln(B_T + 1) \quad (4.63)$$

In this case, \dot{m}_F depends on the *Spalding* number for the temperature, B_T :

$$B_T = \frac{(T_\infty - T_\zeta) \dot{m}_F C_P}{-\Phi_g^c} \quad (4.64)$$

The fact of having two expressions for the mass flux can be exploited by equating them to have a relation between B_M and B_T

$$B_T = (1 + B_M)^{\frac{Sh}{Nu Le_F}} - 1 \quad (4.65)$$

with the *Lewis* number of the fuel species $Le_F = Sc_F / Pr = \mu / [\rho D_F] \cdot \lambda / (\mu C_P)$.

A rearrangement of equation 4.64 yields:

$$\Phi_g^c = \frac{\dot{m}_F C_P}{B_T} (T_\zeta - T_\infty) \quad (4.66)$$

By replacing the mass flux \dot{m}_F using equation 4.63, one obtains Φ_g^c as a function of the known temperatures T_ζ and T_∞ as well as of B_T . This equation is still implicit in Φ_g^c . In practice however, B_M is already available from the calculation of the mass evolution which allows to calculate B_T using equation 4.65.

$$\Phi_g^c = \lambda 4\pi r_\zeta (T_\zeta - T_\infty) \frac{\ln(B_T + 1)}{B_T} = \lambda \pi d_p Nu (T_\zeta - T_\infty) \frac{\ln(B_T + 1)}{B_T} \quad (4.67)$$

Note that in the limit of $B_T \rightarrow 0$, the term $\ln(B_T + 1)/B_T$ tends to 1. In that case, equations 4.67 and 4.54 are equivalent which shows that the result obtained under the assumption of a negligible *Stefan* flux can also be found as a particular solution of the more general result given by equation 4.67.

Advanced evaporation models

The model used in the scope of this work is of the infinite conductivity type, taking into account the Stefan flux for heat transfer (equations 4.67 and 4.47). Note that there are more advanced models available in literature. An example is the one proposed by Abramzon and Sirignano [2], which takes into account the finite thickness of the fuel mass fraction and thermal boundary layers, resulting in modified expressions for the Nusselt and Sherwood numbers. It necessitates an iterative part, which increases numerical cost, in particular of the Lagrangian approach. Other examples with increasing complexity are non-equilibrium formulations like the Langmuir-Knudsen model (Bellan and Summerfield [12]), or finite conductivity models that take spatially non-uniform droplet temperatures or even convective effects into account (Sazhin et al. [131]). An overview and evaluation of the cited examples can be found in the work of Sazhin et al. [131] as well as Miller et al. [97].

The “1/3-rule”

In equations 4.10 and 4.11, μ and \bar{C}_P depend on properties of the gas surrounding the droplet. In the preceding paragraphs, these values have been assumed to be constant over the radial distance from the droplet. However, by simply passing the nodal values from the gas solver to the particle, these constant quantities are taken equal to their values in the far-field, a rather arbitrary choice to which the simulation may be sensitive. Better results can be obtained with an interpolation between ζ and ∞ weighted with a factor $a = 1/3$ (Hubbard et al. [68], Miller et al. [97]). This interpolation should be performed on the temperature and the mass fractions from which μ and \bar{C}_P are calculated.

$$T_R = T_\zeta + a(T_\infty - T_\zeta) \quad (4.68)$$

$$Y_{k,R} = Y_{k,\zeta} + a(Y_{k,\infty} - Y_{k,\zeta}) \quad (4.69)$$

The corrected values for the viscosity, μ_R and the heat capacity at constant pressure of the mixture, $\bar{C}_{P,R}$ can be obtained by:

$$\mu_R = \mu(T_R) \quad (4.70)$$

$$\bar{C}_{P,R} = \sum_k C_{P,k}(T_R)Y_{k,R} \quad (4.71)$$

In a Lagrangian framework, this correction can have a very high impact on computational cost because it involves the interpolation and the transfer to the particles of all species mass fractions Y_K , resulting in a major increase of memory requirements and operations during the interpolation. A compromise is the application of the 1/3-rule at nodal level and the passing of the corrected values of μ and \bar{C}_P to the particles. This, however, does not allow to take individual droplet surface temperatures T_ζ of all droplets present in a given control volume into account. Instead, the mean droplet temperature in the considered node’s control volume, \bar{T}_ζ , is used to calculate the alternative reference Temperature $T_{R'}$. This temperature is a good approximation in the case of a relatively homogeneous spray, where all droplets have a similar history of the evaporation process and thus relatively low temperature differences.

$$T_{R'} = \bar{T}_\zeta + a(T_\infty - \bar{T}_\zeta) \quad (4.72)$$

In the case of the viscosity, the corrected quantity $\mu_{R'}$ is passed to the particles instead of μ , thus being neutral in terms of memory and adding one evaluation of the viscosity law per node.

$$\mu_{R'} = \mu(T_{R'}) \quad (4.73)$$

In the case of C_P , the necessary values to be passed to the particles reduce to two parameters, $C_{P,1}$ and $C_{P,2}$ from which the corrected heat capacity $C_{P,R'}$ can be calculated:

$$\bar{C}_{P,R'} = C_{P,1} + \frac{2}{3}Y_{F,\zeta}C_{P,2} \quad (4.74)$$

The expressions to obtain $C_{P,1}$ and $C_{P,2}$ are:

$$C_{P,1} = \sum_{k \neq F} \left[C_{P,k}(T_{R'}) \frac{Y_{k,\infty}}{\sum_{k \neq F} Y_{k,\infty}} \left(1 - \frac{1}{3} Y_{F,\infty} \right) \right] + \frac{1}{3} C_{P,F}(T_{R'}) Y_{F,\infty} \quad (4.75)$$

$$C_{P,2} = C_{P,F}(T_{R'}) - \sum_{k \neq F} \left[C_{P,k}(T_{R'}) \frac{Y_{k,\infty}}{\sum_{k \neq F} Y_{k,\infty}} \right] \quad (4.76)$$

4.3.4 Coupling terms for heat transfer

While the fluxes Φ_g^c , Φ_g^{ev} , Φ_l^c and Φ_l^{ev} are relevant for the temporal evolutions of a single droplet's enthalpies, Π_g and Π_l denote the enthalpy transfers (gas/liquid) per unit volume. Π_g represents the source term that is passed to the energy equation of the gaseous solver (see equation 2.2).

Euler-Lagrange

In the EL framework, the distribution procedure is analogous to section 4.2.1.

$$\Pi_g = \frac{1}{V_j} \sum_{k \in \mathcal{D}_j} \Theta_{j,e}^{(k)} (\Phi_g^c + \Phi_g^{ev})^{(k)} \quad (4.77)$$

$$\Pi_g = \frac{1}{V_j} \sum_{k \in \mathcal{D}_j} \Theta_{j,e}^{(k)} \left(\lambda \pi d_p Nu (T_p - T) \frac{\ln(B_T + 1)}{B_T} - \dot{m}_p h_{s,F}(T_p) \right)^{(k)}$$

The term for convective heat exchange Φ_g^{ev} is given in equation 4.31, whereas the term for conductive heat exchange Φ_g^c can be obtained from equation 4.40 for the d^2 -law and equations 4.54 and 4.67 for the formulation with and without Stefan flux respectively. Throughout the present work, only the latter formulation is applied as detailed in the second line of equation 4.77. The expression for the weights $\Theta_{j,e}^{(k)}$ of this distribution scheme can be found in equation 5.28.

Euler-Euler

In the case of EE, the source terms are defined as the statistical average over a single droplet's heat transfer contributions. The source term for the gaseous equations, Π_g , appears in equations 2.2 and 3.37. The term appearing on the liquid side can be found in equations 3.22 and 3.37.

$$\begin{aligned} \Pi_g &= \rho_l \check{\alpha}_l \left\langle \frac{1}{m_p} (\Phi_g^c + \Phi_g^{ev}) \right\rangle_l \\ &= \lambda \pi \check{n}_l \check{d} Nu \left(\check{T}_l - T \right) \frac{\ln(B_T + 1)}{B_T} + \Gamma h_{s,F}(\check{T}_l) \end{aligned} \quad (4.78)$$

$$\begin{aligned} \Pi_l &= \rho_l \check{\alpha}_l \left\langle \frac{1}{m_p} (\Phi_l^c + \Phi_l^{ev}) \right\rangle_l \\ &= -\Pi_g - \rho_l \check{\alpha}_l \left\langle \frac{1}{m_p} (\dot{m}_p h_{s,corr}) \right\rangle_l \\ &= -\Pi_g + \Gamma_l h_{s,corr} \end{aligned} \quad (4.79)$$

4.3.5 Treatment of droplet boiling

A particularity of the method described above is saturation, i.e. the case where the fuel mass fraction at the droplet surface, $Y_{F,\zeta}$, nears a value of one. In this case, the mass transfer number B_M approaches a singularity.

The equations for mass- and heat transfer are coupled via the *Clausius-Clapeyron* law (eq. 4.26), which gives the partial pressure of the fuel and eventually determines the fuel mass fraction as a function of the droplet's surface temperature. The *Clausius-Clapeyron* law as well as the laws for mass- and heat transfer have been derived as equilibrium laws. Consequently, the relation between the droplet *equilibrium* surface temperature and the partial pressure of the fuel at the surface will follow the *Clausius-Clapeyron* saturation curve. In other words, at equilibrium and for a given droplet surface temperature, the mass fraction of the fuel is fixed (and will never be greater than one).

For rapidly varying droplet temperatures, e.g. in proximity of a flame, this is not necessarily true. In some cases, a droplet which enters a hot zone may even attain a temperature for which *Clausius-Clapeyron* gives a partial pressure of $P_{F,\zeta} > P$ which leads to $Y_{F,\zeta} > 1$. In the numerical implementation, this case is treated in the following way:

A surface fuel mass fraction of $Y_{F,\zeta} = 1$ would correspond to the boiling of the droplet, a state that is characterized by a constant surface temperature. Consequently, when exceeding $Y_{F,\zeta} = 1$ during a given timestep, it has to be assumed that the droplet has begun to boil and thus, T_p is kept constant:

$$\frac{dT_p}{dt} = 0 \quad (4.80)$$

The *Spalding* law for the mass transfer is no longer valid, however, \dot{m}_p can now be evaluated directly using equation 4.47 which takes the form

$$\frac{dm_p}{dt} = \frac{\Phi_g^c}{h_{s,F}(T_\zeta) - h_{s,p}(T_\zeta) - h_{s,corr}} \quad (4.81)$$

From equation 4.46, it follows that $\Phi_l^c = 0$ in saturated conditions. The source term for the Eulerian liquid phase equations, Π_l , reduces to

$$\Pi_l = \rho_l \check{\alpha}_l \left\langle \frac{1}{m_p} \Phi_l^{ev} \right\rangle_l \quad (4.82)$$

For the gaseous source term Π_g , equations 4.77 and 4.78 remain valid.

4.3.6 Vanishing droplets in EL

If a droplet would evaporate more than its initial mass during the current timestep ($m_p + \dot{m}_p \Delta t < 0$), the disappearance of the droplet has to be taken into account. This is done by replacing the mass decrement during the timestep considered $\Delta m = \dot{m}_p \Delta t$ with the remaining particle mass $\Delta m = m_p$. To ensure mass- and energy conservation, the evaporation source terms that are passed to the gas solver (Γ_g , Π_g) are re-calculated using $\dot{m}_p = m_p / \Delta t$ instead of the value for \dot{m}_p that has been obtained by the evaporation model. The droplet in question is subsequently removed from the calculation.

This procedure still allows droplet radii of arbitrary values and can lead to droplets with a mass that is very close to zero which causes problems in equation 4.47 where m_p is in the denominator. This $1/m_p$ term reflects the fact that droplets with very little mass heat up rapidly when the surrounding gas temperature changes and the resulting conductive heatup is not immediately equilibrated by the cooling effect of a higher evaporation rate. The result can be huge variations of the temperature if (a) the slope of the temperature evolution is calculated correctly but the timestep (assumed constant in this version of the code) is too long, or if (b) numerical errors in the balance between Φ_g^c and $\dot{m}_p L_v$ grow to unacceptable levels due to the denominator term.

A very simple approximation is used to limit these variations of T_p for very small droplets. It consists in defining a limit particle mass $m_{p,limit}$ and in replacing the hyperbolic behaviour of the term $1/m_p$ by its tangent in this point for all particle masses $m_p < m_{p,limit}$ (see figure 4.5 for a schematic illustration).

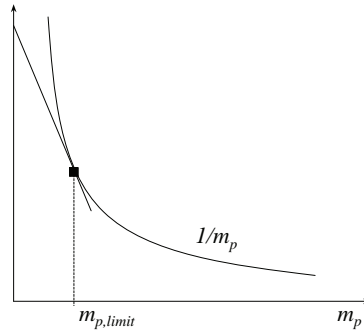


Figure 4.5: Sketch of the approximation of the term $1/m_p$ with its tangent for small droplets with masses of $m_p < m_{p,limit}$

Equation 4.46 is then replaced with

$$\frac{dT_p}{dt} = \frac{1}{m_{p,limit}} \left(2 - \frac{m_p}{m_{p,limit}} \right) \frac{1}{C_{p,l}} \Phi_l^c \quad \text{for } m_p < m_{p,limit} \quad (4.83)$$

This has no direct physical justification, however, it can be assumed that droplets nearing the end of evaporation have reached the equilibrium state at the "wet bulb temperature". By artificially limiting the denominator term to finite values in an expression with a vanishing numerator, the present approximation gradually takes the temperature evolution to a state of "forced equilibrium" when the particle mass tends to zero.

4.4 Summary of the liquid phase governing equations

This summary provides an overview of the governing equations for the liquid phase in the Lagrangian and Eulerian formulation. The terms related to the evaporation model have been retained in the form with the most physical detail that is implemented in the AVBP solver and used throughout the present work.

Euler-Lagrange

$$\begin{aligned}
 \frac{dx_{p,i}}{dt} &= u_{p,i} \\
 \frac{du_{p,i}}{dt} &= \frac{1}{\tau_p} (u_i - u_{p,i}) \\
 \frac{dm_p}{dt} &= -\pi d_p Sh [\rho D_F] \ln(1 + B_M) \\
 \frac{dT_p}{dt} &= \frac{1}{m_p C_{p,l}} \left(\frac{dm_p}{dt} L_v(T_p) - \lambda \pi d_p Nu (T_p - T) \frac{\ln(B_T + 1)}{B_T} \right)
 \end{aligned}$$

Euler-Euler

$$\begin{aligned}
 \frac{\partial \check{n}_l}{\partial t} + \frac{\partial}{\partial x_j} \check{n}_l \check{u}_{l,j} &= 0 \\
 \frac{\partial}{\partial t} \rho_l \check{\alpha}_l + \frac{\partial}{\partial x_j} \rho_l \check{\alpha}_l \check{u}_{l,j} &= -\Gamma \\
 \frac{\partial}{\partial t} \rho_l \check{\alpha}_l \check{u}_{l,i} + \frac{\partial}{\partial x_j} \rho_l \check{\alpha}_l \check{u}_{l,i} \check{u}_{l,j} &= -\Gamma \check{u}_{l,i} + \frac{\rho_l \check{\alpha}_l}{\tau_p} (u_i - \check{u}_{l,i}) \\
 \frac{\partial}{\partial t} \rho_l \check{\alpha}_l \check{h}_{s,l} + \frac{\partial}{\partial x_i} \rho_l \check{\alpha}_l \check{u}_{l,i} \check{h}_{s,l} &= -\Gamma \left(h_{s,F}(\check{T}_l) + h_{s,corr} \right) - \lambda \pi \check{n}_l \check{d} Nu \left(\check{T}_l - T \right) \frac{\ln(B_T + 1)}{B_T}
 \end{aligned}$$

Chapter 5

The numerical approach

Contents

5.1	Introduction	83
5.2	The cell-vertex approach	84
5.3	The convection schemes for the gaseous phase	85
5.3.1	The Lax-Wendroff scheme	86
5.3.2	The TTGC scheme	86
5.4	The convection schemes for the dispersed phase	86
5.4.1	The PSI scheme	87
5.5	The diffusion scheme	90
5.6	Calculation of the timestep	90
5.6.1	Liquid phase timestep	90
5.7	Artificial viscosity models for the gaseous phase	91
5.7.1	Introduction	91
5.7.2	The sensors	92
5.7.3	The operators	93
5.7.4	The sensors for the Eulerian dispersed phase	93
5.8	Boundary conditions	94
5.9	Numerical aspects of the Euler-Lagrange solver	95
5.9.1	Time integration	95
5.9.2	Interpolation methods	95
5.9.3	Two-way coupling terms	95
5.10	Wall interaction of Lagrangian particles	96

5.1 Introduction

In this chapter, the numerical methods used in the AVBP solver are described. Aspects relevant for the developments carried out for the present work are discussed in more detail. Elements like numerical schemes that are applied but not modified are briefly described. For more detail, the reader is referred to the cited literature.

5.2 The cell-vertex approach

The *cell-vertex* approach is one of the common discretization methods for finite volume schemes, the very popular alternative being the *cell-centered* formulation [63, 148]. While in the latter case, flow variables are stored at the center of the cells, they are stored at the grid nodes in the former.

The key difference is the computation of fluxes through cell boundaries. For cell-centered schemes, the flux through a cell boundary is based on the interpolation of variables situated to *either side* of the cell edge, i.e. from the *centers* of two neighbouring cells. In a cell-vertex scheme, the flux is obtained from the values at the *vertices*, i.e. at either end of the cell edge. Here, vertices are to be understood as points that coincide with the grid nodes but are associated to a grid cell. This means that one grid node can coincide with several vertices, one for each grid cell the node is connected to. The formalism described in the following corresponds to the one used in the AVBP solver and is described in detail by Lamarque [80].

Written in flux variables, the Navier-Stokes equations take the very compact form

$$\frac{\partial \mathbf{U}}{\partial t} + \vec{\nabla} \cdot \vec{\mathcal{F}} = \mathbf{S} \quad (5.1)$$

where \mathbf{U} is the vector of the conservative flow variables, $\vec{\mathcal{F}}$ the flux tensor of \mathbf{U} and \mathbf{S} the vector of source terms. The flux tensor can be decomposed in a convective part $\vec{\mathcal{F}}^C$ and a viscous part $\vec{\mathcal{F}}^V$:

$$\vec{\mathcal{F}} = \vec{\mathcal{F}}^C(\mathbf{U}) + \vec{\mathcal{F}}^V(\mathbf{U}, \vec{\nabla} \mathbf{U}) \quad (5.2)$$

The first important aspect of the *cell-vertex* method is the definition of metrics, in particular of the normal vectors. Here, \vec{S}_f denotes the normal vector of a given element face (or edge in 2D), defined as pointing towards the exterior. Its length is weighted by the area of the element face (resp. edge length). The normal vector \vec{S}_k at the vertex k of an element (pointing inward) is obtained by

$$\vec{S}_k = \sum_{f \ni k} -\frac{d}{n_v^f} \vec{S}_f \quad (5.3)$$

where d is the number of spatial dimensions and n_v^f the number of vertices of face f . Figure 5.1 illustrates the process of calculating \vec{S}_{k_1} , the normal at the vertex $k = k_1$ for a triangular and a quadrilateral element. It has to be noted that this method differs for domain boundaries as explained for diffusive fluxes at the end of this section.

Based on this element description, equation 5.1 can be written in a semi-discretized form at node j :

$$\frac{d\mathbf{U}_j}{dt} = -\vec{\nabla} \cdot \vec{\mathcal{F}}^C|_j - \vec{\nabla} \cdot \vec{\mathcal{F}}^V|_j + \mathbf{S}|_j \quad (5.4)$$

To obtain the divergence of the convective fluxes $\vec{\nabla} \cdot \vec{\mathcal{F}}^C|_j$ the element residual R_e is calculated summing flux values located at all vertices k of the element e (the ensemble of these vertices being K_e):

$$\mathbf{R}_e = -\frac{1}{dV_e} \sum_{k \in K_e} \vec{\mathcal{F}}_k^C \cdot \vec{S}_k \quad (5.5)$$

Here, V_e is the element volume which is defined as (d being the number of spatial dimensions):

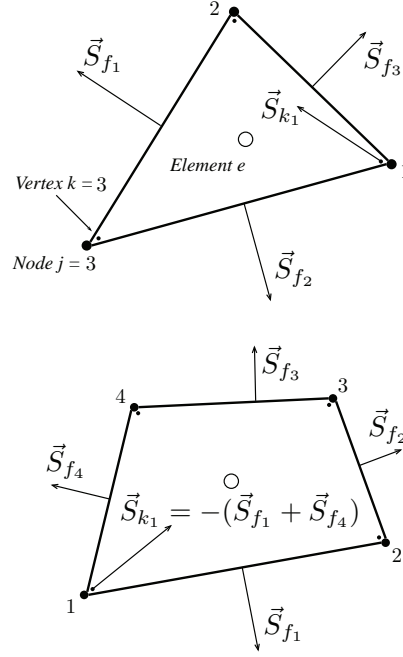


Figure 5.1: Schematic of the face- (f) and vertex- (k) normals of a triangular and a quadrilateral element.

$$V_e = -\frac{1}{d^2} \sum_{k \in K_e} \vec{x}_k \cdot \vec{S}_k \quad (5.6)$$

The nodal value of the flux divergence is then obtained by summing the weighted residuals $V_e \mathbf{R}_e$ of all cells having a vertex coinciding with the node j (the ensemble of these cells being noted \mathcal{D}_j):

$$\vec{\nabla} \cdot \vec{\mathcal{F}}^C|_j = \frac{1}{dV_j} \sum_{e \in \mathcal{D}_j} \underline{\mathbf{D}}_{j,e} V_e \mathbf{R}_e \quad (5.7)$$

This summation, called *scatter-operation*, is schematized in figure 5.2. The nodal volume $V_j = \sum_{e \in \mathcal{D}_j} V_e / n_v^e$ is called *dual cell* as it acts as a control volume during the residual *scatter*. Here, n_v^e is the number of vertices of an element e . The residual distribution matrix $\underline{\mathbf{D}}_{j,e}$ is a central part of the numerical schemes that is built upon the cell-vertex formalism. The convection schemes used in this study are briefly described in sections 5.3 and 5.4.

5.3 The convection schemes for the gaseous phase

AVBP includes several numerical schemes, both for the gas phase and the dispersed phase in the EE formulation. A detailed overview can be found in the thesis of Lamarque [80]. The following section is limited to the schemes that are used in the scope of the present work.

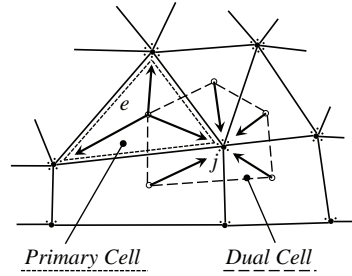


Figure 5.2: Schematic of the cell-vertex formalism. The dotted line delimits an element e (primary cell), the dashed line the control volume of the node j (dual cell), arrows symbolize the scatter operation of an element residual to the surrounding nodes (equation 5.7).

5.3.1 The Lax-Wendroff scheme

This scheme is the adaptation of the classical Lax-Wendroff scheme [84] to the cell-vertex formulation. It uses an explicit time integration with a single Runge-Kutta step. Its accuracy in both space and time is of second order, which is a unique property for a scheme with a stencil this compact. Although it is a centered scheme in space, it is quite robust due to a diffusive term that stabilizes it very effectively. Furthermore, it is characterized by low computational cost.

5.3.2 The TTGC scheme

TTGC is a version of the two-step Taylor-Galerkin (TTG) schemes available in AVBP. This family of schemes is based on the finding that finite-volume methods in a cell-vertex framework can be interpreted as a finite-element approach, allowing the development of Taylor-Galerkin type schemes. TTGC as the most commonly used version, is of third order in time and space. Furthermore, it is characterized by very good properties regarding dissipation and dispersion, making it well-suited for LES applications. On the other hand, it is less robust than the LW scheme and approximately twice as costly.

It has to be pointed out that both, Lax Wendroff and TTGC are centered schemes that necessitate artificial viscosity for stabilization. Information on the methods for its application can be found in section 5.7 and in the thesis of Lamarque [80].

5.4 The convection schemes for the dispersed phase

The requirements on a scheme for the dispersed phase differ from those for the gaseous phase. An analogy allows to interpret the Eulerian formulation of a spray as a highly compressible gas. Therefore, very strong gradients can be expected to appear in turbulent flow. Furthermore, the mesoscopic formulation used in the scope of this work does not allow the crossing of spray structures with different directions, such as crossing jets or certain turbulent structures. This leads to the appearance of so-called δ -shocks (sharp peaks of particle density at the location of impact) that threaten the stability of the numerical scheme. Finally, there are problems like the injection of particle-laden jets that naturally lead to very sharp gradients at the spray boundary, the most extreme case being a jet-in-a-crossflow configuration (see chapter 8). In essence, a scheme for the liquid phase has to be more robust than one conceived for a (subsonic) gaseous flow. Usually, more robust schemes are characterized by increased numerical diffusion,

which is of course an issue for the liquid phase, too. However, as there is no equivalent to a turbulent energy cascade in a spray (the movement in turbulent flow being mainly conditioned by the coupling with the gaseous phase), diffusion by the scheme has different implications as for the gaseous phase where correct turbulent energy dissipation is a very important aspect for numerical schemes for LES.

The numerical schemes described for the gaseous phase (Lax-Wendroff, TTGC) are also available for the Eulerian solver of the liquid phase. For the cited examples, due to the method of implementation, the same scheme is used for both phases. An exception is the PSI scheme that is applied exclusively on the liquid phase and shall be described in the following.

5.4.1 The PSI scheme

The PSI (for Positive Streamwise Invariant) scheme [146] is highlighted here, because it is extensively used in all EE applications of the present work. It is a representative of the so-called fluctuation splitting methods [35]. As such, it is a multi-dimensional upwinding method, which renders it very robust but also more dissipative than a comparable centered scheme.

In its current form, it is of first order in time and of second order in space for steady state problems. However, It loses its spatial accuracy for unsteady problems [1]. Having been implemented in AVBP only recently by Lamarque [80] and Roux [126], it is still subject to extensive validation and testing, fo example by Sanjosé [129], Linkes [90] and Kraushaar.

Crossing of jets

A first example that illustrates the differences between centered schemes and the PSI scheme is the crossing of jets in a 2D configuration. This example is taken from the thesis of Roux [126], which, alongside the work of Lamarque [80], Sanjose [129] as well as Linkes [90] is recommended as an additional source of information on numerical schemes for the Eulerian liquid phase.

This test case contains two of the cited difficulties, namely the injection of a particle-laden jet with sharp spray boundaries as well as the formation of δ -shocks at the location where the jets meet. The result, shown in figure 5.3, reveals a typical behaviour of both schemes: the TTGC scheme necessitates a high amount of artificial viscosity in order to support the strong gradients at the jet boundary. As the resulting diffusion is isotropic, both jets are smeared out almost completely after entering the domain. In the case of PSI, the jets remain perfectly intact as the numerical diffusion created by the upwinding scheme is limited to the streamwise direction. At the location where the jets meet, the result obtained with the PSI scheme reveals the formation of a zone with high particle density, which remains well-controlled in terms of numerical stability.

The influence of artificial viscosity on accuracy

The case of two crossing jets has highlighted the negative effect that high levels of artificial viscosity have on the TTGC scheme. It therefore becomes clear, that the performance of numerical schemes needs to be compared in a realistic numerical approach, i.e. with the amounts of artificial viscosity that is typically needed to keep a simulation stable. Such a comparison is provided in the work of Linkes [90] who considered the convection of a gaussian as well as a top-hat perturbation on the liquid volume fraction α_l using TTGC, Lax-Wendroff and PSI

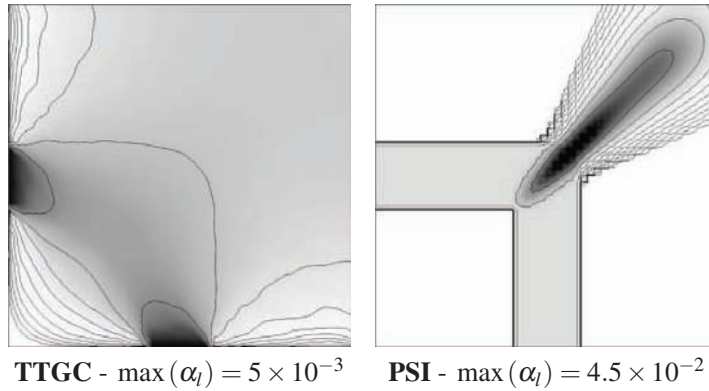


Figure 5.3: Liquid volume fraction fields for the 2D case of two crossing jets. Figure from Roux [126]

along other schemes that shall not be considered here. The case of a gaussian peak convection does not involve artificial viscosity (figure 5.4, left).

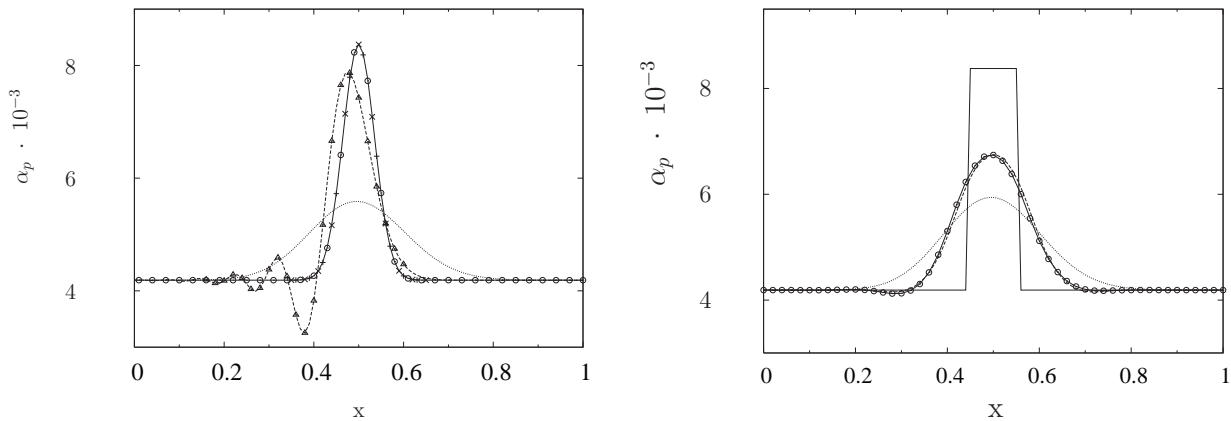


Figure 5.4: 1D convection for different numerical schemes. Left: gaussian perturbation, right: top-hat perturbation. — Initial solution, \cdots PSI, $---$ LW, Δ RK3, \circ TTGC, \times TTG4A, $++$ GRK. Diagrams from Linke [90]

After one turnover time, both centered schemes retain the magnitude of the perturbation and show little (Lax-Wendroff) to no diffusion (TTGC). The Lax-Wendroff scheme additionally reveals a certain amount of dispersion. The PSI result is considerably diffused with less than half of the peak magnitude being retained. The left diagram in figure 5.5 shows the order of TTGC and PSI resulting from a grid convergence study. While TTGC is of third order, the precision of the PSI scheme is clearly inferior (less than first order).

However, in the case of a top-hat perturbation in conjunction with an amount of artificial viscosity that is typical for realistic applications (figures 5.4 and 5.5, right), the results of the centered schemes approach the behaviour of PSI for the diffusion of the perturbation after one turnover. Most interestingly, TTGC in conjunction with a realistic amount of artificial viscosity loses its precision to a point where it drops to a less than first-order accuracy comparable to the PSI scheme.

Three-dimensional example

A final example (taken from the thesis of Roux [126]) illustrates the differences between TTGC and PSI in a lab-scale combustor (figure 5.6). Three fields of droplet number density are compared: The first (from left to right) shows the field obtained with the TTGC scheme, the second

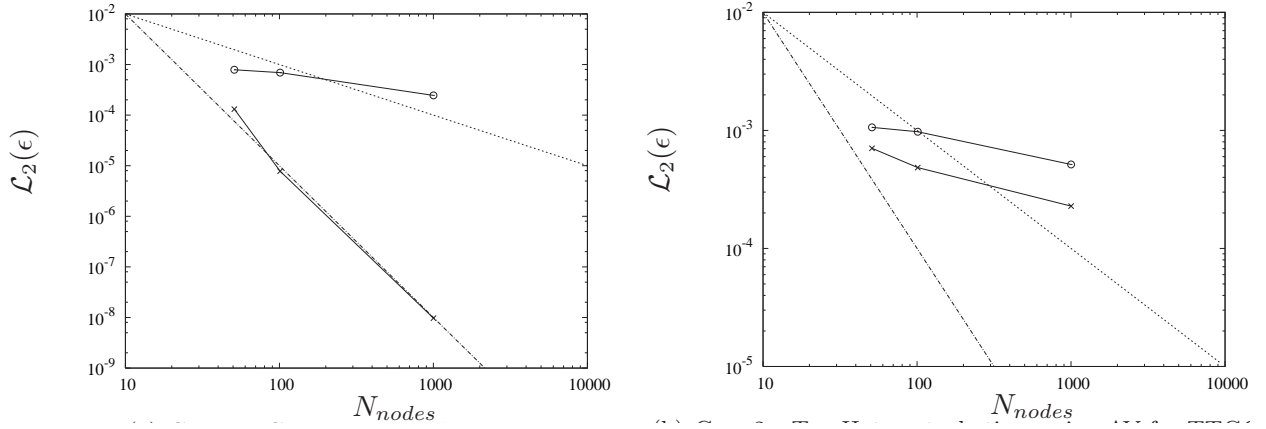


Figure 5.5: Grid convergence for TTGC and PSI. Left: gaussian perturbation, right: top-hat perturbation. \circ – PSI, \times – TTGC, \cdots First order, $--$ Second order. Diagrams from Linkes [90]

the PSI result and the third a view of the experiment, illuminated with a laser sheet in the same plane. An accumulation of droplets in zones of weak vorticity can be observed on all three visualizations. The comparison between TTGC and PSI shows that the centered scheme has a tendency to diffuse the sharp gradients of droplet density. This tendency is observed to a lesser degree for the PSI scheme.

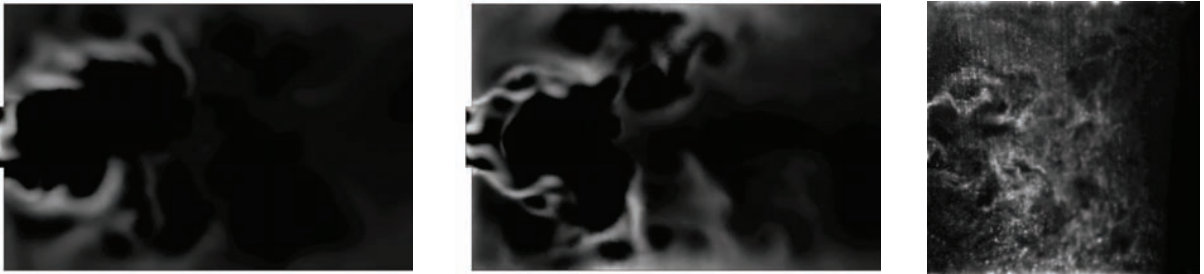


Figure 5.6: Instantaneous fields of droplet number density. Non-reactive spray in an academical combustor. Left: TTGC, middle: PSI, right: experimental result (laser tomography). All images from Roux [126]

It has to be noted that the performance of the TTGC scheme depends strongly on the way artificial viscosity is applied. Significant advances on homogeneous isotropic turbulence cases have been achieved by Sanjosé [129] as well as Vié and Martínez [150] by introducing new sensors for artificial viscosity and by applying models for the random uncorrelated motion, which appear as diffusive terms in the equations and thus stabilize the scheme based on a physical argument. For injection problems, however, these improvements cannot match the inherent robustness of an upwinding scheme

Due to the cited qualities, in particular at the injection of droplet-laden sprays that take an important place in the present work (see chapter 8), the PSI scheme will be employed exclusively despite its drawbacks in terms of accuracy.

In the AVBP code, the PSI scheme has been developed for the application on the dispersed phase only. In calculations using this scheme, the gaseous equations are solved using the Lax-Wendroff scheme. Although it is possible in principle, the combination with other schemes for the gaseous phase is not available at the present date.

5.5 The diffusion scheme

The diffusive fluxes are calculated using the so-called 2Δ operator, which stands for its compact stencil. For the divergence of the viscous terms $\vec{\nabla} \cdot \vec{\mathcal{F}}^V$, the method applied differs from the one used for the convective fluxes (equation 5.7). In a first step, the gradient of the conservative variables $(\vec{\nabla} \mathbf{U})_e$ is calculated on the element e . Using this gradient and the nodal value \mathbf{U}_j allows to calculate the viscous flux tensor from element- and nodal values:

$$\vec{\mathcal{F}}_{j,e}^V = \vec{\mathcal{F}}^V \left((\mathbf{U})_j, (\vec{\nabla} \mathbf{U})_e \right) \quad (5.8)$$

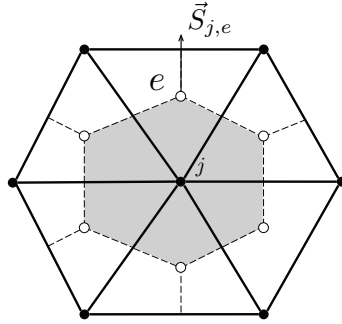


Figure 5.7: Sketch illustrating the 2Δ operator as well as the normal vector $\vec{S}_{j,e}$ used for the diffusion scheme.

The divergence is then obtained by summing all contributions in the *dual cell* associated to the node j :

$$\vec{\nabla} \cdot \vec{\mathcal{F}}^V|_j = \frac{1}{dV_j} \sum_{e \in \mathcal{D}_j} \vec{\mathcal{F}}_{j,e}^V \cdot \vec{S}_{j,e} \quad (5.9)$$

5.6 Calculation of the timestep

In AVBP, the discretized equations are advanced in time in an explicit scheme. Therefore, the global timestep is determined by a CFL (Courant-Friedrichs-Lewy) condition

$$\Delta t_{max} < CFL \frac{\Delta x_{min}}{(|\vec{V}| + c)_{max}} \quad (5.10)$$

that limits the time step as a function of the spatial discretization Δx . In practice, this introduces an important constraint because excessively small grid cells, even if they occur only very locally and in small numbers can considerably increase the computational cost of the entire computation.

5.6.1 Liquid phase timestep

In its present implementation, the timestep is based on gaseous variables only, with liquid phase effects like evaporation or drag not being taken into account. This is deemed acceptable as AVBP is a fully compressible and explicite code, thus resolving acoustic timescales. It is assumed that these timescales are large compared to the droplet relaxation timescale or evaporation timescale

for almost the entire droplet lifetime. A common criterion related to accuracy of evaporation processes is that during an iteration, no more than 10 % of the current droplet mass should be evaporated.

$$\frac{\Delta m_p}{m_p} < 0.1 m_p \quad (5.11)$$

It is widely used for RANS methods with large timesteps to determine the necessary sub-iterations for the liquid phase. Similar criteria exist for heat transfer and drag.

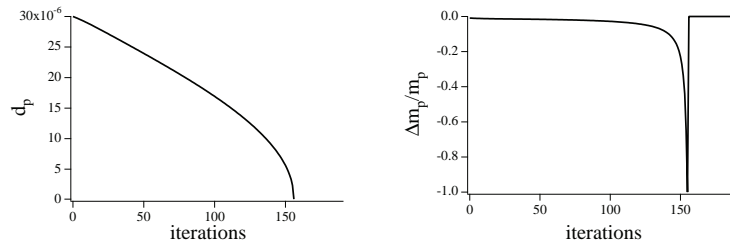


Figure 5.8: Diameter evolution (left) and the ratio of evaporated mass per iteration Δm_p and the current droplet mass m_p over the number of iterations. Results of a 0D evaporation case.

Figure 5.8 shows the evolution of the diameter in a 0D evaporation testcase along with a visualization of the timestep criterion in equation 5.6.1 for a typical timestep. It is clear that this criterion can never be satisfied until evaporation is complete as it inevitably takes the value of -1 in the very last timestep. However, it remains inside the limit until droplets have reached very small diameters. At such diameters, in the EE formulation, evaporation will have been stopped in order to avoid nonzero values, while for EL a special procedure is applied for droplets of vanishing size (see section 4.3.6).

5.7 Artificial viscosity models for the gaseous phase

5.7.1 Introduction

To avoid the small-scale oscillations (also known as “wiggles”) in the vicinity of steep variations and to smooth very strong gradients, it is common practice to add a so-called artificial viscosity (AV) term to the discrete equations. Such a method avoids accumulation of energy in these non-physical modes without altering the quality of the solution.

These AV models are based on a combination of a “shock capturing” term (called 2^{nd} order AV) which smoothes under-resolved gradients and a “background dissipation” term (called 4^{th} order AV) which dissipates the wiggles. They are characterized by the “linear preserving” property which leaves unmodified a linear solution on any type of element.

The introduction of AV is done in two steps. First, a sensor detects if AV is necessary, as a function of the flow characteristics. In LES, the sensor must be active only in spatially limited zones to avoid interacting with the subgrid stresses. Then, a certain amount of 2^{nd} and 4^{th} order AV is applied, depending on the sensor value and on user-defined parameters.

5.7.2 The sensors

A sensor ζ_e is a scaled parameter that is defined for every cell e of the domain that takes values from zero to one. $\zeta_e = 0$ means that the solution is well resolved and that no AV should be applied while $\zeta_e = 1$ signifies that the solution has strong local variations and that AV must be applied. This sensor is obtained by comparing different evaluations (on different stencils) of the gradient of a given scalar (pressure, total energy, mass fractions, ...). If these gradients are identical, then the solution is locally linear and the sensor is zero. On the contrary, if these two estimations are different, local non-linearities are present, and the sensor is activated. The key point is to find a suitable sensor-function that is non-zero only at places where stability problems occur.

Two sensors are available in AVBP: the so-called ‘Jameson-sensor’ (ζ_e^J) [72] and the ‘Colin-sensor’ (ζ_e^C) [31] which is an upgrade of the previous one.

The Jameson sensor

For every cell e , the Jameson cell-sensor ζ_e^J is the maximum over all cell vertices of the Jameson vertex-sensor ζ_k^J :

$$\zeta_e^J = \max_{k \in e} \zeta_k^J \quad (5.12)$$

Denoting S the scalar quantity the sensor is based on (usually S is the pressure), the Jameson vertex-sensor is:

$$\zeta_k^J = \frac{|\Delta_1^k - \Delta_2^k|}{|\Delta_1^k| + |\Delta_2^k| + |S_k|} \quad (5.13)$$

Where the Δ_1^k and Δ_2^k functions are defined as:

$$\Delta_1^k = S_e - S_k \quad \Delta_2^k = (\vec{\nabla} S)_k \cdot (\vec{x}_e - \vec{x}_k) \quad (5.14)$$

where a k subscript denotes cell-vertex values while e is the subscript for cell-averaged values.

$(\vec{\nabla} S)_k$ is the gradient of S at the node coinciding with the vertex k .

Δ_1^k measures the variation of S inside the cell e (using only quantities defined on this cell). Δ_2^k is an estimation of the same variation but on a wider stencil (using all the neighbouring cell of the node coinciding with k).

It is important to note that this sensor is smooth: it is roughly proportional to the amplitude of the deviation from linearity.

The Colin sensor

As said above, the Jameson sensor is smooth and was initially derived for steady-state computations. For most unsteady turbulent computations it is however necessary to have a sharper sensor, which is very small when the flow is sufficiently resolved, and which is nearly maximum when a certain level of non-linearities occurs.

This is the aim of the so-called Colin-sensor, whose properties can be summarized as follows:

- ζ_e^C is very small when both Δ_1^k and Δ_2^k are small compared to S_e . This corresponds to low amplitude numerical errors (when Δ_1^k and Δ_2^k have opposite signs) or smooth gradients that are well resolved by the scheme (when Δ_1^k and Δ_2^k have the same sign).
- ζ_e^C is small when Δ_1^k and Δ_2^k have the same sign and the same order of magnitude, even if they are quite large. This corresponds to stiff gradients well resolved by the scheme.

- ζ_e^C is big when Δ_1^k and Δ_2^k have opposite signs and one of the two term is large compared to the other. This corresponds to a high-amplitude numerical oscillation.
- ζ_e^C is big when either Δ_1^k or Δ_2^k is of the same order of magnitude as S_e . This corresponds to a non-physical situation that originates from a numerical problem.

The exact definition of the Colin-sensor is:

$$\zeta_e^C = \frac{1}{2} \left(1 + \tanh \left(\frac{\Xi - \Xi_0}{\delta} \right) \right) - \frac{1}{2} \left(1 + \tanh \left(\frac{-\Xi_0}{\delta} \right) \right) \quad (5.15)$$

with:

$$\Xi = \max_{k \in e} \left(0, \frac{\Delta^k}{|\Delta^k| + \epsilon_1 S_k} \zeta_k^J \right) \quad (5.16)$$

$$\Delta^k = |\Delta_1^k - \Delta_2^k| - \epsilon^k \max \left(|\Delta_1^k|, |\Delta_2^k| \right) \quad (5.17)$$

$$\epsilon^k = \epsilon_2 \left(1 - \epsilon_3 \frac{\max \left(|\Delta_1^k|, |\Delta_2^k| \right)}{|\Delta_1^k| + |\Delta_2^k| + S_k} \right) \quad (5.18)$$

The numerical values used in AVBP are:

$$\Xi_0 = 2.10^{-2} \quad \delta = 1.10^{-2} \quad \epsilon_1 = 1.10^{-2} \quad \epsilon_2 = 0.95 \quad \epsilon_3 = 0.5 \quad (5.19)$$

5.7.3 The operators

There are two AV operators in AVBP: a 2nd order operator and a 4th order operator. All AV models in AVBP are a blend of these two operators. These operators have the following properties:

- 2nd order operator: it acts like a “classical” viscosity. It smoothes gradients, and introduces artificial dissipation. It is thus associated to a sensor which determines where it must be applied. Doing this, the numerical scheme keeps its order of convergence in the zones where the sensor is inactive, while ensuring stability and robustness in the critical regions. Historically, it was used to control shocks, but it can actually smooth any physical gradient.
- 4th order operator: it is a less common operator. It acts as a bi-Laplacian and is mainly used to control spurious high-frequency wiggles.

Both operator contributions are first computed on each cell vertex, and are then scattered back to nodes (there is no divergence here, as it is done directly during the scattering operation).

5.7.4 The sensors for the Eulerian dispersed phase

For the gas phase, the sensors are based on the pressure, as it is assumed that this variable is most sensitive to any perturbation of the flow. In the EE formulation for the dispersed phase, there is no direct equivalent to the pressure. Furthermore, considering only one variable to detect the wiggles and the strong gradients in the spray is not sufficient. Therefore, sensors are calculated from a choice of variable fields of the dispersed phase and the maximum value is retained.

For the dispersed liquid phase two types of sensors are used:

- A sensor based on extrema ζ_{extr} : this sensor checks whether the liquid variables, especially liquid volume fraction, droplets number density and droplet diameters, stay in the physical domain.
- A sensor based on gradients ζ_{tpf} : this sensor tries to target numerical instabilities.

Each sensor is evaluated at the cell, e , and the maximum value of both sensors is applied. For both sensors, different models are available in AVBP. The basic formulations used for the gradient based sensors in the present work are the Jameson-Riber-sensor and an adapted Colin-sensor.

5.8 Boundary conditions

Boundary conditions are an important ingredient of a LES because the concept is unsteady by nature and, in the case of AVBP includes also acoustic waves. This means that boundary conditions need to satisfy certain criteria of non-reflectivity. A direct imposition of boundary values onto the conserved variables leads to a total reflection of acoustic perturbations and additionally to numerical artifacts. For this reason, the concept of characteristic boundary conditions has been introduced by Poinso and Lele [114], [115] (NSCBC approach). This method is an extension of the characteristic decomposition of the Euler equations on viscous flows and allows to define waves that can directly be acted upon by the boundary condition.

There are several ways to impose boundary conditions in the discretized equations. Consider the a simplified form with a single-step time advancement, where \mathbf{U}_j^n is the vector of conservative variables on the node j at the timestep n . The hard way to impose Dirichlet boundary conditions is to replace the flow variables predicted by the scheme for the timestep $n + 1$ by the imposed value at the nodes located on the domain boundary $\partial\Omega$:

$$\mathbf{U}_j^{n+1} = \mathbf{U}_j^n - \frac{\Delta t}{V_j} (d\mathbf{U}_j^n)_{\text{scheme}} \quad \forall j \in \{\Omega \setminus \partial\Omega\} \quad (5.20)$$

$$\mathbf{U}_j^{n+1} = (\mathbf{U}_j^{n+1})_{\text{BC}} \quad \forall j \in \{\partial\Omega\} \quad (5.21)$$

For Neumann boundary conditions, the correction is applied after the calculation of the fluxes. The boundary condition is used to determine a corrected nodal residual $d\mathbf{U}_j^n$ that replaces the residual predicted by the scheme before advancing the equations in time to obtain a new vector of flow variables \mathbf{U}_j^n :

$$\mathbf{U}_j^{n+1} = \mathbf{U}_j^n - \frac{\Delta t}{V_j} (d\mathbf{U}_j^n)_{\text{scheme}} \quad \forall j \in \{\Omega \setminus \partial\Omega\} \quad (5.22)$$

$$\mathbf{U}_j^{n+1} = \mathbf{U}_j^n - \frac{\Delta t}{V_j} (d\mathbf{U}_j^n)_{\text{BC}} \quad \forall j \in \{\partial\Omega\} \quad (5.23)$$

This method is used for the non-characteristic application of Neumann boundary conditions (for example the wall shear stress predicted by a wall model), but also for the characteristic boundary conditions (Neumann and Dirichlet type) that also modify the residual at the boundary nodes.

5.9 Numerical aspects of the Euler-Lagrange solver

Numerical methods of the Lagrangian approach turn around two main aspects, the time-integration method and the methods to couple the set of Lagrangian particles with the Eulerian representation of the gas phase with a fixed computational grid.

5.9.1 Time integration

The time integration method used in the scope of the present work is a first-order forward Euler method of the form

$$f^{(n+1)} = f^{(n)} + \left(\frac{df}{dt}\right)^{(n)} \Delta t \quad (5.24)$$

where n is a given timestep and f an arbitrary variable that is transported by a Lagrangian particle. If the numerical scheme of the gaseous phase has several time-integration steps, the Lagrangian solver updates the particles and the source terms only at the initial iteration and remains inactive for the subsequent subiterations. A second-order time integration method has been developed by Senoner in his thesis [135].

5.9.2 Interpolation methods

The gaseous values needed for calculations at the particles are interpolated from the Eulerian grid to the particle position $x_{p,i}$. The expression for an arbitrary quantity f is recalled (see also section 3.2.1):

$$f_{g@p} = \sum_{j \in K_e} w(x_{p,i}, x_{j,i}) \bar{f}_{g,j} \quad (5.25)$$

The term $w(x_{p,i}, x_{j,i})$ stands for a generic interpolation function. Note that the values transferred to the particles in a LES are always the resolved (or filtered) ones. Three different interpolation methods are available:

- A first-order interpolation using a Taylor series for the values of the flow field
- A linear least-squares method
- A method based on Lagrange polynomials

A detailed description of these interpolation methods can be found in the thesis of García [49].

5.9.3 Two-way coupling terms

For two-way coupling terms, quantities obtained for a set of particles are passed to the Eulerian grid of the gas phase (see section 3.2.1). The distribution scheme for a generic source term, noted S_p , generated at a particle k that is located inside the grid cell e is recalled:

$$S_j = \frac{1}{V_j} \sum_{k \in \mathcal{D}_j} \Theta_{j,e}^{(k)} S_p^{(k)} \quad (5.26)$$

Here, the contribution of this source term that is received by a given grid node j is obtained by the summation of all weighted contributions from all particles inside \mathcal{D}_j , the set of cells having a vertex coinciding with j (see figure 3.1 for a schematic).

As the source terms in the gaseous equations are quantities measured per unit volume, the sum is divided by V_j , the nodal control volume or the median dual cell. The weights $\Theta_{j,e}^{(k)}$ that are applied to the contribution of the particle (k) can be obtained from the ration of the inverse distances to the target node j and the sum of all inverse distances to the nodes of the cell K_e in which the particle is located:

$$\Theta_{j,e}^{(k)} = \frac{\frac{1}{|x_{p,i}^{(k)} - x_{j,i}|}}{\sum_{n \in K_e} \frac{1}{|x_{p,i}^{(k)} - x_{n,i}|}} \quad (5.27)$$

Another form to express these weights avoids a singularity when particle and node coincide:

$$\Theta_{j,e}^{(k)} = \frac{\prod_{n \neq j} |x_{p,i}^{(k)} - x_{n,i}|}{\sum_{r \in K_e} \prod_{m \neq r} |x_{p,i}^{(k)} - x_{m,i}|} \quad (5.28)$$

This is the method that is actually implemented in the Lagrangian solver of AVBP. The original description of the methods described here can be found in the thesis of García [49].

5.10 Wall interaction of Lagrangian particles

In a Lagrangian approach, there are no boundary conditions in the classical sense. What corresponds best to an inlet condition is the placement of particles at prescribed positions, as it is described for an injection case in chapter 8. Outlet conditions are not needed, because particles that propagate into regions outside the Eulerian grid are simply not found by the search algorithm and disappear from the calculation. The only veritable boundary condition is needed for solid walls, which can pose a quite complex problem to solve, depending on the physical detail one wishes to include. The physics involved in droplet-wall interaction comprise phenomena like rebound, splashing and film formation just to name a few (see [47] for more detail). In the scope of the present work, only the case of an elastic rebound is considered, which can be justified under certain circumstances for hot surfaces as they are routinely encountered in combustion chambers. Mainly, however, this method serves the purpose of ensuring mass-conservation.

The actual procedure consists in flagging a closed layer of all grid cells adjacent to the walls, while establishing the connectivity between a given cell and the underlying boundary normal (see figure 5.9 for a schematic). If a particle enters this layer, which can be assumed to be very thin compared to the dimensions of the computational domain, the wall-normal component of its velocity is reversed, which results in a behaviour very close to an elastic rebound on the wall. Alternatively, the wall-normal velocity can be set to zero, which results in a completely inelastic impact after which the particle will continue to move in wall-parallel direction.

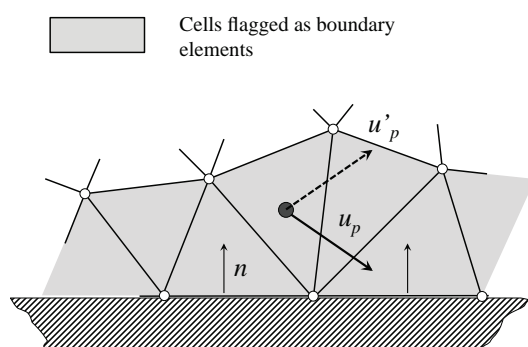


Figure 5.9: Schematic of the wall treatment for Lagrangian particles.

Part III

Preliminary studies

Chapter 6

Wall modeling

Contents

6.1	Introduction	101
6.1.1	The turbulent boundary layer	102
6.2	Wall-function implementation methods	106
6.2.1	The cell-vertex approach for wall-boundaries	106
6.2.2	The use of wall functions in LES solvers	108
6.2.3	Implementation with slip velocity at the wall	109
6.2.4	Corner problem	110
6.2.5	Implementation without slip velocity at the wall	111
6.2.6	Limitations of the no-slip approach	112
6.3	Applications and Results	113
6.3.1	Turbulent channel flow	114
6.3.2	Flow over a sudden expansion	116
6.3.3	Injector for aero-engines (TLC configuration)	118
6.4	Analysis of limits of wall function approaches	123
6.4.1	Implementation method	123
6.4.2	Grid dependency	125
6.4.3	The influence of the subgrid-scale viscosity model	125
6.5	Conclusion	131
6.6	Summary of the elements applied on the TLC configuration	132

6.1 Introduction

A correct treatment of walls in Large Eddy Simulations (LES) of industrial-scale complex geometries remains a challenging task. Despite growing computing resources, mainly in the form of massively parallel machines, the resolution of boundary layer flows remains out of reach for routinely application [110] [111], making wall modeling a crucial ingredient of practical LES [98].

Wall-functions avoid to resolve the turbulent eddies that are proportional in size to the wall-normal distance (as opposed to wall-resolved LES), as well as the strongest gradients in the viscous sublayer (which is still necessary when resolving RANS equations near the wall, as it is done in DES approaches). The gain in terms of grid resolution is considerable [111], while very

satisfying precision can be obtained even for complex flows [98].

Since the pioneering work by Deardorff [34] and Schumann [133], published studies on wall-functions are mainly concerned with extending the underlying wall-model to take into account more physical detail, such as heat fluxes (Grötzbach [53]), streamwise pressure gradients (Hoffmann and Benocci [65]) or chemical reactions (Cabrit [22]) just to name a few. On the other hand, relatively few sources treat the actual implementation of wall-functions into a flow-solver. In this chapter, several ways to couple wall-functions with a numerical scheme will be explained and it will be demonstrated that these differences can significantly affect the results of a LES. In particular, this is the case in configurations with a flow over a sudden expansion (or simply a step) and more generally in complex geometries. The study is limited to cell-vertex-type solvers at the example of the AVBP code. In the first part, the wall-modeling approach is laid out, followed by a description of the cell-vertex formalism, the methods of implementing wall-functions therein and the related problems that can occur. In the following section, the different methods are evaluated and compared on several testcases ranging from a turbulent channel flow to a premixing swirler for aero-engines. Finally, different sources of error involved in a wall function approach shall be discussed.

As wall modeling in itself is not the main interest of the present work, the following section will be used to present a most basic model derived from classical boundary layer theory to lay the groundwork for the following discussion of different implementation methods. It should be noted that these implementation strategies can in principle be combined with other, more sophisticated wall law formulations. Furthermore, although turbulent heat transfer is an important part in a wall-modeling approach, it shall be excluded in this study, which will be focused on momentum conservation.

6.1.1 The turbulent boundary layer

The fully developed turbulent boundary layer flow over an infinite flat plate is considered. This implies that, in a Reynolds-averaged form, the problem is steady ($\partial/\partial t = 0$) and one-dimensional ($\partial/\partial x = 0$, $\partial/\partial z = 0$) with the wall-distance y being the only relevant spacial direction and the streamwise velocity \bar{u} the sole non-zero mean velocity component. Here, Reynolds-averaged variables are denoted with the bar-operator ($\bar{}$) and the index w identifies quantities at the wall. The density ρ as well as the heat capacity at constant pressure C_P are considered constant in this context. An additional assumption is the absence of chemical reactions. The momentum equation of the time-averaged flow then reduces to:

$$\frac{\partial \bar{p}}{\partial x} = \frac{\partial \bar{\tau}_{xy}}{\partial y} - \frac{\partial}{\partial y} \underbrace{\bar{\rho} u'v'}_{\tau_t} \quad (6.1)$$

Where $\tau_{xy} = \bar{\mu} \partial \bar{u} / \partial y$ is the remaining non-zero term of the viscous stress tensor and τ_t the only non-zero term of the Reynolds-tensor which is related to the velocity gradient via a turbulent velocity, μ_t , according to the Boussinesq assumption:

$$\tau_t = -\mu_t \frac{\partial \bar{u}}{\partial y} \quad (6.2)$$

The case of a flat plate is characterized by the absence of a longitudinal pressure gradient $\partial \bar{p} / \partial x = 0$. The momentum equation written in terms of μ and μ_t then takes the following

form:

$$\frac{\partial}{\partial y} \left(\frac{\partial \bar{u}}{\partial y} (\bar{\mu} + \mu_t) \right) = 0 \quad (6.3)$$

This equation states that the total level of friction, $\tau_{tot} = \bar{\tau}_{xy} - \bar{\tau}_t$ is constant throughout the boundary layer. It implies that the total friction must be equal to the wall-friction, which corresponds to the viscous wall shear stress $\tau_w = \bar{\mu} \partial \bar{u} / \partial y|_w$, since the turbulent vanishes at the wall due to the absence of any fluctuations. Integration of equation 6.3 and making use of $\tau_{tot} = \tau_{wall}$ yields:

$$\frac{\partial \bar{u}}{\partial y} (\bar{\mu} + \mu_t) = \tau_w \quad (6.4)$$

For the following steps, it is convenient to introduce wall units, based on the friction velocity $u_\tau = \sqrt{\tau_w / \rho_w}$ and defined as:

$$y^+ = \frac{\rho_w u_\tau y}{\mu_w} \quad u^+ = \frac{\bar{u}}{u_\tau} \quad \mu^+ = \frac{\bar{\mu}}{\mu_w} \quad \mu_t^+ = \frac{\mu_t}{\mu_w} \quad (6.5)$$

It can be noted that y^+ is in fact a Reynolds number that is valid at the wall distance y . For channel- or pipe flows, it is very common to define the friction Reynolds number as

$$Re_\tau = \frac{\rho_w u_\tau \delta_c}{\mu_w} \quad (6.6)$$

with δ_c being the channel half-width.

Equation 6.4 written in wall units takes the form:

$$\frac{d u^+}{d y^+} (\mu^+ + \mu_t^+) = 1 \quad (6.7)$$

In order to obtain an analytical expression for the turbulent boundary layer, it is necessary to find a closure for μ_t and to integrate the differential equation. To simplify the problem, the classical approach consists in tackling two subparts separately. Considering the structure of a turbulent boundary layers, three zones can be distinguished (see figure 6.1): the part very close to the boundary layer (typically $y^+ < 5$ to 6) is characterised by laminar viscosity being the predominant mechanism for generating friction. This region where $\mu \gg \mu_t$ is called the viscous sublayer. Away from the wall, for values of y^+ superior to 30, the momentum exchange in y direction generated by turbulence is the main contribution to the local shear stress and separated in scale from viscous stress so that $\mu_t \gg \mu$. This region is called the inertial layer. The inertial- and the viscous sublayer are connected by the buffer layer where μ_t and μ are of the same order.

The viscous sublayer

We consider first the viscous sublayer. In the case of equation 6.7, the basic assumptions for this case translate to $\mu^+ \gg \mu_t^+$. The momentum equation reduces to:

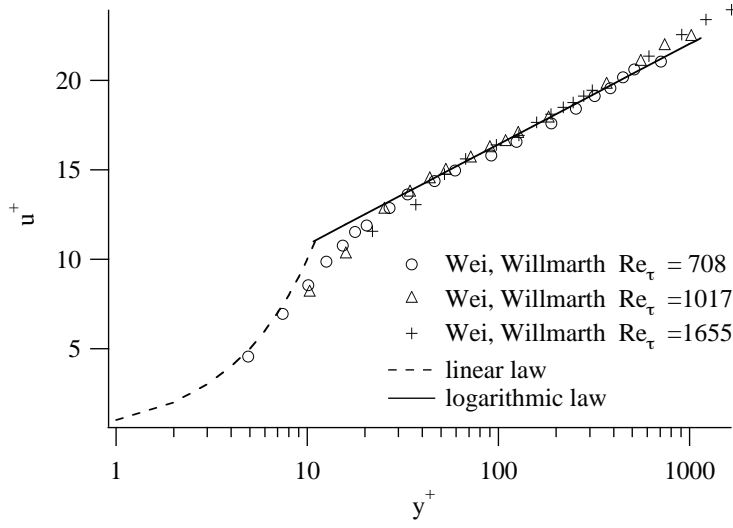


Figure 6.1: *Experimental velocity profiles of a turbulent channel flow [153], theoretical velocity profiles of a turbulent boundary layer (linear and logarithmic law)*

$$\frac{du^+}{dy^+} \mu^+ = 1 \quad (6.8)$$

For further simplification, the viscous sublayer is assumed to be quasi-isothermal, which allows to write: $\mu^+ = \bar{\mu}/\mu_w \approx 1$. One obtains a simple law for the velocity:

$$u^+ = y^+ \quad (6.9)$$

The inertial layer

In wall units, the inertial layer is characterized by: $\mu_t^+ \gg \mu^+$. The momentum equation reduces to:

$$\frac{du^+}{dy^+} \mu_t^+ = 1 \quad (6.10)$$

To provide a closure for the turbulent viscosity, the Prandtl mixing length model [117] is introduced:

$$\mu_t = \rho l_m^2 \left| \frac{d\bar{u}}{dy} \right| \quad (6.11)$$

It depends on the mixing length $l_m = k y$, where k is the universal Von Kármán constant [151]. In wall units, the model translates to:

$$\mu_t^+ = \rho^+ (k y^+)^2 \frac{du^+}{dy^+} \quad (6.12)$$

A further simplification is to consider the boundary layer as incompressible, and thus $\rho^+ = \bar{\rho}/\rho_w \approx 1$.

$$\mu_t^+ = (k y^+)^2 \frac{du^+}{dy^+} \quad (6.13)$$

This expression for μ^+ is injected into equation 6.10 and the result is integrated, giving

$$u^+ = \frac{1}{k} \ln(y^+) + C \quad (6.14)$$

which is the classic logarithmic boundary layer velocity profile. The constant C can be obtained experimentally and is case-dependent. As two typical examples, C takes a value of 5.5 for a channel flow and 5.2 for an external boundary layer.

The central core

For the flow over a flat plate, logarithmic laws are theoretically valid for any given wall distance above the buffer layer, which corresponds to the case of $Re \rightarrow \infty$. For finite Reynolds numbers, typically when considering flows in channels or pipes, the domain of validity is limited to a window of approximately $y^+ > 30$ and $y \ll \delta_c$ (the upper limit depends on the Reynolds number). The effect can be observed in the experimental velocity profiles in figure 6.1 where a deviation from the logarithmic law is noticeable for values of y^+ superior to approximately 600. In the numerical application, this implies that the level of y^+ at which logarithmic laws are evaluated has to be inside this domain of validity.

Analytical laws for finite Reynolds numbers exist and can be grouped into two main types, one based on logarithmic laws, the other having the form of a power law. There is controversy about the theoretical justification of either type [21]. Generally, power-law profiles tend to better reproduce the upper boundary layer while logarithmic laws are more accurate in the lower regions.

The type based on logarithmic laws, has a form similar to the classical logarithmic law (6.14) but includes a characteristic length scale, most commonly the boundary layer thickness δ which can also correspond to the half-width of a channel or a pipe. A well-known example is the so-called law of the wake proposed by Coles [30]:

$$\frac{\bar{u} - u_{cl}}{u_\tau} = \frac{1}{k} \ln\left(\frac{y}{\delta}\right) + C_c \quad (6.15)$$

Where u_{cl} is the velocity outside the boundary layer (for example on the centerline of a channel) and C_c is a case-dependent constant that is obtained experimentally. A very common example for the second, power law type is the Barenblatt law [10]. It includes the parameters α and β which depend on a Reynolds number that is based on the bulk velocity and the pipe diameter or channel width $Re = \rho u_{bulk} 2\delta_c / \mu$.

$$u^+ = \beta (y^+)^{\alpha} \quad \beta = \frac{1}{\sqrt{3}} \ln(Re) + \frac{5}{2} \quad \alpha = \frac{3}{2 \ln(Re)} \quad (6.16)$$

This law is not predictive for the velocity profile as it depends on the bulk velocity via the

Reynolds number. However, Barenblatt has shown that the law 6.16 presents an implicate link between Re and Re_τ :

$$Re_\tau = \frac{1}{2} \left(\frac{e^{\frac{3}{2\alpha}} \alpha (1 + \alpha) (2 + \alpha)}{\sqrt{3} + 5 \alpha} \right)^{\frac{1}{1+\alpha}} \quad (6.17)$$

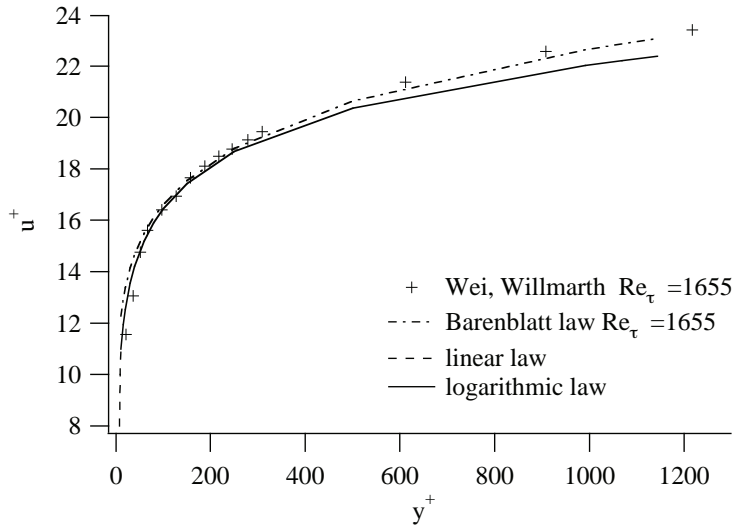


Figure 6.2: *Experimental and theoretical mean velocity profiles of a turbulent channel flow (Wei, Willmarth [153], Barenblatt law [10] at $Re_\tau = 1655$); theoretical profiles of a turbulent boundary layer.*

As Re_τ can be determined independently in many cases, this law is a good candidate to serve as an analytical reference solution. Figure 6.2 shows the dimensionless velocity profiles of a channel flow with $Re_\tau = 1655$ and compares the Barenblatt solution to an experiment of Wei and Willmarth [153]. The linear and logarithmic laws are also included for comparison. The Barenblatt law tends to follow the measurement data quite well at the center of the channel where the logarithmic law visibly drops to lower values outside its domain of validity. The main weakness of the Barenblatt law is its overestimation of the velocity in the buffer layer ($8 < y^+ < 30$) and below. However, when considering more global quantities such as the mass flux, this weakness is of relatively low influence.

6.2 Wall-function implementation methods

6.2.1 The cell-vertex approach for wall-boundaries

The cell-vertex approach has an important implication on the way wall models are implemented. This is due to the fact that the flow variables are located at the grid nodes, and therefore also at locations coinciding with the domain boundary. The cell-vertex approach is described in chapter 5. Here, the explanation begins with recalling the diffusion scheme that is of interest for the type of wall-model considered.

For the divergence of the viscous terms $\vec{\nabla} \cdot \vec{\mathcal{F}}^V$, the method applied differs from the one used

for the convective fluxes. First, the gradient of the conservative variables $(\vec{\nabla} \mathbf{U})_e$ is calculated for the element e . Using this gradient and the nodal value \mathbf{U}_j allows to calculate the viscous flux tensor from element and node values:

$$\vec{\mathcal{F}}_{j,e}^V = \vec{\mathcal{F}}^V \left((\mathbf{U})_j, (\vec{\nabla} \mathbf{U})_e \right) \quad (6.18)$$

The divergence is then obtained by summing all contributions in the *dual cell* associated to the node j :

$$\vec{\nabla} \cdot \vec{\mathcal{F}}^V|_j = \frac{1}{dV_j} \sum_{e \in \mathcal{D}_j} \vec{\mathcal{F}}_{j,e}^V \cdot \vec{S}_{j,e} \quad (6.19)$$

The normal vectors $\vec{S}_{j,e}$ used in this operation are located at the center of a given element e and associated to the node j . Figure 6.3 schematizes the location and direction of these normals. It can be shown that they are equal to the vertex normals \vec{S}_k , where the vertex k coincides with the node j considered.

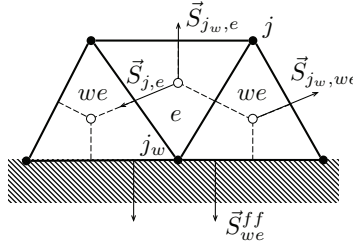


Figure 6.3: Sketch of the normals $\vec{S}_{j,e}$ used for the diffusion scheme and the face-based normals \vec{S}_{we}^{ff} appearing at the application of Neumann boundary conditions on elements with boundary faces, noted we .

Applying Neumann boundary conditions in a finite volume framework corresponds to imposing fluxes through the domain boundary. To do this efficiently, the diffusive flux divergence operation in equation 6.18 is modified for nodes located on wall boundaries, noted j_w (see figure 6.3): the prediction of the diffusion scheme is corrected by adding fluxes given by the boundary condition, $\vec{\mathcal{F}}_{j_w,we}^{BC}$.

$$\vec{\nabla} \cdot \vec{\mathcal{F}}^V|_{j_w} = \underbrace{\frac{1}{dV_{j_w}} \sum_{e \in \mathcal{D}_{j_w}} \vec{\mathcal{F}}_{j_w,e}^V \cdot \vec{S}_{j_w,e}}_{\text{Diffusion scheme prediction}} + \underbrace{\sum_{we \in \mathcal{D}_{j_w}} \vec{\mathcal{F}}_{j_w,we}^{BC} \cdot \vec{S}_{we}^{ff}}_{\text{Boundary correction}} \quad (6.20)$$

Instead of $\vec{S}_{j,e}$, the correction term uses face-based normal vectors, noted \vec{S}_{we}^{ff} . They are defined as the normals of an element face located on the boundary, as shown in figure 6.3 for the boundary elements (denoted by we).

6.2.2 The use of wall functions in LES solvers

In sections 6.1.1 and 6.2.1, the wall model and the numerical framework have been described. The missing ingredient for the implementation of wall laws is how numerics and wall model are combined *in a LES context*. For the sake of clarity, the following paragraphs are limited to a one-dimensional view (in wall-normal direction), analogous to turbulent boundary layer theory. The shear balance in the element adjacent to the wall (noted ‘ we ’) takes the form:

$$\tau_{xy}|_{we} = \frac{d\hat{u}}{dy}\Big|_{we} (\mu|_{we} + \mu_{sgs}|_{we}) = \frac{\hat{u}_2 - \hat{u}_1}{\Delta y} (\mu|_{we} + \mu_{sgs}|_{we}) \quad (6.21)$$

where u_1 and u_2 are the velocities at directly on the wall and on the first grid point respectively, ‘ $\hat{\cdot}$ ’ is the LES filter operator, Δy is the wall-distance of the first point and μ_{sgs} the subgrid-scale viscosity. In cases of low near-wall grid resolution, this equation cannot yield correct results: the subgrid-scale viscosity is given by a LES model that is designed to account for stresses in the unresolved scales of turbulence. Near the wall, however, typical models will fail to predict the wall shear stress correctly, as they are not based on physical arguments related to under-resolved, wall-bounded flows. Instead, their behaviour is known to be often unphysical in under-resolved boundary-layers or generally in zones of pure shear [104], for instance in the case of the Smagorinsky model [140].

The central idea of wall functions consists in locally using boundary layer theory (of the type layed out in section 6.1.1) in lieu of the diffusion scheme to restore the correct balance in equation 6.21. In the element adjacent to the wall, the predicted shear stress $\tau_{xy}|_{we}$ is corrected by a value obtained from a wall model, $\bar{\tau}_w^{model}$.

$$\tau_{xy}|_{we} = \bar{\tau}_w^{model} \quad (6.22)$$

In the present study, $\bar{\tau}_w^{model}$ is obtained from the logarithmic law (equation 6.14). Although this law is very common for wall function approaches, other relations exist, for example in the form of a power law, as applied in the very popular method by Werner and Wengle [154]. Written in flow variables, it reveals its practical property of relating the wall shear stress to any point in the velocity profile located inside the inertial layer:

$$\hat{u} = \frac{1}{k} \sqrt{\frac{\bar{\tau}_w}{\rho_{we}}} \ln \left(\frac{\rho_w y \sqrt{\bar{\tau}_w / \rho_{we}}}{\mu|_{we}} \right) + C \quad (6.23)$$

In practice, this equation can be numerically resolved to provide the wall shear stress as a function of the velocity \hat{u}_2 at the first off-wall point with the wall distance Δy (assuming ρ_{we} and μ_{we} to be constant):

$$\bar{\tau}_w = f(\Delta y, \hat{u}_2) \quad (6.24)$$

Note that this approach involves Reynolds-averaged variables (noted with the bar operator ‘ $\bar{\cdot}$ ’) as filtered variables of the LES. In a wall function approach, it is generally assumed that the near-wall control volume contains a sufficient number of turbulent structures for a Reynolds averaged view to be justified, even in an instantaneous flow field [111]. RANS quantities in the first cell can therefore be combined with instantaneous variables of the LES.

The following sections describe in detail different options of applying equation 6.23 to the numerical scheme as a wall boundary condition.

6.2.3 Implementation with slip velocity at the wall

The first, classical method to implement wall functions starts from the idea that corrections should be limited to the nodes on the domain boundary. This can be considered an advantage on unstructured triangle- or tetraedra meshes, where element type and topology are of little influence. In view of the cell-vertex formalism, this means that the predictions of the diffusion scheme have to be modified when summing the contributions of the viscous fluxes at the dual cell associated to each boundary node (eq. 6.19). This procedure, illustrated in figure 6.4, consists in having the scheme calculate the wall-normal momentum flux τ_{xy} and subsequently replacing the contributions headed to the wall nodes by the value corrected with the wall function τ_{we} . In an arbitrary 3D geometry, this correction is applied selectively on the wall-normal component of the momentum flux, the direction of shear being aligned with the wall-parallel velocity vector. Finally, the wall-normal velocity is set to zero ($u_{1,\perp} = 0$) as a Dirichlet-type boundary condition (classical Dirichlet or the NSCBC (for Navier Stokes Characteristic Boundary Conditions) [114] equivalent). As nothing is imposed for the wall-parallel velocity, a non-negligible slip-velocity appears on the wall as the scheme advances in time. This velocity has no physical meaning: it should be regarded as a free parameter in the computation as its value depends predominantly on the level of subgrid-scale viscosity in the wall element. This becomes clear when rearranging equation 6.21 at the wall-element with $\bar{\tau}_w$ obtained from the wall function.

$$\left. \frac{d\hat{u}}{dy} \right|_{we} = \frac{\bar{\tau}_w(\hat{u}_2, y_2)}{\mu|_{we} + \mu_{sgs}|_{we}} \quad (6.25)$$

Assuming that the velocity at the first node above the wall behaves ideally and thus coincides with the log-law for a given $\bar{\tau}_w$ and the molecular viscosity μ is constant, this equation yields a gradient that will establish between y_1 and y_2 , which depends only on μ_{sgs} (see figure 6.5 for an illustration). This relation reveals that the method is well-suited for the use in conjunction with the Smagorinsky model, which provides for (unphysically) high levels of subgrid-scale viscosity near the wall, leading to a moderate gradient. In contrast, when used with turbulence models that yield near-zero subgrid-scale velocity at the wall (e.g. WALE [104]), this gradient will be very steep and can lead to reversed slip-velocities, causing spurious oscillations.

For the Smagorinsky model, one can further estimate the magnitude of the slip-velocity obtained on the wall by writing it in a time-averaged ($\langle \rangle$ -operator), one-dimensional form (assuming a linear discretization of the velocity profile):

$$\langle \mu_{sgs}|_{we} \rangle = \langle \rho_{we} \rangle (C_s \Delta)^2 \frac{(\langle \hat{u}_2 \rangle - \langle \hat{u}_1 \rangle)}{y_2} \quad (6.26)$$

Here, C_s is the Smagorinsky constant and Δ a length scale for the cell size. The slip-velocity can be estimated as:

$$\langle \hat{u}_1 \rangle = \langle \hat{u}_2 \rangle - y_2 \frac{\langle \bar{\tau}_w \rangle}{\langle \mu|_{we} \rangle + \langle \mu_{sgs}|_{we} \rangle} \quad (6.27)$$

Combining equations 6.26 and 6.27 finally allows to obtain the average slip velocity $\langle \hat{u}_1 \rangle$ explicitly:

$$\langle \hat{u}_1 \rangle = \langle \hat{u}_2 \rangle - \frac{y_2}{2 \langle \rho_{we} \rangle (C_s \Delta)^2} \left(-\langle \mu|_{we} \rangle + \sqrt{\langle \mu|_{we} \rangle^2 + 4 \langle \rho_{we} \rangle^2 (C_s \Delta)^2 \langle \bar{\tau}_w \rangle} \right) \quad (6.28)$$

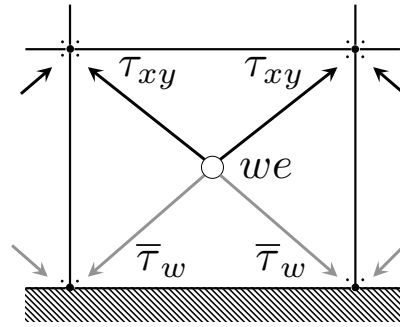


Figure 6.4: Application of the wall functions in the slip-wall formulation. Schematic of the scatter operation of the momentum flux contributions. Black arrows correspond to contributions calculated by the diffusion scheme, grey arrows to contributions corrected by the wall function.

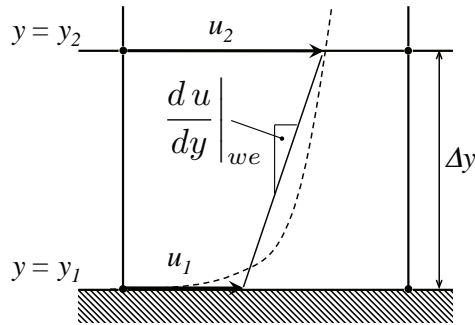


Figure 6.5: Overview of the most important variables appearing in the formulation with a slip velocity.

6.2.4 Corner problem

The procedure, described in section 6.2.3 leads to a difficulty at corner points. Unlike the Neumann boundary conditions that are applied on the boundary face (see equation 6.20), the Dirichlet conditions of zero wall-normal velocity are applied directly on the conservative variables at the nodes. At the node coinciding with the corner, the definition of the wall-normal vectors is ambiguous (see figure 6.6). Following the standard procedure of calculating the nodal wall normal \vec{S}_j^b as the average of the surrounding boundary-face normals \vec{S}_e^{ff} , the resulting normal at the corner point $\vec{S}_{j,c}^b$ (and consequently also the velocity vector) would take an unphysical angle of ≈ 45 degrees. Therefore, at the corner point only, the normal is either chosen equal to the one of the upstream boundary face or set to zero (removing all constraints on the direction of the velocity). Both methods lead to a nodal velocity vector that is aligned with the upstream wall. As a result, however, mass conservation will no longer be respected because of a flux through the boundary face situated at the downstream wall, as illustrated in figure 6.7.1. To correct that, a (face-based) Neumann boundary condition of zero mass flux can be applied instead of the Dirichlet condition of zero normal velocity. This ensures mass conservation but the correction of the face downstream of the corner effectively reduces the slip-velocity at the corner, leading to perturbations of the flow-field in this area. As the wall-element in a mesh adapted for wall functions is of a relatively large size in order to reach into the inertial layer, these perturbations can take magnitudes that lead to unphysical flow fields or numerical instabilities

(see section 6.3.2).

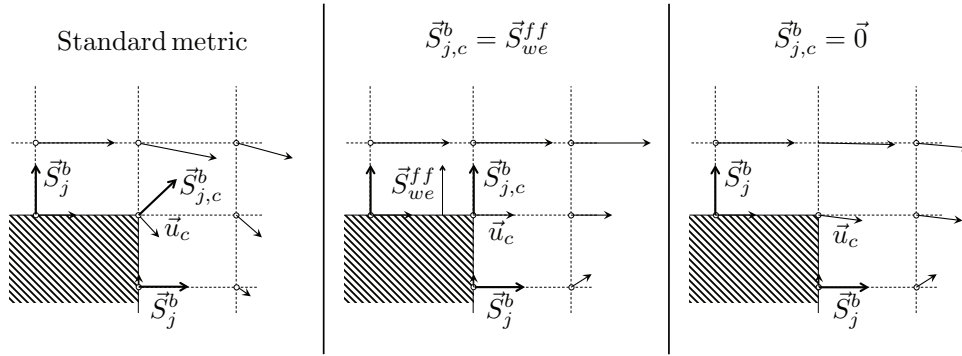


Figure 6.6: Schematic illustration of different definitions of the nodal normal vector $\vec{S}_{j,c}^b$ at the corner node. Generic configuration of a flow over a corner.

Note that these difficulties are limited to the cell-vertex approach, as illustrated in figure 6.7: for a cell-centered formulation (figure 6.7.3), the wall-normal vector ambiguities and problems of mass-conservation do not appear due to the location of the velocity vectors at the cell-center. In a cell-vertex formalism, these problems can easily be overcome if a no-slip condition is imposed at the wall nodes as shown in figure 6.7.2. The following sections are therefore dedicated to wall functions with a no-slip condition at the wall.

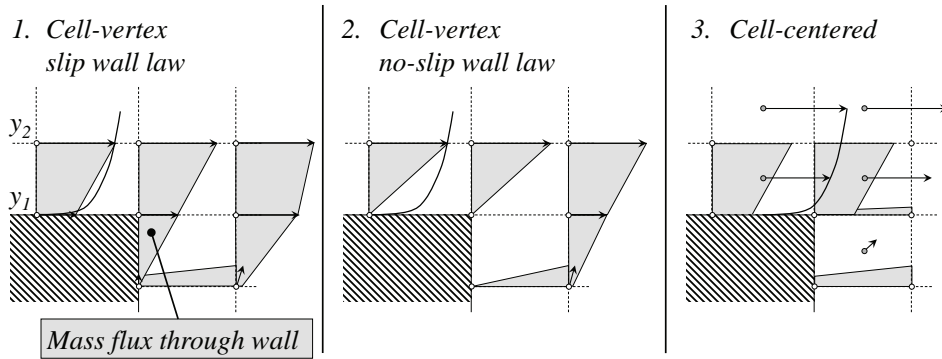


Figure 6.7: Schematic of mass fluxes in vicinity of a corner (\rightarrow symbolizes a momentum vector), comparing a cell-vertex scheme with/without slip velocity to the cell-centered approach. Generic configuration of a flow over a corner.

6.2.5 Implementation without slip velocity at the wall

The need for an alternative implementation method of wall functions in cell-vertex solvers arises from the problems listed in section 6.2.4. The idea is consequently to impose a no-slip condition on the wall nodes, which, however, prohibits the application of the wall shear stress at the same location. This is because, in a given timestep, the corrected contributions of the diffusion scheme τ_{we} exclusively affect the nodes they are directed to. Neighbouring nodes are only influenced indirectly in subsequent timesteps. A Dirichlet-condition, imposed after the computation of the diffusive terms will therefore cancel out any effect of the numerical scheme on these nodes. The logical alternative is to apply the wall function away from the wall, at the upper nodes of the first cell, as shown in figure 6.8. This choice is in fact consistent with the underlying boundary layer theory, as equation 6.3 clearly shows that the shear is constant throughout the first wall

cell (equal to τ_w). The fact that the gradient inside the wall element (figure 6.9) is unphysically high has no consequence in this case, because the diffusion scheme is completely inactive in this cell, its predictions being entirely replaced by the wall function and the no-slip condition.

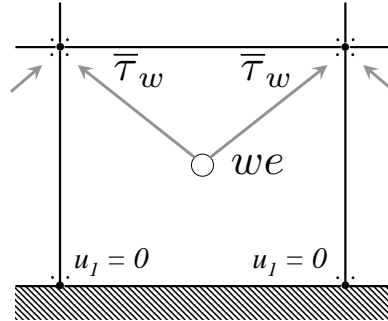


Figure 6.8: Application of the wall functions in the no-slip formulation. Schematic of the scatter operation of the momentum flux contributions. Grey arrows symbolize the contributions corrected by the wall function.

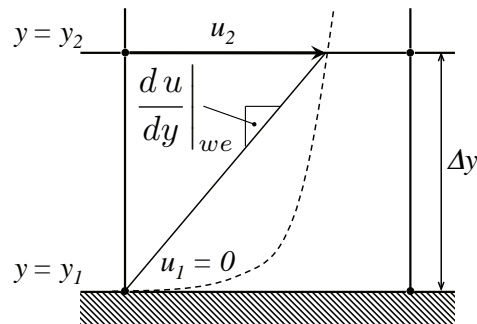


Figure 6.9: Overview of the most important variables appearing in the no-slip formulation.

An overview of the key differences between both implementation methods can be obtained from figure 6.1, where a simplified sequence of events during a numerical timestep is shown.

6.2.6 Limitations of the no-slip approach

The no-slip formulation avoids all difficulties related to domains with corners. However, it has a certain limitation with respect to the type of elements that are supported at the wall. The slip-wall formulation can be deployed on any type of mesh, as it is a surface-based approach limited to the boundary of the domain. The no-slip approach, as it acts inside the fluid *volume*, cannot sensibly be implemented for arbitrary element types. A typical example is a pure tetraedra mesh, which will have a layer of elements near the wall that can have a triangle, an edge or a single node coinciding with the boundary, leading to different kinds of ‘upside-down’ tetraedra. The algorithms needed to search those vertices of wall elements that are *away* from the wall (where the wall-function would be applied) and to establish the connectivity with the respective boundary normal are complex and costly. Figure 6.10 shows this type of element topology where applying the correction at the vertices neighbouring the node number 3 would give rise to the

said difficulty. Furthermore, the irregular wall-distances (like the one noted Δy_{23} in figure 6.10) have lead to oscillatory behaviour in the tests that were conducted.

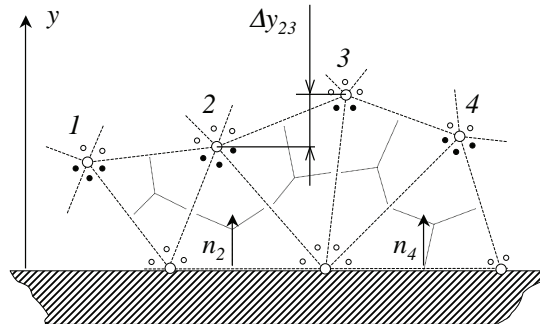


Figure 6.10: Example for the application of no-slip wall functions on pure tetrahedra grids.

The no-slip approach is therefore limited to all sorts of prismatic elements (typically prisms and hexaedra) that ensure uniform wall-distance and straightforward access (in terms of connectivity) to the ‘upper’ element vertices. A 2D example of such a prismatic layer in an otherwise unstructured mesh is shown in figure 6.11. The capability of treating hybrid meshes is therefore a prerequisite for the use of no-slip wall functions in complex geometries.

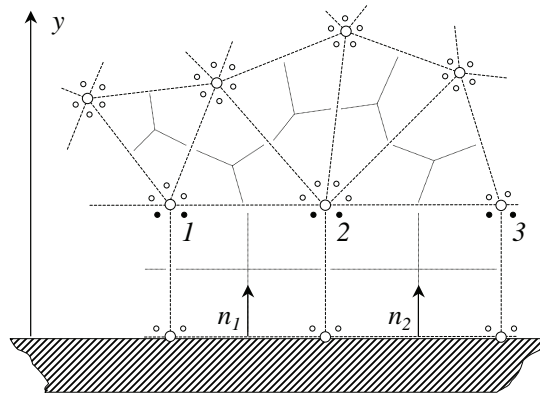


Figure 6.11: Example for the application of no-slip wall functions on hybrid hexaedra/tetrahedra grids.

6.3 Applications and Results

In the following, both implementation methods are applied to three different cases with increasing complexity. Each application, together with a discussion of the results is presented in an individual section.

No-slip wall law		Slip wall law
Initial field of conservative variables \mathbf{U}		
Calculation of the flux tensor $\vec{\mathcal{F}}$		
Neumann boundary conditions		
τ_w at y_2 (1st off-wall node)		τ_w at y_1 (wall)
Advancement in time: $\partial\mathbf{U}/\partial t + \vec{\nabla} \cdot \vec{\mathcal{F}} = \mathbf{S}$		
New field of conservative variables \mathbf{U}		
Correction of conservative variables \mathbf{U} Dirichlet boundary conditions		
$u_1 = 0$		$u_{1,\perp} = 0$
Final field of conservative variables \mathbf{U}		

Table 6.1: Comparative overview of the no-slip and slip wall function implementations. Simplified sequence of events during one computational time step.

6.3.1 Turbulent channel flow

A Large Eddy Simulation of a periodic channel flow serves as a first test case for the validation of both wall-function implementations. The configuration consists of a doubly periodic box (in x - and z direction) with walls on the top and bottom surfaces (in y -direction). Six different cases are considered (a summary is given in table 6.2), distinguished by different Reynolds number, based on bulk properties (subscript ‘b’), defined as:

$$Re_b = \frac{\rho_b D_h u_b}{\mu_b} \quad (6.29)$$

Where $D_h = 4\delta$ is the hydraulic diameter. The mesh in all cases is of uniform, cartesian type with grid resolutions adapted to the respective Re_b .

Certain additional results are obtained in a comparable configuration at $Re_\tau = 1500$ with a near-wall grid spacing of $y^+ = 100$. An exemplary flow field, obtained under those conditions using a second-order Lax-Wendroff scheme and a wall law in no-slip formulation is shown in figure 6.12. It combines a field of velocity magnitude inside the flow with a visualization of the wall friction levels on the wall surface.

Detailed statistics are presented in figures 6.13 and 6.14 for a single, typical case (# 4) at $Re_b = 200\,000$, which corresponds to a friction Reynolds number of $Re_\tau \approx 2524$. Figure 6.13 shows profiles of dimensionless longitudinal velocity u^+ . There is a good agreement between the logarithmic law, DNS data of Hoyas and Jiménez [66] and both LES simulation results near the first grid point, showing that the most direct effect that wall functions have on the flow is correctly reproduced. In the region of the first few grid points towards the center of the channel, profiles from both wall functions start to deviate from the logarithmic law, an effect that is slightly stronger in the no-slip formulation. This is most probably due to under-resolved

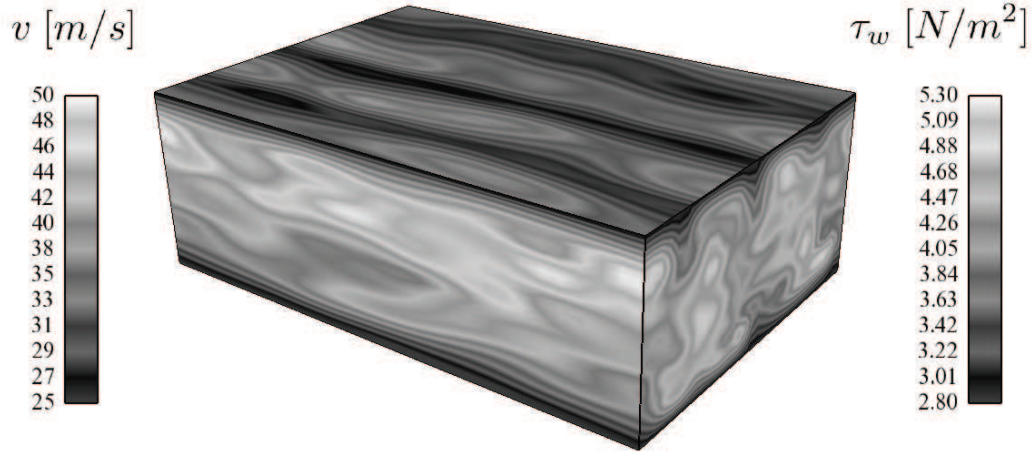


Figure 6.12: Turbulent channel, field of velocity magnitude v [m/s] (side surfaces) and wall friction τ_w [N/m^2] (top surface). LES using no-slip wall functions and a second order Lax-Wendroff scheme.

#	Re_b	Re_τ	y^+	grid nodes	2δ [m]
1	20 000	≈ 322	≈ 30	29 x 21 x 29	$1.5 \cdot 10^{-3}$
2	40 000	≈ 594	≈ 50	33 x 25 x 33	$3.0 \cdot 10^{-3}$
3	80 000	≈ 1100	≈ 100	25 x 23 x 25	$6.0 \cdot 10^{-3}$
4	200 000	≈ 2524	≈ 100	33 x 51 x 33	$1.5 \cdot 10^{-2}$
5	400 000	≈ 4798	≈ 150	33 x 61 x 33	$3.0 \cdot 10^{-2}$
6	2 000 000	≈ 20816	≈ 1000	41 x 41 x 41	$1.5 \cdot 10^{-1}$

Table 6.2: Summary of the turbulent periodic channel cases.

and thus unphysical turbulent mechanisms near the wall, which are a result of the inherent lack of grid resolution that is described, for instance, by Nicoud et al. [103] (in the context of a wall function approach) and studied in a more general context by Piomelli et al. [112]. In this intermediate layer, the subgrid-scale viscosity is given by a LES model and therefore takes values that are lower than a turbulence model in a RANS approach would predict, leaving a share of the stress balance to be accounted for by resolved Reynolds stresses. On the other hand, the grid resolution in these zones is determined by the wall function approach and therefore too coarse to resolve turbulent structures at scales small enough for a LES to result in correct Reynolds stresses. A study of the resolution requirements in LES of shear flows can be found in the work of Baggett et al. [9]. A more detailed discussion of the limits a wall function approach faces in terms of accuracy is presented in section 6.4.

Differences between both formulations can be observed on the velocity fluctuation profiles shown in figure 6.14 where the peak of the no-slip wall functions is displaced by approximately one point away from the wall with respect to the one of the slip-wall function. This indicates that for the slip-formulation the under-resolved near-wall vortical structures can be accommodated by the wall nodes thanks to the presence of a slip velocity, whereas in the case of the no-slip results, these structures are shifted away from the wall (see figure 6.26 and section 6.4.1 for a more detailed analysis), which seems to slightly increase their negative effect.

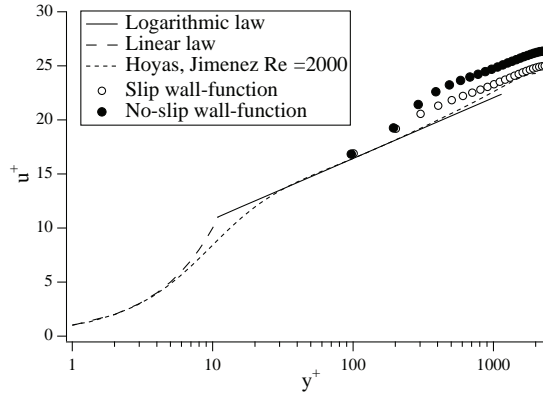


Figure 6.13: *Turbulent channel, dimensionless velocity profiles. Comparison between the analytical profile, DNS data [66] and LES results, obtained with a second-order Lax-Wendroff scheme, using wall functions in slip- and no-slip formulation. Case of $Re_b = 200000$.*

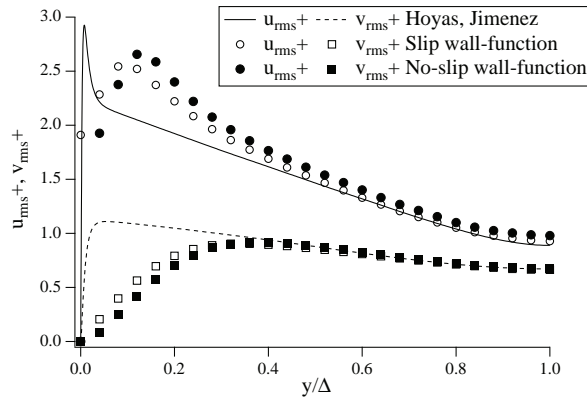


Figure 6.14: *Turbulent channel, dimensionless velocity fluctuation profiles. Comparison between the analytical profile, DNS data [66] and LES results, obtained with a second-order Lax-Wendroff scheme, using wall functions in slip- and no-slip formulation. Case of $Re_b = 200000$.*

An overview of the global performance of both wall functions over a wide range of Reynolds numbers is shown in figure 6.15. Here, the mean friction coefficient C_f of the channel flow is compared to the classical correlations of Kármán and Nikuradse [75] as well as Petukhov [109]. The general trend observed is that for low Reynolds numbers, the slip-formulation yields superior results but deteriorates slightly for increasing Re_b . Inversely, the no-slip formulation shows the largest errors for low Reynolds numbers with increasingly good agreement for growing Re_b , eventually surpassing the accuracy of the slip-formulation. This observation can be explained by the diminishing influence of the near-wall effects relative to the channel height that work to the disadvantage of the no-slip formulation.

6.3.2 Flow over a sudden expansion

The flow over a sudden expansion is well-suited as a test case for the corner problem. It consists of a circular upstream tube of diameter D from which the flow enters a larger tube of diameter $2D$ (see figure 6.16). This corresponds to the experiment of Dellenback et al. [36] from which experimental data is available. The mesh is composed entirely of hexaedral elements with 10 cells across the diameter of the upstream tube, which results in a first off-wall grid point situated

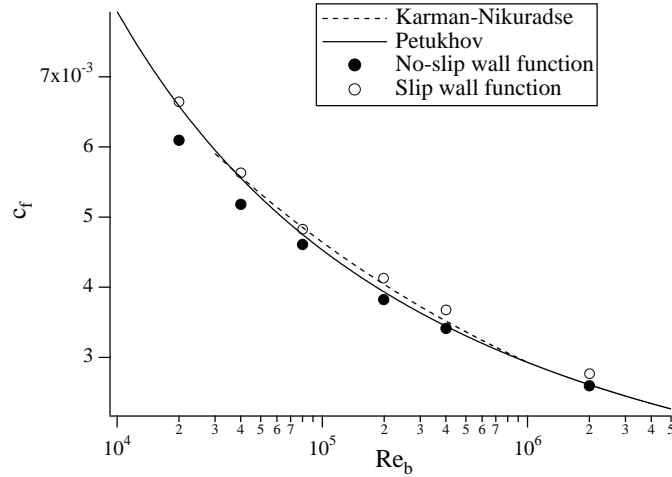


Figure 6.15: Wall friction coefficient c_f as a function of the Reynolds number Re_b based on the bulk velocity in the channel. Comparison of slip- and no-slip results with correlations of Karman and Nikuradse [75] as well as Petukhov [109].

at approximately 160 wall units. The mean velocity profile from experimental data is imposed at the inlet. The resulting flow has a Reynolds number of 30 000 and transitions naturally to a turbulent state after the step. The degree of physical detail in this simulation is clearly insufficient for an accurate representation of the flow phenomenon at hand, but in this case, this is not the intent. Instead, this geometry, in conjunction with the very coarse grid resolution, is typical of certain geometrical details in very large LES cases, which often include small-scale jets that are emitted by tubes or conduits into a larger reservoir. Examples are dilution holes in combustion chambers or the narrow passage around the valves of an internal combustion engine, which are often meshed quite coarsely. It is typically in this kind of configuration that the corner problem leads to undesired modifications of the flow field or to numerical artefacts.

Qualitative differences between the wall-law formulation can be observed on the iso-contours of mean axial velocity shown in figure 6.17. The flow field remains totally unaffected (figure 6.17, top) for slip wall functions in their non-conservative form, i.e. without correction of wall-normal mass flux (see section 6.2.4, figure 6.7). Note that the absence of this correction leads to an unphysical mass flux through the wall downstream of the step that amounts to approx. 15 % of the global mass flux. On the other hand, a clear distortion at the height of the step can be observed when the mass-flux correction is applied. This correction reduces the slip velocity at the corner points and leads to an unphysical acceleration of the flow in the center (figure 6.17, center). Furthermore, this very localized modification of the flow field causes numerical point-to-point oscillations. The said distortion is not observed for wall functions in the no-slip formulation (figure 6.17, bottom).

A more quantitative view of the problem is presented in figure 6.18, which shows the normalized, mean axial velocity on the centerline in direct vicinity of the step ($x = -0.5D$ to $x = D$) compared to experimental data [36]. As the flow is virtually incompressible, one would expect the centerline velocity to remain constant in this area, which is confirmed by the experiment. The simulation results of the slip wall function, however, show a clearly unphysical acceleration. The result using no-slip wall functions is a clear improvement as the centerline velocity remains globally constant despite a slightly oscillatory behavior at the coordinate of the step.

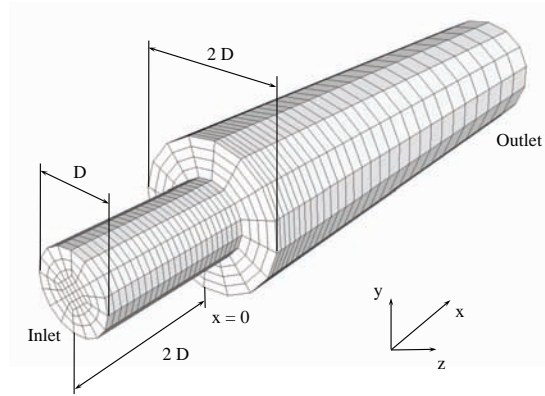


Figure 6.16: *Flow over a sudden expansion: Mesh and geometry overview.*

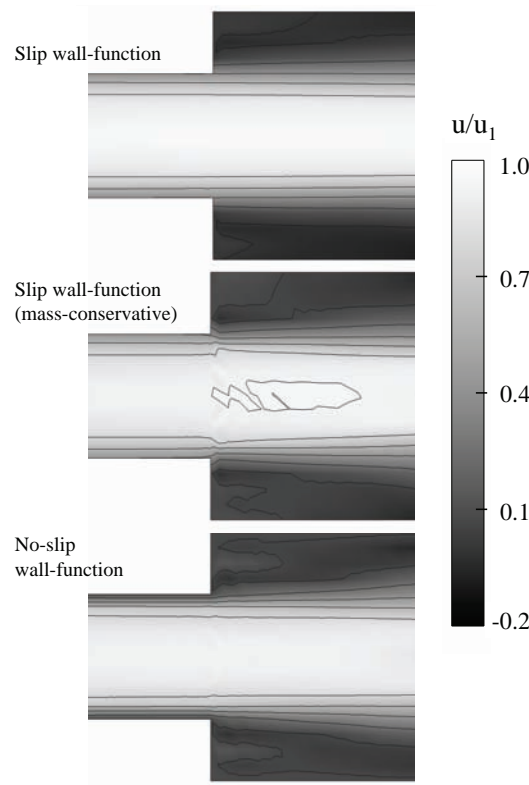


Figure 6.17: *Flow over a sudden expansion: iso-contours of the mean axial velocity, normalized by the centerline velocity in the upstream tube. Top left: slip wall function without correction (not mass-conservative). Top right: slip wall function with correction. Bottom right: no-slip wall function*

6.3.3 Injector for aero-engines (TLC configuration)

The last application is the full TLC configuration as described in chapter 9. It is an example for one of the more complex geometries encountered in LES, as it is characterized by three swirler stages, each composed of a series of narrow channels separated by the guide vanes. Here, it is operated in a purely aerodynamic regime (described in more detail in chapter 10) in order to assess the capability of the novel wall-model implementation. The chamber is pressurized at 4.3 bar, the air fed into the plenum is pre-heated to 473 K, which corresponds roughly to the

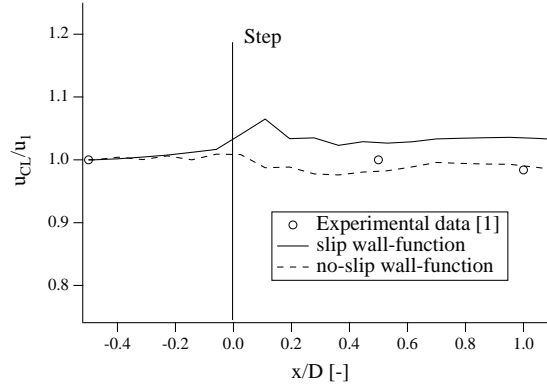


Figure 6.18: *Flow over a sudden expansion: Ratio of centerline velocities u_{CL} and the centerline velocity at $x = -0.5D$, u_1 , for slip- and no-slip wall functions compared to experimental data (Dellenback et al. [36]). The diagram shows time-averaged results.*

operating conditions of an engine at partial load. The airflow from the plenum to the chamber is split between the three-staged swirler and a cooling film placed near the circumference of the chamber upstream wall.

Owing to the complexity of the computational domain, the grid is composed of tetraedral elements in its volume and of one single layer of prismatic elements at the boundary where wall functions are applied (see section 6.2.6 for details on the necessity of this method). This approach is applicable in arbitrary geometries as it simply consists in extruding the triangular tessellation of the domain boundary towards the inside. However, the more prismatic layers one chooses to apply or the thicker the layers are, the more the prisms tend to be distorted on sharp edges or corners. A view of the mesh and a detail of the prismatic layer is shown in figure 6.19. The thickness of the prism layer is varied locally and carefully adapted to be as close as possible to 100 wall units. The resulting mesh comprises approximately 8.5 million cells and 1.6 million nodes. The simulations were performed using the second-order accurate Lax-Wendroff scheme. In the two simulations compared below, the only difference is the wall treatment. Everything else remains the same (mesh, algorithms, timestep).

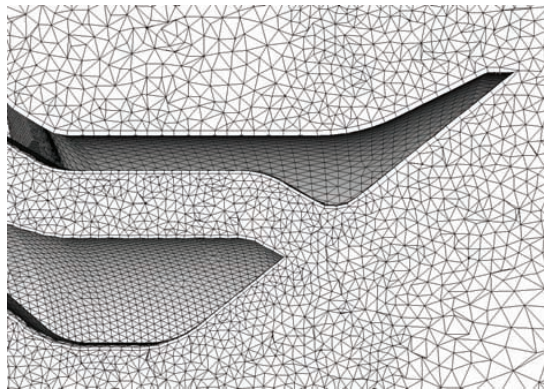


Figure 6.19: *Detail of the single prismatic layer in the hybrid, unstructured mesh.*

Quantitative results are presented in the form of mean velocity profiles (figure 10.16) and RMS velocity profiles (figure 10.17). In both figures, the axial and tangential components obtained with both wall function formulations are compared to experimental data provided by ONERA Fauga-Mauzac. The profiles are extracted over three transverse lines positioned at 10, 15 and 30 mm downstream of the swirler exit (see figure 6.20). The agreement of the no-slip results in axial direction with experimental data is excellent, both the position and the magnitude of the

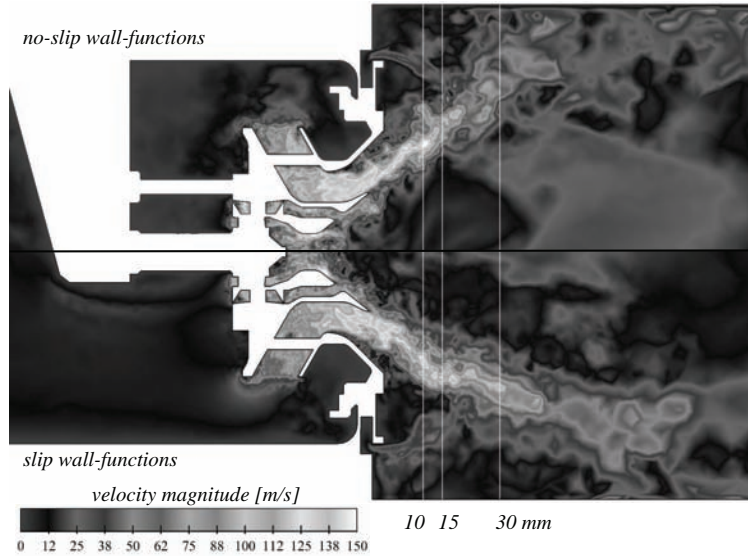


Figure 6.20: Instantaneous velocity magnitude contours on a central cross-section through the domain. Upper half: result obtained using no-slip wall functions. Lower half: result obtained using slip wall-function. White lines: positions of the extraction of velocity profiles.

peaks corresponding to the central flow and the cooling films are accurately reproduced. This is observed on all three measurement positions. The results of the slip wall functions are less satisfying because the peaks of the main flow are shifted slightly towards the center, indicating that the opening angle of the cone-shaped flow is too small. Purely qualitatively, this discrepancy in opening angle can also be observed on the instantaneous velocity field, shown in figure 6.20. As a consequence, the peak magnitudes increase, a behavior that is observed consistently at all three positions. In the tangential direction, the same observations can be made: very good agreement for the no-slip formulation and an over-estimation of tangential velocity peaks due to a under-estimated opening of the main flow.

Differences are less pronounced for the axial velocity fluctuations shown in figure 10.17. Here, the magnitude of the strongest fluctuations in the turbulent shear layer between the main flow and the central recirculation zone is well captured in both simulations. Differences are observed on the third measurement line at 30 mm, where the offset of the peaks from the slip wall function results becomes most noticeable. In tangential direction, fluctuations are slightly over-estimated on the first measurement line (10 mm) in both simulations. Downstream, the agreement is better for the no-slip results, while the slip wall functions again show over-estimated peaks displaced towards the inside.

The quality of both LES (without considering the differences resulting from wall modeling) is very satisfying as shown by the results obtained using the no-slip wall function approach. With all other simulation parameters (mesh, numerical scheme, turbulence model etc.) being identical, the discrepancies observed relative to the slip wall function formulation show that the *implementation* of the wall model alone can lead to significantly different results in a realistic application. Here, the reason for the differences is not attributed to the corner problem described in sections 6.2.4 and 6.3.2 but to the tendency of the slip velocity (which forces the near-wall momentum in wall-parallel direction) to keep the flow closely attached to curved geometrical features. In this case, the main flow concentrates along the shape of the inner lip of the injector cone, which results in a more confined shape of the overall flow.

Note that the favourable behaviour of the no-slip formulation should not be confounded with the capability to predict boundary layer detachment, which remains out of reach for a wall-model

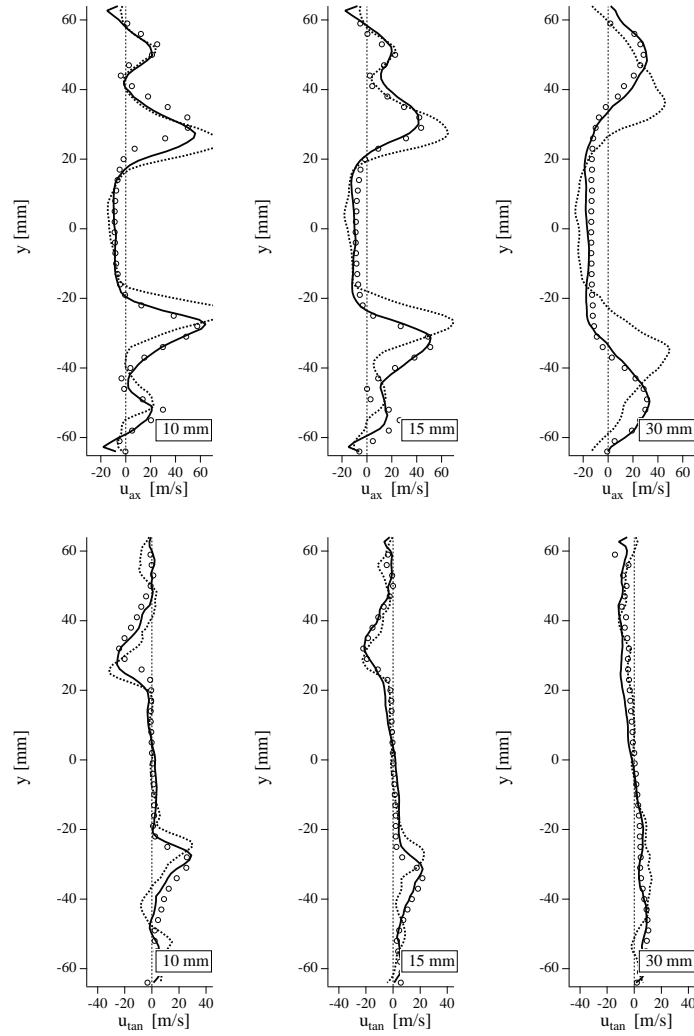


Figure 6.21: Mean velocity profiles. Axial component (upper diagram) and tangential component (lower diagram). Comparison of no-slip wall-functions (—), slip wall-functions (- - -) and experimental data (ooo)

that neglects the streamwise pressure gradient. However, even with a suitable underlying wall-model, the slip-wall formulation still cannot be expected to predict detachment correctly. This is because the near-wall momentum is transported to a non-negligible extent by the slip velocity, which is necessarily aligned with the wall and in its magnitude depends mainly on the level of subgrid scale viscosity μ_{sgs} , as highlighted by equations 6.27 and 6.28. This means that the onset of the detachment (a vanishing slip-velocity) would be piloted by the LES subgrid-scale turbulence model – a clearly non-physical mechanism.

Another important aspect is the numerical robustness of either approach. An instructive way of looking at this issue is to observe the temporal evolution of pressure and slip velocity at a set of probes located on the wall of a narrow channel. The arrangement of the three probes considered is shown in figure 6.23. The evolution of the slip velocity x-component, presented in figure 6.24 reveals its very unstable behavior. While it is observed in the turbulent channel flow that the slip-velocity accommodates to the natural near-wall fluctuations to a certain extent (see fig. 6.14), it becomes clear that in the case of a less resolved and less regular mesh, the slip-velocity reveals a non-physical strong oscillatory tendency up to the point of briefly taking counterstreamwise orientations. The resulting pressure fluctuations are five times stronger than in the case of the no-slip formulation, as shown in figure 6.25. Obviously, this would become an

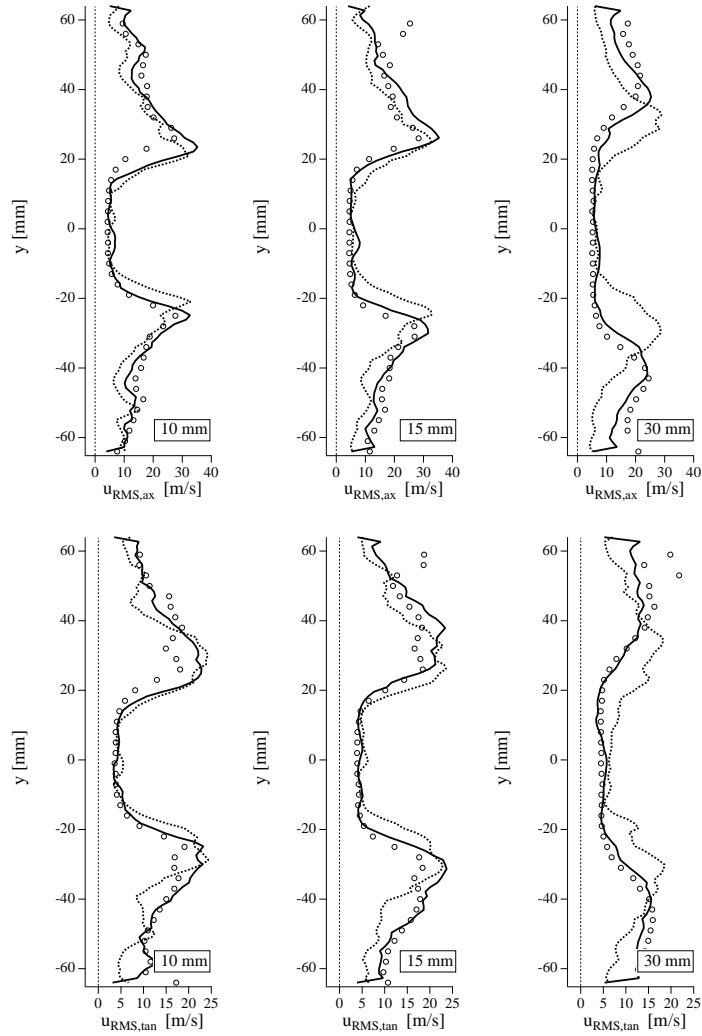


Figure 6.22: Velocity fluctuation profiles. Axial component (upper diagram) and tangential component (lower diagram). Comparison of no-slip wall-functions (—), slip wall-functions (- - -) and experimental data (ooo)

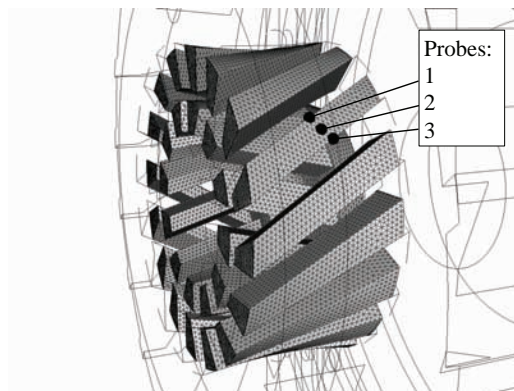


Figure 6.23: Location of the pressure probes. View of the two innermost swirler stages.

issue if the LES was used for aeroacoustics simulations, where wall functions in slip-formulation create a non-physical noise. Furthermore, the advantages of the no-slip formulation in terms

of a problem-free (i.e. more robust at locations that are prone to destabilizing the numerics) application by the end-user and the gained rapidity in setting up a simulation should not be under-estimated.

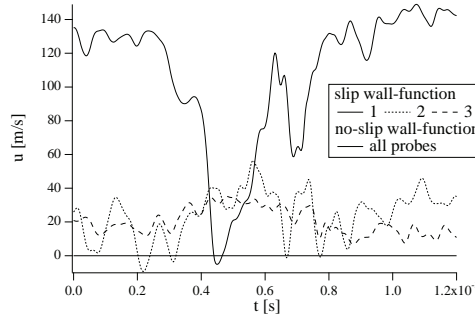


Figure 6.24: *x*-component of the velocity recorded at the three probes over a period of 1.2 milliseconds. Comparison of results from slip- and no-slip wall-functions.

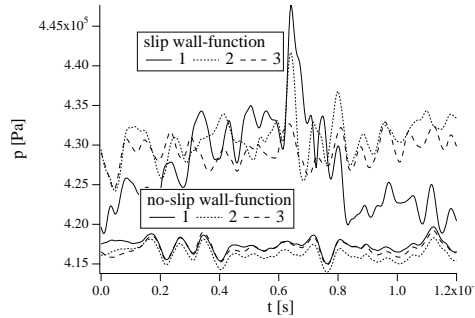


Figure 6.25: Pressure signal recorded at the three probes over a period of 1.2 milliseconds. Comparison of results from slip- and no-slip wall-functions.

6.4 Analysis of limits of wall function approaches

Wall-function based approaches to model a turbulent boundary layer in a Large Eddy Simulation generally suffer from several sources of inaccuracy. Most often, the wall-model itself is not the cause of these errors, provided it is applied in coherence with the assumptions used to derive it (i.e. steady, attached turbulent boundary layers). Instead, errors are generated by several mechanisms related to the interaction of the wall model with the rest of the flow. Some - partly significant - differences in complex geometries due to different implementation methods have already been pointed out in the preceding sections. In the following, this aspect will be analyzed in more detail. Furthermore, the influence of the near-wall grid resolution and the subgrid-scale viscosity will be discussed.

6.4.1 Implementation method

Apart from the differences observed in realistic configurations related to the corner problem or the tendency to stay attached excessively to curved surfaces, there are also very basic mechanisms at work, which can be observed in the turbulent channel flow. In particular, this is the stronger

deviation of the velocity profile from the logarithmic law for the no-slip formulation compared to the profile of the slip wall formulation (see figure 6.13). The explanation for this is not very intuitive because the derivation of the wall-function itself shows that the prediction of the (constant) total shear inside the logarithmic layer must be equivalent in both cases. The reason for the discrepancy should therefore be sought in the LES region near the wall. The argument is as follows: in a turbulent boundary layer, the wall-normal momentum exchange is to a great extent effected by small-scale longitudinal vortical structures, called streaks. In a LES with a wall model, these structures are not resolved. Instead, a similar mechanism at larger scale (the smallest scale the grid allows to resolve) is observed and contributes to wall-normal momentum transport in a very similar way. A corresponding phenomenon (sometimes named super-streaks) has been described by Piomelli et al. [112] as well as Baggett et al. [8] in studies about zonal RANS-LES approaches. These authors show that the resolved turbulence cycle is artificial and physically incorrect. Although there is no proof that the structures at hand in a wall function approach constitute the same phenomenon, it is safe to assume that they are equally artificial because of their scale. In section 6.4.3, this aspect will be further discussed - here, it shall simply be assumed that the mechanism exists. Figure 6.26 schematically shows a cross-section through such a near-wall vortex. In the case of the slip wall function, this vortex can be accommodated by the first few near-wall cells, starting *directly on the wall*, thanks to the presence of the slip velocity. For the no-slip formulation, a comparable vortex is generated but due to the no-slip condition at the wall nodes, it is shifted away from the wall by approximately one cell height. Evidence for this can be found in figure 6.14, where the velocity fluctuation profiles have practically the same shape, with the no-slip result being shifted by one point towards the center of the channel. In this case, the result is an increase of total stress at comparable wall-distances which eventually leads to the steeper velocity profile in the near-wall region.

It should be noted that, although the behaviour of the slip wall function leads to better results, the slip velocity that is the helping mechanism behind the improvement is not physically justified. As will be seen in the following, it can, under certain conditions, behave in an unfavourable way, reversing the positive influence observed in this example. Additionally, the near-wall vortices that generate the differences are an artificial turbulent cycle, so none of the shifted positions is necessarily more correct than the other.

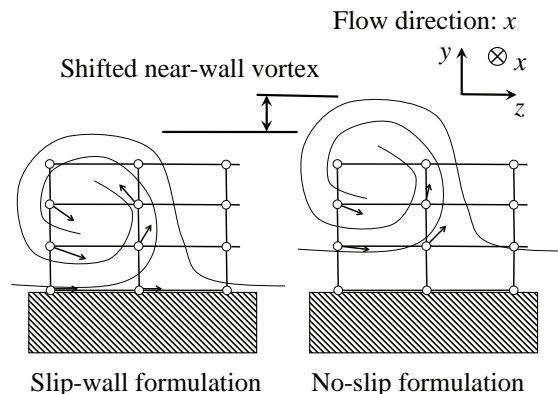


Figure 6.26: Sketch explaining the shifted near-wall vortical structures between slip- and no-slip implementation.

6.4.2 Grid dependency

It is generally difficult to coherently integrate wall models into a standard LES. The reasons for this are two-fold: on the one hand, classical wall models are derived from time- or ensemble-averaged equations for a turbulent boundary layer. This presents a conceptual incoherence with the LES approach that is based on a spatial filtering argument. It can, however, be argued [111] that if the first near-wall grid cell is large enough, it contains a sufficient number of turbulent structures (with typically faster turnover times than the outer flow) to justify the application of a wall model based on the ensemble-average of these structures in an unsteady LES. This in turn leads to the second problem, which is related to grid resolution requirements for LES. Baggett et al. [9] derive a criterion for the resolution requirement in regions of strong shear in a LES using the dynamic Smagorinsky model, which can be summarized by a filter width that has to be less than 1/10 of the turbulent integral lengthscale that is proportional to the wall-normal distance $L_\epsilon \propto y$. As Nicoud et al. [103] point out, this leads to a conflict of objectives in the mesh region directly above the first off-wall grid point. Here, the LES side would optimally require very small, relatively isotropic grid cells that diminish in size towards the wall, whereas the wall model demands relatively large grid cells that reach into the logarithmic layer (typically $\Delta y^+ \approx 100$ and ideally $\Delta x^+ \approx 1500$ streamwise and $\Delta z^+ \approx 700$ in spanwise direction [111] for the statistical argument to hold). A typical mesh is a compromise between both requirements, i.e. near-wall cells of $\Delta y^+ \approx 100$ but more isotropic in x - and z -direction and maintaining this spacing above the wall. The result is an intermediate zone between wall-law region and the outer flow where the mesh is too coarse for a LES with a standard subgrid-scale turbulence model to work properly. It has to be noted that in a RANS approach, this conflict does not necessarily exist as these turbulence models adapt with wall-distance and resolution requirements do not depend on the turbulent length-scales. Furthermore, there is no requirement for cell isotropy, which facilitates wall-normal grid size adaptation.

Statistics of calculations that compare different grid resolutions are shown in figures 6.27 to 6.29. The bulk Reynolds number of both cases is identical at $Re_b = 80\,000$, whereas the grid spacing is varied between $y^+ \approx 100$ with $25 \times 23 \times 25$ points (case # 3 in table 6.2) and $y^+ \approx 50$ with $41 \times 45 \times 41$ points. In both cases, the no-slip formulation for the wall functions has been used. It can be observed that the magnitude of the mismatch between the results and the log-law is nearly identical in both cases. The zone of over-estimated near-wall velocity gradients is limited to the first three grid points on both meshes. Consequently, the deviation occurs closer to the wall for the finer mesh. The evolutions of velocity fluctuations (figure 6.28) and the total shear stress (figure 6.29) are qualitatively very similar in both cases but the near-wall behaviour is spread over a larger region on the coarse grid. Distinctive features like the near-wall increase of velocity fluctuations and the position of the maximum appear to be governed by the number of grid points rather than the actual wall distance. This gives a strong indication that the deficiencies considered here are in fact due to the inevitable lack of grid resolution at the interface between wall-law and LES region that is independent of absolute grid spacing.

6.4.3 The influence of the subgrid-scale viscosity model

This systematic lack of grid resolution for the intermediate layer between the wall model and the outer flow leads to a challenging environment for the subgrid-scale turbulence model. As already pointed out, the resolution requirements stated by Baggett et al [9] are valid for an isotropic turbulence model, in this example the dynamic Smagorinsky approach. More sophisticated models that are better suited in regions of strong anisotropy should provide better results. The WALE model [104] has proven to be well adapted to shear layers and could therefore be

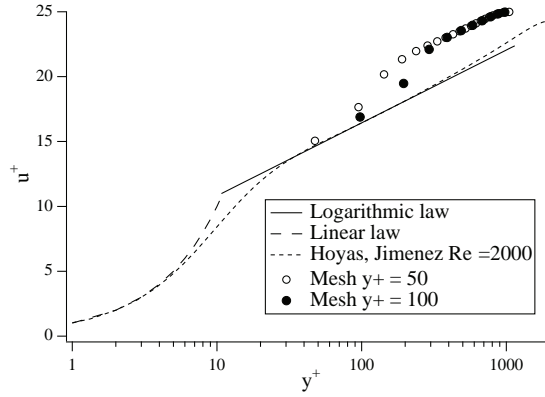


Figure 6.27: *Turbulent channel, dimensionless velocity profiles. Comparison between the analytical profile, DNS data [66] and LES results, obtained on different grids with a second-order Lax-Wendroff scheme, using wall functions in the no-slip formulation. Case of $Re_b = 80\,000$.*

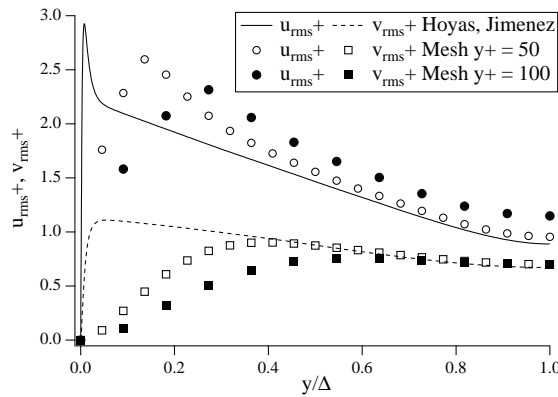


Figure 6.28: *Turbulent channel, dimensionless velocity fluctuation profiles. Comparison between the analytical profile, DNS data [66] and LES results, obtained on different grids with a second-order Lax-Wendroff scheme, using wall functions in the no-slip formulation. Case of $Re_b = 80\,000$.*

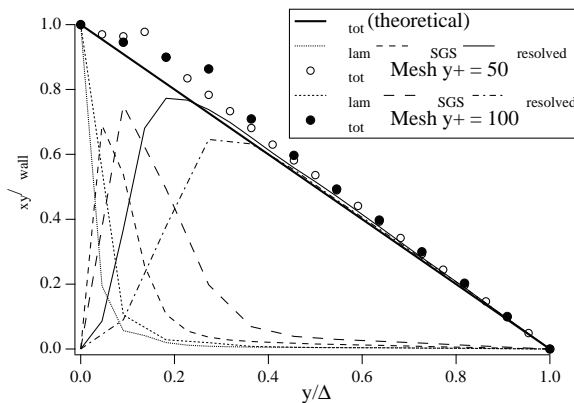


Figure 6.29: *Turbulent channel, shear stress balance. Comparison between the analytical profile, DNS data [66] and LES results, obtained on different grids with a second-order Lax-Wendroff scheme, using wall functions in the no-slip formulation. Case of $Re_b = 80\,000$.*

considered a good candidate for improving the quality of results for the turbulent channel flow.

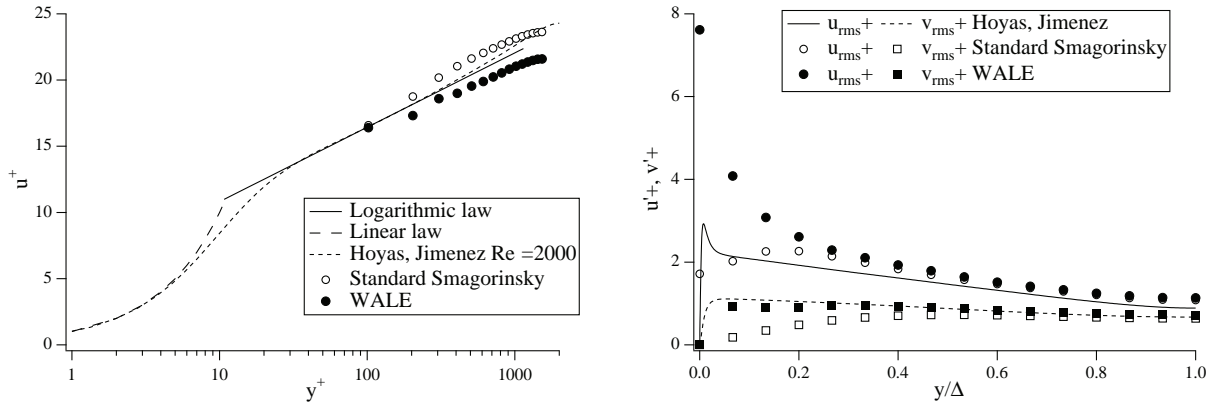


Figure 6.30: Turbulent channel, dimensionless velocity- (left) and fluctuation profiles (right). Comparison between the analytical profile, DNS data [66] and LES results, obtained with different SGS turbulence models, using wall functions in the slip-formulation. Simulation at $Re_\tau = 1500$.

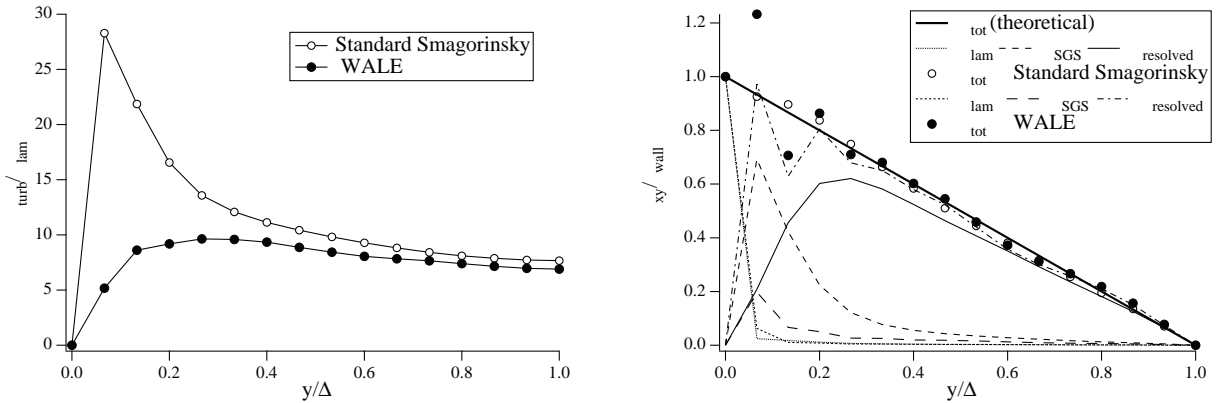


Figure 6.31: Turbulent channel, SGS viscosity ratio profiles (left) and shear stress balance (right). Comparison between the analytical profile, DNS data [66] and LES results, obtained with different SGS turbulence models, using wall functions in the slip-formulation. Simulation at $Re_\tau = 1500$.

What is observed instead on the results shown in figures 6.30 and 6.31 is a clear deterioration of the results. Streamwise velocity fluctuations take rather extreme values which lead to spurious variations of the resolved shear stresses in the near-wall region. As a result, the velocity profile deviates from the logarithmic law leading to under-estimated velocities throughout the channel. An explanation can be drawn from the expression for the slip velocity (equation 6.27), where μ_{sgs} is found in the denominator. As the WALE model correctly predicts near-zero subgrid-scale viscosity in proximity of the wall, velocity gradients necessary to maintain the shear level imposed by the wall-function become very high. The resulting slip velocity at the wall decreases and can in some cases even take negative values. Generally, the equilibrium between the wall-model and the slip-velocity is very ill-conditioned and natural fluctuations in the flow are therefore amplified at the wall nodes. The Smagorinsky model produces (unphysically) elevated subgrid-scale viscosity levels near the wall, which leads to moderate velocity gradients and thus relatively stable slip velocities. Additionally, velocity fluctuations are also damped for roughly another three grid points leading to moderate levels of resolved shear. The resulting shear balance only slightly over-estimates total shear near the wall and is free of spurious oscillations.

This comparison demonstrates that surprisingly, a better turbulence model (WALE) can lead

to worse results when used in conjunction with a wall function approach because of an apparent incompatibility, in particular with the slip-wall formulation.

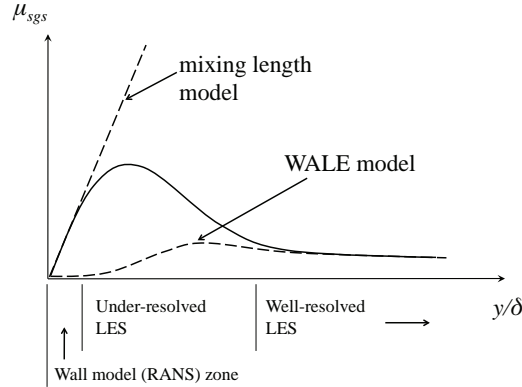


Figure 6.32: Zonal application of subgrid-scale viscosity using a blending approach.

In view of these findings, a tentative study to make the wall-law approach and the WALE model more compatible shall be presented in the following. The starting point is to admit that, for the various reasons cited above, an unaltered LES approach cannot be expected to work properly in an intermediate layer. Moreover, it has been demonstrated that increasing the quality of the near-wall approach from a LES point of view even has an adverse effect. Therefore, it could be expected that applying the paradigms of the wall model rather than those of the LES to this zone should be preferable. In practice, this means that the subgrid-scale turbulence model of choice should be the mixing length model on which the wall function is actually based. This idea can already be found in the work of Schumann from 1975 [133], who saw the necessity to rely on the mixing length model in the near-wall regions of strong anisotropy. In practice, zones for the validity of each model as well as a transition region of the two have to be defined (see the schematic in figure 6.32). The transition between RANS turbulence models in the near-wall region and LES in the outer flow is also the main idea behind the different incarnations of Detached Eddy Simulation (DES) first proposed by Spalart [141], although this method relies on a no-slip condition without an additional wall-model to predict the wall shear stress. If one assumes a logarithmic velocity profile, the resulting turbulent viscosity evolves linearly over the wall distance y :

$$\mu_{t,ML} = \sqrt{\rho_w \tau_w} k y \quad (6.30)$$

Cabrit et al. [22] show that in a channel flow, the mixing length assumption stays valid up to 0.2δ , which makes it applicable in this context. Furthermore, it is independent of the local grid resolution, which removes one of the major weaknesses of typical LES models. The SGS viscosity is then obtained from the following expression

$$\mu_{sgs,blend} = C_{blend} \mu_{t,ML} + (1 - C_{blend}) \mu_{sgs,WALE} \quad (6.31)$$

where $C_{blend} = f(y)$ is a blending function that varies between 1 in the near-wall region and 0 in the outer flow where the WALE model is applied in an uncorrected form. Naturally, the main difficulty is to find a suitable transition between both models, whose evolutions do not naturally intercept (see figure 6.32). Baggett [8] et al use blending functions obtained a priori from an uncorrected LES calculation and a target velocity profile to transition between

RANS and LES regions in the zonal approach they consider. In the present study, the blending functions are obtained in a simpler way, based on a dimensional argument. As the mixing length viscosity increases linearly with y , the blending functions vary like $1/y^2$. Assuming that the WALE viscosity stays approximately constant over y , the resulting SGS viscosity should blend smoothly with a behaviour $\propto 1/y$ into the uncorrected WALE viscosity.

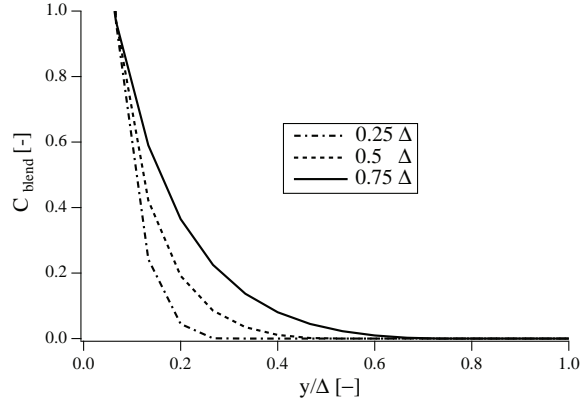


Figure 6.33: Blending functions for three different fractions of the channel half-width δ .

The fraction of δ to which the blending region extends is not easy to determine, although it can be stated that it should adapt to the Reynolds number of the flow. In the testcases presented here, three fixed fractions of δ are compared, 0.25, 0.5 and 0.75. The corresponding blending functions for these values are shown in figure 6.33.

The results of calculations using the no-slip formulation and the described blending method are presented in figures 6.34 and 6.35. Judging purely by the velocity profiles, a clear improvement is observed for growing influence of the mixing length model. The initially large deviation from the logarithmic profile observed is effectively reduced by the blending technique. The fluctuation profiles reveal that the unphysically high RMS values near the wall that are observed for the results of the WALE model are damped by the increased SGS viscosity levels near the wall. Towards the outer flow, the fluctuation curves are approaching each other and finally merge at a common level.

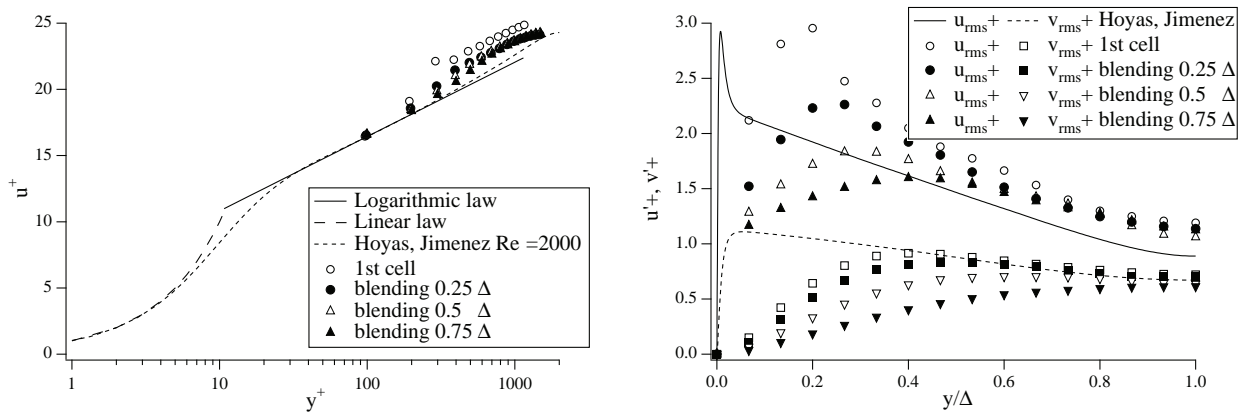


Figure 6.34: Dimensionless velocity profiles (left) and fluctuation profiles (right) for different blending functions. Simulation at $Re_\tau = 1500$.

The results for the viscosity ratio shown in figure 6.35 illustrate the effect of the blending

approach. The cases with the best results in terms of the resulting velocity profile and avoidance of excessive near-wall fluctuation levels (0.5δ and 0.75δ) are those where the blending zone begins before the SGS viscosity levels of the WALE model start to drop off towards the wall. The stress balances, presented in the right half of figure 6.35, reveal the over-estimated near-wall total stress for low influence of the mixing length model. For larger blending zones, the total stress approaches the theoretical linear evolution. In the process of increasing the blending zone, the influence of the subgrid stresses naturally extends further into the channel and the areas of significant resolved stresses recede towards the center.

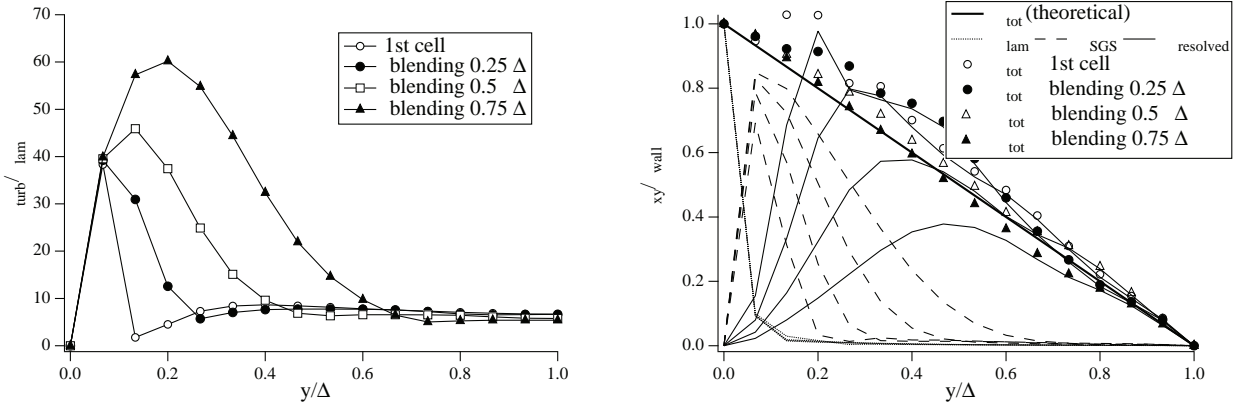


Figure 6.35: Subgrid scale viscosity levels (left) and stress balance (right) for different blending functions. Simulation at $Re_\tau = 1500$.

The key to the improved results is the suppression of resolved stresses in regions where the resolved scales are mainly under the influence of all sources of inaccuracy described in the preceding sections. In particular, this is the under-resolved grid in the intermediate layer, which leads to unphysical near-wall vortical structures that are also influenced by the implementation method that affects the wall-distance at which these structures will appear.

In fact, when analyzing the flow fields from simulations with large blending zones, it becomes clear that the near-wall region has been deprived of a considerable fraction of its turbulent structures. The near-wall vortices do not disappear completely but they are more sparse and less volatile. It is somewhat surprising that the reduction of this unphysical feature has a very positive effect, regardless of the fact that the evolution of SGS viscosity in the intermediate layer is more or less arbitrary and governed mainly by the shape of the blending functions. These findings also provide an explanation on why the standard Smagorinsky model leads to relatively convincing results although its prediction of near-wall SGS turbulence levels is obviously poor. Here, the simple fact of substantially increasing SGS viscosity helps keeping the influence of the resolved stresses low. In other words, it seems generally to be the case that ill-resolved near-wall LES does more harm to the quality of the wall-modeling approach than errors on subgrid-scale viscosity due to (i) an ad-hoc blending concept or (ii) the exploitation of the more or less accidentally favorable behaviour of the Smagorinsky model.

Another mechanism that could play a role in this context and should therefore be mentioned here is described by Piomelli et al. [113]. These authors report improved results from LES in a periodic channel flow, when the wall functions take into account a shift in streamwise direction between the wall-friction and the point in the log-layer from which it is obtained. This is deemed necessary because of a characteristic angle of near-wall turbulent structures that results in a slight time-delay between velocity peaks in the log-layer and the resulting increased shear stress at the wall, as found experimentally by Rajagopalan et al. [119]. In view of the blending approach, which ultimately leads to strongly decreased near-wall fluctuations, it is clear that

errors related to neglecting this effect in the present study, would be effectively reduced.

As a concluding remark, it should be stressed that the suppression of near-wall vortical structures still is not a convincing solution in general. The more the quasi-steady RANS approach extends into the intermediate layer through blending, the more it will negatively affect the quality of the unsteady flow away from the wall. In all cases where nascent turbulence from near-wall regions interacts strongly with the outer flow, this approach is certainly not advisable. It will, as it bears a certain resemblance to a DES or zonal type of approach, face very similar drawbacks, which are well-covered by literature. For instance, several publications therefore consider the *generation* of turbulent structures at the interface of zonal methods (ex. [76], [112]) showing the importance of the turbulent boundary layer as a source of turbulence. Interestingly, these authors cite the destruction of the super-streaks through stochastic forcing as one of the main reasons for their methods being successful.

Therefore, the blending approach described here should be considered as a demonstration that adds to the understanding of the inherent problems of a wall-function approach, and it is not pursued in the realistic application cases like the TLC configuration considered in this thesis.

6.5 Conclusion

Two different implementation methods of wall functions in cell-vertex type solvers have been laid out. The classical method imposes the shear-stress from the wall model directly at the boundary, which results in a slip-velocity at the wall itself. The artificial nature of this slip-velocity and its negative consequences on certain configurations encountered in real-world LES applications has been highlighted. To avoid these difficulties, a formulation with a no-slip condition at the wall is proposed. The wall shear-stress is applied at the first off-wall node, which leads to the necessity of using hexaedral or prismatic meshes in near-wall regions.

Both formulations are compared in three different test cases. The first is the turbulent, periodic channel flow, which allows to verify the capability of both approaches to reproduce the quantities given by theory and DNS data. The second is the flow over a sudden expansion, which reveals the problems created by the slip wall functions at corner points and shows that the no-slip formulation is not affected. The third case is an injector for aero-engines that is typical of complex geometries in realistic applications.

It is shown that the proposed no-slip formulation has superior qualities in reproducing the experimental velocity profiles, which is explained by the increased tendency of the slip wall functions to force the flow into wall-parallel direction along curved surfaces, resulting in a slightly altered flow topology. Furthermore, the tendency to oscillatory behaviour of the slip-velocity in certain cases and its impact on numerical robustness is highlighted.

It can be stated that in realistic applications, the way a wall-model is implemented in a given code and the way it interacts with the numerical methods used (in particular: scheme and SGS turbulence model) *can* influence the results as much as the wall-model itself. While the present work uses a very basic model, the performance of the proposed no-slip formulation in conjunction with more sophisticated models should be further investigated.

Additionally, an analysis of the limits of a wall function approach in terms of accuracy has been conducted. The central element that negatively affects the correct prediction of velocity profiles in a channel flow is the grid resolution in an intermediate layer between the wall and the central core. This lack of resolution is systematic as the wall function ideally requires large grid cells while the LES needs a continuous grid refinement towards the wall. As a result, the under-resolved turbulence near the wall behaves in an unphysical way if typical LES subgrid-scale turbulence models are used.

A simple method to adapt the near-wall behaviour of the turbulence model using blending functions has been investigated with positive results.

6.6 Summary of the elements applied on the TLC configuration

In this chapter, a certain number of different formulations for the wall model has been presented. Here, the wall modeling approach used for the TLC configuration (chapters 9, 10 and 11) shall be summarized.

- In view of the results shown in section 6.3.3, the no-slip formulation is retained. The mesh is adapted accordingly by the introduction of a single layer of prismatic elements at the walls.
- The height of the prismatic layer is carefully chosen to be of the order of 100 wall units. This necessitates the adaptation of individual zones, with further adjustments and re-meshing conducted after verification of the result from initial simulations.
- The Smagorinsky model is retained because of its good behaviour at interacting with the wall function approach. The WALE model would be preferable, in particular for the numerous free shear layers present in the TLC configuration. However, the problems occurring when used in conjunction with the wall model (see section 6.4.3) and the experimental development state of the blending approach lead to this conservative choice.

Chapter 7

Pressure drop in LES of complex geometries

Contents

7.1	Pressure drop in complex geometries	133
7.1.1	Pressure drop definitions	134
7.2	Sources of error on pressure drop	135
7.2.1	Convergence study of a single passage of a swirler	135
7.2.2	Analytical study of the error due to near-wall discretization	139
7.3	A method for very small scale geometric details (PPSG)	144
7.3.1	The numerical test case of a single perforation	147
7.4	Application of the PPSG method to the TLC configuration	148
7.5	Conclusion	149

7.1 Pressure drop in complex geometries

A crucial ingredient for many applications of LES on internal flows is to have a correct prediction of pressure drop, in particular in complex geometries. Examples for this are internal combustion engines, where pressure losses in the admission duct and around the valves play an important role in overall efficiency, or premixing swirlers of aeronautical engines where pressure losses directly affect engine efficiency. LES, in comparison with RANS, may be less accurate with respect to pressure-drop prediction because wall treatment in LES is not as developed and tuned as in RANS. In this section, the actual error of a typical LES is quantified, and broken down into different contributors. The study is focused on effects of complex geometrical features and aimed at the aeronautical premixing swirler that is also discussed in chapters 6 and 10.

Two typical scenarii can be distinguished in which pressure drop has to be correctly predicted or at least where one should be able to quantify the error. The first, and generally less critical one is a configuration with only one connection between an upstream position (e.g. a plenum) and a downstream one (e.g. a combustion chamber). An example is an injector with only a single swirler stage. In this case, assuming that the correct mass flow rate is imposed but the swirler's discharge coefficient is incorrect, velocities might locally be unphysical inside the swirler channels and the plenum pressure will differ from measurement. Yet, the velocity field and pressure level in the chamber will largely remain unaffected by this error. If the pressure drop of the

swirler, which is needed to determine the overall performance of the combustion system, can be quantified separately (e.g. experimentally), a LES will still correctly provide insight into the dynamics of the combustion chamber.

However, if there are multiple connections between plenum and chamber, as for example several swirler stages and/or secondary channels for cooling air, dilution holes etc., incorrect discharge coefficients will likely result in altered mass flow rate distribution *between* different channels. This imbalance of mass fluxes may affect the flow field at the swirler exit and therefore make a LES inaccurate in terms of the flow topology even if the prediction of pressure drop is not of interest in the case considered.

In theory, correctly predicting the discharge coefficient for a LES of a flow through one or multiple channels of complex geometry is a question of sufficient grid resolution and a turbulence model that is adapted for flows with strong shear phenomena, in particular near walls [104]. In practice, a resolved boundary layer is out of reach for this type of application, and a modeling strategy that aims at the reduction of resolution requirements is needed. Typically, the method of choice is the use of approximate wall-boundary conditions (or wall-functions), which correctly predict overall friction levels in a turbulent channel flow but lead to a more substantial error when applied to complex geometries.

An additional difficulty arises from the use of an explicit code, where the global time-step is linked to the minimum cell size via the CFL condition, which is a strong incentive not to introduce very small grid cells. Although the use of wall-functions remedies much of this constraint, some configurations include local, small-scale parts of their geometry that are in themselves smaller than the smallest allowable grid cell. Furthermore, there is often a very large number of these details (typically perforations), which means that meshing them is prohibitive, even if size and number of grid cells would be tolerable for a single element.

In this chapter, these two issues are considered separately. First, the predictive capability of a wall-function approach in a representative geometry will be assessed to quantify the error on pressure drop typically involved and to identify its main contributors. Second, different ways of modeling small-scale geometrical features are discussed. A method, involving a so-called surrogate geometry, is presented in detail and applied to the TLC configuration, a geometry with multiple flow passages. Finally, the challenges involved in simultaneously applying different modeling approaches on a realistic case are described and the necessity of a strategy for a conscious handling of the errors on pressure drop involved is highlighted.

7.1.1 Pressure drop definitions

The notion of pressure drop is a classical concept in hydraulics, where it is used as a term in the 1D *Bernoulli*-equation. The discharge coefficient c_d characterizes an element in a hydraulic circuit that leads to a pressure drop Δp on a streamtube with the velocity u .

$$\Delta p = c_d \frac{\rho u^2}{2} \quad (7.1)$$

Mass conservation ($\dot{m} = \rho u S$) allows then to relate a certain mass flux \dot{m} through a hydraulic element with the cross-section S to a resulting pressure drop:

$$\Delta p = \frac{c_d}{2\rho} \left(\frac{\dot{m}}{S} \right)^2 \quad (7.2)$$

In a system of n parallel fluid streams, leading to a mass flux \dot{m}_{glob} , the pressure drop between

a common, upstream reservoir and a common downstream point in the flow can be obtained by the following expression:

$$\Delta p = \frac{\dot{m}^2}{2\rho} \frac{1}{\left(\sum_i^n \frac{S_i}{\sqrt{c_{d,i}}}\right)^2} \quad (7.3)$$

In this system, the ratio of the mass flux of a given channel $i \in 1\dots k$ and the global mass flux is given by

$$\frac{\dot{m}_k}{\dot{m}_{glob}} = \frac{S_k}{\sqrt{c_{d,k}}} \frac{1}{\sum_i^n \frac{S_i}{\sqrt{c_{d,i}}}} \quad (7.4)$$

Errors on c_d can lead to different outcomes, depending on the condition if Δp or \dot{m} is fixed in the problem. In the first case, a too high discharge coefficient $c_{d,k}$ will lead to an underestimated mass flux \dot{m}_k , in the latter the pressure drop will be over-estimated. A relation between those two cases is:

$$\frac{\dot{m}_{err}}{\dot{m}} = \sqrt{\frac{\Delta p}{\Delta p_{err}}} \quad (7.5)$$

where values denoted *err* are the ones obtained with the wrongly predicted discharge coefficient $c_{d,err}$.

7.2 Sources of error on pressure drop

7.2.1 Convergence study of a single passage of a swirler

This test case has been chosen to be representative of the flow through the main swirler of the TLC configuration (see chapter 9) but at the same time be small enough to perform a grid convergence study. It corresponds to a single swirler channel of the main injector stage, through which about 90 % of the airflow passes. The channel is isolated from the swirler geometry and combined with a small plenum and downstream settling chamber (see figure 7.1 for an illustration). This case comprises all three geometrical features that are generally related to pressure drop [70]: An inflow, a short stretch of duct (with variations of cross-section) and an outflow. All three elements are of relatively complex shape, with skew angles and sharp edges where massive flow separation can be expected.

At the plenum inlet, a mass flux is imposed that is determined as a fraction of the flow passing through the main swirler stage. The constant pressure imposed at the outlet corresponds to the chamber pressure of the experiment. The convergence study comprises four calculations. The first three use wall functions in the no-slip formulation at all wall boundaries in conjunction with the Smagorinsky model (which corresponds to the approach used in the full TLC configuration, see section 6.6). Therefore, all meshes are of hybrid type, composed of a single layer of prisms at the wall and tetraedral elements everywhere else in the domain. The baseline mesh (case 1), which defines the reference near-wall grid spacing 1.0Δ , corresponds the mesh used in the full TLC configuration. The two finer meshes differ from the baseline case in the cell size in the near-wall prism layer that is scaled to 0.5Δ (case 2) and 0.2Δ (case 3). The parameters for

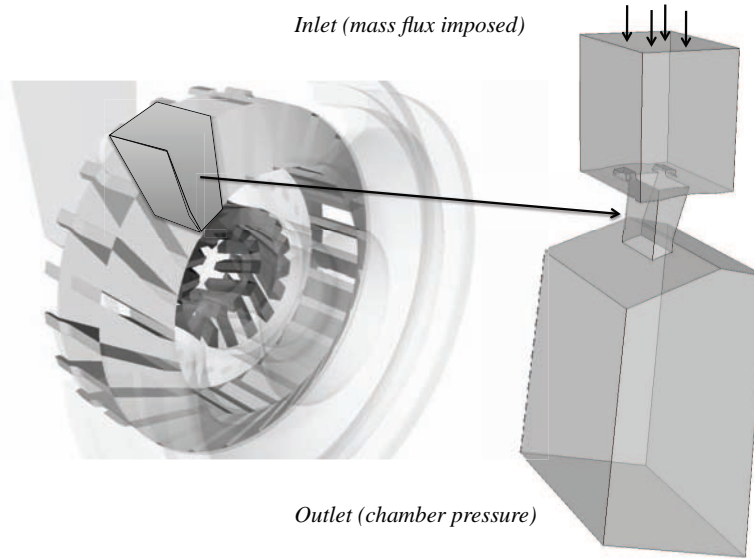


Figure 7.1: Computational domain of the single swirler channel testcase, compared to the full swirler and its positioning therein.

the rest of the mesh remain unchanged, however, as the stretching ratio of the tetraedral cells is kept constant at 1.7, the mesh inside the channel refines accordingly. Figure 7.2 shows the channel region of the resulting meshes, an overview of the cases considered is shown in table 7.1.

#	Grid spacing	y^+	Number of cells	Turb. model	Wall model
1	1.0Δ	≈ 100	$\approx 410\,000$	Smagorinsky	Wall functions (no-slip)
2	0.5Δ	≈ 55	$\approx 606\,000$	Smagorinsky	Wall functions (no-slip)
3	0.2Δ	≈ 30	≈ 1.6 million	Smagorinsky	Wall functions (no-slip)
4	wall resolved	≈ 2	≈ 9.1 million	WALE	none

Table 7.1: Summary of the cases for the single swirler passage.

The fourth case is a wall-resolved LES using the WALE turbulence model and serves as a reference that can be expected to deliver sufficiently accurate results. To limit the number of grid cells and to increase the quality of the resolved boundary layer flow field, this mesh has 10 prismatic layers with an initial thickness of approximately 2 wall units (on average) and an isotropic grid spacing of around 6 wall units in wall-parallel directions. The wall-normal stretching ratio is 1.15. This near-wall grid topology and the chosen grid spacing correspond to those of Nicoud and Ducros [104] who obtained good results for a wall-resolved turbulent pipe flow with a similar numerical approach. Details of this mesh are shown in figure 7.3.

Figure 7.4 shows iso-contours of the first off-wall grid point wall distance in wall units, as determined by the wall functions. For the baseline grid, shown on the left-hand side, a certain variation of y^+ over the swirler channel's surface is observed, but the overall levels are of the order of 100. This corresponds to a typical choice for a mesh destined for the use of wall-functions, as the first grid point can be expected to be in the logarithmic region even if rather large fluctuations occur. This grid-spacing has been carefully chosen while meshing the TLC configuration. On the other hand, the case of 0.2Δ , shown on the right-hand side of figure 7.4, reveals an y^+ of about 30, which is clearly on the lower end of the range of wall-distances for which the wall-function approach is still fully valid. It can therefore be considered to constitute a

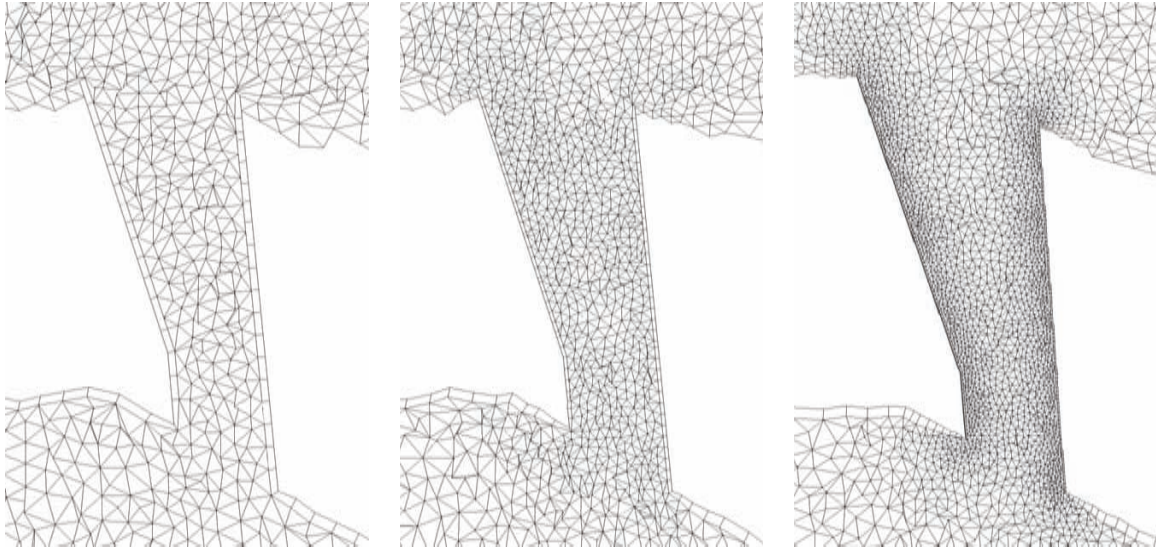


Figure 7.2: Meshes of the single swirler channel testcase, grid convergence study using wall-funtions. From left to right: Baseline mesh (equivalent to full swirler mesh) defined as 1.0Δ (case 1, table 7.1), refined mesh at 0.5Δ (case 2), refined mesh at 0.2Δ (case 3)

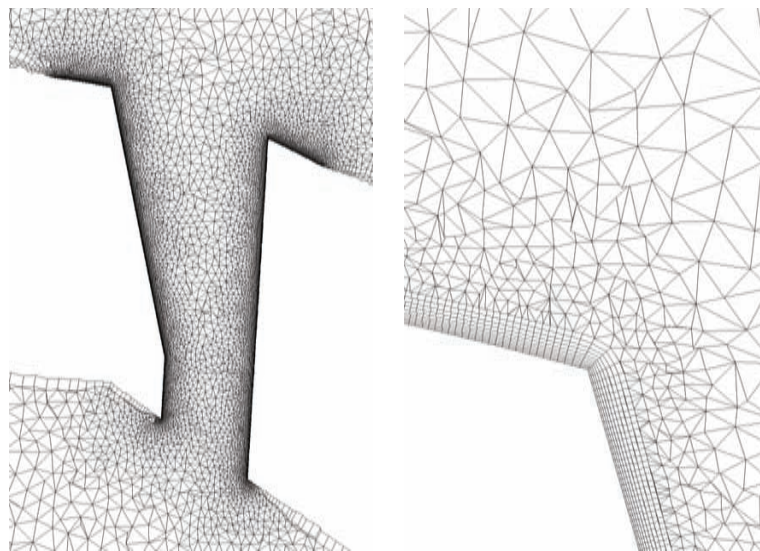


Figure 7.3: Mesh of the single swirler channel testcase, reference case with a wall-resolved LES approach (case 4, table 7.1).

certain limit of what a wall-function based LES can provide in terms of pressure drop prediction.

Q-criterion iso-surfaces for the baseline case and the 0.2Δ grid are compared in figure 7.5. The fine grid shows a distinctive pattern of coherent structures formed by the detached boundary layer and subsequent vortex rollup. This mechanism is limited to the edges with the relatively sharp angles that are created by the inclination of the channel. This results in a quite inhomogeneous flow field, that is characterized by large detached zones and strong, longitudinal vortices on the one side and the lack of comparatively strong turbulent effects on the other. On the coarsest grid, almost nothing of this is observed, apart from a single, short structure that bears a certain similarity to the strong activity observed along the same edge on the fine grid.

The way in which this turbulent vortex pattern interacts with the boundary layer and thus ultimately with the friction levels is illustrated in figure 7.6, which shows a result from the

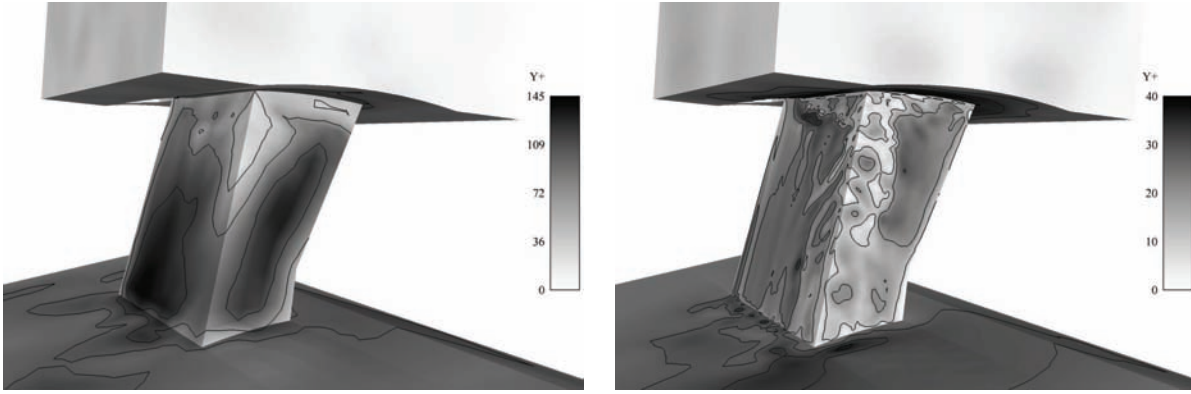


Figure 7.4: Iso-contours of the instantaneous value of near-wall grid spacing in wall units (y^+). Left: coarsest grid $\Delta/\Delta_{Baseline} = 1$ (case 1, table 7.1). Right: finest grid $\Delta/\Delta_{Baseline} = 1/5$ (case 3, table 7.1).

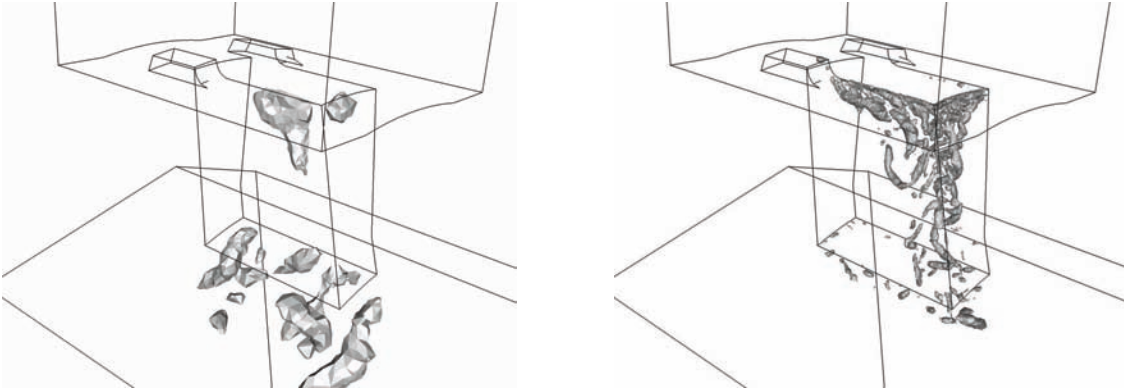


Figure 7.5: Visualization of turbulent flow features of the single swirler channel. Left: coarsest grid $\Delta/\Delta_{Baseline} = 1$; Q -criterion iso-surface at $3.9 \cdot 10^8$ (case 1, table 7.1). Right: finest grid $\Delta/\Delta_{Baseline} = 1/5$; Q -criterion iso-surface at $5.5 \cdot 10^9$ (case 3, table 7.1).

wall-resolved simulation. Here, the velocity field on a plane in direct proximity of the wall is considered. The high-velocity zone due to vortex-rollup along the edge at the entry into the channel can clearly be distinguished. To either end of this edge, low velocity zones, which correspond to simple separation bubbles are observed. In the first two-thirds, the boundary-layer is fairly chaotic as a result of these elements interacting. Only in a very limited zone on the downstream end to the left-hand side of the viewer, a homogeneous boundary layer with the typical streaks that roughly resembles an undisturbed channel flow is present.

As a purely qualitative observation, this shows that wall-friction in a complex geometry may depend to a certain extent on phenomena like the vortex rollup or large detached zones as observed in this case. It is clear, that these phenomena are very insufficiently resolved on the coarsest mesh, which can be expected to be a non-negligible source of error on pressure drop.

The quantitative part of the study relies on measuring the pressure drop for each case of table 7.1. This is done from an averaged solution, to exclude possible oscillations of the background pressure in time from the results. The probes are placed in relatively calm zones in the plenum and the chamber. The relative pressure drop is defined as

$$\Delta p_r = \frac{\Delta p}{p} = \frac{p_{t,u} - p_{t,d}}{p_{t,u}} \quad (7.6)$$

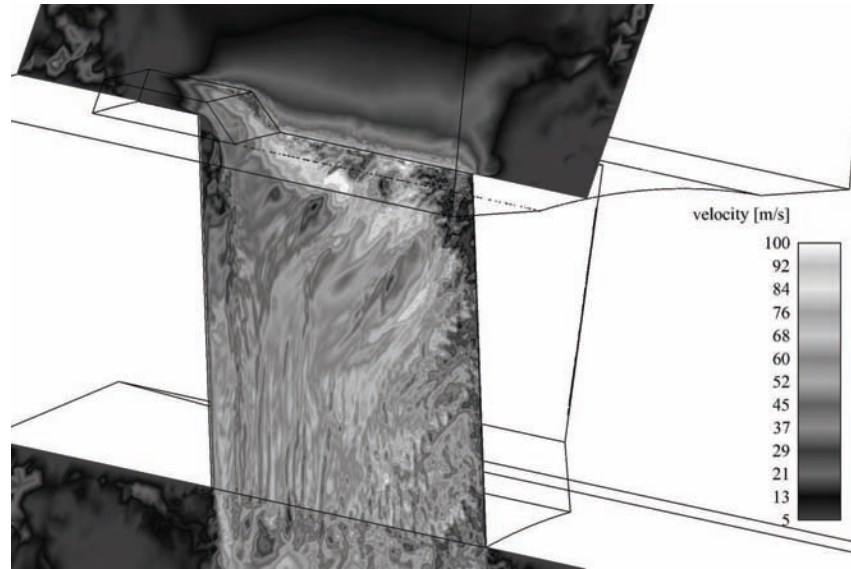


Figure 7.6: Wall-resolved simulation (case 4, table 7.1): velocity field in direct proximity of the wall as an illustrative example for the flow topology.

where p_t is the total pressure $p_t = p + \rho/2 v^2$ and the indices u and d stand for ‘upstream’ and ‘downstream’ respectively. For the chosen measurement locations, both pressures can be assumed to be equal $p_t \approx p$.

The wall-resolved case is assumed to have zero error, the error of the remaining cases is calculated relatively to this reference point. The result is shown in figure 7.7. Values of pressure drop obtained are summarized in the left half, ranging from 2.04 % for the wall-resolved case to 2.73 % on the baseline grid. There is virtually no difference observed between the finest wall-modeled simulation and the wall-resolved one. While there is no certainty that the prediction by the wall-resolved simulation is accurate, this result reveals, that provided a sufficient resolution, a wall-model based approach is capable to deliver very good results in terms of pressure drop prediction, even in complex geometries. Furthermore, this finding reinforces the assumption that the resolution of the dominant vortical structures in the channel is of importance, most probably more so than the additional details contributed by the resolution of the wall boundary layer.

The relative error based on the wall-resolved results is shown on the right-hand side of figure 7.7, amounting to up to 33 % for the baseline grid. This is also the error to be expected in the swirler of the complete TLC configuration, as all swirler channels are meshed with parameters identical to case 1 of table 7.1 in terms of y^+ values of the first off-wall grid point or the number of grid cells placed across the channel width.

7.2.2 Analytical study of the error due to near-wall discretization

While the previous section revealed the global error on pressure drop and identified complex flow patterns as one possible contributor to this error, another proportion of it can be related directly to the wall model. Both wall function approaches considered here (slip and no-slip, see chapter 6) result in velocity profiles that correspond as closely as possible to the logarithmic law in the inertial layer. However, even if the velocity profile is assumed to be exact at all grid nodes, a discretization error on the resulting mass flux is introduced. Due to the different velocities at the wall node, this discretization error depends on the implementation method of the wall function. Figure 7.8 shows a schematic of the mass fluxes in each node’s control volume, revealing the difference between slip- and no-slip formulation. In certain cases, these

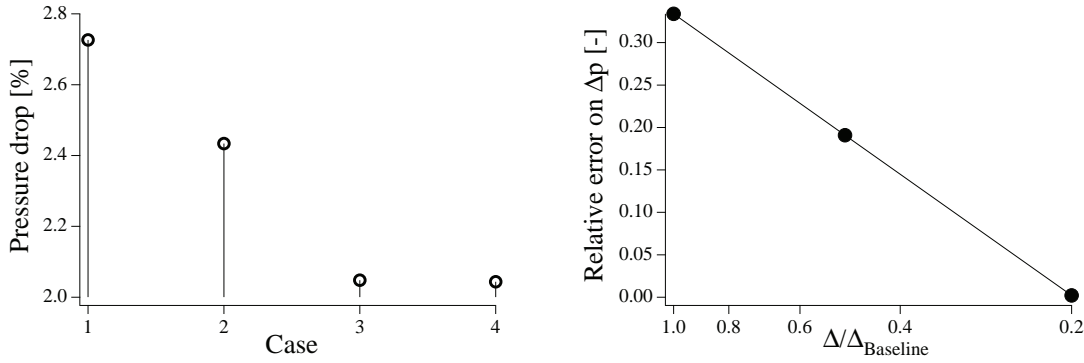


Figure 7.7: Left: pressure drop of the cases 1 (baseline grid) to 3 (0.2Δ) as well as the wall-resolved case 4. Right: relative error on pressure drop (based on the wall-resolved case 4) as a function of grid resolution.

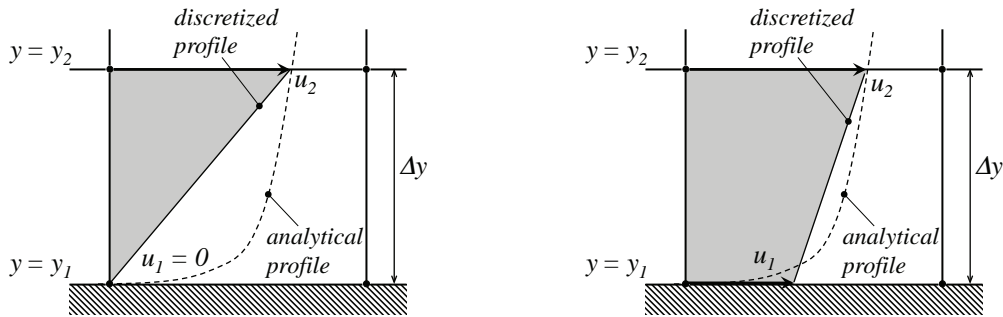


Figure 7.8: Schematic of the differences in global mass flux between no-slip (left) and slip wall functions (right). Analytical velocity profile (---), discretized velocity profile (—).

differences can have a quite marked influence, as for example in a coarsely meshed conduit flow, as illustrated by figure 7.9. Setting the velocity at the wall nodes to zero results in a loss of mass-bearing cross-section. The slip-wall formulation the other hand, seems to alleviate this problem, but it remains unclear if the resulting near-wall mass flux is closer to reality as the slip velocity u_1 is an artificial concept, governed mainly by the SGS viscosity model.

This prompts the necessity to investigate the problem in quantitative terms. The first part of this analysis is limited to the mass flux inside the first grid cell as the most general case. In a second step, these findings are applied on the case of a single swirler passage.

Estimation of the mass flux in the first near-wall cell

In this part, only the discretization error in the first grid cell adjacent to the wall is considered. There is an additional error in the following grid cells, but as the gradients in this region are less steep it can be expected to be small. Furthermore, this error does not depend directly on the wall function implementation.

In the first cell, it is assumed that the wall functions behave in an exact manner, i.e. velocities at the first grid point ($y = y_2$) are identical to the ones obtained by the logarithmic profile (equation 6.14). At first, the analytical reference solution is needed. A simple way to obtain

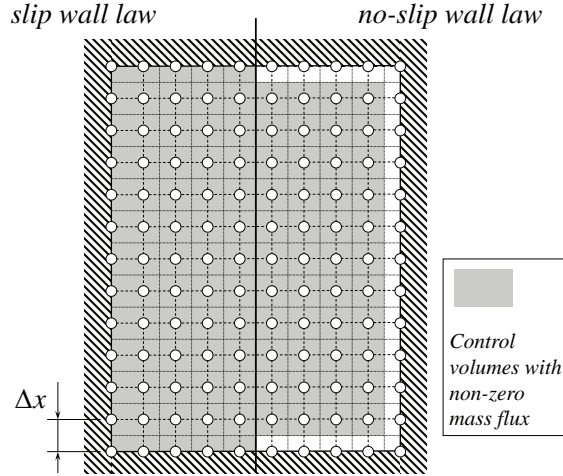


Figure 7.9: Schematic of the differences in global mass flux between no-slip and slip wall functions in an example grid representing a channel cross-section

it is to integrate the linear and logarithmic law (equations 6.9 and 6.14). Neglecting the buffer layer, the point of intersection between both curves, y_{int} marks the upper bound of the linear law's integration, which is located at $y_{int}^+ = 11.33$. In the following, the density is assumed to be constant. The integration of the linear law then yields:

$$\frac{\dot{m}_{c1,lin}}{\Delta z} = \rho_w \int_{y_1}^{y_{int}} u(y) dy = \frac{\mu_w}{2} (y_{int}^+)^2 \quad (7.7)$$

The logarithmic profile is then integrated between y_{int} and y_2 , yielding:

$$\frac{\dot{m}_{c1,log}}{\Delta z} = \rho_w \int_{y_{int}}^{y_2} u(y) dy = \frac{\mu_w}{\kappa} (y_2^+ \ln(y_2^+) + (C-1)y_2^+ - y_{int}^+ \ln(y_{int}^+) - (C-1)y_{int}^+) \quad (7.8)$$

Finally, the analytical mass flux in the first cell, $\dot{m}_{c1,a}$, is obtained as a sum of both contributions.

$$\frac{\dot{m}_{c1,a}}{\Delta z} = \rho_w \int_{y_1}^{y_2} u(y) dy = \frac{\dot{m}_{c1,lin}}{\Delta z} + \frac{\dot{m}_{c1,log}}{\Delta z} \quad (7.9)$$

In addition to the analytical profile, the discretized solution for the mass flux using both wall law formulations is needed. For a no-slip wall law, writing the mass flux per unit length in the first grid cell next to the wall is relatively simple because it only depends on the known value of $u(y_2)$. The contribution of the wall-node is zero per definition.

$$\frac{\dot{m}_{c1,wlns}}{\Delta z} = \rho_w u(y_2) \frac{\Delta y}{2} = \frac{\mu_w}{2k} y_2^+ \ln(y_2^+) + C \quad (7.10)$$

In the case of the slip wall law, obtaining an expression for the mass flux is less straightforward because it contains the slip-velocity at the wall, u_1 :

$$\frac{\dot{m}_{c1,wls}}{\Delta z} = \rho_w \left(u(y_2) \frac{\Delta y}{2} + u(y_1) \frac{\Delta y}{2} \right) \quad (7.11)$$

For the Smagorinsky model, an average value of the slip velocity u_1 can be written explicitly (see section 6.2.3 for more detail):

$$u_1 = u_2 - \frac{y_2}{2\rho_w(C_s\Delta)^2} \left(-\mu_w + \sqrt{\mu_w^2 + 4\rho_w^2(C_s\Delta)^2 u_\tau} \right) \quad (7.12)$$

Having expressions for the mass fluxes of both wall-functions $\dot{m}_{c1, wls}$ and $\dot{m}_{c1, wlns}$ as well as an analytical reference $\dot{m}_{c1, a}$ at hand, it is now possible to quantify the discretization error on mass flux in the first cell near a wall and show the influence of grid spacing. This is done for an exemplary channel flow that approximately corresponds to the narrowest section of the single swirler channel testcase (see figure 7.11 for an illustration). Here, the wall-distance of the first point, y_2^+ , is varied between 20 and 200 wall units.

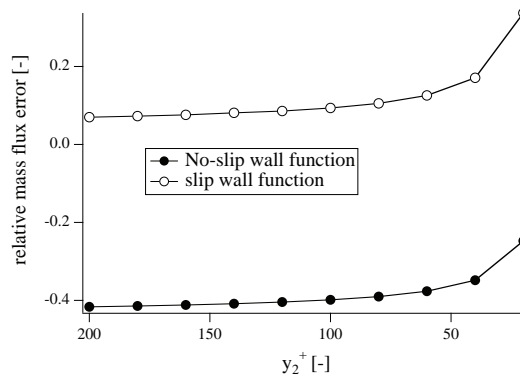


Figure 7.10: Comparison of the relative error (with respect to the analytical solution) of mass fluxes inside the first cell per z -unit length for different cell sizes.

The results are presented in figure 7.10 and generally show an over-estimation of the mass flux by the slip wall function and an under-estimation by the no-slip formulation. The resulting curves reveal that for y^+ of about 50 and smaller, the relative error of both formulations is of the same order but with opposed signs. For growing cell sizes, both relative errors tend to a constant value. In the case of the slip wall law, the relative error diminishes and stabilizes at less than 10 %. The no-slip wall law shows a relative error that continues to grow, exceeding 40 % for y^+ above 200, which can be expected as the first grid point then begins to reach into the central core, where the velocity profile is relatively flat. The upper limit for the error of the no-slip formulation is of course 50 %, which occurs if the first grid point is placed in the center of a channel or at infinite wall-distance on a flat plate.

Application on the single swirler passage

As a second part of the analysis of mass flux errors, the global mass flux of the simplified single swirler channel is considered. The analytical solution for the global mass flux through the cross-section of the computational domain is derived using the *Barenblatt*-law (equations 6.16 and 6.17) for an estimated $Re_\tau \approx 750$ in this testcase. In the region *outside* of the first cell, it is assumed that the *Barenblatt* profile is exact for both wall-law formulations. The mass flux inside the first cell is obtained using the derivations presented in the first part of this section, based on the logarithmic law.

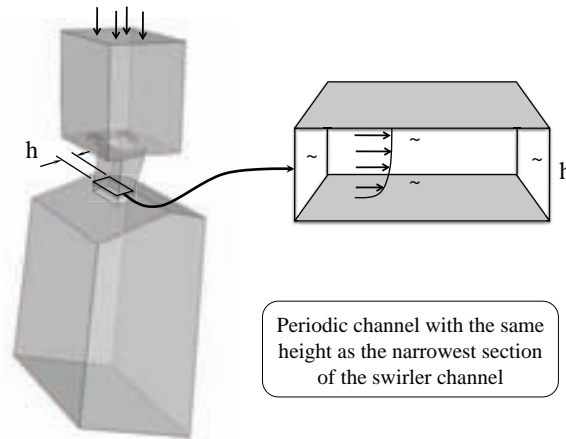


Figure 7.11: Illustration of the channel flow used for the analytical estimation of wall-model related errors, based on the geometry and conditions of the single swirler channel testcase.

The results are shown in figure 7.12. On the left side, the global mass fluxes of the analytical solution is compared to the values obtained with the wall-functions in both formulations. The slight variations of the analytical mass flux over y_2^+ are due to the discrepancies between the logarithmic law and the *Barenblatt* law for low values of y^+ , which can be observed in figure 6.2. The resulting mass fluxes of the different wall-law formulations both depart gradually from the analytical solution with the slip wall laws increasingly over-estimating global mass flux and the no-slip formulation under-estimating it. The right part of figure 7.12 shows the error in terms of global mass flux relative to the analytical solution. Contrarily to the local relative error inside the first cell, the global, relative error does not tend towards a steady level but grows linearly with increasing cell size. However, there is a difference in magnitude between the slip wall-law formulation of which the error stays below 0.4% and the no-slip formulation which reaches an error slightly over 4% for an y_2^+ of 200.

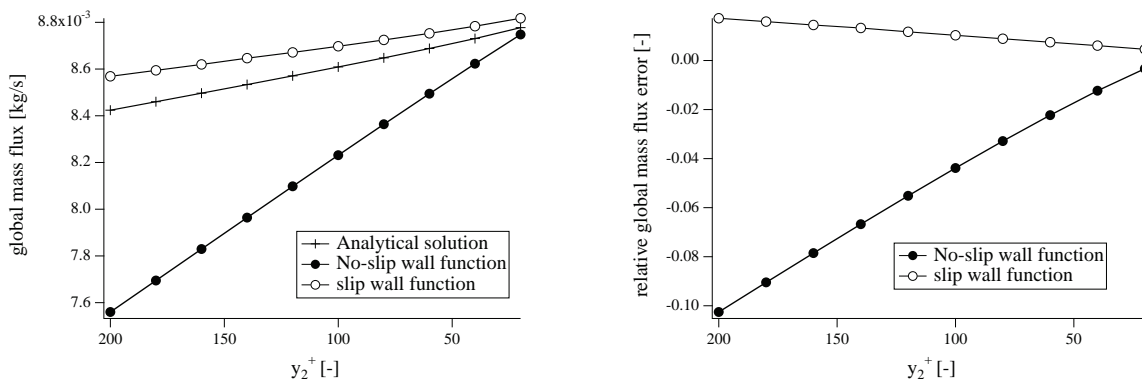


Figure 7.12: Left: comparison of the global mass fluxes through a cross-section of the turbulent channel for different cell sizes (variation of y_2^+ between 20 and 200). Right: comparison of the relative error (with respect to the analytical solution) of the global mass fluxes through a cross-section of the turbulent channel for different cell sizes.

Finally, these findings can be translated (using equation 7.5) into an estimation of the relative error on pressure drop for the single channel test case, which allows to measure the fraction of the global error that can be attributed to the wall-function. The results are shown in 7.13, where the wall-distance of the first point is translated into the multiples of the baseline grid of the

single channel simulations. The maximum error on Δp is observed for the no-slip formulation and takes a value of 2.3 % on the baseline grid. This error reduces to less than half a percent in the case of the finest grid. For the slip-formulation, the relative error stays below 0.5 % and nears zero for the finest grid resolution. This leads to the conclusion that, compared to the global error on pressure drop that is of the order of 35 % on the baseline grid, the influence of the wall-model is very limited.

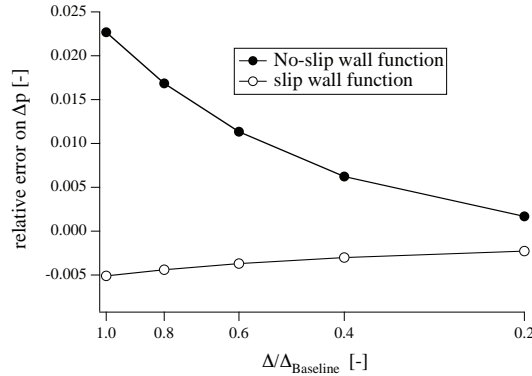


Figure 7.13: Application of the wall function in a formulation with non-zero velocity at the wall nodes.

7.3 A method for very small scale geometric details (PPSG)

The method described in this section is called PPSG (for Poly Perforation Surrogate Geometry) and has been developed for the treatment of multiple perforations that can be found in many combustors for cooling or dilution. These poly-perforations (as opposed to the more common term “multi-perforation”) should be understood as an arbitrary series of holes or filigrane channels connecting two regions between which a pressure difference exists. The previous sections have shown that a high grid resolution is needed for an accurate prediction of pressure drop (or flow rate). Therefore, in a typical LES, resolving these geometric details might lead to undesirable effects like the generation of locally very small grid cells that limit the global time step excessively or to the intolerable growth of the number of grid points and the degree of complexity due to the large number of such features.

Figure 7.14 shows a generic configuration on the left hand side. A popular strategy to model a poly-perforation is to replace it with a coupled pair of wall boundary conditions, which allow a mass flux to pass from one side to the other, governed by an assumed global discharge coefficient C_D . This method is very well suited to the particular case of multi-perforated plates (e.g. cooling liners in combustion chambers) that are characterized by a very large number of perforations, which are arranged in a homogeneous pattern. This case is well-covered by literature, a review has been published by Hay and Lampard [58]. The different effects that are studied include the inclination of the holes or cross-flow effects [52]. A detailed study of the flow using direct simulation can be found in the work of Mendez et al. [92, 94]. Models for this type of configuration often consist of wall boundary conditions with an additional mass flux per surface unit that is determined from the pressure differential using empirical correlations for the discharge coefficient [93, 24].

Quite often, one might be confronted with configurations where the assumption of homogeneous properties over a surface comprising a large number of perforations no longer holds, as illustrated

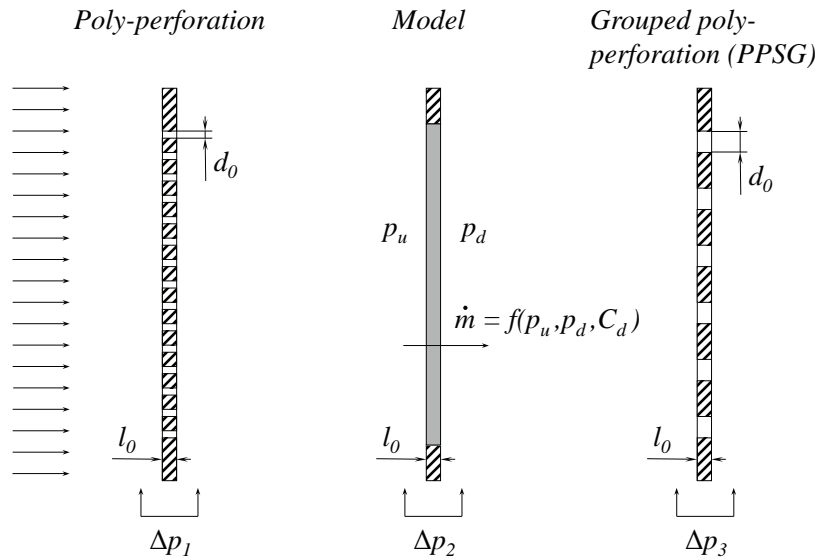


Figure 7.14: Different strategies for poly-perforations in a LES.

on the example of the TLC configuration, shown in figure 7.15 as well as in the left part of figure 7.16. Here, the cooling films consist in a series of perforations of which a fraction is slightly inclined relative to the chamber walls (series 1). These holes are aligned with the exit slot of the cooling films and form a focused sheet of high-velocity airflow. Another part (series 2) is a relatively small number of perpendicular holes (of a different diameter than those of the first series) in the dividing wall between the plenum and a flat cavity that collects air flow and guides it towards the exit slot of the cooling films. This diverse and non-homogeneous arrangement of holes, a typical example for what is called poly-perforation in the scope of this study, is treated with a different approach.

The main idea of the PPSG method, illustrated on the right-hand side of figure 7.14, is to group several holes together and to choose their diameter in such a way that the discharge coefficient through the multi-perforation remains globally the same. In the present case, as shown in the right half of figure 7.16, this allows to take into account the directionality of the outer perforations. The downside of this method is that the replacing diameter must be chosen even before the mesh is generated. Later adjustments are only possible with a considerable effort. In the following, strategies that allow to determine this diameter will be laid out and discussed.

The choice of the replacing diameter is influenced by several aspects. A first estimation for the diameter $d_{0,s}$, substituting n_s holes of the original diameter d_0 is the equivalent surface.

$$d_{0,s} = \sqrt{n_s} d_0 \quad (7.13)$$

This is only a rough estimate because the discharge coefficient varies with the Reynolds number [70] which is effectively changed by this approach. A more sophisticated approach, which takes this effect into account is to choose a diameter that matches the discharge coefficient, based on empirical correlations. Starting from the expression for the pressure drop Δp resulting from a mass flux \dot{m} passing through a circular hole of the diameter d_0 with a density ρ that is assumed to be constant:

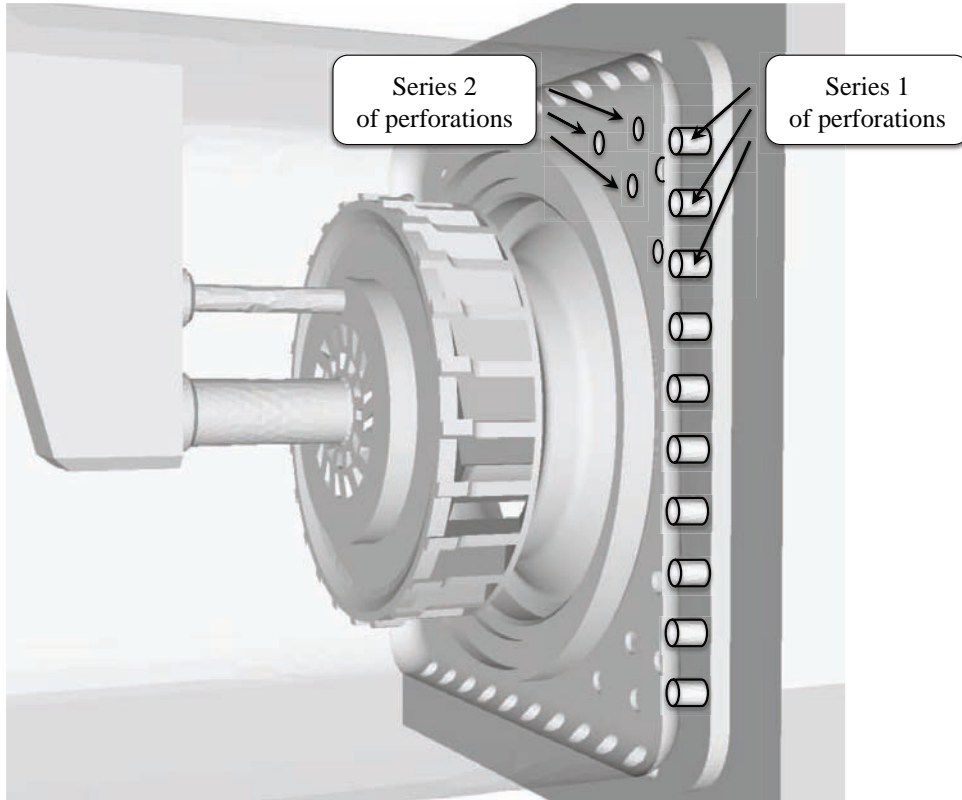


Figure 7.15: Illustration of the different perforation series (1 & 2) in the cooling films of the TLC configuration.

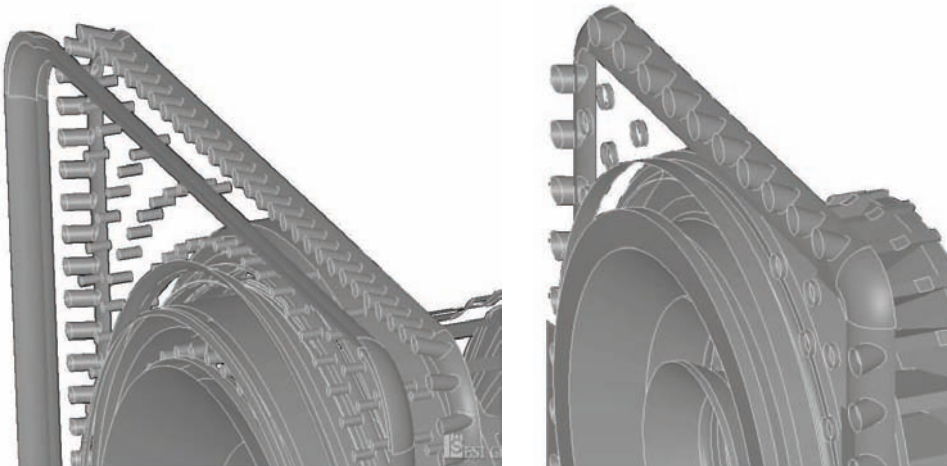


Figure 7.16: Surrogate geometry for a series of perforations that form a cooling film in the TLC configuration. Left: original geometry, right: surrogate geometry.

$$\Delta p = \frac{c_d(Re)}{2\rho} \left(\frac{\dot{m}}{\pi/4 d_0^2} \right)^2 \quad (7.14)$$

one can equate the values for pressure drop of the original geometry, Δp and the surrogate geometry Δp_s .

$$\frac{\Delta p_s}{\Delta p} \stackrel{!}{=} 1 = \frac{c_d(Re)}{c_{d,s}(Re)} \left(\frac{n_s d_{0,s}^2}{d_s^2} \right)^2 \quad (7.15)$$

As the discharge coefficients depend on the Reynolds number, which in turn is determined by the diameter and indirectly by the mass flux, the resulting expression is implicit and can be solved numerically.

$$\left(\frac{d_{0,s}}{n_s d_s} \right)^4 = \frac{c_d(\dot{m}, d_0)}{c_{d,s}(\dot{m}/n_s, d_{0,s})} \quad (7.16)$$

An example for the discharge coefficient of a single perforation with the length l and an orifice cross-section $S_0 = \pi/4d_0^2$, preceded by a larger duct of the cross-section S_u is given by Idel'cik [70]:

$$c_d = \frac{1}{2} + \left(1 - \frac{S_0}{S_u} \right)^2 + \lambda \frac{l}{D_H} \quad (7.17)$$

where $D_H = 4S_0/\pi d_0$ is the hydraulic diameter of the perforation and λ the friction factor of a smooth conduit.

In practice, the numerical application poses an additional problem as the grid resolution of the geometrical features considered can be expected to be relatively poor. This means that the error introduced by the insufficient grid resolution or the wall-modeling approach in this area will vary between the original- and the surrogate geometry and can be great compared to the Reynolds number dependency that the PPSG method aims to take into account.

An alternative strategy to be proposed here is to start out by admitting that with a reasonable grid resolution, the effective discharge coefficient of the surrogate geometry embedded into a given numerical framework cannot sensibly be determined a priori. On the other hand, as the surrogate geometry already is an *artificial* construct with the goal to reduce the necessary number and size of grid points in this area, one can as well turn the underlying argument around: in this case, the starting point is a given grid resolution and the surrogate geometry is then determined in such a way that the discharge coefficient of the new geometry plus the given mesh and numerical approach takes the desired value. Of course, this makes some preliminary calculations necessary, which will be described in the following section.

7.3.1 The numerical test case of a single perforation

Figure 7.17 shows the configuration. It is a short stretch of duct with a square cross-section (20 mm side-length), interrupted by a sudden contraction. The narrowest part has a circular section with the diameter d_0 and the length l_0 . At the upstream entry of the duct, a mass flux with a constant profile is imposed whereas a constant pressure is prescribed at the outflow. There is no wall-modeling, a simple no-slip condition is imposed on all solid surfaces.

The baseline geometry has a diameter d_0 that corresponds to the equivalent surface of the grouped perforations. The subsequent geometries have diameters $d_{0,s}$ of growing ratios of $d_{0,s}/d_0$. The mesh is composed of tetraedral elements with identical grid resolutions in the upstream and downstream sections. In the region near the perforation, the characteristic cell size at mesh

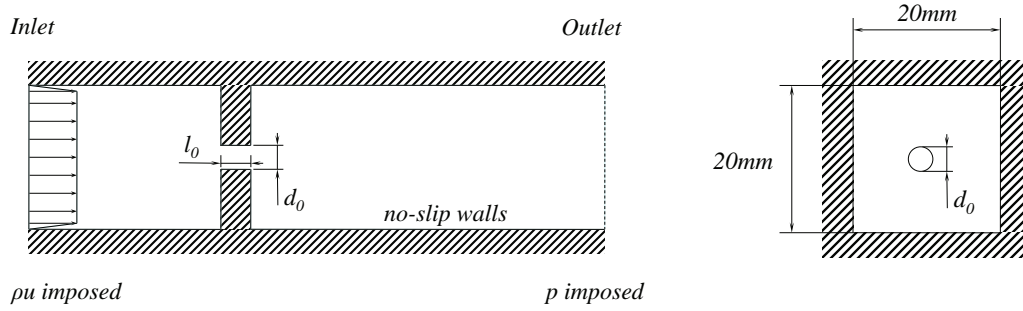


Figure 7.17: Computational domain of the single perforation test case.

generation is chosen at $d_{0,s}/5$ in order to obtain an equal number of grid cells across the orifice for all cases considered.

Simulations are run separately for the two different types of perforations present in the TLC configuration (see 7.15). In each case, a set of geometries and meshes is generated, starting from the baseline case $d_{0,s}/d_0 = 1$ and subsequently increasing this ratio in steps of 0.2 until the desired pressure drop is reached. The results are shown in figure 7.18. It is notable that in this case, characterized by a very coarse mesh, the baseline simulation, which corresponds to the equivalent surface approach, produces a pressure drop of more than five times the targeted value, showing effectively the practical limitations of this method. The surrogate diameter is determined by interpolating the target value of Δp in the data from the simulations. The target is obtained by a standard empirical correlation from Idel'cik [70] (equation 7.17). The resulting diameters $d_{0,s}$ are incorporated into the surrogate geometry of the TLC configuration, as shown in the right half of figure 7.16.

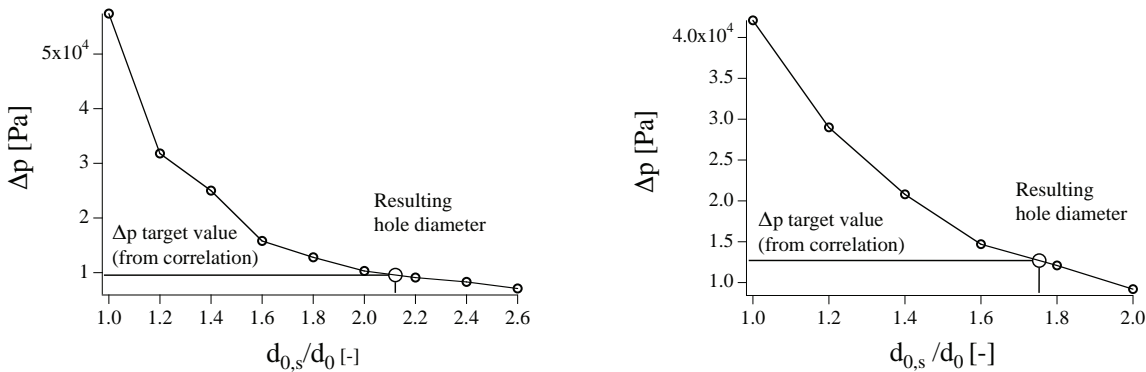


Figure 7.18: Pressure drop over a single circular contraction as a function of the ratio of the contraction diameter $d_{0,s}$ to the diameter of equivalent surface d_0 . Left: perforation series 1, right: perforation series 2. The correlation for Δp is given in equation 7.17.

7.4 Application of the PPSG method to the TLC configuration

The PPSG method for poly-perforated cooling films yields a large scale representation of the filigrane perforations with very little impact on overall mesh- and minimum cell-size and a very low error on the predicted pressure drop. Ironically, these very good characteristics become problematic when used in the complete TLC configuration: while for the cooling films, the issue of over-predicted pressure losses has been circumvented very effectively, it still persists for the

swirler itself, which is subjected to errors that reach up to 40 % as was evidenced in section 7.2.1. As shown in equation 7.4, this leads to a change in the distribution of fluxes between the swirler and the cooling films. In the example of the TLC configuration, the effect is quite pronounced and well visible on the mean velocity profiles. The consequence is that, in a configuration with multiple flow paths, it is not enough to produce the best possible quality in pressure drop prediction for *each individual* flow path. Instead, the amount of error in all parallel flow paths has to be at least of the same order to avoid mass flux imbalances. In practice, this means that if errors in some of the parallel paths cannot be avoided, the quality of other, less critical elements may have to be deliberately *deteriorated* (for example by reducing the grid resolution) to restore the proper flux balance.

From the experience gained in the present work, a strategy for management of error on pressure loss prediction can be proposed. A schematic overview of the elements is shown in figure 7.19. The starting point is to produce a surrogate geometry or use a multi-perforation (film cooling) model for those regions that cannot be meshed due to their small-scale geometrical features. In the ideal case, these approaches will yield a very low error on pressure drop, because both are fine-tuned to match empirical correlations, which can be expected to be sufficiently precise. For the larger-scale geometrical features, the wall modeling approach described in chapter 6 is used. In this context, it is crucial to have at least a rough estimate of the error this method generates. This can be done at the example of the present study using a representative geometrical element that can be simulated with resolved boundary layers. An alternative could be to consider a generic geometry like a channel with a sudden contraction for which experimental data or empirical correlations exist.

As a next step, the surrogate geometry or multi-perforation model needs to be tuned to reach approximately the same error as encountered in the other flow parts. In the case of a multi-perforation model, the discharge coefficient on which it is based can simply be adapted. For the PPSG method, the case is slightly more difficult, as modifications of the geometry and re-meshing can be time-consuming. Other parameters that allow a controlled increase of the discharge coefficient of the surrogate geometry are the local grid resolution or the artificial increase of wall friction levels.

7.5 Conclusion

To conclude this chapter, the global error of the entire TLC configuration are compared to reference data. The results, summarized in table 7.2, are based on a simulation using a no-slip wall-law formulation inside the swirler and an error-corrected surrogate geometry in the cooling films. The global pressure drop in the LES reaches a value of 5.86 %, which is 29 % higher than a prediction provided by SNECMA (using an engineering code) and 53 % higher than in the experiment. This level of error is consistent with the estimation provided by the single swirler channel simulations. It has to be noted that LES results are obtained with an artificially increased discharge coefficient for the cooling films to ensure a correct mass flux balance. Without this increase, the pressure drop would naturally be closer to experimental data.

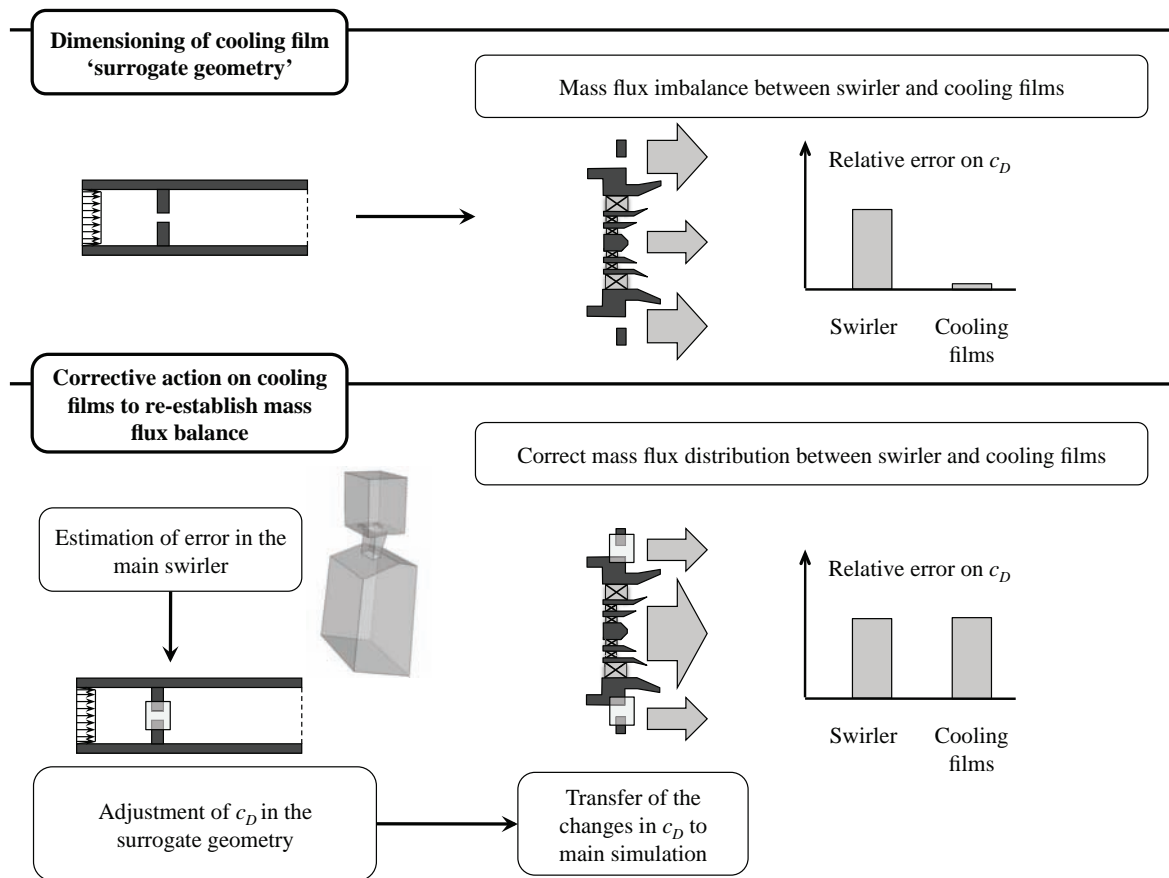


Figure 7.19: Schematic of the procedure to maintain the correct mass flux balance between poly-perforations with the surrogate-geometry approach and a swirler with a wall-function approach.

The main findings of this study can thus be summarized as follows:

- Industrial-scale LES with wall-modeling approaches and grid resolutions that are typical for today's state-of-the art computations may not be predictive in terms of pressure loss in complex geometrical regions. The use of wall-models, however, is not the main contributor to the error. With a sufficient grid resolution (near-wall *and* away from the wall), a pressure drop prediction comparable to the one of a wall-resolved LES can be achieved.
- Although errors of up to 50 % seem to indicate a problem of accuracy, the quality of such simulation regarding aspects other than pressure drop is in general not compromised by this imperfection.
- Quantifying and managing the error on pressure drop such a simulation is still crucial, in particular in configurations with multiple, parallel flow paths.

Pressure drop		
LES	SNECMA	Experimental data
5.86 %	4.53 %	3.82 %

Table 7.2: Pressure drop in the TLC configuration - comparison of the LES result with a dedicated engineering code (SNECMA) and experimental data

Chapter 8

Injection for multipoint systems

Contents

8.1	Introduction	153
8.1.1	Atomization of liquid jets in a crossflow	154
8.2	Injection methods	156
8.2.1	Modeling of the injection near-field	156
8.2.2	Implementation of the model for Euler-Lagrange	159
8.2.3	Implementation of the model for Euler-Euler	160
8.3	The experimental setup	163
8.3.1	Computational domain	163
8.4	Gaseous flow field	164
8.5	Euler-Euler numerical scheme	165
8.6	Test cases	167
8.7	Results	168
8.7.1	Flow and spray topology	169
8.7.2	Comparison of averaged results	173
8.8	Computational cost	176
8.9	Conclusion	176
8.10	Tables	178

8.1 Introduction

Injection in the TLC configuration relies on two separate systems, the hollow-cone injector of the pilot stage and the multipoint system for the main stage. The hollow-cone injection can be considered the standard type for aeronautical combustors [85]. Modeling the spray formed by the pilot injection is discussed in the thesis of Sanjose [129] in the framework of EE simulations. A phenomenological model has been derived and tested on the MERCATO configuration [136]. Early work on hollow cone injection also covers the injector present in the TLC configuration, but mounted in a different type of combustion chamber and without multipoint injection, as presented in the thesis of Lavedrine [81]. Results for the TLC configuration in the present form, again considering primarily the hollow-cone injector have been obtained in the diploma thesis of Simsont [138].

In view of the solid base of results on the hollow cone injection, the present work concentrates entirely on the multipoint injection system. This method of injecting a series of small liquid fuel

jets into a transverse airflow is common in different kinds of air-breathing aeronautical propulsion systems. Typical examples are ramjet and scramjet engines [27] where they allow to perform injection without introducing solid obstacles into the airflow. Moreover, liquid jet atomization at high subsonic or supersonic airspeeds is very effective. Today, multipoint injection systems are becoming more widespread in aero-engines for subsonic transport aircraft. The reason for this lies in the trend towards staged premixing swirlers that allow to optimize the combustion process for a wide range of operating conditions. Staging an injector usually leads to designs that feature several swirlers of which at least the outermost one has an annular form, enclosing a central part. A straightforward way to promote quick mixing and a homogeneous fuel vapour distribution in these outer parts of the injector is to use a series of small fuel jets, i.e. a multipoint injection.

For the design of a multipoint injection system, the main parameters of interest are:

- Jet penetration, as it determines with which parts of the flow the resulting spray will interact (bulk airflow, boundary layer, wall-impact etc.).
- Atomization, because it determines the evaporation timescale and droplet dynamics. The resulting droplet size distribution (locally and spatially) depends strongly on the crossflow properties and indirectly on jet penetration, as different penetration lengths let the droplets encounter different crossflow properties.
- Mixing behaviour, as turbulent dispersion of the spray conditions the mixing of the evaporated fuel. It depends mainly on crossflow (turbulent) properties and droplet size and therefore indirectly on jet penetration.

The configuration of a liquid jet in a gaseous crossflow (LJCF) is a proper testcase for numerical and experimental studies of multipoint injection systems. Representing one single injection point, it allows to analyze all important physical mechanisms in detail while reducing geometrical complexity and computational cost (see figure 8.1). The present work is based on the extensive experimental study by Becker et al. [11] at pressure conditions typical for aeronautical engines.

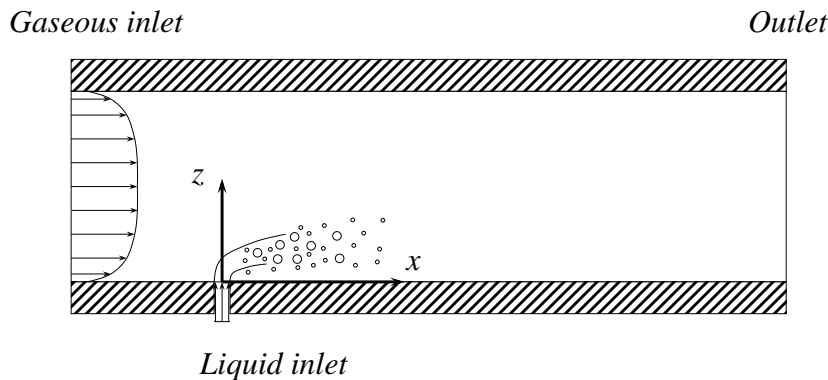


Figure 8.1: Test case of a liquid jet in a gaseous crossflow.

8.1.1 Atomization of liquid jets in a crossflow

Experimental studies on the liquid jet in a crossflow [156, 27, 11, 3, 48] identify two main phenomena to characterize the primary breakup mechanisms of the liquid jet after injection. The first is column breakup, which occurs when surface waves on the liquid column are amplified and lead to its disintegration into ligaments and the subsequent formation of a spray. The

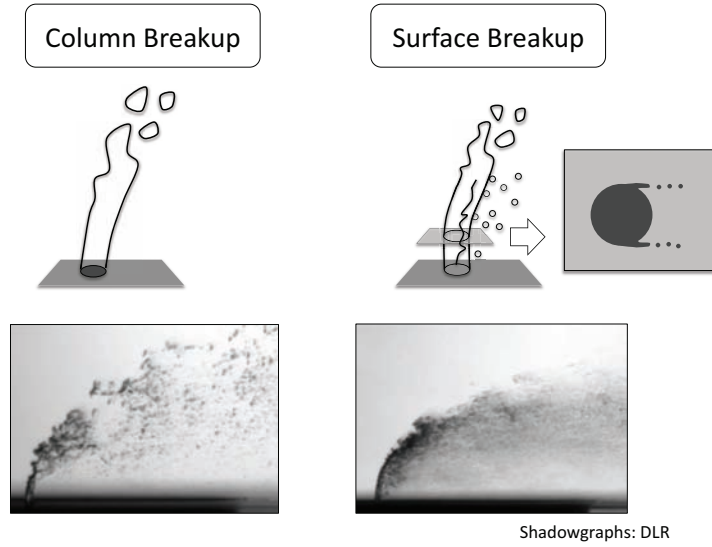


Figure 8.2: Schematic of the column and surface breakup regimes. Shadowgraphs by Freitag and Hassa [46].

second is called surface breakup and means the stripping of small droplets through shear from either side of the liquid column. Figure 8.2 shows a schematic illustration of these breakup mechanisms, as well as two exemplary shadowgraphs. While column breakup can be the only mechanism present, as shown on the left-hand side shadowgraph, surface breakup occurs in addition to column breakup under certain circumstances. Wu et al [156] proposed a classification of the conditions under which one of the two mechanisms is predominant, depending on the aerodynamic Weber number based on the diameter of the liquid column and the gaseous velocity of the crossflow, $We_{ae} = \rho_g D_{inj} u_g^2 / \sigma$, where σ is the surface tension, and the momentum flux ratio $q = \rho_l w_{l,inj}^2 / (\rho_g u_g^2)$, where u_g is the bulk velocity of the crossflow and $w_{l,inj}$ the injection velocity of the liquid jet. This classification is shown in the form of a diagram in figure 8.3. Two main zones are distinguished: for low We_{ae} numbers and low q , column breakup is predominant, while for high We_{ae} and q , surface breakup appears as an additional mechanism. The dividing line between both regimes as proposed by Wu et al. [156] is a linear function. In the present study, the aerodynamic Weber number is kept constant at values typical for gas-turbine combustors, while the momentum flux ratio is varied to obtain cases which correspond to different breakup regimes, as highlighted by three grey dots that mark the cases of $q = \{2, 6, 18\}$.

Numerical studies of this problem may rely on several approaches (see figure 8.4). As primary and secondary breakup mechanisms play an important role, a direct simulation using an interface tracking method [61], [60] would capture most of the physics involved (fig. 8.4a). However, such methods are out of reach for realistic applications because of the high computational cost. Two examples of simplifying approaches are Apte et al. [5] who use a Lagrangian method, neglect the liquid column but take secondary breakup into account (fig. 8.4b), as well as Rachner et al. [118] who use a Lagrangian method combined with simple laws for drag and surface/column breakup derived from empirical correlations (fig. 8.4d). Elements such as the drag law and the surface breakup model used in the present study are similar to the method proposed by Rachner et al. [118] for a Reynolds averaged Navier-Stokes (RANS) framework. A method that combines an empirical model for the liquid column with a model for secondary breakup is currently investigated by Senoner [135] (fig. 8.4c).

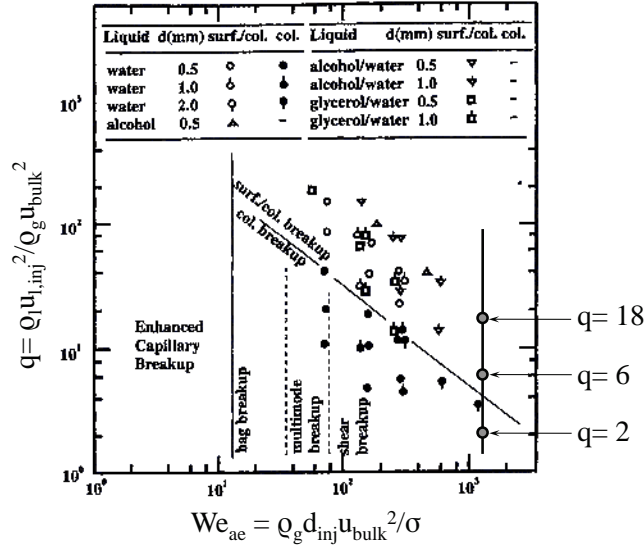


Figure 8.3: Diagram of liquid jet breakup regimes from Wu et al. [156].

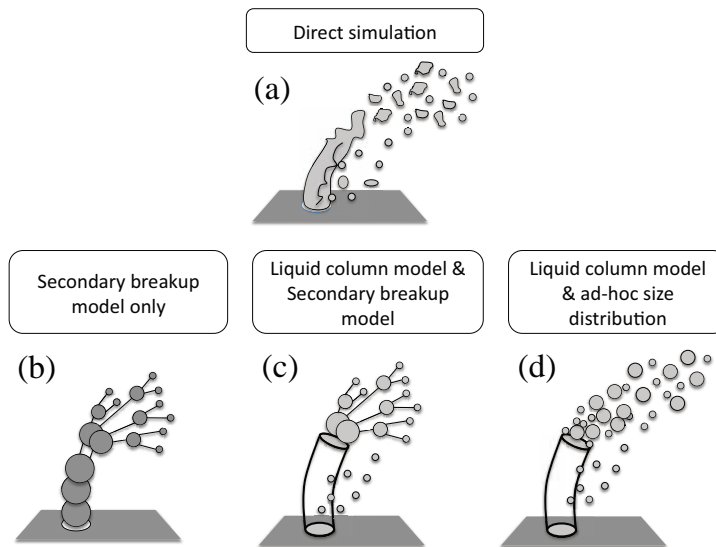


Figure 8.4: Schematic of modeling approaches for the liquid jet in crossflow case.

8.2 Injection methods

Near the liquid injection point, the classical assumptions in EE or EL do not hold. These methods become valid only after the resulting spray reaches a fully developed state in the far-field. Therefore, in the injection zone, additional models are needed as described below.

8.2.1 Modeling of the injection near-field

The modeling approach for the near-field includes the presence of a liquid column, the droplet stripping from its surface and the reconstruction of the droplet diameter field generated by atomization.

Liquid column trajectory and breakup

The far-field penetration length of the LJCF is influenced by several mechanisms. The first one is the existence of a liquid column at the injection point. The trajectory of this column differs strongly from the ones of spherical droplets. The second mechanism is the downstream disintegration of the liquid column because it leads to a significant change in drag coefficient, which strongly influences the spray trajectory. For the liquid column as well as for the region of fully developed spray, simple laws for drag can be formulated. In an intermediate zone, where very transient structures such as column fragments and later on large droplets undergoing secondary breakup dominate, drag is changing rapidly and difficult to model. In the present work, this transition zone is assumed to be very compact and of negligible influence on the far-field (see figure 8.5 for a schematic).

In practice, the model for the liquid column region consists in locally modifying the law of particle drag to obtain a good representation of the liquid column *trajectory*. This requires (a) an estimation of the location of the column disintegration and (b) a new law for drag that is applied to all particles between injection and the predicted column breakup point.

Point (a) is handled using experimental results: Fuller et al [48] studied a liquid jet in a crossflow experimentally and introduced a breakup timescale, τ_{ab} , which has been found to apply to a large variety of breakup processes by Hsiang and Faeth [67]:

$$\tau_{ab} = C_{ab} \frac{D_{inj}}{u_\infty - u_l} \sqrt{\frac{\rho_l}{\rho_g}} \quad (8.1)$$

Applied to the breakup of the liquid column, Fuller et al. [48] showed that in the aerodynamic breakup regime (which generally applies in gas-turbine conditions), the breakup coefficient C_{ab} is relatively constant at a value of $C_{ab} = 2.58$. The breakup point (x_b, y_b, z_b) can then be estimated from:

$$\frac{x_b - x_{inj}}{D_{inj}} = \frac{C_D C_{ab}^2}{\pi} \quad y_b = y_{inj} \quad (8.2)$$

$$\frac{z_b - z_{inj}}{D_{inj}} = C_{ab} \frac{w_{l,inj}}{u_\infty} \sqrt{\frac{\rho_l}{\rho_g}} \quad (8.3)$$

These relations provide the zone, relative to the injection $(x_{inj}, y_{inj}, z_{inj})$, in which a modified law for particle drag is applied (point *b*). Such a law is provided in the work of Fuller et al. [48] and in a similar form by Wu et al. [156]. It contains several simplifications because the liquid column undergoes substantial deformation from its initial cylindrical shape and a change in angle of attack as its trajectory is deflected, leading to a constantly evolving drag coefficient. The cited authors circumvent this complexity by introducing an average drag coefficient C_D and by neglecting drag normal to the freestream velocity. By further assuming that $(w_g - w_l)^2 / (u_g - u_l)^2 \ll 1$ (this ratio attains a maximum value of 0.163 for $q = 18$ in the present study), the axial momentum equation with an average drag coefficient takes the form (see Fuller et al. [48] for the derivation):

$$\frac{du_l}{dt} = \frac{2C_D}{D_{inj}} \frac{\rho_g}{\pi \rho_l} (u_g - u_l)^2 \quad (8.4)$$

Drag in wall-normal and transverse direction as well as the gravitational force, which is small compared to aerodynamic forces, are neglected.

$$\frac{dv_l}{dt} = \frac{dw_l}{dt} = 0 \quad (8.5)$$

The average column drag coefficient is obtained by Fuller et al. [48] through an experimental study: $C_D = 4.39$. It remains valid over a wide range of conditions, up to momentum flux ratios of over 100.

Liquid column surface breakup

As described in the introduction (section 8.1), the developed spray is not only produced by secondary breakup of the products of the disintegrating liquid column but also by surface breakup, i.e. the lateral stripping of the liquid boundary layer from the column surface. A basic model simulating droplets produced by this mechanism needs to predict at least two quantities: the mass flow rate per unit length of liquid column and a characteristic diameter. The mass flow rate can be obtained by adapting a model developed for the stripping of a liquid boundary layer from a spherical droplet by Ranger and Nicholls [120] to the case of a liquid column. These authors approximate the fully developed boundary layer velocity profiles with the expressions:

$$\frac{u_{BL,l}}{u_g} = A \exp\left(\frac{-y_{BL}}{\sqrt{a_l(x)}}\right) \quad (8.6)$$

$$\frac{u_{BL,g}}{u_g} = 1 - (1 - A) \exp\left(\frac{-y_{BL}}{\sqrt{a_g(x)}}\right) \quad (8.7)$$

where $u_{BL,g}$ and $u_{BL,l}$ are the velocities of the gaseous and the liquid phase in the curvilinear reference frame of the boundary layer and A is the dimensionless velocity at the interface. Formulating the integral momentum equations and equating the shear stresses at the interface

$$-\mu_l \frac{\partial u_{l,BL}}{\partial y_{BL}} \Big|_{y_{BL}=0} = \mu_g \frac{\partial u_{g,BL}}{\partial y_{BL}} \Big|_{y_{BL}=0} \quad (8.8)$$

allows to obtain a_l and A on either side of the column, at the position located at an angle of 90 degrees relative to the freestream velocity.

$$a_l = \sqrt{\left(\frac{8}{3} \frac{\mu_l}{\rho_l}\right) / A u_\infty} \quad A = \left(\frac{\rho_g \mu_g}{\rho_l \mu_l}\right)^{\frac{1}{3}} \quad (8.9)$$

The flux of liquid mass $dm_{l,SB}/dt$ stripped from a liquid column segment of the length l_{col} with a constant diameter D_{inj} and which is assumed to be oriented perpendicularly to the airstream is then

$$\frac{dm_{l,SB}}{dt} = 2l_{col}\rho_l \int_0^\infty u_{l,BL} dy \quad (8.10)$$

$$= \frac{3}{2} l_{col} \rho_l \sqrt{\pi D_{inj}} A a_l u_\infty \quad (8.11)$$

The second important quantity to model, a characteristic diameter of droplets formed by surface breakup, can be determined following the work of Chou et al. [28] who did an experimental study on surface breakup of spherical droplets. The same physical arguments (based mainly on the liquid boundary layer at the droplet surface) should be applicable to a cylindrical element of the liquid column.

Two regimes are distinguished: the transient shear breakup regime and the quasi-steady shear breakup regime. The quasi-steady regime is characterized by a fully developed liquid boundary layer which has therefore a thickness proportional to the column diameter $d_{col} \sim \delta$. The liquid boundary layer of the column starts to develop at the injection and is convected upwards with the column. It shall be assumed that the zone of a developing boundary layer is short compared to the length of the entire column. If further the amount of liquid removed from the column is assumed to be small compared to the overall liquid volume, it can be assumed that $d_{col} \approx D_{inj} = const$. Chou et al. [28] show that the stripped droplets have a diameter that is proportional to the boundary layer thickness. As the boundary layer thickness is proportional to the original drop diameter (or the liquid column diameter in the present case), Chou et al. [28] obtain a relation between the parent structure (drop / column) diameter and the child drop diameter:

$$SMD_{SB} = 0.09 D_{inj} \quad (8.12)$$

Secondary breakup after liquid column disintegration

Once the disintegration of the liquid column is complete and spherical droplets are formed, the spray enters a regime of secondary breakup. Models for this regime exist in a Lagrangian framework [106, 122, 5, 7] and can provide a realistic global particle diameter distribution of the fully developed spray. However, since the main focus of this work is to compare EL and EE approaches and breakup models are much less developed in EE codes, secondary breakup is neglected here and a fully developed particle size distribution is assumed. Becker et al. [11] provide a local diameter distribution obtained at the point of maximum liquid mass flux (i.e. at the core of the fully developed spray plume) for the case $q = 6$. The global diameter distribution of the simulations is based on an analytical log-normal distribution fitted to this data (figure 8.6). Becker et al. [11] further show that characteristic diameters of the spray depend mainly on the dynamic pressure of the freestream and only very weakly on the momentum flux ratio q . All three cases, $q = \{2, 6, 18\}$ are therefore based on the same diameter distribution of the form:

$$P(d, \bar{d}, \sigma) = \frac{1}{d\sigma\sqrt{2\pi}} e^{-\frac{(\ln(d)-\bar{d})^2}{2\sigma^2}} \quad (8.13)$$

where d is a given droplet diameter, \bar{d} the mean diameter and σ the standard deviation.

8.2.2 Implementation of the model for Euler-Lagrange

In the Euler-Lagrange formalism, the application of the liquid column model presented in section 8.2.1 is straightforward. The column breakup point is determined using equations 8.2 and 8.3. Droplets with variable diameter (according to the distribution shown in figure 8.6) are injected at the jet orifice. If a droplet has not yet traveled beyond the breakup point, drag is obtained from equation 8.4, regardless of its actual diameter. Thus, all droplets follow the trajectory of the liquid column. Once they have cleared the breakup point, they instantly regain their original properties in terms of drag and act as a fully developed spray. Figure 8.5 shows an illustration of this procedure.

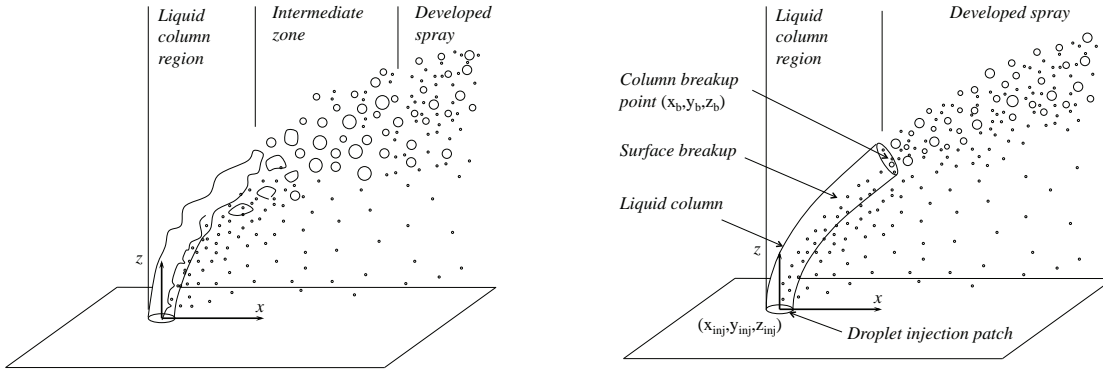


Figure 8.5: Left: classification of different regions of the liquid jet atomization. Right: schematic of the column model, which neglects the intermediate zone of non-spherical structures and secondary breakup.

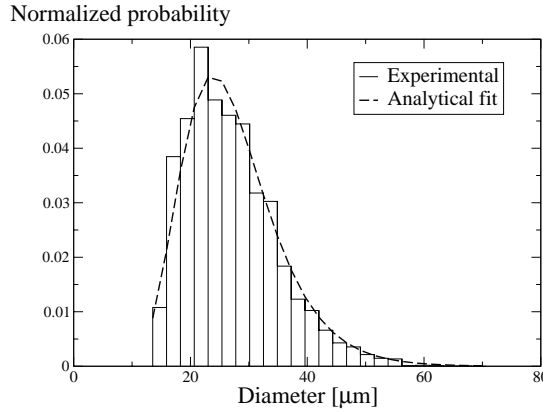


Figure 8.6: Diameter distribution of the fully developed spray. Experimental data from [11], measured at the point of maximum liquid volume flux in the case of $q = 6$. Analytical fit using a log-normal distribution, applied in all simulations.

The model for surface breakup calculates the liquid mass flux that is removed from the liquid column and the characteristic diameter from equations 8.11 and 8.12. Among the particles generated randomly per timestep Δt at the jet orifice, a number that corresponds to $(dm_{l,SB}/dt)\Delta t$ and that falls within 10% into the diameter range of SMD_{SB} is flagged as candidates for surface breakup. The flagged particles are released at a random location (with a uniform probability distribution) along the liquid column length.

A summary of the main steps performed by the liquid column model in its Lagrangian implementation is given in table 8.1.

8.2.3 Implementation of the model for Euler-Euler

Tackling a LJCF with a Eulerian method leads to three difficulties. The first is a liquid volume fraction of order unity (plain jet) in the near-field, which puts considerable strain on the numerical scheme. The second is the very small diameter of the injection orifice, which leads to very small grid cells if at least 5 to 10 cells are to be placed across the diameter (see figure 8.7, left). The third is the Eulerian approach in its present form being locally monodisperse.

Euler-Lagrange	
1	Calculate point of column breakup (x_b, y_b, z_b) , eqs. 8.2, 8.3.
2	Define liquid column region between $(x_{inj}, y_{inj}, z_{inj})$ and (x_b, y_b, z_b) .
3	Inject particles at $(x_{inj}, y_{inj}, z_{inj})$ with a diameter distribution (fig. 8.6).
4	At injection, flag particles for surface breakup (eqs. 8.11, 8.12).
5	Inside the column region, apply modified law for particle drag (eqs. 8.4, 8.5).
6	Along the column trajectory, randomly release flagged surface breakup particles.
7	After clearing the column region, continue with unmodified EL calculation.

Table 8.1: Summary of the EL implementation of the liquid column model

A new method proposed here solves these problems by artificially enlarging the injection diameter (Broadened Injection Method, called BIM). In the present case, the diameter of the injection patch, D_{inj} is increased by a factor 5 (figure 8.7, right), which leads to cells of roughly the boundary layer grid spacing. In this injection patch, liquid phase velocities are fixed to their values in the initial injector so that the liquid volume fraction in the injector section reduces to a value of 1/25.

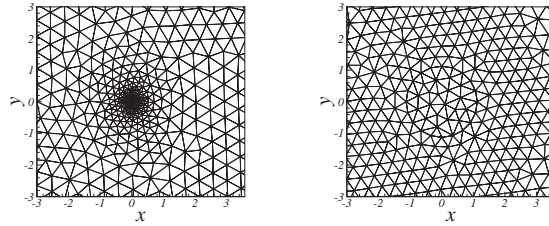


Figure 8.7: Surface grid in proximity of the jet injection patch. Left: original diameter, right: augmented diameter for Eulerian simulations.

The spatial diameter distribution found in the far-field is an important feature of the LJCF that cannot be reproduced by a *globally* monodisperse simulation. Alternatively, as the EE method allows for *spatially* varying diameters, a variable diameter profile can be imposed as a boundary condition on the injection patch, especially if this patch has been broadened (figure 8.7). The idea behind this technique is the following: droplets injected from a single point, perpendicularly into an airstream will be sorted naturally by their diameter due to their different ballistic properties. Trajectories of the largest diameters will penetrate farthest into the crossflow, the smallest ones will be deflected very rapidly and generally, trajectories do not cross. Therefore, the polydisperse character of the spray can be mimicked by injecting droplets with the largest diameters at the upstream end of the injection patch and the smallest at the downstream limit: suppose that the diameter histogram (figure 8.6) is composed of n_{bin} diameter classes. The normalized probability for the diameter class $i \in \{1 \dots n_{bin}\}$ shall be noted P_i . In a spatial diameter distribution, the circular surface of the inlet patch is discretized with a set of n_{bin} rectangular subdomains of the size $2 \Delta x_k \Delta y_k$ (figure 8.8). The injection procedure consists in imposing a monodisperse spray with a constant speed $u_{l,inj} = f(q)$, a constant liquid volume fraction $\alpha_{l,inj} = 1/25$ and with the local droplet diameter d_k corresponding to a given diameter class into each subdomain $k \in \{1 \dots n_{bin}\}$, sorted from largest to smallest droplets from upstream to downstream. The remaining Eulerian variable to impose on the subdomain k is the droplet number density per unit volume $n_{l,k}$, which is linked to the diameter and the liquid volume fraction by:

$$n_{l,k} = \frac{\alpha_{l,inj}}{\pi/6 d_k^3} \quad (8.14)$$

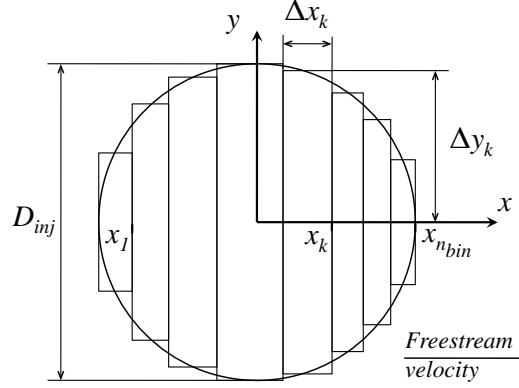


Figure 8.8: Streamwise discretization of the injection patch into n_{bin} subdomains.

To match the targeted diameter histogram, the ratio of the number of droplets injected per time unit on the subdomain k and the global number of droplets injected must correspond to the normalized probability of the diameter class P_i , $i = k$:

$$\frac{n_{l,k} u_{l,inj} \Delta x_k 2 \Delta y_k}{\sum_{n=1}^{n_{bin}} n_{l,n} u_{l,inj} \Delta x_n 2 \Delta y_n} \stackrel{!}{=} P_i, \quad i = k \quad (8.15)$$

The goal is therefore to find a distribution of streamwise and transverse intervals Δx , Δy that can satisfy this ratio for a given diameter histogram. As the injection patch is of circular shape, a relation between Δx and Δy can be stated:

$$\Delta y_k = \sqrt{\left(\frac{1}{2} D_{inj}\right)^2 - \left(x_k - \frac{\Delta x_k}{2}\right)^2} \quad (8.16)$$

where x_k is the current x -coordinate relative to the center of the injection patch at $\vec{x} = (0, 0, 0)$.

$$x_k = -\frac{1}{2} D_{inj} + \sum_{i=1}^k \Delta x_i \quad (8.17)$$

Simplification and rearrangement of equation 8.15 yields an expression for the streamwise interval k .

$$\Delta x_k = \frac{P_k}{n_{l,k} \Delta y_k} \sum_{n=1}^{n_{bin}} n_{l,n} \Delta x_n \Delta y_n \quad (8.18)$$

The condition $\sum_{i=1}^k \Delta x_i \stackrel{!}{=} D_{inj}$ allows to obtain

$$\Delta x_k = \frac{P_k}{n_{l,k} \Delta y_k} \frac{D_{inj}}{\sum_{n=1}^{n_{bin}} \frac{P_n}{n_{l,n} \Delta y_n}} \quad (8.19)$$

Equations 8.19 and 8.16 can be solved iteratively. Here, a good initial solution is to assume equidistant streamwise intervals $\Delta x_k = \text{const} = D_{inj}/n_{bin}$. The number and size of the bins is based on experimental data (31 size classes of $2.47 \mu\text{m}$ width). The resulting streamwise injection diameter distribution is shown in figure 8.9. To apply this distribution as an injection boundary condition, it must be interpolated on the grid points.

A summary of the main steps performed by the liquid column model in its Eulerian implementation is given in table 8.2.

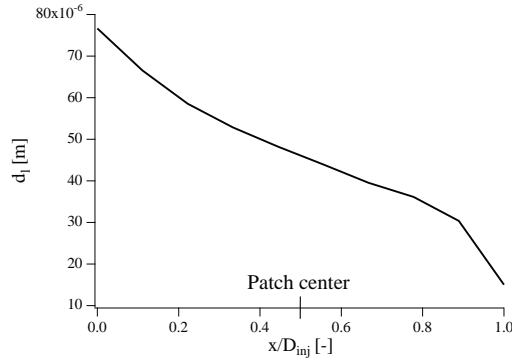


Figure 8.9: Spatial diameter distribution over the streamwise diameter D_{inj} of the jet injection patch.

Euler-Euler	
1	Calculate point of column breakup (x_b, y_b, z_b) , eqs. 8.2, 8.3.
2	Define liquid column region between $(x_{inj}, y_{inj}, z_{inj})$ and (x_b, y_b, z_b) .
3	Define boundary condition with variable diameter profile (fig. 8.9).
4	Inside the column region, apply modified law for particle drag (eqs. 8.4, 8.5).
5	Outside the column region, perform unmodified EE calculation.

Table 8.2: Summary of the EE implementation of the liquid column model

8.3 The experimental setup

A drawing and a photograph of the experimental setup used by Becker et al. [11] are shown in figures 8.10 and 8.11. It consists of a test section of rectangular cross-section and flat lateral surfaces of which three are equipped with quartz windows to allow optical access. The air enters the test section from a pressurized reservoir and exits through a throttle with a sonic throat. The transverse liquid jet injection is located on the centerline of the lower surface. Measurements relevant for the present work are shadowgraphs obtained with standard photographic equipment and PDA measurements of the liquid volume flux and diameter data at a position downstream of the injection.

8.3.1 Computational domain

The computational domain represents a short stretch of the measurement duct from the experiment of Becker et al. [11]. Its dimensions are shown in figure 8.12. The injection nozzle for

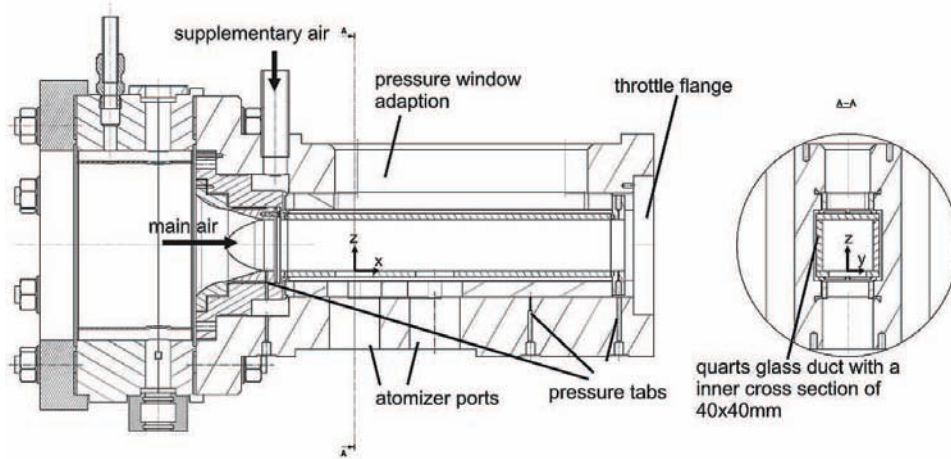


Figure 8.10: Photography of the test bench at DLR Cologne.

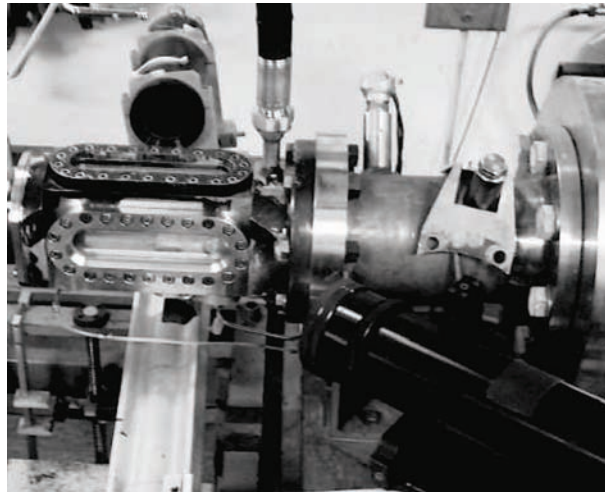


Figure 8.11: Photography of the test bench at DLR Cologne.

the liquid jet is situated on the centerline of the lower wall, defined here as the origin of the coordinate system with x being the streamwise coordinate and z the wall-normal coordinate pointing in the direction of the jet. The boundary in negative x -direction from the injection is the inlet, the opposite surface the outlet and all lateral surfaces are modeled as walls.

8.4 Gaseous flow field

In all cases considered here, the gaseous flow parameters are identical. The air flow is characterized by a bulk velocity of 100 m/s, a pressure of 6 bar and an air temperature of 290 K. Due to the relatively long upstream duct in the test bench, it is assumed that the flow inside the computational domain is turbulent and fully developed. Therefore, turbulence injection is performed at the inlet. The fluctuation field is generated using the methods of Klein et al. [77] as well as Kraichnan [78]. These synthetic turbulent fluctuations are imposed at the inlet using the boundary condition of Guézennec and Poinso [55] to minimize the injected noise. The necessary input data (profiles of mean- and rms values of all velocity components as well as the correlations $\langle uv \rangle$, $\langle uw \rangle$ and $\langle vw \rangle$) is not available from measurement. Therefore, a preliminary simulation of a periodic stretch of duct of identical cross-section and mesh properties is performed. This has the additional advantage that the statistics obtained from this case are

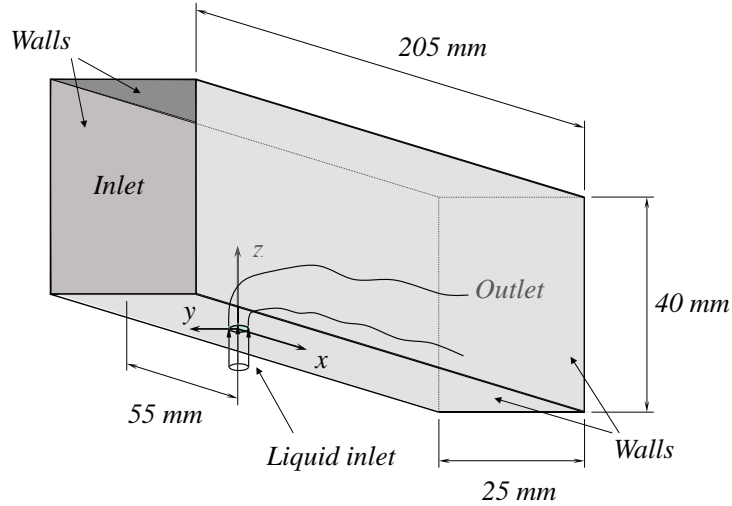


Figure 8.12: Computational domain.

already filtered fields, using the same LES filter width. The global Reynolds number of the flow, based on the channel width is $Re_g = 1 \cdot 10^6$. Wall boundaries are modeled using wall functions in the slip-wall formulation (see chapter 6).

8.5 Euler-Euler numerical scheme

For the Euler-Euler simulation, the choice of the numerical scheme has proven to be a crucial ingredient for the success of simulations of the jet-in-crossflow case. Out of the schemes available in the AVBP code, three are considered here for comparison: the second-order accurate (space and time) Lax-Wendroff scheme, the third-order accurate (space and time) TTGC scheme as well as the PSI (for Positive Streamwise Invariant) scheme [146] (see section 5.4.1), which is of first order in space and time [1]. It has been implemented in AVBP and applied in the PhD thesis of Lamarque [80] as well as Roux [126], yielding good results in a number of test cases, including particle-laden homogeneous isotropic turbulence, even compared to the third-order TTGC scheme. Being a multi-dimensional upwinding scheme (in contrast to the centered LW and TTGC schemes), PSI is characterized by a high robustness, which makes it very well-suited for injection problems, as demonstrated by Roux [126]. Due to strong gradients of liquid volume fraction and liquid phase velocity at the spray boundary, the case of a liquid jet in a crossflow relies heavily on this robustness. A scheme comparison is performed on a simplified jet-in-crossflow case at $q = 18$, without any model for the liquid column and using a constant droplet diameter. All simulations start with the same, very high level of artificial viscosity. It is successively reduced to the least amount allowed by the calculation to run reliably. Final coefficients for the Colin sensor (see section 5.7.2) are summed up in table 8.3, most notably revealing a factor 30 between PSI and both centered schemes. The corresponding results are shown in figures 8.13 to 8.16. Figure 8.13 shows a comparison of liquid volume flux isocontours to visualize the spray boundaries. It is clear that in the LW and TTGC calculations the jet is quickly and considerably diffused, causing it to dissolve into a broad spray cloud attached to the wall instead of showing a well-delimited plume detached from the wall, as it is observed for the PSI scheme. The evolution of mean liquid volume flux over the wall-distance z , shown in figure 8.14, further emphasizes this behaviour of the jet. The additional curve of PSI results using the liquid column fits experimental data. It is included to underline the fact that results obtained with the PSI scheme are indeed physically sound.

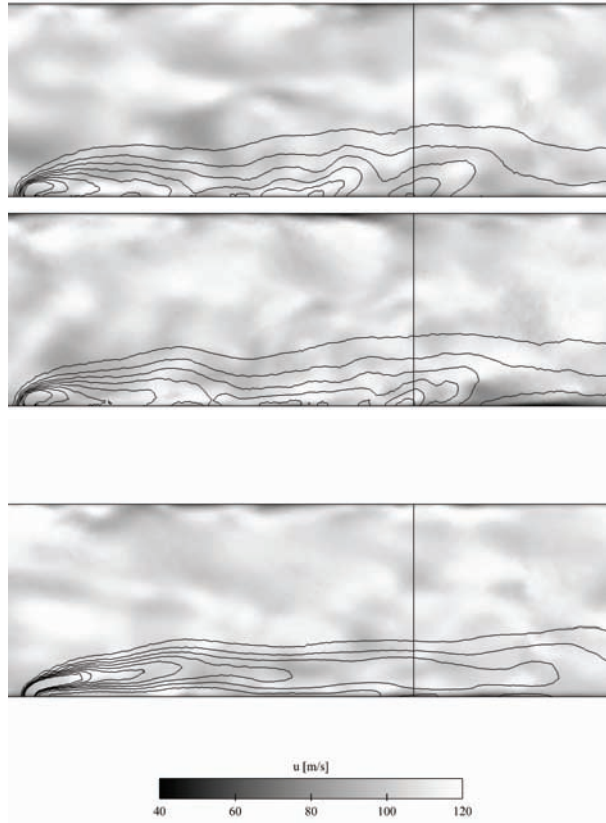


Figure 8.13: Euler-Euler results for different numerical schemes, case of $q=18$: Instantaneous axial gaseous velocity field on the plane $y = 0$, overlaid with iso-contours of liquid volume flux Φ_l . Cases from top to bottom: Lax-Wendroff, TTGC, PSI.

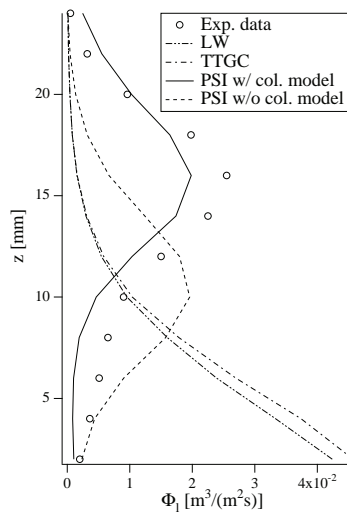


Figure 8.14: Comparison of the spatial distribution of liquid volume flux Φ_l at a downstream location of $x = 80$ mm, over the wall-normal distance z . Comparison of experimental data [11] (ooo) and Euler-Euler results using different numerical schemes.

In figures 8.15 and 8.16, the mechanisms involved are revealed in more detail. Figure 8.15 shows a liquid phase velocity vector field overlaid with liquid volume flux iso-contours. In figure 8.16, the same iso-contours are combined with the sensor for artificial viscosity. Note that the presence of an activated sensor only means that artificial viscosity is applied at this location, but it does not allow to conclude about the actual amount applied (indicated in table 8.3). It can clearly

be seen in these visualizations that the main differences are located at the upstream face of the jet, where liquid and gaseous velocities meet perpendicularly. For both centered schemes, this zone is thickened by the diffusive effect of artificial viscosity, as can be seen in figures 8.15a/b and 8.16a/b, resulting in a smooth transition between jet and crossflow vector orientations. The thickened transition zone affects the entire jet, leading to its complete disintegration. When the PSI scheme is used, the zone, where velocity vectors change direction by almost 90 degrees is very thin in comparison, occupying only about two grid cells. As a result, the bulk flow inside the jet region is not affected and remains intact.

While this conclusion can not be generalized, it is clear that in this particular case, the high robustness of an upwinding scheme outweighs the higher spatial order of the centered schemes, when the latter have to be combined with artificial viscosity. Artificial viscosity leads to an isotropic diffusion of the spray that is very destructive in view of the end result. The PSI scheme needs very little artificial viscosity and is therefore spared from these effects. It is, however, no less dissipative but due to the intrinsic directionality of numerical diffusion, it performs particularly very well in all jet-like applications.

As a consequence, only the PSI scheme is retained for all Euler-Euler simulations presented in this work (including the full TLC configuration of chapter 11).

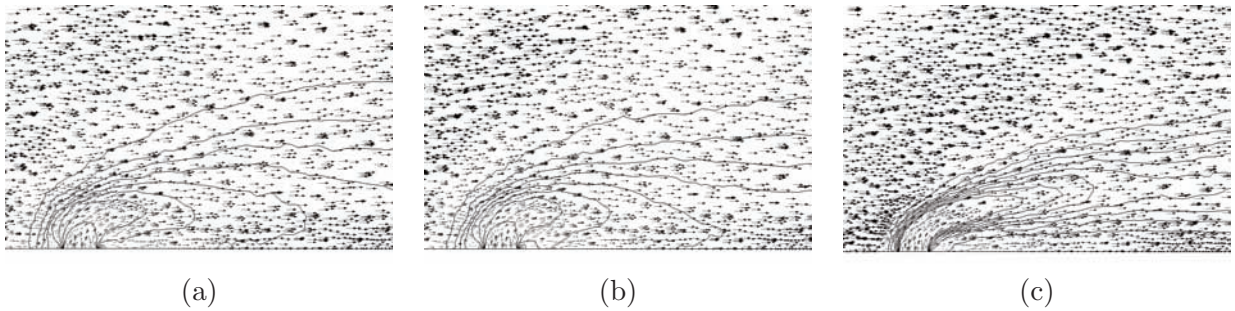


Figure 8.15: Liquid velocity vector field on the plane $y = 0$, overlaid with iso-contours of liquid volume flux Φ_l . Cases from left to right: (a) Lax-Wendroff, (b) TTGC, (c) PSI.

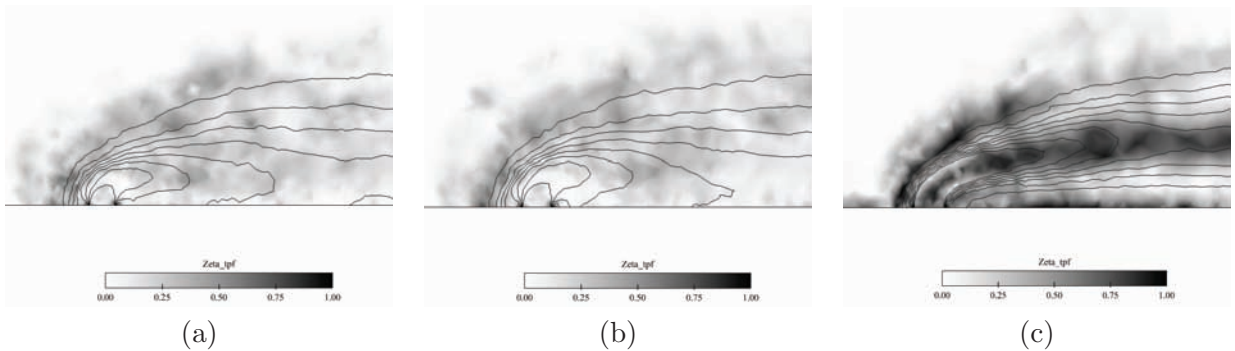


Figure 8.16: Field of the artificial viscosity sensor to visualize the zones where artificial viscosity is applied, overlaid with iso-contours of liquid volume flux Φ_l . Cases from left to right: (a) Lax-Wendroff, (b) TTGC, (c) PSI.

8.6 Test cases

Apart from the test cases used to assess different numerical schemes, Twelve different cases are considered, comprising six cases for each liquid phase simulation approach, of which a series of three uses the liquid column model while in the other series, the spray is injected ‘as is’,

Artificial viscosity coefficients			
	LW	TTGC	PSI
2nd order coeff.	0.3	0.3	0.015
4th order coeff.	0.01	0.01	0.001

Table 8.3: Necessary second- and fourth-order artificial viscosity coefficients for the Colin sensor [32].

without model for the liquid column. Each of the remaining subseries of three considers the different momentum fluxes at $q = \{2, 6, 18\}$. A summary is given in tables 8.4 to 11.6 (section 8.10).

The meshes are of unstructured type, comprising approximately 320 000 nodes (1.5 million grid cells) for the Lagrangian cases and 360 000 nodes (1.8 million grid cells) in the Eulerian cases with an additional refinement in the injection region. Sections through the meshes on the mid-plane of the domain ($y = 0$) are shown in figures 8.18 and 8.17 for EL and EE respectively. Both meshes are refined towards the boundary layer with the first point situated at roughly 500 wall units. For the Reynolds number at hand, this near-wall resolution corresponds to the near-wall grid cell still well inside the logarithmic layer, which is consistent with the wall-function approach used here [71]. Averages are obtained over at least three convective times, which are based on the distance between the injection point and the outlet.

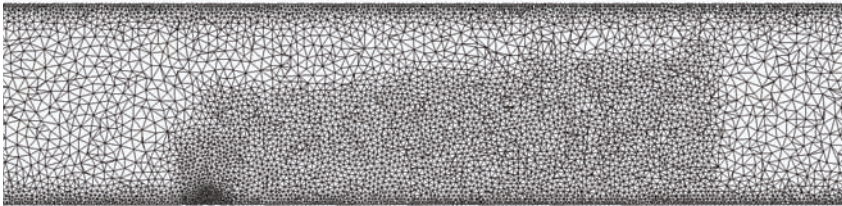


Figure 8.17: Cross-section (midplane) of the mesh used for the Euler-Euler simulations.

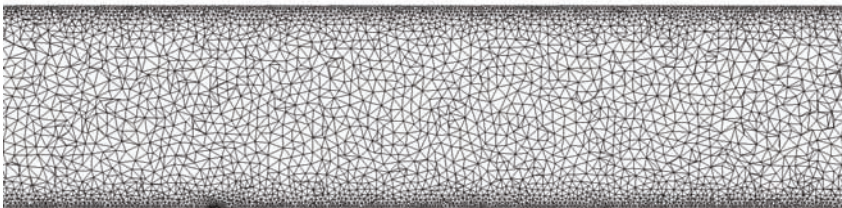


Figure 8.18: Cross-section (midplane) of the mesh used for the Euler-Lagrange simulations.

8.7 Results

Results are presented in two parts: the first focuses on qualitative observations of instantaneous properties of the flow field and spray behaviour (section 8.7.1). The second is dedicated to a comparison of LES averaged quantities with experimental data (section 8.7.2).

8.7.1 Flow and spray topology

Figures 8.19 and 8.20 show the velocity field and spray topology on the mid-plane of the domain. In the EL case, particles inside a 1 mm slab in front of the mid-plane are visualized by a black dot. In the EE case, the location of the spray plume is visualized by iso-contours of the liquid volume flux.

In terms of jet trajectory and penetration height of the developed spray plume, there is a good

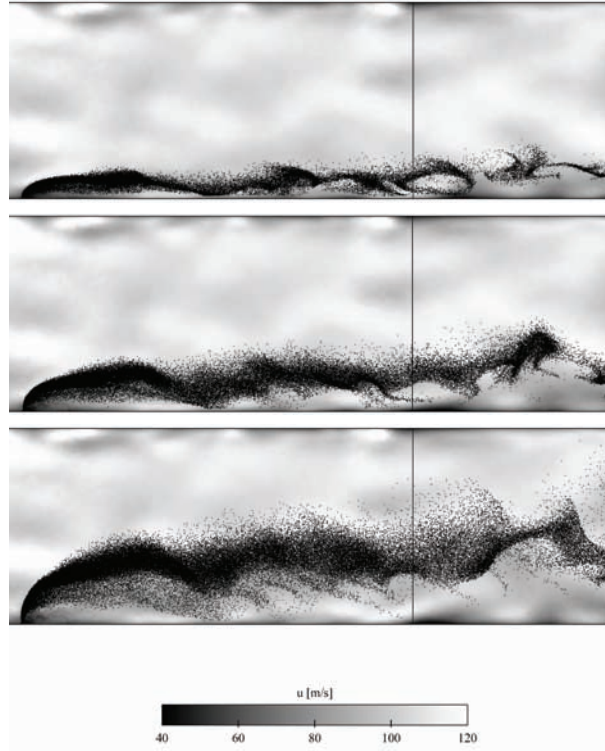


Figure 8.19: *Euler-Lagrange results for cases 1, 2 and 3: instantaneous axial gaseous velocity field on the plane $y = 0$, overlaid with the positions of Lagrangian droplets in a neighbourhood of 1 mm to this plane. Cases from top to bottom: $q = 2$, $q = 6$, $q = 18$. The black vertical line marks the distance of 80 mm from the injection point.*

agreement between EL and EE. The effect of momentum flux ratio is predicted correctly: the spray is attached to the wall at a certain distance downstream of the injection for $q = 2$ (top image in figure 8.19) and is clearly detached for $q = 18$ (bottom image in figure 8.19). In the Lagrangian droplet field, for higher momentum flux ratios, the relatively sparse spray issued by the surface breakup model can be distinguished from the denser regions of the main jet. Interaction with turbulence is quite pronounced in the EL results, where droplets are entrained by the resolved turbulent structures of the LES. Spray fluctuations in the EE results are less developed. This may in part be related to the numerical scheme's low temporal and spatial order. A major portion of the lacking fluctuation levels are, however, a natural consequence of the mesoscopic approach, which does not contain fluctuations due to the random uncorrelated motion. This part has been shown to be non-negligible, for instance by Riber [124], but also in the present work, as shown in section 11.3.3.

Another important insight on the spray distribution can be gained by considering transverse cross-sections of the spray plume at a downstream distance of 80 mm. The spray is visualized by iso-contours of the liquid volume flux. In the EL case, shown in figure 8.21, these iso-contours are obtained by averaging over a short time interval to obtain smooth curves. For EE simulations, instantaneous fields are considered, as shown in figure 8.22. For the case $q = 6$, a

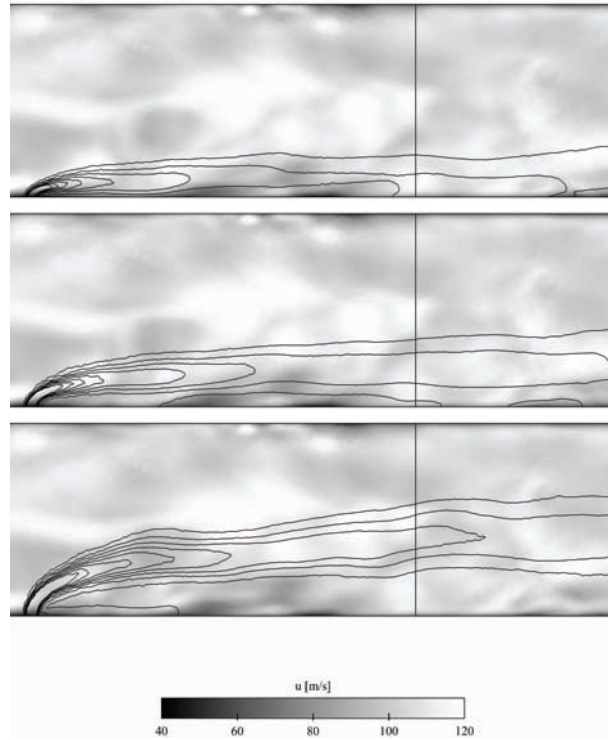


Figure 8.20: Euler-Euler results for cases 7, 8 and 9: instantaneous axial gaseous velocity field on the plane $y = 0$, overlaid with iso-contours of liquid volume flux Φ_l . Cases from top to bottom: $q = 2$, $q = 6$, $q = 18$. The black vertical line marks the distance of 80 mm from the injection point.

similar plot is available from the publication of Becker et al. [11], which is shown for qualitative comparison. EE and EL results are reasonably similar and for the case $q = 6$, they match the experimental data. As the most notable difference, EL isocontours of the liquid volume flux are vertically elongated while their EE counterparts have a round shape. This can be attributed to the influence of the ballistic sorting mechanism that vertically separates droplet trajectories of different size classes in EL. EE results appear to be more realistic in this respect. Note the presence of droplet-wall interaction in the lower peripheral regions of the spray plume, observed for the cases $q = 2$ and $q = 6$, which is consistent with experimental results.

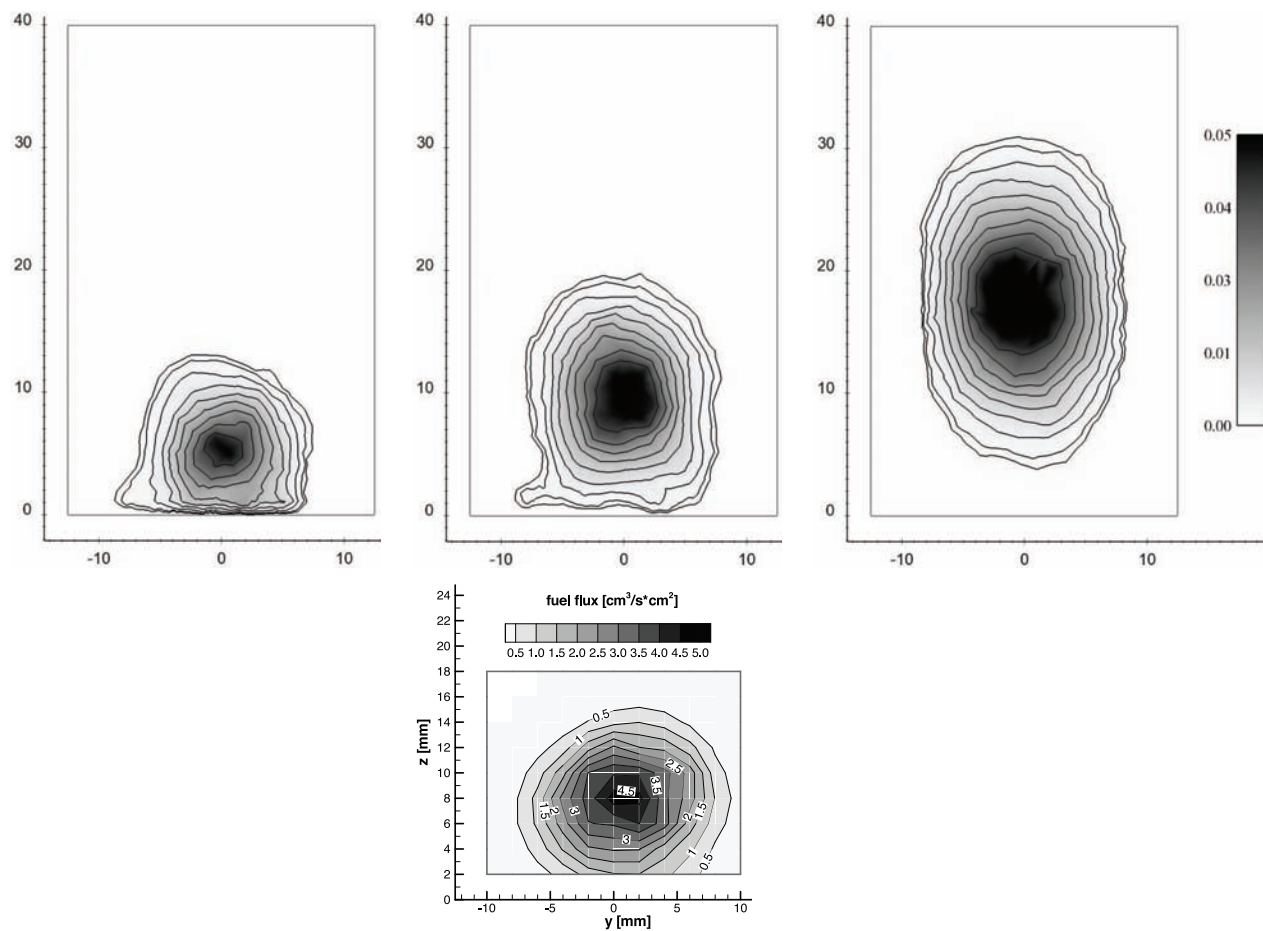


Figure 8.21: Euler-Lagrange results for cases 1, 2 and 3: Iso-contours of the liquid volume flux Φ_l [$\text{m}^3/(\text{s m}^2)$] on the plane $x = 80$ mm. Cases from left to right: $q = 2$, $q = 6$, $q = 18$. Bottom row: liquid volume flux [$\text{cm}^3/(\text{s cm}^2)$] diagram from experimental data (case: $q = 6$) by Becker et al. [11] for qualitative comparison.

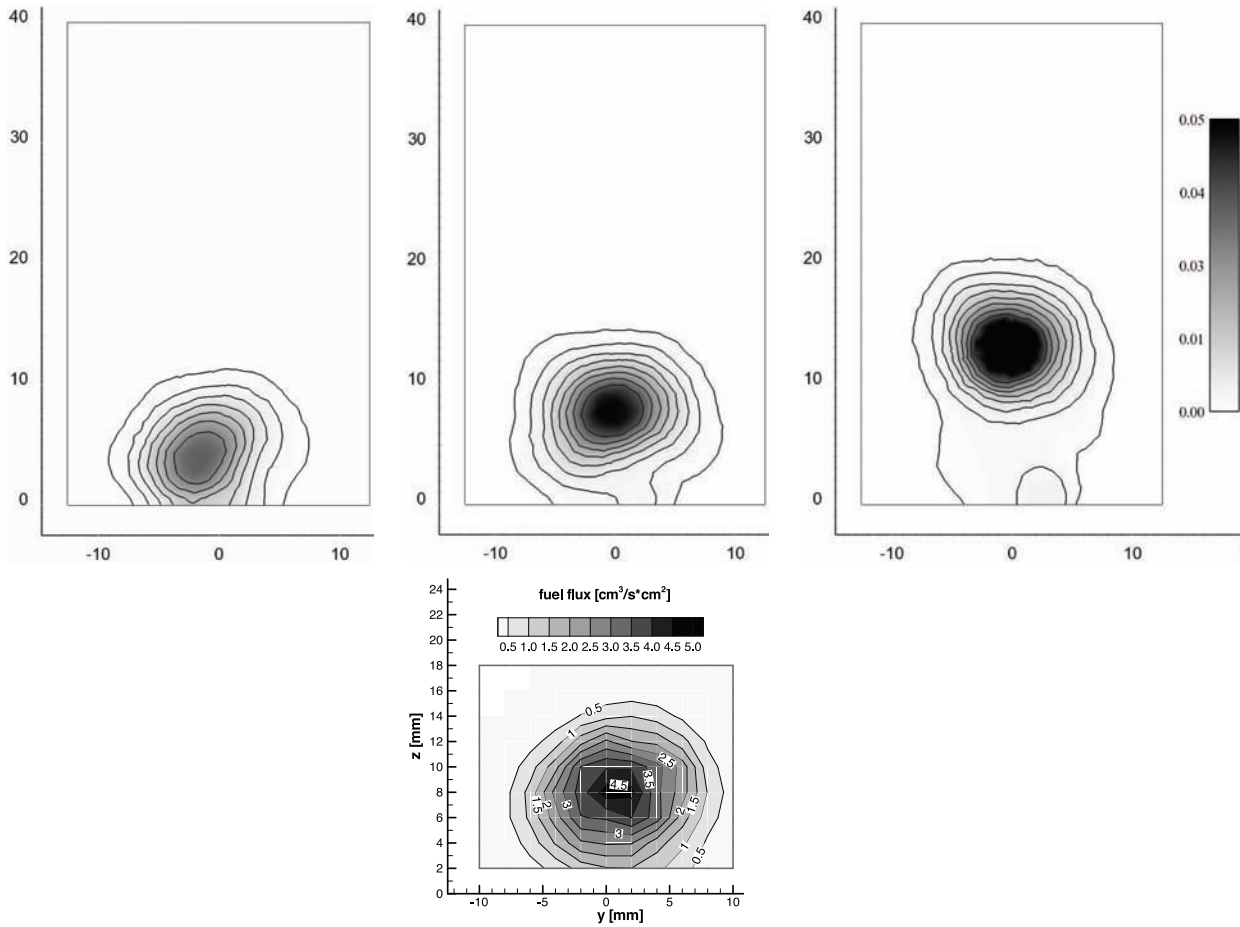


Figure 8.22: Euler-Euler results for cases 7, 8 and 9. Iso-contours of the liquid volume flux Φ_l [m³/(s·m²)] on the plane $x = 80$ mm. Cases from left to right: $q = 2$, $q = 6$, $q = 18$. Bottom row: liquid volume flux [cm³/(s·cm²)] diagram from experimental data (case: $q = 6$) by Becker et al. [11] for qualitative comparison.

8.7.2 Comparison of averaged results

This section compares LES and measurement data at a downstream location of 80 mm (the same position as the cross-sections previously discussed). Data is obtained at different wall distances and then averaged in transverse (y -) direction as illustrated in figure 8.23. Two quantities are considered: the liquid volume flux Φ_l and the Sauter mean diameter. For the latter, the values to be averaged along y are additionally weighted by the local liquid volume flux in order to remove the influence of regions with very few droplets. These procedures are equivalent to the post-processing of Becker et al. [11].

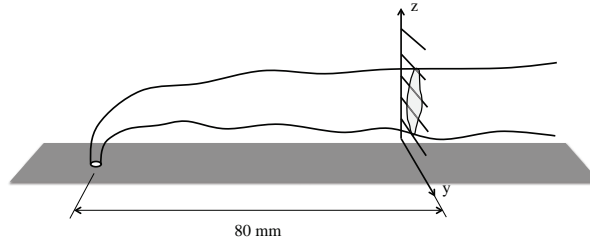


Figure 8.23: Sketch of the different z -locations used for averaging operations (in y -direction) at a downstream position or $x = 80\text{ mm}$.

First, EE and EL are compared using the liquid column model for both formulations. The maxima of the average fluxes, shown in figure 8.24, agree well with the experiment for all momentum flux ratios in the EE case. In the EL results, the flux maxima are shifted slightly upwards in comparison to both EE and the experiment. As the law for particle drag in the column region is identical in the two cases, the discrepancy is likely to originate from the zone directly after the column breakup point where particle drag is not correctly predicted (see section 8.2.1). The difference between EE and EL is due to the use of the BIM model for Eulerian simulations: in EL, more air is entrained in the dense spray region after column breakup leading to lowered particle drag, which is not the case for the artificially diluted spray in the EE simulations.

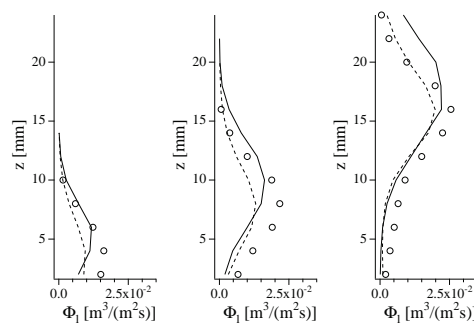


Figure 8.24: Liquid volume flux Φ_l at a downstream location of $x = 80\text{ mm}$, over the wall-normal distance z . Comparison of experimental data [11] ($\circ\circ\circ$), Euler-Lagrange simulation results obtained with the column model (cases 1, 2 and 3) (—) and Euler-Euler results with the column model (cases 7, 8 and 9) (- - -).

The spatial distribution of the Sauter mean diameter is shown in figure 8.25. In the EL results, the SMD at the z -coordinate of the maximum liquid volume flux is correct in all cases. Above and below this wall-distance, discrepancies range from minor for $q = 18$ to pronounced for $q = 2$. In all cases, the evolution of SMD over z is steeper than in the experiment, which shows that the extent to which ballistic separation of trajectories (which still occurs after the point of liq-

uid column breakup) is governing the diameter distribution is over-estimated. An additional aspect is revealed by the experimental curve for the case of $q = 2$. Here, the SMD increases towards the wall, which is explained by Becker et al. [11] with the influence of the boundary layer: when products of the column breakup encounter the reduced gaseous velocities of the boundary layer instead of the freestream, the resulting far-field SMD is larger. Clearly, this effect is not captured by the modeling approach used on this work. The EE diameter profiles agree with experimental data between the wall and the point of maximum liquid volume flux. Above this point, the diameter profile falls off. This is a consequence of the Eulerian approach, where regions without droplets are characterized by a near-zero value for droplet diameter. In the LJCF, the largest diameters are found near the upper spray boundary, which should lead to a sharp transition towards the neighbouring near-zero values. The actual transition is smoothed out, which is enhanced by turbulent mixing. This effect is limited to the outer regions of the spray and does not affect the quality in the regions of high volume flux.

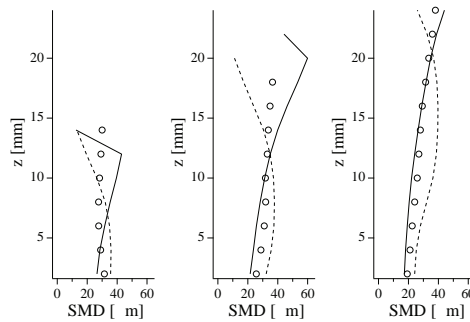


Figure 8.25: Sauter mean diameter profiles at a downstream location of $x = 80$ mm, over the wall-normal distance z . Comparison of experimental data [11] ($\circ \circ \circ$), Euler-Lagrange simulation results obtained with the column model (cases 1, 2 and 3) (—) and Euler-Euler results with the column model (cases 7, 8 and 9) (- - -).

To assess the improvement contributed by the liquid column model, EL and EE results are considered separately, each time comparing results obtained with and without the model. In the case of EL, presented in figure 8.26, the wall distance of the maximum liquid volume flux is either slightly over-estimated (with the column model), or slightly under-estimated without it. In the EE results, the wall-normal distance of the liquid volume flux maximum is well predicted with the column model and strongly under-estimated without model. When comparing the slight influence of the model for EL (figure 8.26) with the significant effect observed for EE (figure 8.28), it becomes clear that the numerical approach influences the result. This supports the previous conclusion that the EL method creates a strong air entrainment in dense regions resulting in reduced particle drag, an effect which does not affect the artificially diluted EE injection (BIM method).

Considering the SMD distribution in the EL results (figure 8.27), the column model induces slight but significant changes: it reduces the gradient of the SMD distribution, indicating that the ballistic sorting effect is reduced, which brings the results nearer to the behavior observed in the experiment. In particular for $q = 18$, this results in a better prediction of SMD in the area of maximum liquid volume flux.

In the EE results (figure 8.29), there is a vertical shift of the otherwise identical SMD profiles by the amount the penetration height changes with the introduction of the column model.

For both EE and EL, at momentum flux ratios of $q = 2$ (or lower), the liquid column model no

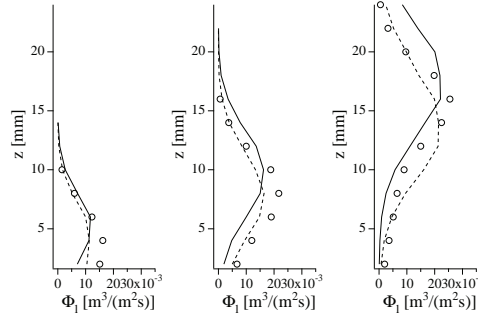


Figure 8.26: Liquid volume flux Φ_l at a downstream location of $x = 80$ mm, over the wall-normal distance z . Comparison of experimental data [11] ($\circ \circ \circ$), Euler-Lagrange simulation results obtained with the column model (cases 1, 2 and 3) (—) and without the column model (cases 4, 5 and 6) (- -).

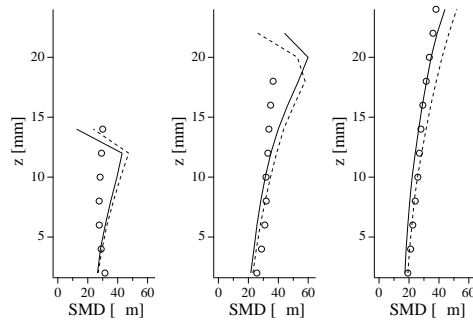


Figure 8.27: Sauter mean diameter profiles at a downstream location of $x = 80$ mm, over the wall-normal distance z . Comparison of experimental data [11] ($\circ \circ \circ$), Euler-Lagrange simulation results obtained with the column model (cases 1, 2 and 3) (—) and without the column model (cases 4, 5 and 6) (- -).

longer results in significant changes (figures 8.26, 8.27, 8.28 and 8.29): this is due to the diminishing length of the liquid column for low values of q . Inversely, the model has an increasingly positive effect for high momentum flux ratios ($q = 6$ and higher), where the liquid column is an important part of the physics.

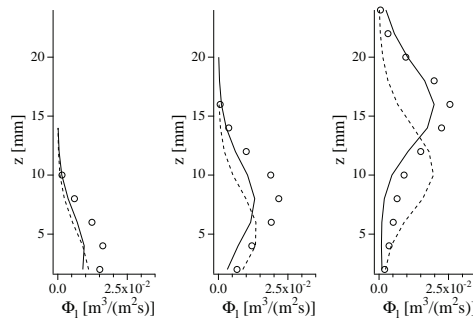


Figure 8.28: Liquid volume flux Φ_l at a downstream location of $x = 80$ mm, over the wall-normal distance z . Comparison of experimental data [11] ($\circ \circ \circ$), Euler-Euler simulation results obtained with the column model (cases 7, 8 and 9) (—) and without the column model (cases 10, 11 and 12) (- -).

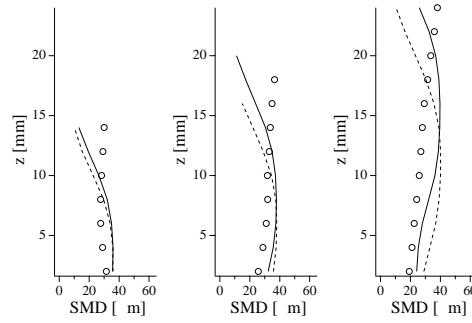


Figure 8.29: Sauter mean diameter profiles at a downstream location of $x = 80$ mm, over the wall-normal distance z . Comparison of experimental data [11] ($\circ\circ\circ$), Euler-Euler simulation results obtained with the column model (cases 7, 8 and 9) (—) and without the column model (cases 10, 11 and 12) (- - -).

8.8 Computational cost

The cost in terms of CPU time associated with EE and EL is an important part of the comparison between both methods. For the EL simulations, it is case dependent as the number of particles in the simulation differs between approx. 300 000 for $q = 2$ and 800 000 for $q=18$. The associated cost amounts to 2 200 s and 2 800 s respectively per convective time. In the EE simulations, CPU time is case independent but with 10 000 s per convective time, it is higher than in all EL cases. This is partly due to the increased grid resolution in the area of the spray plume that is not necessary for EL (see section 8.6). All CPU times were obtained on 32 processors of a IBM JS-21 cluster.

Note that performance on massively parallel architectures becomes important for large, industrial-scale simulations. Parallelization of EE is straightforward, since it relies on the same solver structure as the gaseous phase. The EL approach additionally needs to take into account (dynamic) particle load balancing to ensure the parallel efficiency of the computation [49] so that the present conclusion may not hold on thousands of processors.

8.9 Conclusion

Large-eddy simulations of a liquid jet in a gaseous crossflow have been carried out and compared to experimental data. Euler-Lagrange and Euler-Euler methods have been employed for the liquid phase. These formulations may not handle dense spray regions in the near-field of the injection and a model based on empirical correlations is needed to predict the liquid column trajectory and breakup point.

For the implementation of this model, different techniques are necessary for Eulerian and Lagrangian approaches. In the Eulerian framework, numerical difficulties are identified. A method based on the artificial broadening of the injection region (BIM) that effectively solves these problems is proposed. It furthermore allows to reconstruct variable diameter fields in the far-field by applying a spatial diameter evolution at the injection.

The evaluation of the results includes the comparison between Eulerian and Lagrangian simulations and the influence of the column model in either case. Good agreement in terms of penetration height and diameter evolution is obtained for Lagrangian and Eulerian simulations with the column model.

The positive influence of the column model increases with the momentum flux ratios (i.e. increasing jet velocities). It leads to a better prediction of penetration height and, in particular for Lagrangian simulations, to a better agreement of the spatial diameter distribution with experimental data.

In terms of computational cost, the case considered here reveals a clear advantage for the Lagrangian methods.

8.10 Tables

Inlet	
BC type:	Turbulence injection
Temperature	290 K
Velocity	Profiles from precursor simulation (Bulk velocity $u_b = 100 \text{ m/s}$)
Outlet	
BC type:	Non-reflective pressure outlet condition
Pressure	6 bar
Walls	
BC type:	Adiabatic wall laws, slip-wall formulation

Table 8.4: Boundary conditions for the gaseous phase

Numerical scheme (gas phase)	Lax Wendroff
Scheme spatial precision	2nd order
Scheme temporal precision	2nd order
Numerical scheme (liquid phase)	PSI
Scheme spatial precision	2nd order
Scheme temporal precision	1st order
Liquid phase coupling terms	two-way-coupling evaporation no model for the random uncorr. motion
SGS model (gas)	standard Smagorinsky
SGS model (liquid)	Yoshizawa + Smagorinsky [100]
Artificial viscosity (gas)	Colin sensor [32]
2nd order coefficient	0.1
4th order coefficient	0.08
Artificial viscosity (liquid)	Colin sensor [32]
2nd order coefficient	0.05
4th order coefficient	0.005

Table 8.5: Numerical parameters used in the Euler-Euler simulations

Numerical scheme (gas phase)	Lax Wendroff
Scheme spatial precision	2nd order
Scheme temporal precision	2nd order
Liquid phase coupling	two-way-coupling evaporation
Interpolation method	Taylor
Phys. particles per parcel	1
SGS model (gas)	standard Smagorinsky
Artificial viscosity (gas)	Colin sensor [32]
2nd order coefficient	0.1
4th order coefficient	0.08

Table 8.6: Numerical parameters used in the Euler-Lagrange simulations

Lagrangian injection parameters						
Case #	1	2	3	4	5	6
q	2	6	18	2	6	18
Mass flux [g/s]	1.7	2.95	5.11	1.7	2.95	5.11
Injection velocity [m/s]	13.46	23.31	40.38	13.46	23.3	40.38
Droplet temp. [K]				275		
Liquid phase density [kg/m^3]				795		
particle size distrib.	log-normal, fitted to exp. data (fig 8.6)					
Mean droplet diam.				27.31 10^{-6} m		
Standard deviation				8.35 10^{-6} m		
Minimum diameter				12.35 10^{-6} m		
Maximum diameter				71.63 10^{-6} m		
Injection type	Disk					
Disk diameter	0.45 mm (original orifice diameter)					
Column model	yes			no		

Table 8.7: Injection conditions of the Euler-Lagrange cases

Eulerian injection parameters						
Case #	7	8	9	10	11	12
q	2	6	18	2	6	18
Mass flux [g/s]	1.7	2.95	5.11	1.7	2.95	5.11
Injection velocity [m/s]	13.46	23.31	40.38	13.46	23.3	40.38
Droplet inj. temp. [K]				275		
Liquid phase density [kg/m^3]				795		
Size distrib.	Spatial distrib. (fig 8.9), derived from exp. data					
Inlet condition	Dirichlet-type boundary cond. on the injection patch					
Liquid vol. fraction at inlet				0.04		
Disk diameter	2.25 mm (5 times the original orifice diameter)					
Column model	yes			no		

Table 8.8: Injection conditions of the Euler-Euler cases

Part IV

Application to an aeronautical multipoint injector

Chapter 9

Description of the TLC configuration

Contents

9.1	Introduction	183
9.2	The SNECMA staged premixing swirler	183
9.2.1	Geometry	183
9.2.2	Injection of liquid fuel	185
9.3	The ONERA non-reacting test bench	185
9.3.1	Measurement methods	186
9.4	The numerical setup	187
9.4.1	Modifications of the original geometry	187
9.4.2	The computational grid	188

9.1 Introduction

The final application of this thesis is an aeronautical premixing swirler with multipoint injection. This device is a prototype manufactured by SNECMA moteurs, and has been subject to several experimental and numerical studies in the TLC (for “Towards Lean Combustion”) project of the 6th framework programme of the European Union. The configuration is therefore referred to as “TLC configuration” throughout this manuscript.

9.2 The SNECMA staged premixing swirler

9.2.1 Geometry

An isolated, cut-away view of the premixing swirler is shown in figure 9.1. It represents one of around 20 injectors that are typically mounted on the upstream wall of an annular combustion chamber of an aero-engine. It is a staged design with the objective to divide fuel injection and premixing in two separately controllable zones, in order to allow the optimization of the system for different operating points (see chapter 1 for a detailed explanation). The device is thus composed of two stages, that can be identified by two conical “bowls”, where the central, pilot bowl is nested inside the main stage bowl.

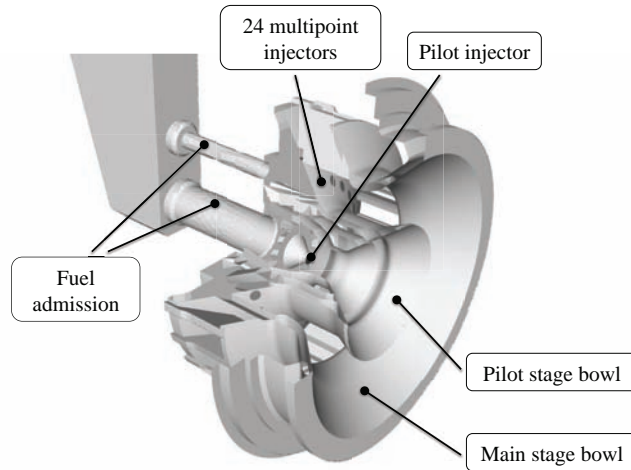


Figure 9.1: *Staged premixing swirler, cut-away view.*

The air traverses the configuration from the plenum through a series of swirlers, an arrangement of channels, divided by guide vanes, that are inclined relative to the main axis and impose a swirling motion to the flow. Figure 9.2 presents a transparent view, highlighting the three swirler stages. Two are of radial type and lead into the pilot bowl. While the innermost swirler discharges into the pilot bowl at its upstream end, the flow from the second one enters the bowl through a circular slot in the side wall just before the pilot flow exits into the chamber. The third swirler can be considered to be of radial type, although it is slightly inclined, leading the flow into the main stage bowl with a non-zero axial velocity component. All three swirler stages are counter-rotating relative to each one's neighbour, which promotes turbulent mixing in the areas where the flows meet.

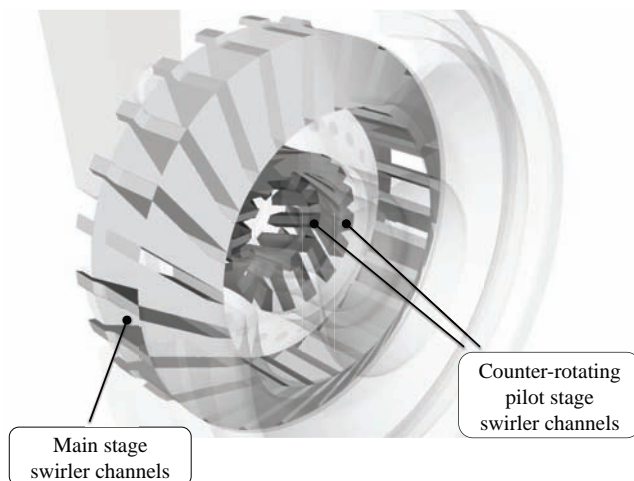


Figure 9.2: *Staged premixing swirler, transparent view with highlighted swirler channels.*

The bulk of the airflow (approx. 90 %) passes through the main swirler stage. The remaining 10 % is divided between the innermost pilot swirler (3 %) and the outer pilot swirler (7%).

9.2.2 Injection of liquid fuel

Liquid fuel is fed into the injector via two separate circuits, which are well visible in figure 9.1. One is connected to the pilot injector, which creates a hollow-cone spray. The pilot fuel atomizer is of the so-called piezo type, featuring a ring of very small orifices on a cone-shaped injector head. The second circuit leads to the multi-point injection system of the main stage, a series of 24 holes located on the inner wall of the main stage, each placed just downstream of a swirler channel's exit. At each point, liquid fuel is injected perpendicularly to the surface through orifices of 0.5 mm in diameter.

The partition of fuel mass fluxes between the pilot stage and the swirler stage can be used as a tool to optimize local equivalence ratio values for different phases of flight. Throughout the present work, the pilot stage will be completely deactivated in order to study the phenomena related to multipoint injection in an isolated way. This, of course, is not a realistic operation condition and only used in the framework of an academic study.

9.3 The ONERA non-reacting test bench

For measurement purposes, the injector described in the preceding section was mounted on various test benches. These include a completely open setup (with the injector directly exiting into the atmosphere) that has been studied experimentally at ONERA DMAE in Toulouse and numerically by Lavedrine [81]. A configuration adapted to reactive experiments has been studied experimentally at ONERA DMPH in Palaiseau [105]. Numerical simulations have been performed by Lavedrine [81] in non-reacting conditions and by Bertier [14] in reacting conditions.

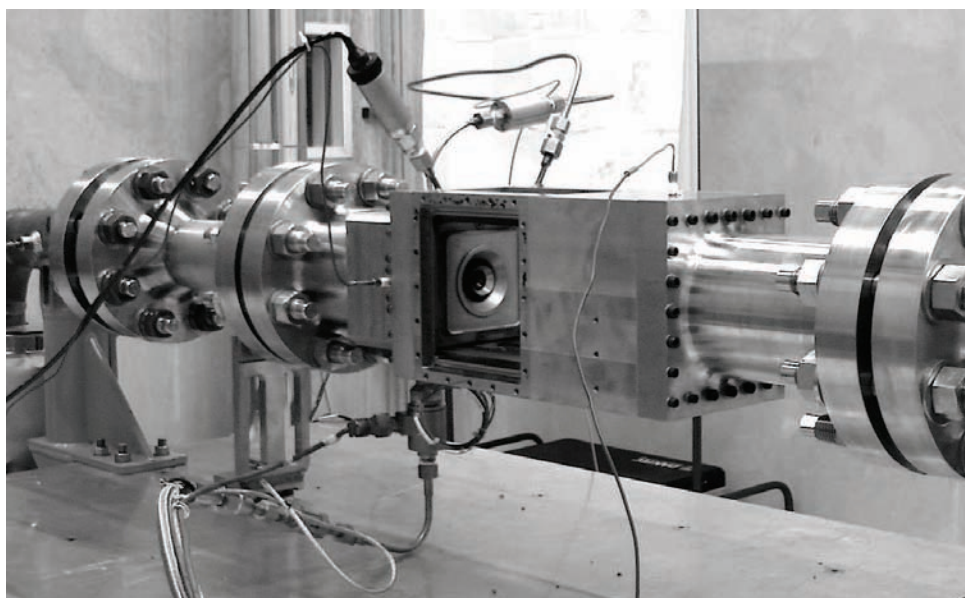


Figure 9.3: *Photography of the installation at the ONERA Fauga-Mauzac center.*

In the present work, a third configuration is considered. It was mounted at the ONERA center at Fauga-Mauzac and allows a detailed study of the non-reacting, two-phase flow [82]. The test bench, pictured in figure 9.3 allows to pressurize and pre-heat the chamber, which is of a simple rectangular shape with a square cross-section, where large observation windows provide optical access for measurements. Air enters through an admission duct that expands into a

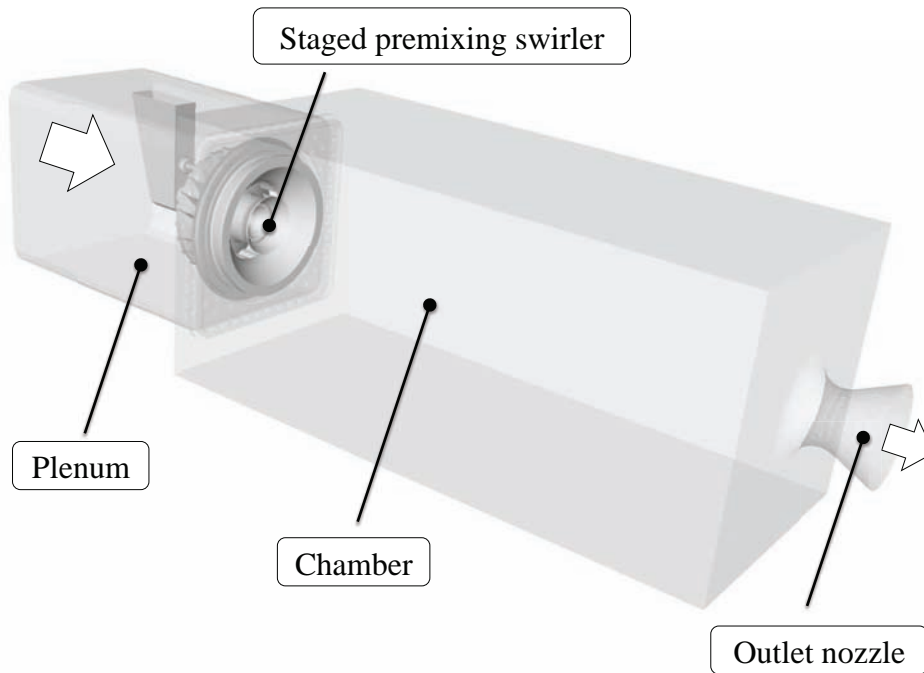


Figure 9.4: *TLC configuration ONERA Fauga-Mauzac*

plenum. The injector is mounted on the dividing wall between this plenum and the chamber. Additionally, this divider is perforated to feed air into cooling films exiting into the chamber at about half the distance between the injector outer diameter and the lateral chamber walls (see figure 9.5). It has to be noted that this film serves no real purpose in the present configuration. It is a remnant of the reacting test bench, where these films are located in direct proximity of the lateral walls and serve as a cooling layer to protect the optical access windows. The chamber exit is formed by a nozzle that reaches supersonic flow at the throat, leading to an acoustically non-reflecting outflow.

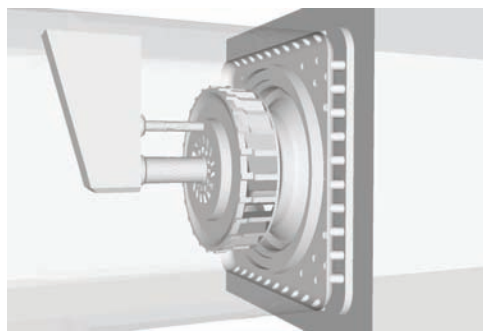


Figure 9.5: *TLC configuration ONERA Fauga-Mauzac - view from the plenum*

9.3.1 Measurement methods

The test bench was equipped for different measurement techniques briefly described in the following. The goal of these measurements was to obtain data on:

- The gaseous phase velocity, using a LDA technique

- The droplet velocity and diameter, using a PDA technique
- The local droplet size distribution, using laser diffraction spectroscopy
- The spatial distribution liquid volume flux, using a patternator technique

The **LDA** (for Laser Doppler Anemometry) measurement method uses a pair of coherent laser beams that are crossed at the location where velocity data is measured. At this location, the beams form interference fringes, which illuminate particles that cross the pattern periodically. The frequency of this light signal can be detected and translated into a velocity. This value corresponds to the velocity component perpendicular to the fringes and the measurement has to be repeated to obtain other velocity components. The gaseous flow is seeded with particles of a very low Stokes number in order to minimize errors due to droplet inertia and to exclude two-way coupling effects.

The **PDA** (for Phase Doppler Anemometry) is an extension of the LDA technique, first proposed by Durst et al. [40], that uses two detectors for the light scattered by the particles, arranged at different locations in space. The resulting phase shift between both doppler signals can be translated into a diameter information of the recorded particle.

The **laser diffraction spectroscopy** uses a laser beam to illuminate the spray. For a single droplet, in close forward direction, diffraction patterns are observed that can be related to the size of a spherical particle using Mie theory [95]. For a polydisperse spray, a complex light intensity distribution is recorded, which can be translated into a droplet size distribution using methods described by Hirleman [62]. The advantage of this technique is that the distribution is obtained instantaneously, from the post-processing of a single image.

The **patternator technique** is based on the very simple principle of placing an array of recipients in the direction of spray movement. The spatial distribution of liquid volume flux can be reconstructed by the amount of liquid that is present in each of the recipients.

For additional information, the reader is referred to the TLC report [82] and for theoretical background to the book of Frohn and Roth [47].

9.4 The numerical setup

9.4.1 Modifications of the original geometry

Modifications are made relative to the original geometry in order to make it suitable for computations. These modifications comprise:

- The air exits the chamber through a supersonic nozzle. In order to render the supersonic boundary condition more stable, the narrowest section is followed by a short, gently diverging tube to reliably establish $Ma > 1$ at the actual domain exit. This has no influence on the computed flow as perturbations do not travel upstream towards the sonic throat.
- The cooling films connected to the plenum through slots in the upstream wall of the chamber are modeled with a surrogate geometry, as explained in detail in chapter 7.
- A cooling film located along the circular outer rim of the injector (called “collar perforation”) is entirely replaced by an equivalent inlet condition. The corresponding mass flux is subtracted from the flux prescribed at the plenum.

- All very small scale features are removed from CAD data. This applies for example to very fine gaps, chamfers, etc. that would lead the grid generation algorithm to create diminutive cells.

9.4.2 The computational grid

The computational grid is a cornerstone of the numerical approach and has proven to be a critical contributor to the quality of the results in the present study. Elements describing the importance of particular features of the grid can be found throughout this manuscript. Here, its most important characteristics are summarized and reference the corresponding chapter.

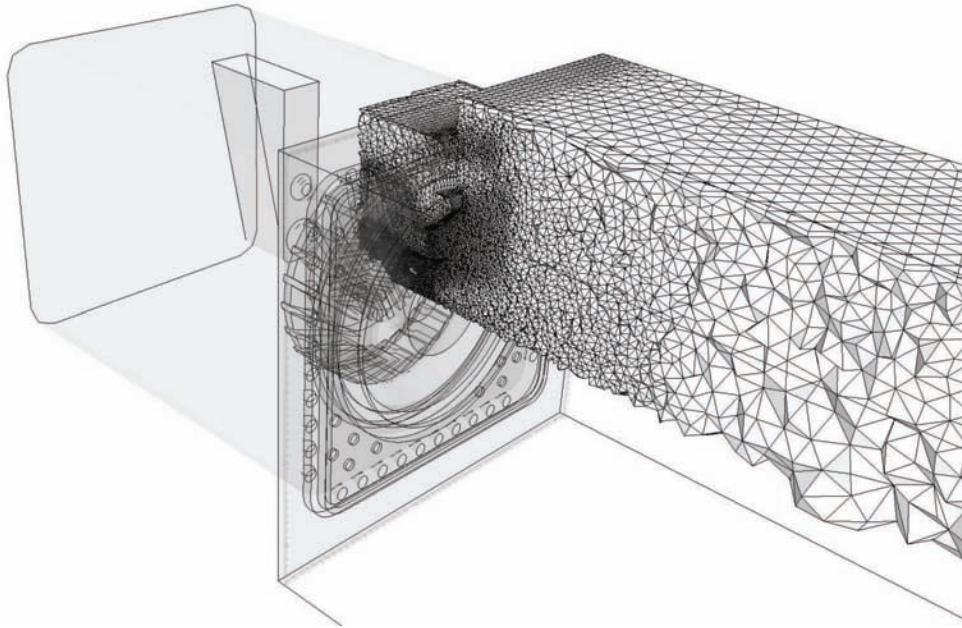


Figure 9.6: *Staged premixing swirler, transparent view with highlighted swirler channels.*

Figure 9.6 shows an overview of the mesh. It is of unstructured, hybrid type, composed of tetrahedral, prismatic and pyramidal elements. The (triangular) prisms form a single, closed layer in all regions where wall functions are used to model the turbulent boundary layer. This layer is necessary for the application of wall functions in the no-slip formulation (see section 6.2.6 for details) but is also advantageous in terms of the overall number of cells, because the near-wall grid refinement can easily be controlled by adapting the prism aspect ratio without leading to an excessive number of near-wall tetraedra. A single layer is chosen because it allows consistent meshing in complex geometries including sharp edges, when multiple layers tend to be more heavily deformed. Figure 9.7 shows a detail of such a prismatic region on the separator between pilot and main stage. Pyramidal elements are used to connect the edge of a prismatic boundary area with an adjacent tetrahedral zone.

The grid has several refined zones inside and downstream the injector. The swirler channels are optimized for the use of wall-functions, with a target for near wall prismatic layer thickness of $y^+ \approx 100$ (see chapter 6 as well as section 10.3.3). Furthermore, the relative grid resolution in the volume of the swirler channels is kept constant between the swirler stages in order to avoid mass flux imbalances (see chapter 7 for details). The second important area of high grid resolution is located in the pilot and main bowl, stretching outwards in areas where the main

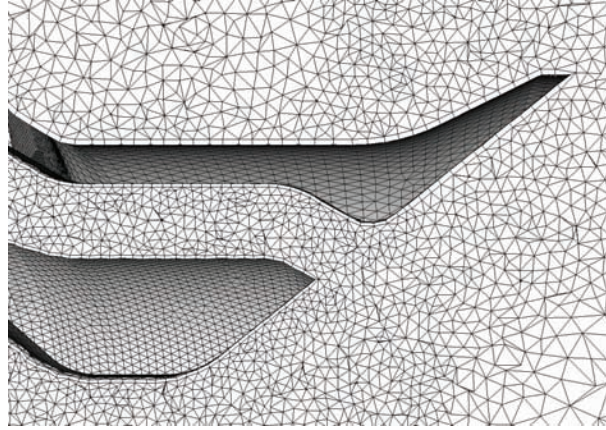


Figure 9.7: *Staged premixing swirler, transparent view with highlighted swirler channels.*

Mesh type	unstructured, hybrid
Cell types	tetraedrae (domain volume) prisms (domain boundary, regions intended for wall-functions) pyramids (link between prisms and pure tetra regions)
Number of grid nodes	1 619 357
Number of grid cells	8 540 311
Number of boundary nodes	186 367

Table 9.1: Mesh parameters

shear layers between the counter-rotating swirler stages or between the high-velocity regions and recirculation zones are located. These refinements were adapted successively to accommodate the shear layers over separated boundary layer zones (see chapter 10). Finally, the grid is refined in proximity of the cooling films. Here, the meshing parameters are determined at the creation of the surrogate geometry used in this area to avoid very small-scale geometrical features (see section 7.3 for details of this method).

Grid refinement is significantly relaxed downstream of the high-shear regions at the injector exit as well as inside the plenum. Although resolution inside these zones is insufficient for a proper LES, this coarsening is needed to render the simulation feasible. The phenomena resolved in these zones are therefore limited to very large scale motion (like the central recirculation zone) or acoustics effects in the case of the plenum.

The only refinement related to the two-phase simulations is a local refinement around the multi-point injection. Due to the artificially enlarged injection zone (see sections 8.2.3 and 11.2.1), the resulting cell sizes are close to the surrounding near-wall resolution. The primary spray regions are already sufficiently refined due to the needs of the gaseous phase. The same mesh is used for all calculations presented in this study, both gaseous and two-phase, regardless of the liquid phase approach (EL or EE). Global parameters of this common mesh are summarized in table 9.1.

Chapter 10

Gaseous flow results of the TLC configuration

Contents

10.1 Introduction	191
10.2 Computational setup	191
10.3 Results	193
10.3.1 Instantaneous flow topology	193
10.3.2 Time-averaged results	197
10.3.3 Comparison with experimental data / LES quality	201

10.1 Introduction

This chapter presents the purely gaseous flow in the TLC configuration. The computations carried out in this context serve two main purposes. The first is to establish a correct representation of the gaseous flow field used for subsequent two-phase flow simulations. The second goal is to apply and validate the developments regarding wall-modeling (chapter 6) and pressure drop prediction (chapter 7).

The operating conditions of the experiment at ONERA Fauga-Mauzac [82] mimic a partial load regime of an aero-engine: The chamber is pressurized at 4.37 bar and the air entering the configuration is pre-heated to 473 K. The same operating conditions are used for the two-phase flow described in chapter 11.

10.2 Computational setup

All simulations presented here use the same computational grid, presented in figures 9.6 and 9.7. This grid discretizes the computational domain that has undergone a number of adaptations compared to the real geometry, described in section 9.4.1.

The boundary conditions applied to the gaseous flow are summarized in table 10.1. Inlet and outlet conditions are of characteristic (NSCBC [114]) type. The wall boundary conditions vary

Boundary conditions	
Plenum inlet	Characteristic inlet condition
Collar perforations	Characteristic inlet condition
Outlet	Supersonic outlet condition
Plenum walls	Isothermal no-slip condition
Surrogate geometry of cooling films	isothermal no-slip condition
Exit nozzle walls	Isothermal slip walls
Swirler and chamber walls	Isothermal wall functions (no-slip formulation)
Detached regions of the main swirler stage	adiabatic no-slip walls (see fig. 10.1)

Table 10.1: Boundary conditions of the gaseous flow

Plenum inlet	
Mass flux	0,365 kg/s
Temperature	473 K
Collar perforation	
Mass flux	0,012 kg/s
Temperature	473 K
Walls	
Wall temperature	473 K

Table 10.2: Boundary values, gaseous flow

depending on the zone considered. In regions with attached, turbulent boundary layers, isothermal wall-functions in the no-slip formulation (see chapter 6) are used. No-slip conditions are applied in detached regions of the flow (see figure 10.1) because basic assumptions of the wall-modeling approach do not hold there. No-slip conditions are also used for the surrogate geometry of the cooling films. Finally, slip-wall conditions are applied at the nozzle as they reduce the strain (near-wall gradients) on the numerical scheme. Corresponding boundary values are given in table 10.2.

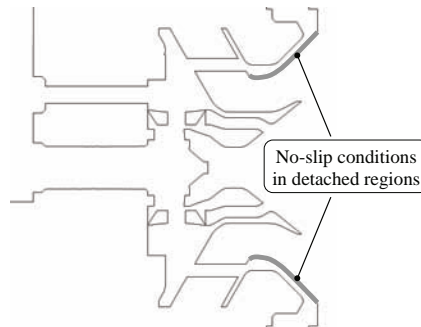


Figure 10.1: Schematic of the zones in detached regions where no-slip conditions are applied instead of wall functions.

The calculation is run with both the Lax-Wendroff and the TTGC scheme. All run parameters, in particular artificial viscosity coefficients, are identical in both cases. The most important numerical parameters are listed in table 10.3.

Numerical scheme	Lax Wendroff (case 1)	TTGC (case 2)
Scheme spatial precision	2nd order	3rd order
Scheme temporal precision	2nd order	3rd order
SGS model	standard Smagorinsky	
Artificial viscosity	Colin sensor [32]	
2nd order coefficient	0.1	
4th order coefficient	0.023	

Table 10.3: Numerical parameters used in the gaseous simulations

10.3 Results

The discussion of the gaseous flow is divided in three parts: first, instantaneous results are used to describe important flow features, which is extended to averaged properties in the second section. The objective of the third part is a quantitative evaluation of the results by comparison to experimental data. It also includes indicators for the quality of the simulation approach. Note that the flow topology is discussed entirely at the example of Lax-Wendroff results (case 1). TTGC results (case 2) are included in the third, quantitative section.

10.3.1 Instantaneous flow topology

The key flow features are schematized in figure 10.2, which shows field of axial velocity on the mid-plane, including annotations: inside the injector main bowl, the flow quickly detaches from the outer walls but remains closely attached to the inner ones (the separator between main- and pilot stage). This boundary layer detachment is an important detail of this particular simulation. A LES with basic wall functions cannot be expected to predict detachment and it is therefore crucial to understand the flow phenomena at hand to carefully adapt the wall treatment accordingly.

Typical for swirled flows, the topology inside the chamber is characterized by a large, central toroidal recirculation zone (CTRZ) [134], [36]. The bulk of the high velocity zones enclosing this recirculation zone is created by the main swirler stage through which 90 % of the total mass flux passes. This flow is strongly swirled and follows approximately the envelope of a cone after entering the chamber. This conical shape is partly due to the curved walls guiding the flow into this direction, and partly due to the swirling movement itself.

The detached flow on the outer swirler walls creates zones of strong shear at the border of the separation bubble, which require fine meshing (insufficient resolution leads to premature re-attachment). As all of the three swirler stages are counter-rotating with respect to the neighbouring ones (which can be observed on the field of tangential velocity in figure 10.3), shear layers also develop downstream of the separators between stages. These shear layers can be visualized through vorticity, shown in figure 10.5. The magnitude of the vorticity (fig. 10.5 left) highlights the said high-shear zones but also a zone of strong vortical activity inside the pilot bowl. The y -component (normal to the mid-plane considered, fig. 10.5 right) allows to identify the sign of the vorticity component (‘direction’ of shear) in the different shear layers.

The particular design of the TLC configuration, and specifically the introduction of an inter-

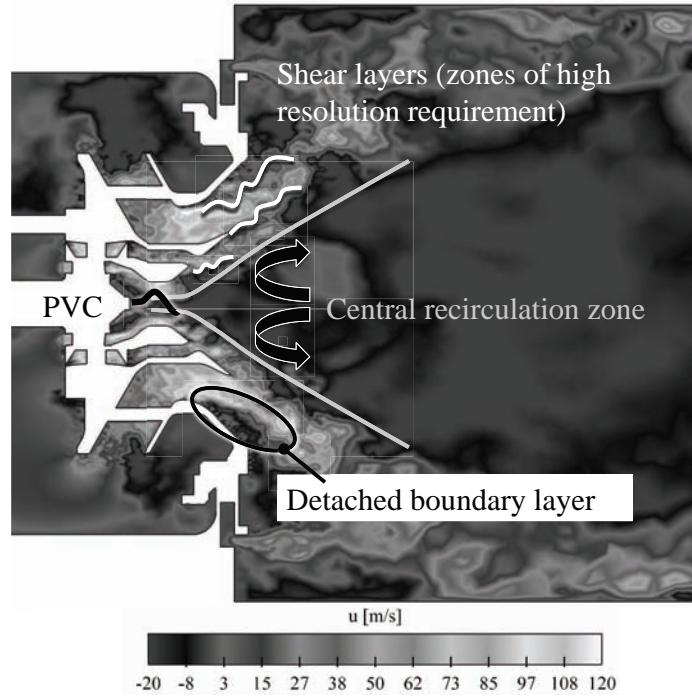


Figure 10.2: Instantaneous axial velocity field on the mid-plane with annotations to highlight key features of the flow field

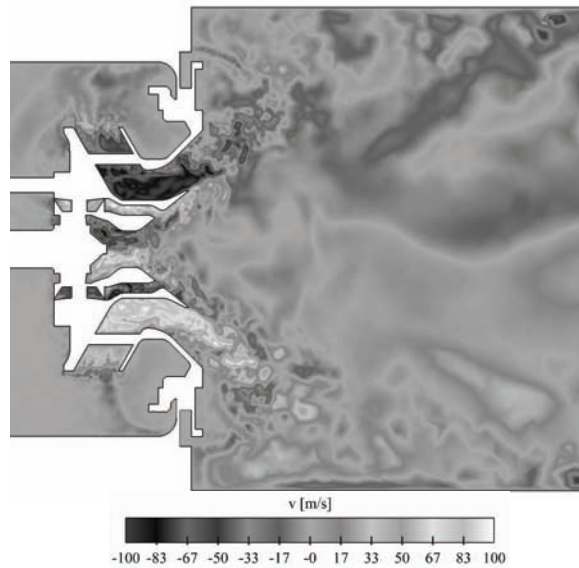


Figure 10.3: Instantaneous tangential velocity field on the mid-plane

mediate, counter-rotating swirler between the main and pilot stages aims at promoting quick mixing inside the swirler. Here, mixing relies on the generation of turbulent structures, which can be visualized by iso-surfaces of the q -criterion [69, 57], shown in figure 10.6. It is defined as:

$$Q = \frac{1}{2} (S_{ij}S_{ij} - Q_{ij}Q_{ij}) > 0 \quad (10.1)$$

where S_{ij} is the rate of strain tensor (equation 2.18) and Q_{ij} is the vorticity tensor

$$Q_{ij} = \frac{1}{2} \left(\frac{\partial u_j}{\partial x_i} - \frac{\partial u_i}{\partial x_j} \right) \quad (10.2)$$

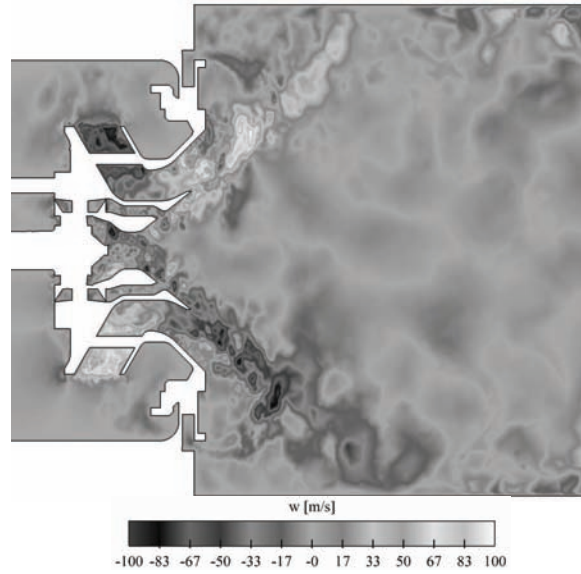


Figure 10.4: *Instantaneous radial velocity field on the mid-plane*

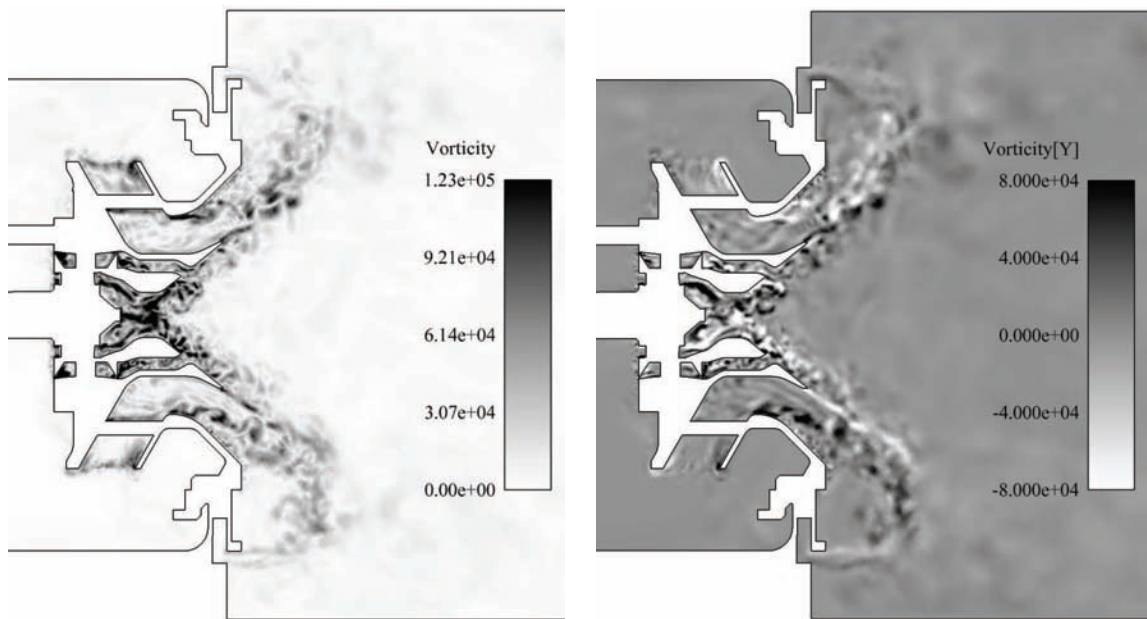


Figure 10.5: *Absolute value (left) of vorticity on the mid-plane $y = 0$, as well as the vorticity component perpendicular to this plane (right).*

Due to the complexity of the flow field, the q -criterion is presented separately for the pilot- and main stages. All structures outside of the zone considered are blanked for clarity. The predominant coherent structures are created as longitudinal vortices from the trailing edge of each swirler guide vane. In the pilot swirler, these structures are convected through the narrowest section and are sustained for a short distance along the CTRZ before losing intensity. In the main swirler stage, the same edge-vortex type of structures is observed. These longitudinal structures (relative to the local direction of flow) remain visible until the onset of boundary layer separation where they are quickly overwhelmed by transverse structures, created by vortex rollup in the shear layer above the separation bubble.

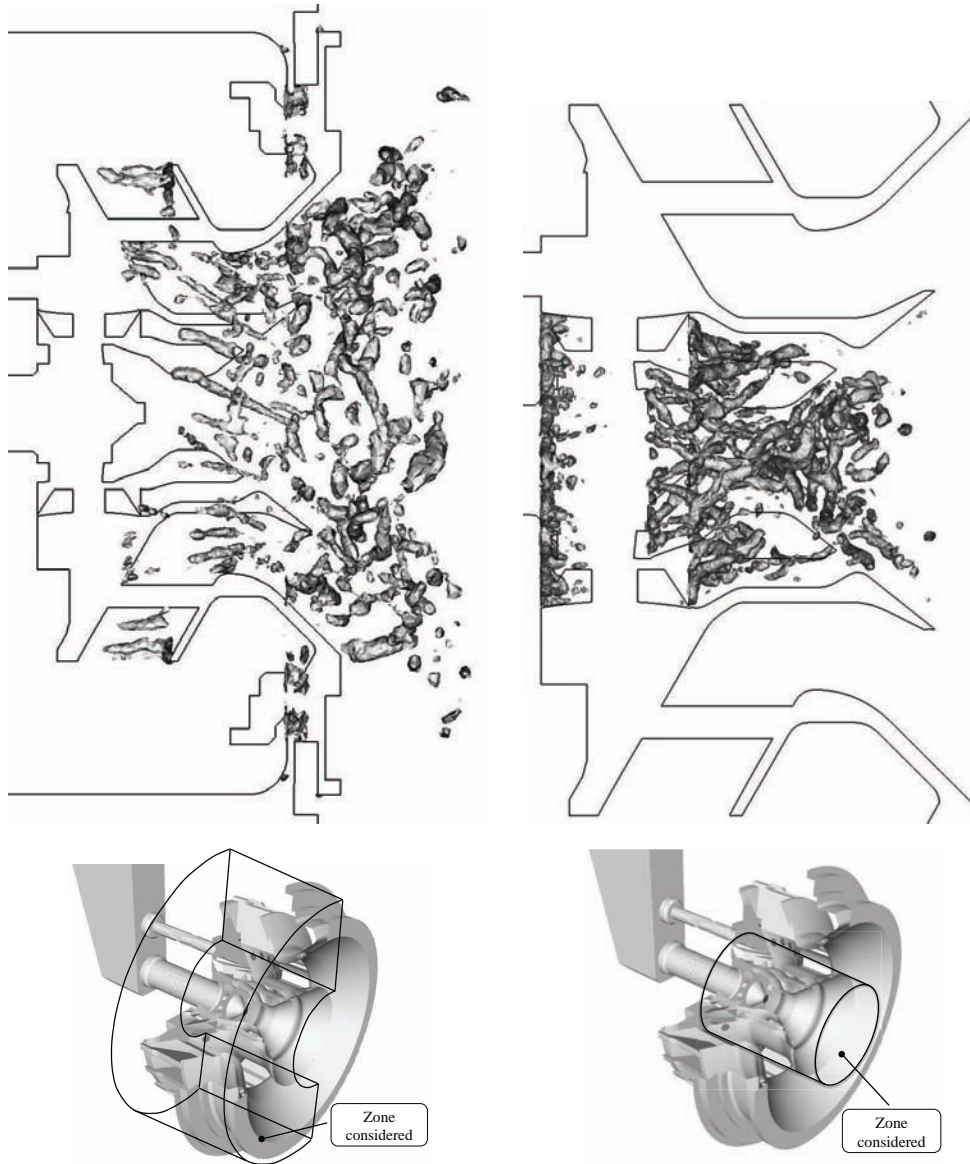


Figure 10.6: Iso surfaces of the q -criterion. Left: iso-surface at 1.210^9 in the main swirler stage (A cylindrical part that encloses the pilot stage as well as all structures behind the mid-plane have been blanked, see schematic below). Right: iso-surface at $3.5 10^9$ in the pilot stage. All structures outside of a central cylindrical region have been blanked.

This interaction of longitudinal structures with the separation region can also be observed on the axial velocity fields on several transverse cross-sections through the injector, shown in figure 10.8. As presented in figure 10.7, four planes $x = \text{const.}$ are extracted at different positions: the first one is located at the exit of the main stage swirler, while the last one is located in the chamber near the upstream wall. On the first plane, the wakes of the main swirler vanes can be distinguished. These wakes with their lower axial velocities form the onset of boundary layer separation (marked by negative axial velocities) that grows on the second and third plane, while the flow between the wakes remains attached longer. On the third plane, the boundary layer is almost completely separated and shows strong deformation created by the rollup of the longitudinal vortices. After entering into the chamber (fourth plane), the cone-shaped flow from the main swirler has already undergone strong radial deformation. As an additional observation, cooling films are clearly visible in the chamber (plane 4), which illustrates the actual flow generated by the ‘surrogate geometry’ (see chapter 7). Furthermore, it is interesting to note the central recirculation zone, which stretches without interruption through the narrowest section

into the pilot bowl.

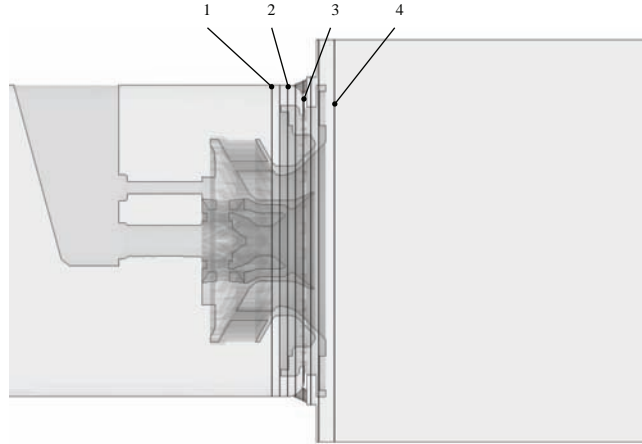


Figure 10.7: Location of the eight transverse cross-sections shown in figure 10.8.

Another typical vortical structure is the so-called ‘precessing vortex core’ (PVC) that is characteristic for swirling flows in combustion chambers [127] [134] but also for vortex breakdown in general [56] [86]. In the TLC configuration, a central vortex can be observed, but it is not a PVC in the classical sense. A pressure iso-surface allows to visualize a strong central vortex in this region, which can be considered the onset of a PVC. Figure 10.9 shows a sequence of such iso-surfaces. It appears that this vortex is at least performing a fluctuating lateral movement that could be interpreted as a precessing behaviour. However, in the narrowest section of the pilot bowl, this vortex is overwhelmed by random turbulence that has been found to be quite intense in this area (see figures 10.6 right and 10.14). Inside the actual chamber, no evidence for a consistent vortex could be found.

10.3.2 Time-averaged results

This section discusses averaged quantities of the flow field. Figure 10.10 shows pseudo-streamlines, created from the averaged velocity field on the mid-plane of the injector. Some flow features appear more clearly than in instantaneous views. In addition to the CTRZ, two recirculation zones can be seen in the upstream corners of the chamber. Inside the pilot bowl, also shown in an enlarged view in the lower part of figure 10.10, a pattern of two counter-rotating, toroidal recirculation zones encloses the cone on which the pilot injector is mounted. Despite the advanced state of convergence, the averaged flow field shows some asymmetry, like for instance the centerline of the CTRZ or the flow pattern in the upstream corners. This can be attributed to the flow meeting obstacles in the plenum before entering the swirler but also the interaction of the swirled primary flow with a chamber of a square cross-section.

Averaged flow-fields of axial, tangential and radial velocity components are presented in figures 10.11, 10.12 and 10.13 respectively. Compared to the instantaneous flow fields, they show additional features: one is the elongated extension of the CTRZ that reaches up to the tip of the pilot injector cone. This feature (also mentioned in section 10.3.1) can be distinguished on the field of mean axial velocity (figure 10.11).

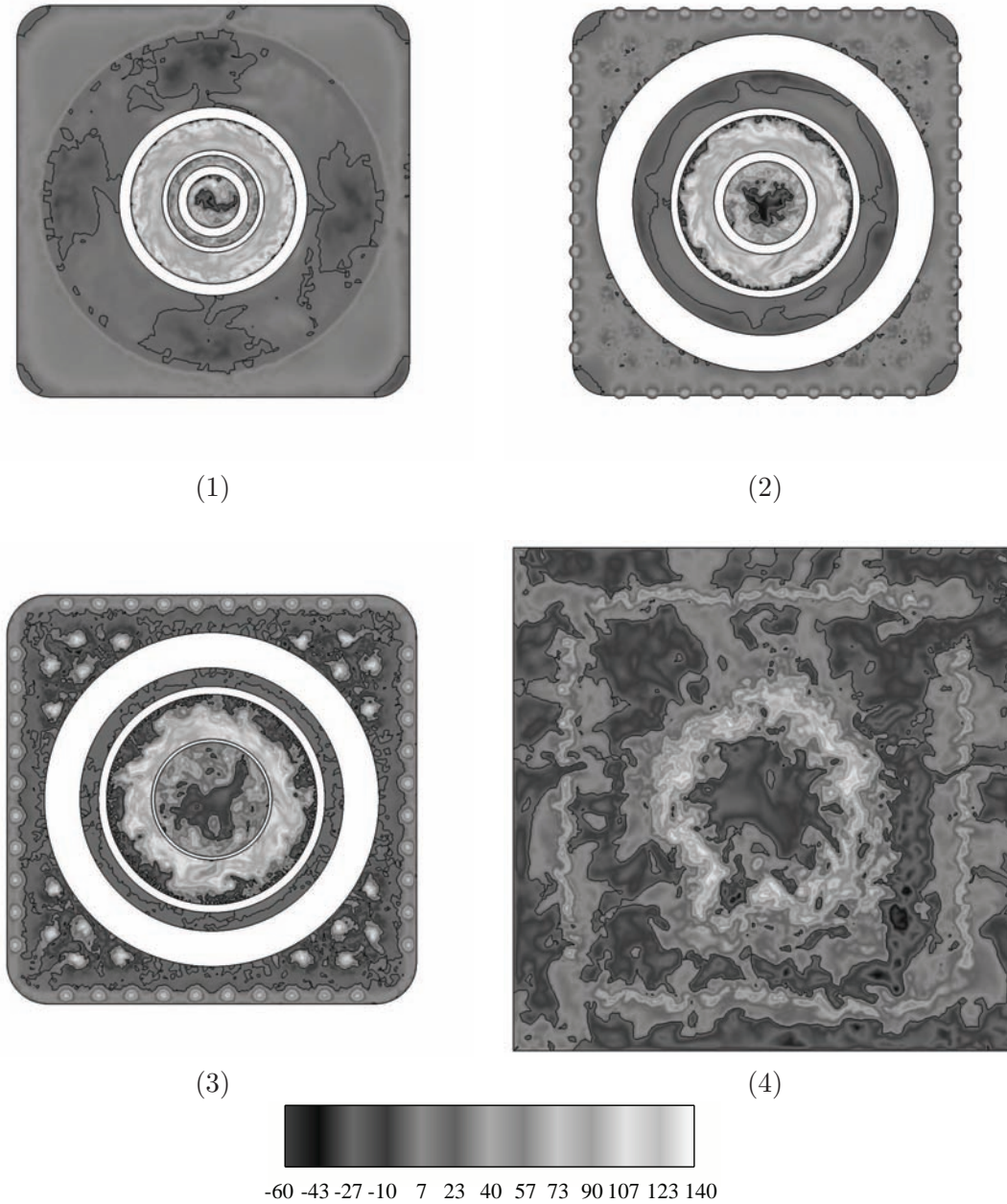


Figure 10.8: Field of axial velocity shown on four transverse cross-sections overlaid with an iso-line of $u = 0$ to mark recirculation regions. The positions of the planes are shown in figure 10.7.

Another detail is the asymmetry between the shapes of the upper and lower separation bubbles inside the main injector bowl (best visible in figure 10.13). This is a visual effect that is due to the flow field being presented on straight cross-sections through a swirling flow, which means that the primary flow is crossing the plane at approximately a 45 degree angle. The periodic velocity maxima and minima near the wall correspond to the wakes of the swirler vanes crossing the mid-plane (see also figure 10.8).

A last point to be noted is a numerical artifact that appears on the averaged fields as point-to-point oscillations near the lateral walls of the chamber. These wiggles are a result of the link between tetraedral and prismatic elements in conjunction with the Lax-Wendroff scheme; they are not observed on results obtained with the TTGC scheme. They are well-controlled in

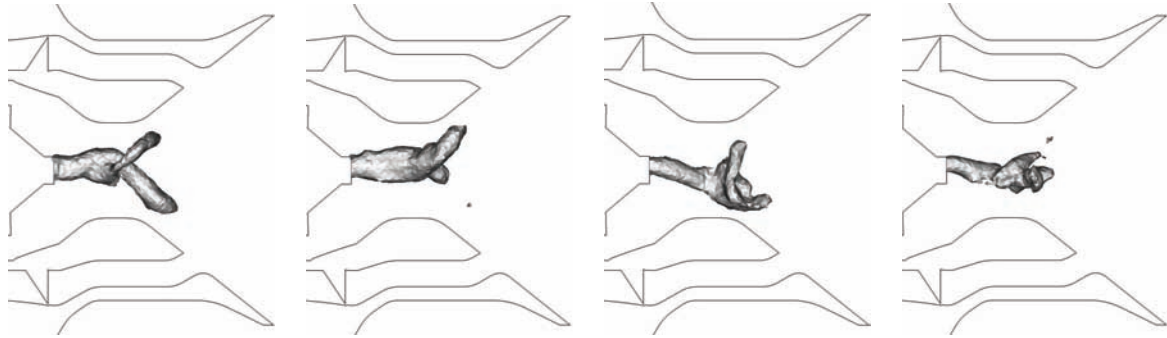


Figure 10.9: Series of instantaneous pressure iso-surfaces to visualize the precessing vortex core (PVC) inside the pilot injector bowl. The Δt between two images in the sequence is approx. 1.43 ms

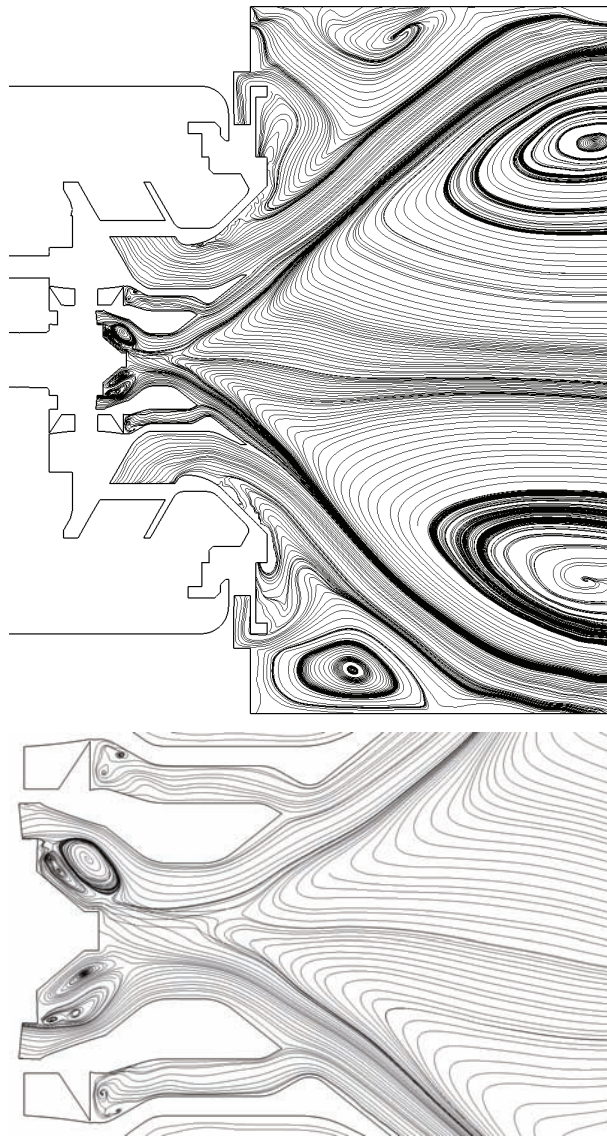


Figure 10.10: Pseudo-streamlines of the averaged velocity field. Top: global view of the injector region. Bottom: detail of the pilot bowl.)

regions of attached flow, such as the entire swirler except on the outer walls of the main stage.

The turbulent fluctuating energy is shown in figure 10.14. As can be expected from the instan-

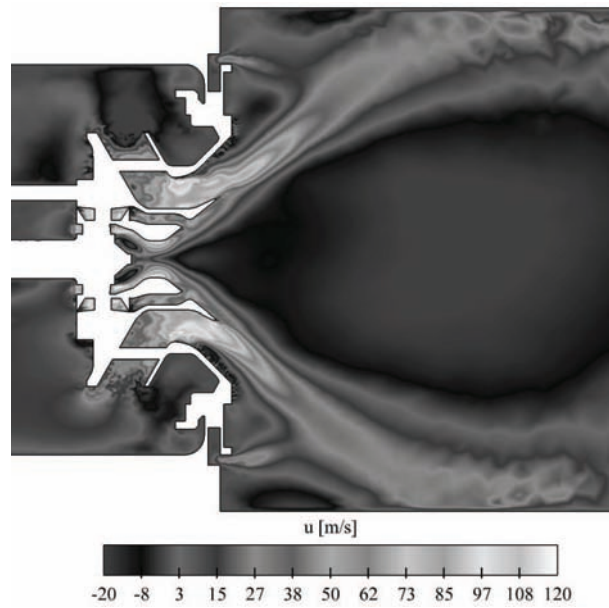


Figure 10.11: *Mean axial velocity field*

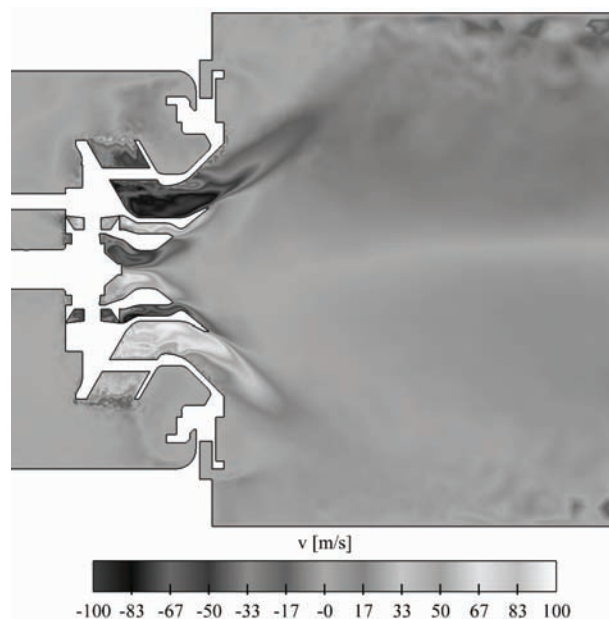


Figure 10.12: *Mean tangential velocity field*

taneous flow fields, there are three major zones of strong fluctuations: the shear layer over the separated boundary layer, the shear layer between the high-speed zones exiting the main swirler and the counter-rotating flow from the pilot stage and finally the narrowest section in the pilot bowl. The latter region is also the zone with the highest fluctuating energy levels in the entire configuration. This can be attributed to the acceleration (and thus stretching) of the turbulence formed inside the pilot bowl, while it passes the narrowed part. As the pilot injector is placed upstream of this region, a very efficient mixing can be expected here. Very low fluctuation levels are observed in the region of the multipoint injection. Therefore, significant turbulent mixing of the spray and evaporated fuel can only be expected after the spray has entered the chamber.

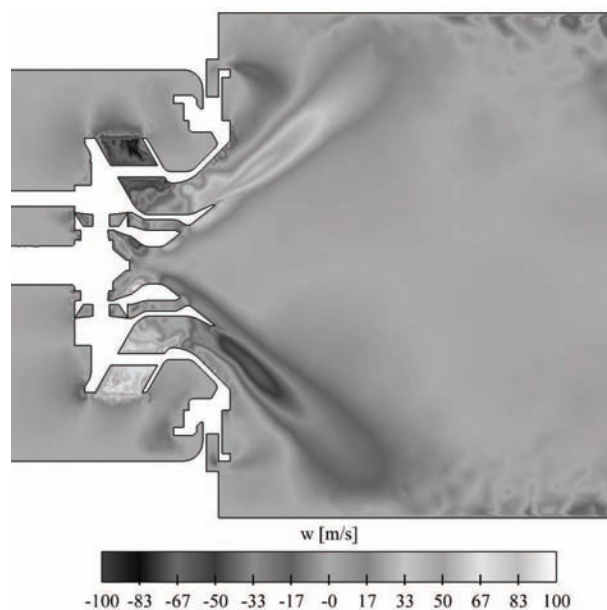


Figure 10.13: Mean radial velocity field

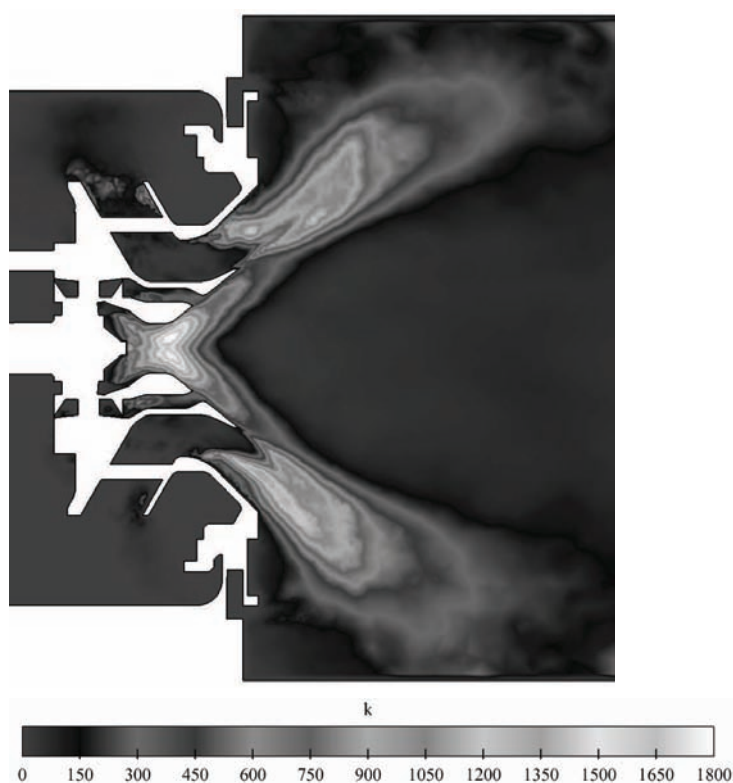


Figure 10.14: Turbulent fluctuating energy k [m^2/s^2]

10.3.3 Comparison with experimental data / LES quality

The accuracy of the results is evaluated by comparing them to experimental data. In this case, measurements of mean and fluctuation velocity profiles in the purely gaseous flow are available. These profiles are situated at three positions at 10, 15 and 30 mm downstream of the swirler exit (see figure 10.15). Additionally, another set of simulation results obtained with the third order accurate TTGC scheme (as opposed to the 2nd order Lax-Wendroff scheme used for

the baseline case) is considered. The results are presented in figure 10.16 for the averaged axial and tangential profiles as well as in figure 10.17 for the axial and tangential fluctuation profiles.

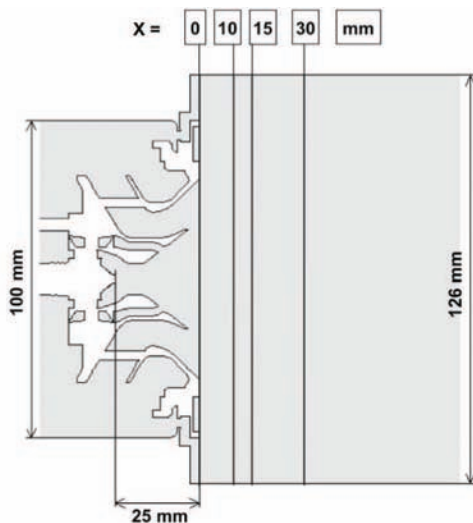


Figure 10.15: *TLC configuration - overview of the measurement lines at 10 mm, 15 mm and 30 mm.*

Agreement with experimental data is overall very good for both numerical schemes. The magnitude of the main velocity peaks, axial and tangential, is reproduced with high accuracy on all measurement planes. The positioning of the velocity peaks deviates slightly from the experiment, but the discrepancies are small and localized (there is no systematic over- or under-estimation of the opening of the flow cone). This is most probably due to slight fluctuations in the angle of the main high-speed flow zones (visible also in figure 10.8), which have relatively large timescales that may not be statistically converged on these profiles.

The secondary peaks that are created by the cooling films are well reproduced in location, while there is a slight dropoff in magnitude compared to the experiment. This is evidence for the effectiveness of the surrogate geometry approach employed for these films.

Finally, judging from time-averaged results, there is no difference between the LW and TTGC results that would point to an advantage of either scheme.

The fluctuation profiles, shown in figure 10.17, also reveal good agreement with experimental results. The slight discrepancies in the lateral positioning of the main peaks are in coherence with the ones observed on the time-averaged profiles. In this case, however, the main peak's magnitude is slightly over-estimated for axial and tangential fluctuation components, at least on the first two measurement planes. As the prediction of the mean velocity profiles is correct, this hints at slight lack of grid resolution in the high-shear regions. The only consistently observed difference between the performance of the numerical schemes is found on the most downstream profile. Here, outside the zone of the main fluctuation peak, the RMS levels of the LW scheme drop slightly below the experimental profiles, while agreement for the TTGC scheme remains very satisfying. While the level of the main fluctuation peak is constantly sustained by energy from the main flow regions that both schemes predict very well, the more sideward zones are filled with decaying turbulence that is more rapidly dissipated by the LW scheme.

The instantaneous flow field has been extensively discussed in section 10.3.1, however, the analysis presented there is based on LW results only. In order to give the reader an impression of the qualitative differences a higher order scheme effects in the results, a comparison of instantaneous axial velocity is given in figure 10.18. While the overall topology of the flow field remains very similar, which is to be expected in view of the quantitative comparison discussed before,

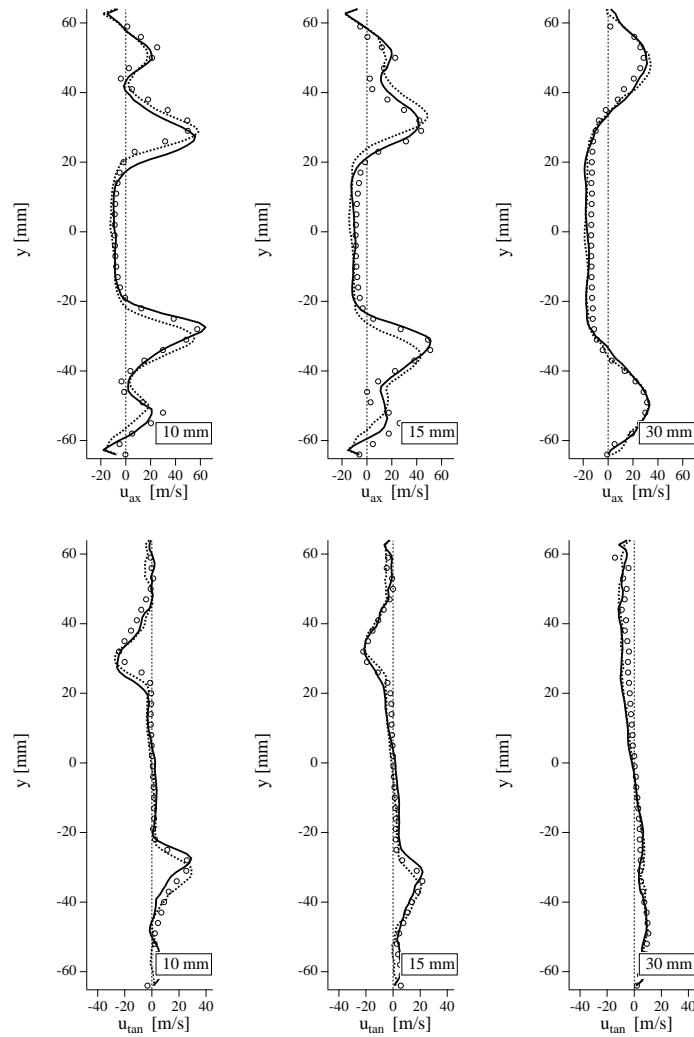


Figure 10.16: Mean velocity profiles. Axial component (upper diagram) and tangential component (lower diagram). Comparison of LES results obtained with the LW scheme (—), the TTGC scheme (- - -), and experimental data (o o o)

the smaller scale of resolved turbulent structures shows the effect of the higher order scheme (TTGC).

The previous findings already suggest that the grid resolution of the LES is sufficient. Another indication of LES quality is given by the ratio of subgrid-scale to laminar viscosity, shown in figure 10.19 for both LW and TTGC simulations. Zones of very high SGS viscosity, marked as black regions due to the saturated greyscale palette are visible. These zones are mainly located well inside the chamber where the grid is coarsened (necessary to limit the high number of grid points). Note that although this is acceptable in the present case, reactive simulations will make further refinement necessary because of the flame that can be expected to extend into this zone. Other regions with elevated viscosity ratios can be found in locations with high shear. This is a consequence of the standard Smagorinsky model, which is known to over-estimate SGS viscosity in zones of pure shear. The choice of using the Smagorinsky model instead of the WALE model [104] (which is better adapted to zones of shear) lies in the unfavourable behaviour in combination with wall-functions that is described in chapter 6. To limit the negative impact of the Smagorinsky models in free shear layers, the grid resolution is increased in all critical zones in order to keep the viscosity ratio below a value of 50.

In zones where turbulence is more or less isotropic like in the separation bubbles or the pilot

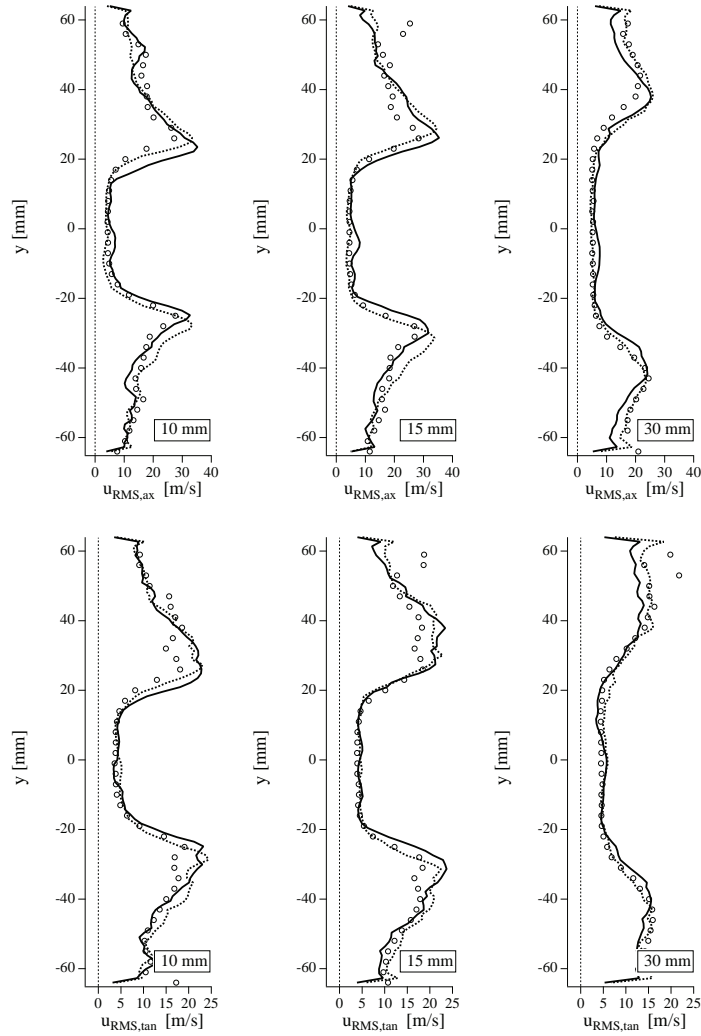


Figure 10.17: Velocity fluctuation profiles. Axial component (upper diagram) and tangential component (lower diagram). Comparison of LES results obtained with the LW scheme (—), the TTGC scheme (---), and experimental data (○○○)

bowl, the viscosity ratio is higher for TTGC simulations. This is consistent with previous work, for instance by Lamarque [80] or Selle [134], who argue that this is a sign of the lower numerical dissipation of the TTGC scheme. In fact, a scheme with low numerical dissipation will preserve more energy in the resolved scales that has to be dissipated by the turbulence model.

It has been seen that the interaction of the flow with walls plays an important role in this configuration. Furthermore, certain criteria for ideal operating conditions for the wall-function approach adopted in this study have been determined in chapters 6 and 7. To see if these criteria are actually met in the full-scale application case, figure 10.20 presents a cut-away view of the narrowest parts of the swirler channels, shaded by the local y^+ -value at which the first grid point is placed that should be in the logarithmic layer. Apart from visible wake regions behind the guide vanes, the values of y^+ are of the order of 100 for the outer channels, which can be considered ideal with respect to the wall model. In the inner channels, the level is generally lower, of the order of 50, which is well within a proper working range of wall-laws. In chapter 7, it was found that even higher near-wall grid resolution in narrow channel-like geometries should be sought when the prediction of pressure drop is to be improved. In the present case, the necessity of limiting the number of grid points motivated the choice to stay within a more

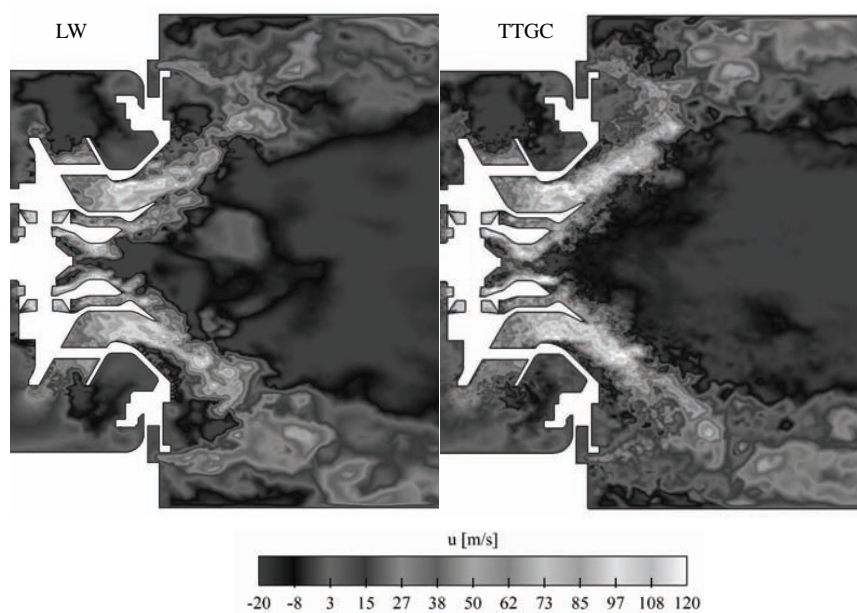


Figure 10.18: Instantaneous axial velocity fields obtained with LW (left) and TTGC (right).

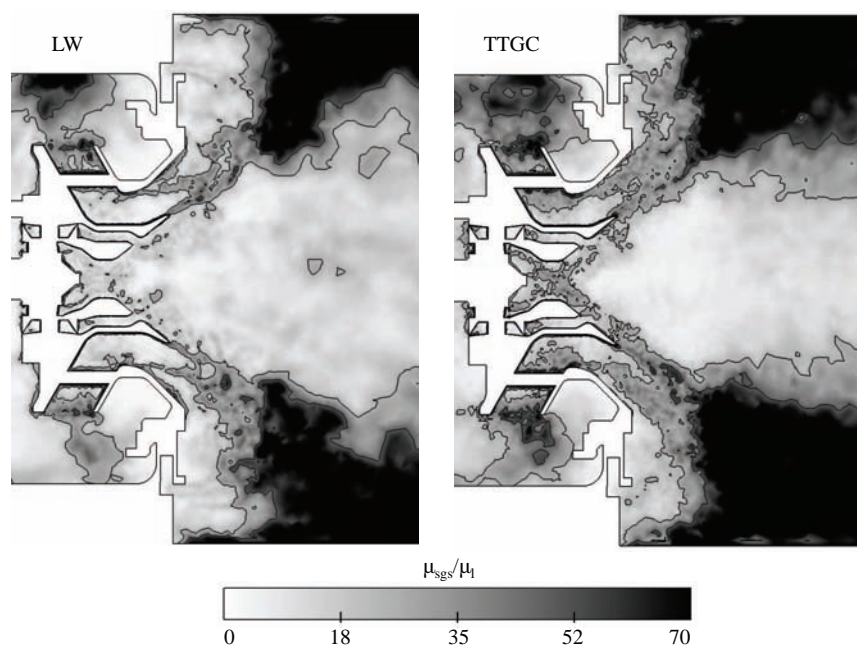


Figure 10.19: Instantaneous viscosity ratio field, overlaid with three iso-contours between 0 and 50 for LW (left) and TTGC (right).

conservative range of grid spacing inside the swirler.

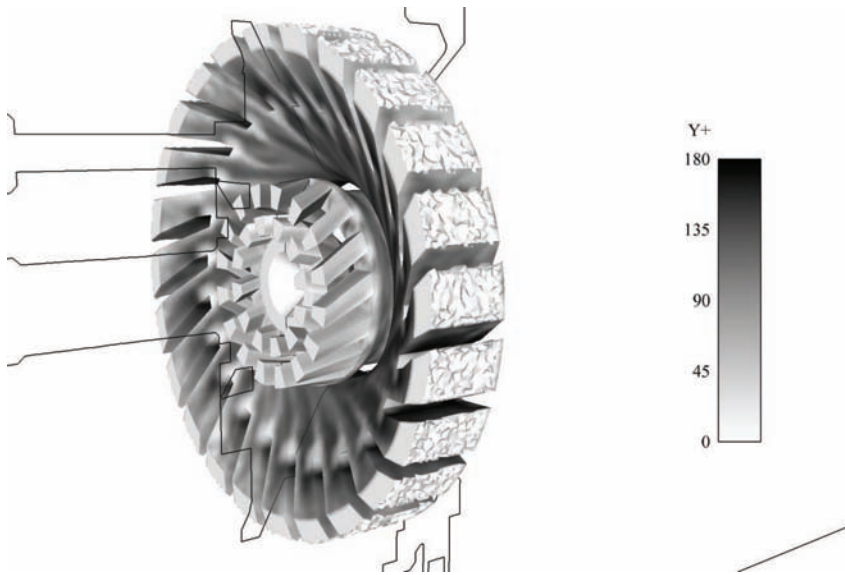


Figure 10.20: *Distance in wall units of the first off-wall grid point (y^+) for the instantaneous flow field.*

Conclusion

Results for the purely gaseous flow show an overall good performance of the LES approach. The second-order accurate Lax-Wendroff scheme performed equally well as the third-order TTGC scheme on the grid employed here, which is an important fact concerning the global strategy of this work (the use of the PSI scheme for the Eulerian two-phase flow simulations, which can at present only be applied in conjunction with the Lax-Wendroff scheme for the gas).

In addition, the equally good performance of both schemes highlights that a LES may rely on other factors than the accuracy of the scheme.

In the present case, the links between the determining factors for the success of the global approach are quite complex: the importance of wall-bounded flows and the associated Reynolds numbers led to the choice of wall-functions to model the turbulent boundary layers. Wall-models are not well-adapted to predict boundary layer separation, which is, however, an important feature of the flow considered, making the selective application of pure no-slip boundaries necessary in carefully chosen areas. Furthermore, the interaction of the wall-model with the WALE model has proven to be problematic, which led to the choice of the standard Smagorinsky SGS turbulence model. The latter made the refinement of the grid necessary in order to improve the performance in shear layers, where the Smagorinsky model is known to over-predict subgrid shear. This refinement is applied in particular focus regions of separated boundary layers and the main shear layer between the swirler stages. As a result, this combination of circumstances leads to a mesh fine enough for the LW scheme to deliver results that are on par with the TTGC scheme in terms of first and second order statistics in comparison to measurement.

Chapter 11

Two-phase flow results of the TLC configuration

Contents

11.1 Introduction	207
11.2 Computational setup	208
11.2.1 Euler-Euler computational setup	209
11.2.2 Euler-Lagrange computational setup	210
11.3 Results	210
11.3.1 Instantaneous two-phase flow topology	210
11.3.2 Evaporation phenomena	214
11.3.3 Time-averaged results, comparison with experimental data	225
11.4 Computational cost	232
11.5 Conclusion	233
11.6 Tables	234

11.1 Introduction

The purely gaseous simulation of chapter 10 is now extended to a two-phase flow. This includes the findings of chapter 8 with respect to spray injection but also regarding the choice of the numerical scheme.

The central aspect of this chapter is a direct comparison between the mesoscopic Euler-Euler and the Euler-Lagrange approaches. This comparison is as direct as possible, using an identical solver for the gaseous phase, an identical grid, identical models for the liquid phase and identical boundary conditions. A similar comparative study (involving an industrial-scale application) is the work of Senoner et al. [137] where an aeronautical injector with a hollow cone type fuel spray is characterized at atmospheric conditions. The aeronautical injector considered here is a step forward in geometrical complexity and towards realistic (i.e. pressurized) operating conditions.

Two-phase flow simulations for the same swirler geometry have been performed by Lavedrine [81] and Simsont [138], both using a EE method and by Bertier [14] using a Lagrangian approach including secondary breakup. Examples for simulations in similarly complex geometries are found in the work of Apte et al. [7] and Moin et al. [99] who used an EL approach including a secondary breakup model at atmospheric as well as pressurized and reactive conditions. The

inclusion of a multipoint injection, however is limited to the work of Bertier [14].

In the present study three simulation cases are considered. The first is an Eulerian simulation and thus locally monodisperse. The capability to handle polydispersion is a central advantage of the EL approach over the mesoscopic EE formulation. On the other hand, a comparison in identical conditions necessitates equivalent boundary conditions, i.e. the injection of a monodisperse spray. Therefore, the EL simulations are performed in two versions, the first with a monodisperse injection as a benchmark case to be compared to EE and the second using a polydisperse injection to independently assess the contributions of polydispersion.

The operating point is based on available measurement data [82], which include several cases differentiated by the value of liquid mass flux. The case with 10 g/s is retained because its dataset is most complete, with measurements being available at two downstream positions. On the gaseous side, operating conditions are identical to the ones of the gaseous flow (chapter 10), i.e. a chamber pressure of 4.37 bar and air entering the plenum pre-heated to 473 K. Under these conditions, one can expect to observe droplet evaporation inside the chamber.

11.2 Computational setup

Simulation parameters of the underlying gaseous flow are identical to the ones used in the Lax-Wendroff case of chapter 10, to which the reader is referred for detailed information.

The momentum flux ratio of a single injection hole takes a value of $q = 0.2$, which is below the cases considered in the study of the liquid jet in a crossflow (chapter 8). Among the findings of this chapter is the negligible influence of the liquid column region for value of $q < 2$. The modified law for drag presented in chapter 8 is therefore not applied in the present case. Another important aspect is the choice of the droplet diameter at injection. For the sake of comparability, the EE and the monodisperse EL simulation share a single injection diameter. From available experimental data, such an injection diameter cannot be deduced in a direct way. In preliminary studies by Simsont [138] and Jiménez [73], good results have been obtained with an injection diameter of $30\ \mu\text{m}$, which is retained in the present work. In comparison with experimental data, this diameter lies between the Sauter mean diameter and mean diameter on the first measurement position, where diameters are still close to their injection value.

For the polydisperse case, in addition to a characteristic diameter, a droplet size distribution that results from primary and secondary breakup near the injection is needed. The estimation of such a distribution is based on measurement data by Becker et al [11], who considered a range of Weber numbers for the jet-in-crossflow experiment that include conditions encountered in the TLC configuration. These authors note that the characteristic diameters of the spray only weakly depends on the momentum flux ratio q but mainly on the cross-flow momentum ρu_{Bulk}^2 . Evidence for this can be found in figure 11.1. Another finding is that the maximum and minimum diameters evolve similarly to the SMD, with the diameter variance remaining more or less constant. Based on these observations, the SMD for the TLC configuration is determined from the correlation proposed by Becker et al. [11]:

$$SMD = 429 (\rho u_{Bulk}^2)^{-0.24} \quad (11.1)$$

The crossflow velocity in the TLC configuration in direct proximity to the injection point is estimated at 100 m/s from the gaseous flow in chapter 10. The diameter variance is kept at the value $8.351\ \mu\text{m}$ obtained by fitting a log-normal distribution to experimental data for the case of

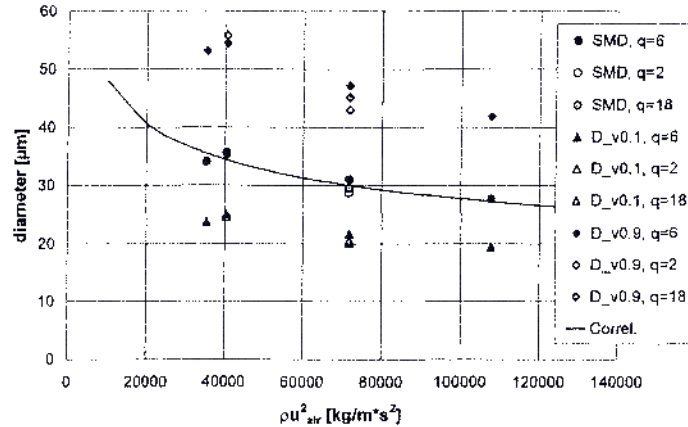


Figure 11.1: *Dependence of characteristic droplet diameters on the crossflow momentum and the momentum flux ratio q . Diagram from Becker and Hassa [11].*

$q = 6$ (see chapter 8 for details). The resulting log-normal distribution is shown in figure 11.2.

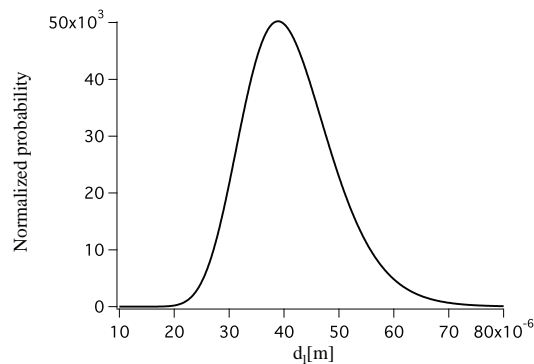


Figure 11.2: *Log-normal distribution of the Lagrangian polydisperse case.*

The simulation parameters that are common to all cases considered here are presented in table 11.2 (section 11.6). The liquid fuel used for all simulations is a surrogate for kerosene. Its most important properties are listed in table 11.3 (section 11.6).

11.2.1 Euler-Euler computational setup

Simulation parameters specific to the EE approach are summarized in table 11.4 in section 11.6 at the end of this chapter. Based on the assessment of the performance of different numerical schemes in the liquid jet in crossflow testcase (chapter 8), the scheme used for the case presented here is PSI, which functions in conjunction with the Lax-Wendroff scheme for the gas phase.

The Eulerian injection parameters are shown in table 11.6 (section 11.6). Similar to the strategy adopted in the liquid jet in crossflow case, the liquid phase inlet condition is applied in an area of five times the diameter of the original injection orifice. This way, the liquid volume fraction at injection is lowered from $\alpha_l = 1$ (the plain jet) to $\alpha_l = 0.04$, which effectively prevents most stability problems for the numerical scheme.

11.2.2 Euler-Lagrange computational setup

Euler-Lagrange simulation parameters are shown in table 11.5 at the end of this chapter (section 11.6). Due to the very large number of droplets present in the simulation, the so-called parcel approach is employed for the Lagrangian cases. Here, 10 physical particles are grouped into a so numerical particle or parcel. The resulting particle number is still of the order of one million and the resulting spray is still rather homogeneous in most areas, with sufficiently high numbers of particles per cell in critical areas to prevent negative effects related to this grouping.

Detailed summaries of injection parameters for the monodisperse case (table 11.7) as well as the polydisperse case (table 11.8) can be found in section 11.6.

11.3 Results

The presentation of the results is divided into three parts. First, a phenomenological discussion of the two-phase flow is based on instantaneous results. This part is followed by a quantitative analysis focused on the comparison to experimental data. Finally, properties of the spray that are related to evaporation are considered in more detail.

Alongside the discussion of the observed two-phase flow phenomena, the comparison of the different methods is an important aspect. Here, EE results are juxtaposed with EL results with monodisperse droplet injection because they differ only in terms of the simulation approach but not in terms of boundary conditions. A second comparison is between monodisperse and polydisperse EL results in order to study the effects attributed to polydispersion.

11.3.1 Instantaneous two-phase flow topology

A global view of the polydisperse Lagrangian simulation is presented in figure 11.3. The result is an instantaneous image, showing all numerical particles (or parcels) at an instant in time where the spray is well-established. Near the multipoint injection, the spray plumes from the 24 injection orifices can be distinguished. After entering the chamber, these droplet streaks are quickly broken up in a diffuse spray that follows large scale turbulent motion. Clearly, the cone-shaped main droplet stream is impacting majoritarily onto the lateral walls. At this location, a certain stagnation of droplets can be observed. Part of this deposition is convected downstream, with a more and more sparse portion of the spray extending to the chamber exit. Another part goes in the reverse direction and is entrained into the lateral corner recirculation zones. As will be seen in the following, many droplets enter the CTRZ and remount into the swirler bowl.

These findings are confirmed by plots of particle trajectories, shown in figure 11.4 (left) for the polydisperse EL case. On the right side of figure 11.4, pseudo-streamlines of an instantaneous liquid phase velocity field are shown. Note that pseudo-streamlines have no direct physical meaning for an unsteady flow and are not equivalent to the (true) particle traces in EL. For clarity, only one trajectory is selected per injection point. Most trajectories rebound on lateral walls but others align with the airflow before contact is made. EL trajectories with a very steep impact angle tend to be entrained into the lateral recirculation zones, which is not observed on the Eulerian pseudo-streamlines.

An interesting detail is the tendency of the spray plumes generated by two or more adjacent injectors to merge after a certain distance. This effect can be observed very clearly in the EL results but also on the iso-surface of liquid volume flux (figure 11.5) that allows to visualize the spray boundaries in the EE results. This feature is not understood in full detail but it appears to be related to longitudinal vortices created by the swirler channels (see chapter 10), where

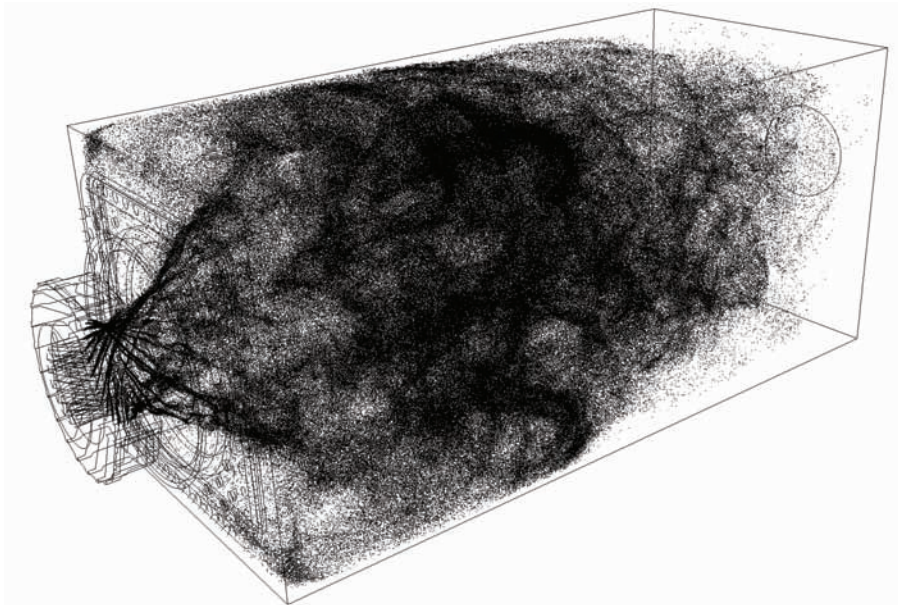


Figure 11.3: *Isometric view of the particle field in the chamber, polydisperse case. Displayed particles are numerical particles (parcels) of 10 physical particles each, represented by spheres that have been scaled for better visibility in printed form. Instantaneous value of physical particles in this view: approx. 11.2 million.*

several spray streaks are entrained by the same vortical structure.

Another way of presenting Lagrangian results, which also allows to better compare them to Eulerian results shown in longitudinal sections, is to isolate a slice of particles that corresponds to a neighbourhood of 5 mm to either side of the cross-section. The first comparison of this type is shown in figure 11.6. Here, the focus is on the general distribution of the spray, visualized by iso-contours of the liquid volume flux to highlight spray boundaries in the EE case. For EL, each numerical particle is represented by a black dot. The two images show a comparable spray topology – the same opening angle, a wall-impact at roughly the same location and the bifurcation of parts of the spray heading upstream, while the majority of it separates again from the wall downstream of the impact region. Inside the swirler, there is little or no interaction between droplets and walls. Instead, following a short stretch or movement parallel to the wall after injection, the droplet stream detaches, which is presumably driven by centrifugal forces as the gaseous flow remains attached.

In general, EE results appear to be more diffuse with the spray almost reaching the opposite wall inside the swirler, whereas for EL, the spray plume remains relatively compact. Of course, it is not clear if either result is more physical than the other because EE is subject to additional diffusion from the scheme and artificial viscosity, while EL suffers from the lack of subgrid-scale turbulent diffusion, which is enhanced by the use of the parcel method. Differences between poly- and monodisperse results, as they can be observed in figure 11.8, mainly concern a more even and more random distribution of droplets for the polydisperse case. This occurs naturally as polydisperse trajectories are more rapidly separated due to varying Stokes numbers right after injection. In the monodisperse case, streaks and groups of droplets are less diffuse and, while heavily deformed by large-scale turbulence, most are still clearly delimited even while remounting in the recirculation zone.

The liquid phase velocity field is presented in figure 11.7. For EE (left), it shows the mesoscopic spray velocity overlaid with an iso-contour of the small-diameter limit at which evaporation

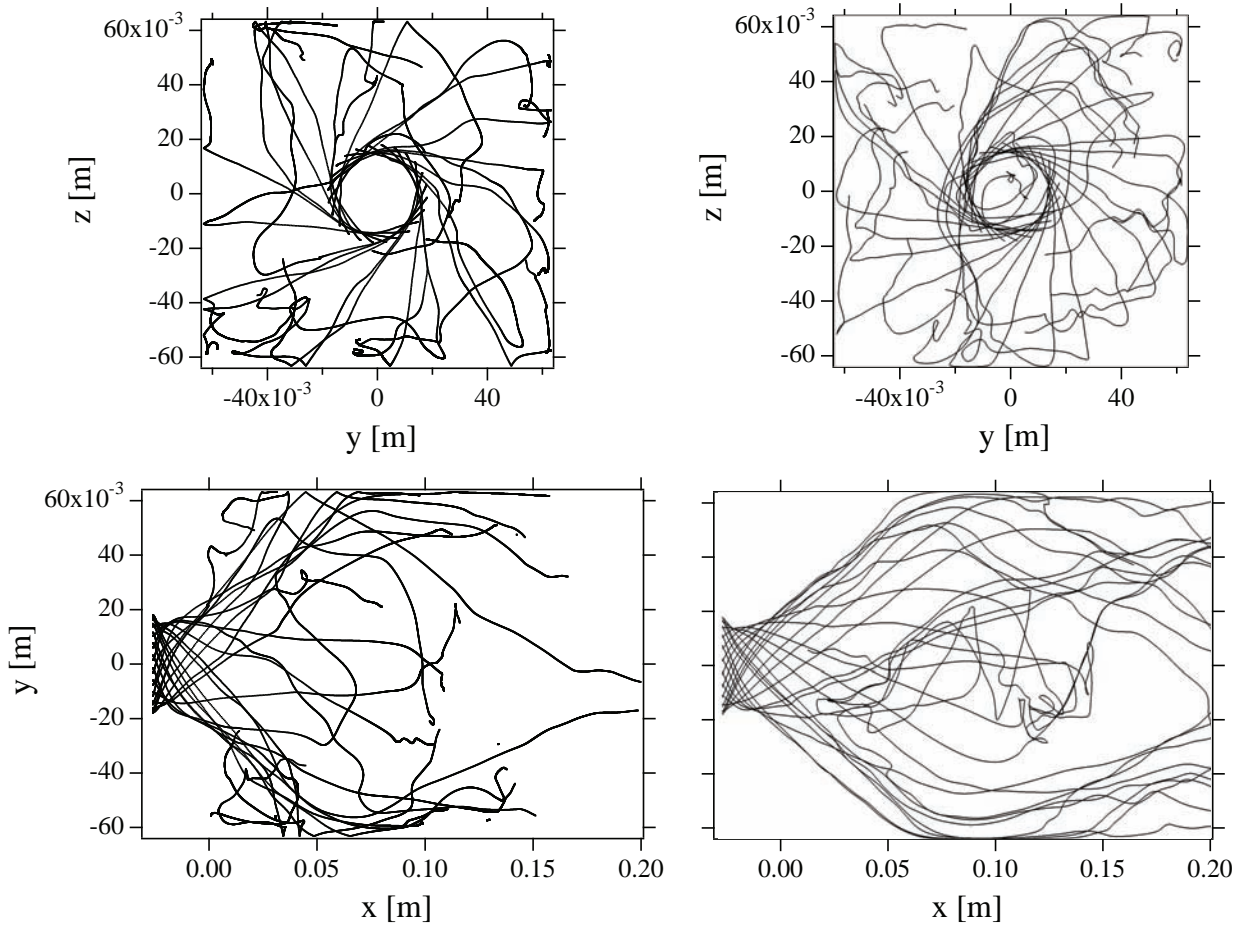


Figure 11.4: Left: polydisperse EL case, particle trajectories (selection of one single particle per injector). Right: EE case, pseudo-streamlines of an instantaneous liquid phase velocity field.

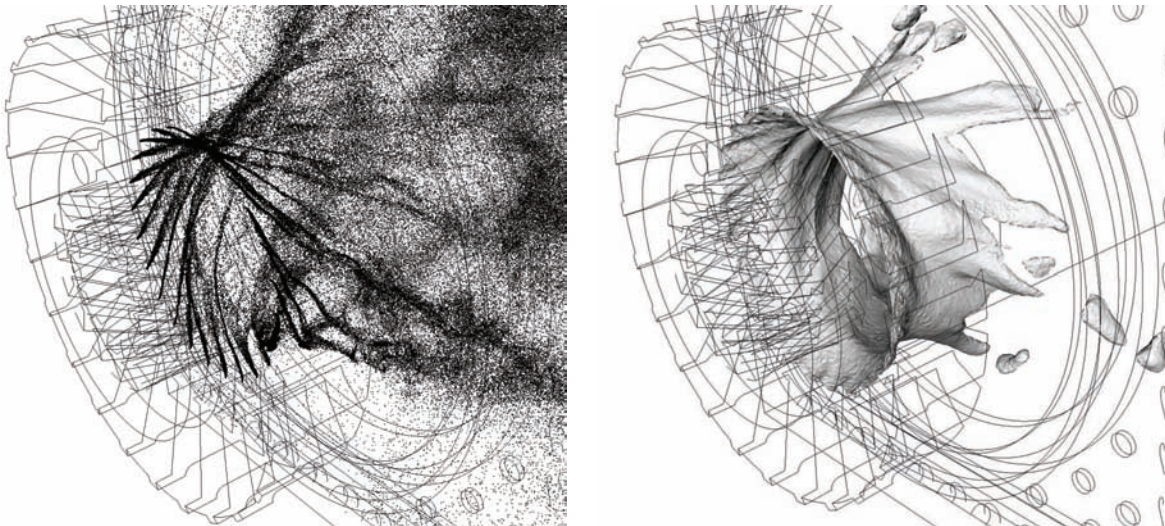


Figure 11.5: Close up views of the multipoint injection. Left: isometric view of the (numerical) particle field in the chamber, polydisperse case. Right: EE results, iso-surface of the liquid volume flux to visualize the spray boundary.

is frozen. Outside this line, the velocity field has no physical meaning. For EL (right), the mesoscopic axial velocity field is reconstructed by averaging over all particles present in a given control volume and distributing the values to the grid nodes (see equation 3.6). Both EE

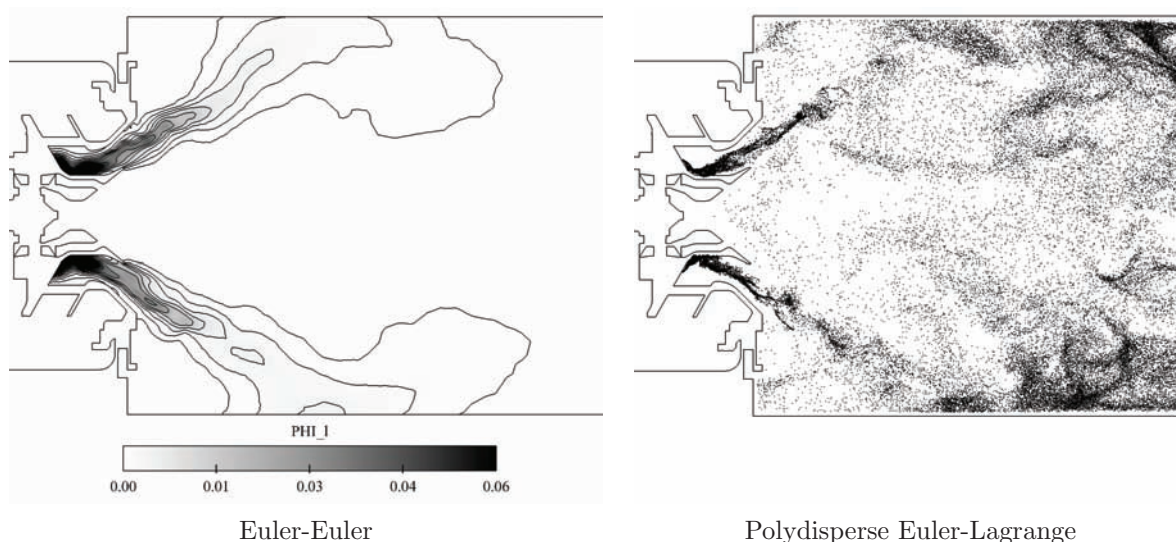


Figure 11.6: Comparison of EE results with polydisperse EL results. Left: iso-contours of liquid volume flux Φ_l [$\text{m}^3/(\text{s m}^2)$] on the plane $y = 0$. Right: numerical particles in a 5 mm neighbourhood of the plane $y = 0$.

and EL fields show a flow topology and velocity levels similar to the gaseous phase. Local zones of negative axial velocity evidence droplets moving upstream into the central and lateral recirculation zones.

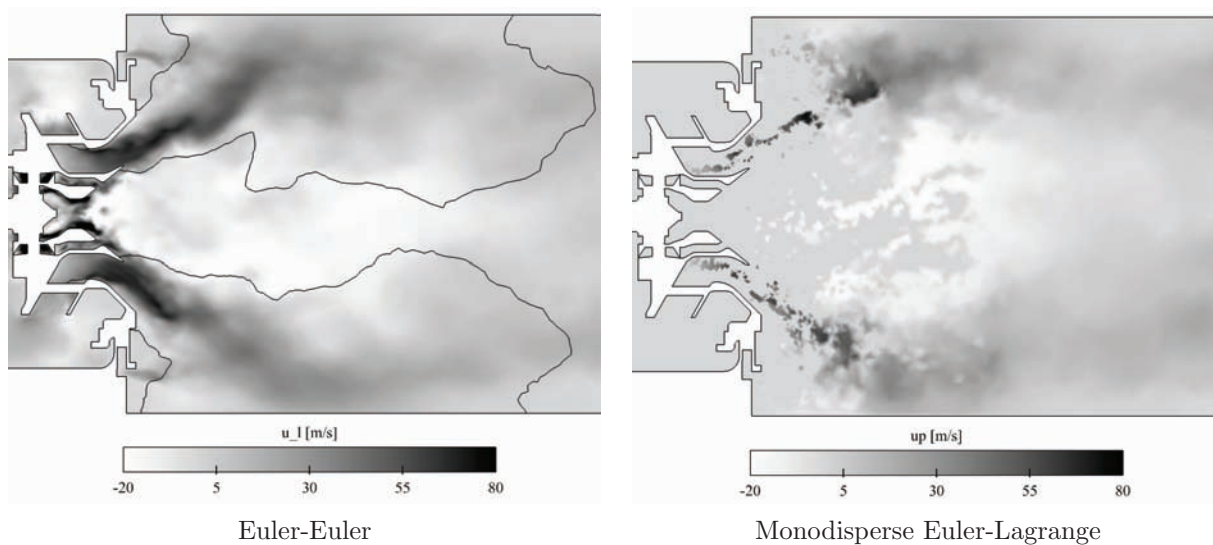


Figure 11.7: Comparison of EE results with monodisperse EL results. Left: field of instantaneous liquid phase axial velocity u_l [m/s] on the plane $y = 0$. Right: field of instantaneous liquid phase axial velocity u_p [m/s] on the plane $y = 0$. Mesoscopic velocity reconstructed from Lagrangian particles, $u_p = 0$ in zones without droplets.

11.3.2 Evaporation phenomena

Droplet diameter evolution

Comparisons of the spatial distribution of droplet diameters are shown in figures 11.8 and 11.9 for EL results. As it is difficult to visualize droplet properties from Lagrangian results on a printed medium, it has been chosen to show parcels, enlarged to four pixels and shaded with a greyscale value representing their diameter. While this method is visually appealing and instructive, retrieving quantitative information on diameter from the greyscale values is difficult. Therefore, the reader is referred to figures 11.10 and 11.12 for a more precise analysis of the diameter evolution.

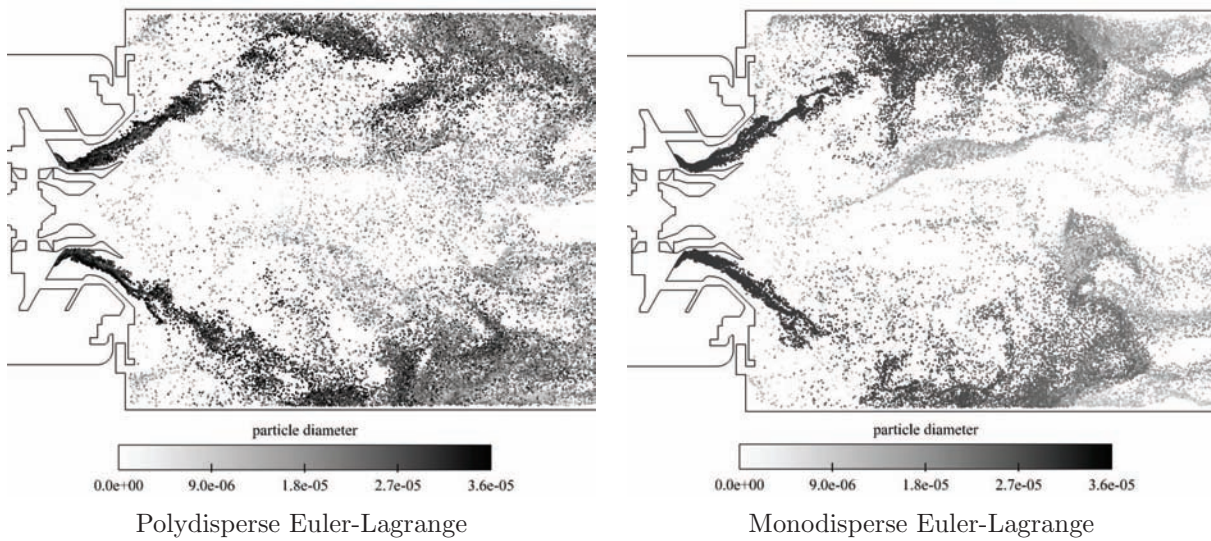


Figure 11.8: Comparison of polydisperse and monodisperse EL results. Left and right: particles in a 5 mm neighbourhood of the plane $y = 0$, shaded with the particle diameter d_p [m].

In both juxtapositions, the trends are very similar with diameters remaining quite close to the injection value until droplets reach a zone where they stagnate or move at reduced speed. This is due to the evaporation timescale that, despite the pre-heating, is larger than the time a droplet usually stays in the main, high velocity flow region. In the polydisperse EL case, high diameter particles can be found relatively far downstream, which is a consequence of the largest droplets generated at the injection having a prolonged evaporation timescale and higher inertia, which keeps them from being caught in a recirculation zone. Inversely, droplets at the lower end of the distribution can be expected to disappear very rapidly and to be entrained into recirculation regions very quickly.

In both the monodisperse EL case and the EE results, droplets quite homogeneously reach diameters lower than $10 \mu\text{m}$ after having entered the lateral or central recirculation regions. In the EE case, evaporation processes are stopped at a diameter of $5 \mu\text{m}$, a threshold that is marked by a white iso-line. All regions of the spray having this diameter are passively convected, thus having no physical meaning.

A different perspective on droplet diameter evolution is to follow the trajectories shown in figure 11.4. Figure 11.10 shows square dimensionless droplet diameters over time, comparing results from the polydisperse and monodisperse simulations. This representation allows to identify approximately linear regions, which signify that the diameter evolution follows the d^2 -law (where the square of the diameter evolution is linear in time) that results from the evaporation model for the particular case of a constant equilibrium droplet temperature (or wet bulb temperature, see section 4.3.3). Initially, the diameter evolutions do not follow the d^2 -law because of a rapidly

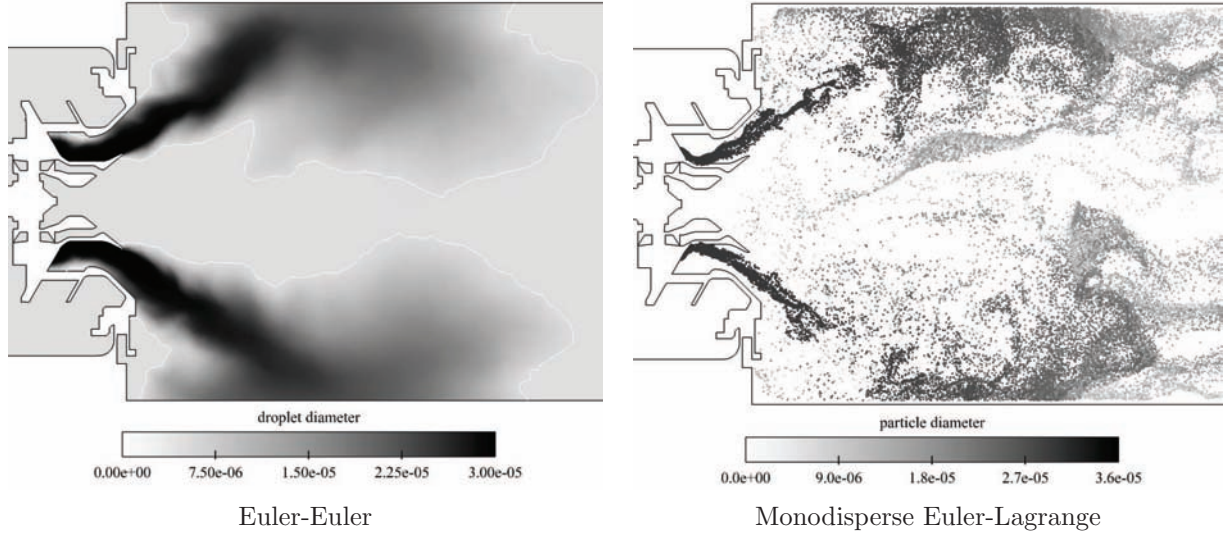


Figure 11.9: Comparison of EE results with monodisperse EL results. Left: droplet diameter field d_l [m] on the plane $y = 0$, overlaid with the iso-contour marking the clipping diameter. Right: numerical particles in a 5 mm neighbourhood of the plane $y = 0$, shaded with the droplet diameter d_p [m].

changing droplet temperature. Two observations can be made: the influence of transient droplet heating is quite significant in both cases as it is in effect during least 20 % of a droplet's lifetime. Furthermore, the spread between temperature evolutions is visibly larger in the polydisperse case.

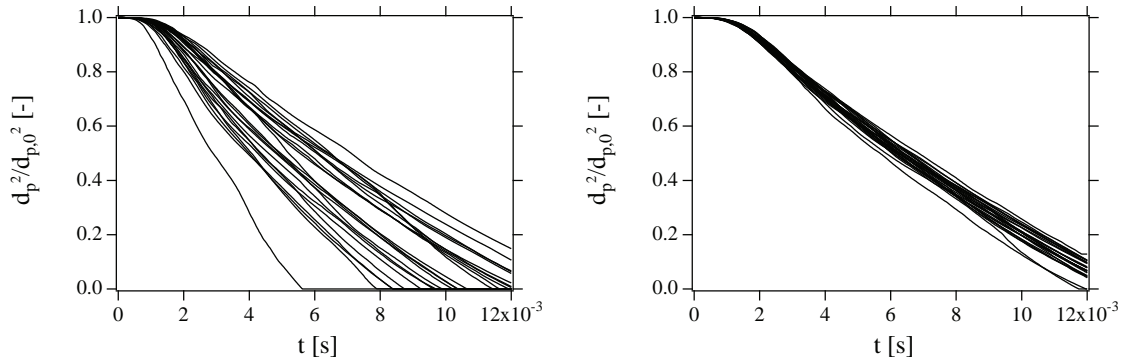


Figure 11.10: Temporal evolution of the square, dimensionless droplet diameter, $d_p^2/d_{p,0}^2$ [-], along 24 representative trajectories (see figure 11.4). Left: polydisperse EL case, right: monodisperse EL case.

To compare with Eulerian the spatial evolution of the diameter is considered. Figure 11.11 shows a single pseudo-streamline of the liquid phase velocity, which is used to approximate the trajectory a hypothetical particle could follow. Along this pseudo-trajectory, Eulerian droplet diameters and liquid phase temperatures are probed at equidistant sample locations. The result, along with data from the 24 monodisperse EL trajectories, is traced over the x -coordinate (i.e. the chamber main axis), as shown in figure 11.12. The EE curve is similar to the trajectories from EL data. Note that this comparison is not unambiguous, as a steep curve can result from a steep trajectory or rapid evaporation. There is, however a certain envelope of possible diameter evolutions to which the Eulerian pseudo-trajectory should be compared. This envelope is respected by the Eulerian results.

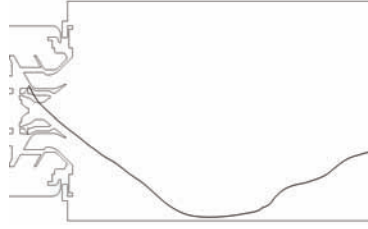


Figure 11.11: Placement of the pseudo-streamline along which the EE diameter and liquid temperature field is probed to obtain data approximately comparable to the evolution along a Lagrangian particle trajectory.

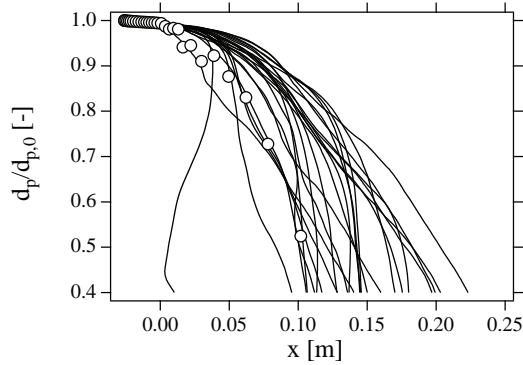


Figure 11.12: Continuous lines (—): evolution of the dimensionless droplet diameter, $d_p/d_{p,0}$, over the axial distance x , traced for 24 representative trajectories (see figure 11.4), monodisperse EL case. Symbols (o o o): EE results along the pseudo-streamline shown in figure 11.11.

Droplet temperature evolution

Droplet heat transfer is a key element in the evaporation process. As the liquid phase is injected at 300 K and the airflow is preheated to 473 K , the onset of evaporation will be marked by a substantial heating of the spray, until it reaches an equilibrium. This can be observed on all three visualizations of the spray temperature (figures 11.13 and 11.14). Here, an initial zone of steadily increasing temperature, from the injection points onwards and stretching approximately up to the point of wall impact is followed by large regions of nearly constant temperature throughout the volume of the chamber. This observation can be made in both, EL and EE results.

To allow a more quantitative view on the liquid phase temperature, its evolution is again displayed for 24 Lagrangian trajectories (figure 11.15). First, the temporal evolution of the polydisperse and the monodisperse case are compared. In both diagrams, an initial rise of droplet temperature is followed by the settling at a common level around 410 K , which is the equilibrium or wet bulb temperature. It can be estimated by a 0D-calculation using the same evaporation model as used in the full simulation (based on chapter 4). This calculation returns the wet bulb temperature for a droplet in a non-evolving gaseous environment. Here, the gaseous input values have been estimated by evaluating the flow fields to a temperature of $T = 460\text{ K}$ and a fuel mass fraction of $Y_F = 0.01$. The resulting equilibrium temperature takes a value of $T_{wb} = 412\text{ K}$. This result can be compared to the results shown in figures 11.15 and 11.16. There is no single equilibrium temperature but rather a range of approximately 5 K in width, due to differences in ambient conditions encountered by each individual droplet, but within this variation, there is a good match with the estimated value. This is also true for the Euler-Euler results, which are included in figure 11.16. Considering the wet bulb temperature is a good single measure for evaluating evaporation processes because it is not obtained explicitly but by two disparate

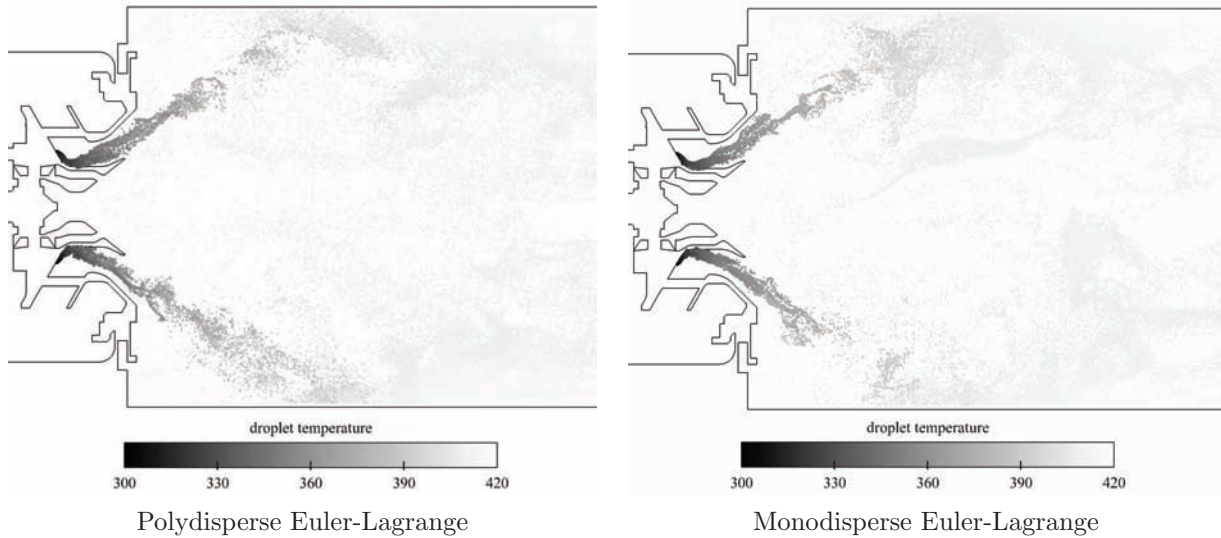


Figure 11.13: Comparison of polydisperse and monodisperse EL results. Left and right: particles in a 5 mm neighbourhood of the plane $y = 0$, shaded with the droplet Temperature T_p [K].

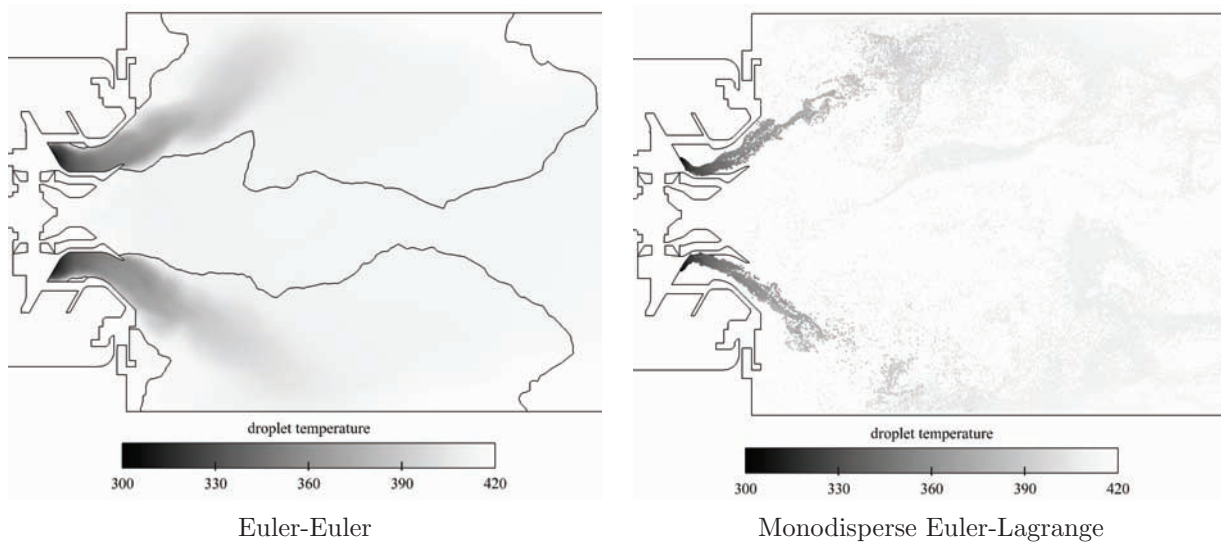


Figure 11.14: Comparison of EE results with monodisperse EL results. Left: droplet temperature field T_l [K] on the plane $y = 0$, overlaid with the iso-contour marking the clipping diameter. Values outside this contour are not physically valid. Right: numerical particles in a 5 mm neighbourhood for the plane $y = 0$, shaded with the droplet Temperature T_p [K].

parts of the model (heat and mass transfer) that reach an equilibrium. Obtaining very coherent results using three different methods gives a certain level of confidence in the results, at least with respect to the proper working of the same model in different frameworks.

The temperature evolution during the transition between injection and the equilibrium state varies between the different trajectories in the EL simulations (figure 11.15). Variations in the monodisperse case are relatively weak and mainly due to droplets being exposed to fluctuating ambient gas temperatures along their path. In the polydisperse case, variations are stronger because additionally, the characteristic timescales for heat transfer differ with droplet diameter. In order to include the Eulerian results into the comparison, information along the pseudo-trajectory shown in figure 11.11 is traced over the axial distance x and compared to data from the monodisperse Lagrangian trajectories. Again it has to be highlighted that this presentation

can be ambiguous as a curve in this diagram is determined simultaneously by the shape of the trajectory and the temperature change over time. Consequently, the main finding to be deduced from the results shown in figure 11.16 is that equilibrium temperatures coincide. During droplet heatup, temperature evolutions of Lagrangian and Eulerian results are very similar, with the Eulerian curve remaining well inside the envelope created by Lagrangian data except for a brief overshoot around $x = 0.1\text{ m}$, which corresponds to the region of wall impact. The increase in temperature is related to the use of isothermal walls: as the Eulerian spray does not elastically rebound like the Lagrangian particles, it stays near the walls over a longer distance (see figure 11.4) where it encounters gaseous conditions close to the wall temperature.

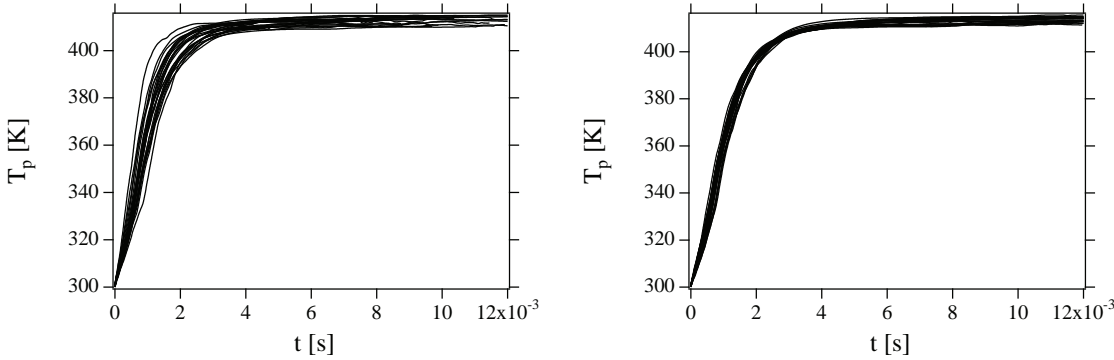


Figure 11.15: Temporal evolution of the droplet temperature, T_p , along 24 representative trajectories (see figure 11.4). Left: polydisperse EL case, right: monodisperse EL case.

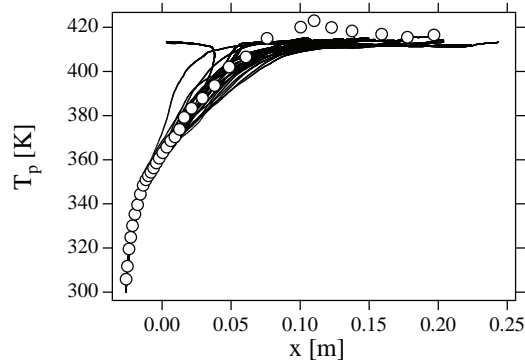


Figure 11.16: Continuous lines (—): evolution of the droplet temperature, T_p , over the axial distance x , traced for 24 representative trajectories (see figure 11.4), polydisperse EL case, right: monodisperse EL case. Symbols (o o o): EE results along the pseudo-streamline shown in figure 11.11.

An alternative way to study evaporation processes is based on histograms, obtained from a series of sample locations that are visualized in figure 11.17. Particle data is recorded inside cubes of 5 mm edge length, situated at an axial distance of 15 mm from the injector exit (which corresponds to the downstream measurement line as shown in section 11.3.3) at three different radial locations. In order to accelerate the obtention of exploitable droplet numbers, a symmetrical pattern with respect to the y and z axis is chosen. This method allows to analyze three regions: the innermost, located at 10 mm radial distance, is representative for long-lasting droplets that have typically followed at least half a cycle of the central recirculation zone. The middle location, at 30 mm radial distance, captures the primary spray issued by the injector. The third and outermost location at 50 mm sees droplets stagnating near the wall or returning from the lateral recirculation regions.

Histogram data is shown for the Lagrangian results only, comparing the monodisperse (figure 11.18) with the polydisperse case (figure 11.19). Droplets injected with a constant diameter of

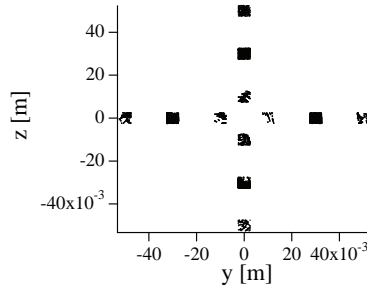


Figure 11.17: Placement of the sampling locations for histogram data in the y - z plane.

$30\mu\text{m}$ in the former case retain both their diameter and the monodisperse character of the spray at the 30 mm sample location. Droplet temperatures have already broadened their distribution, which is consistent with the findings from trajectory data (figure 11.15). A small histogram peak located at the wet bulb temperature shows that a small number of droplets with medium lifetime (which are heated but not yet significantly evaporated) are crossing this area. As their diameter still is close to the initial value, it can be suspected that these droplets return directly from rebounding off the wall and/or a short time of residence in the lateral recirculation zone. Another indication for this is the presence of large diameter droplets at the outer (50 mm) location that have either partially or entirely heated to the equilibrium temperature and seem to belong to the same medium-lifetime class. This kind of droplet is not observed at the inner (10 mm) location, where only completely heated droplets in various states of evaporation (but all significantly lower than the initial diameter) are found. This type of droplet is also observed at the outer location, which in both cases hints at large residence times in either recirculation zone.

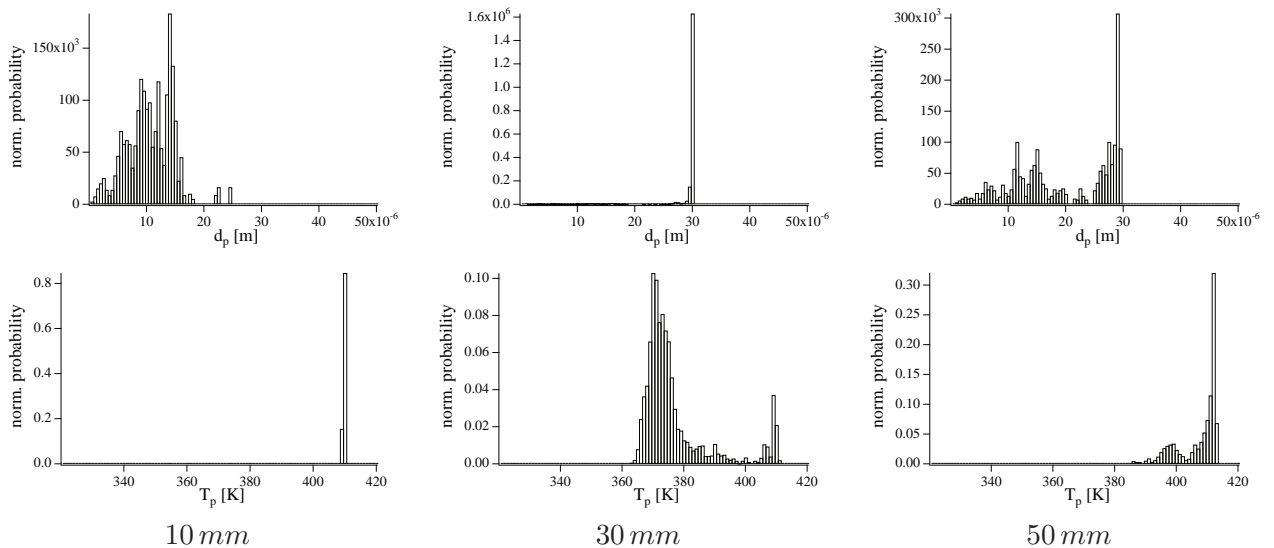


Figure 11.18: Diameter and Temperature histograms of the monodisperse EL simulation. Samples taken in a series of cubes at 15 mm downstream location and 10 mm (left), 30 mm (middle) and 50 mm (right) lateral distance from the centerline. (see figure 11.17 for the exact arrangement).

For the polydisperse case (figure 11.19), the size distribution in the primary spray that is captured at the 30 mm location is clearly apparent. It is accompanied by a broad distribution of droplet temperatures, which is due to the different heating timescales of varying diameter droplets. As in the monodisperse case, a small peak indicating droplets at equilibrium shows the presence of medium-lifetime particles returning (or crossing) the primary spray region. In a similar way, the outer sampling location presents a combination of large and small diameter

droplets, majoritarily but not exclusively at the equilibrium temperature, which is most probably a combination of medium and long lifetime droplets. In the inner region, the findings are identical with the monodisperse case with only long-lifetime droplets at diameters ranging between $\approx 5 \mu\text{m}$ and $\approx 25 \mu\text{m}$ being present in this area.

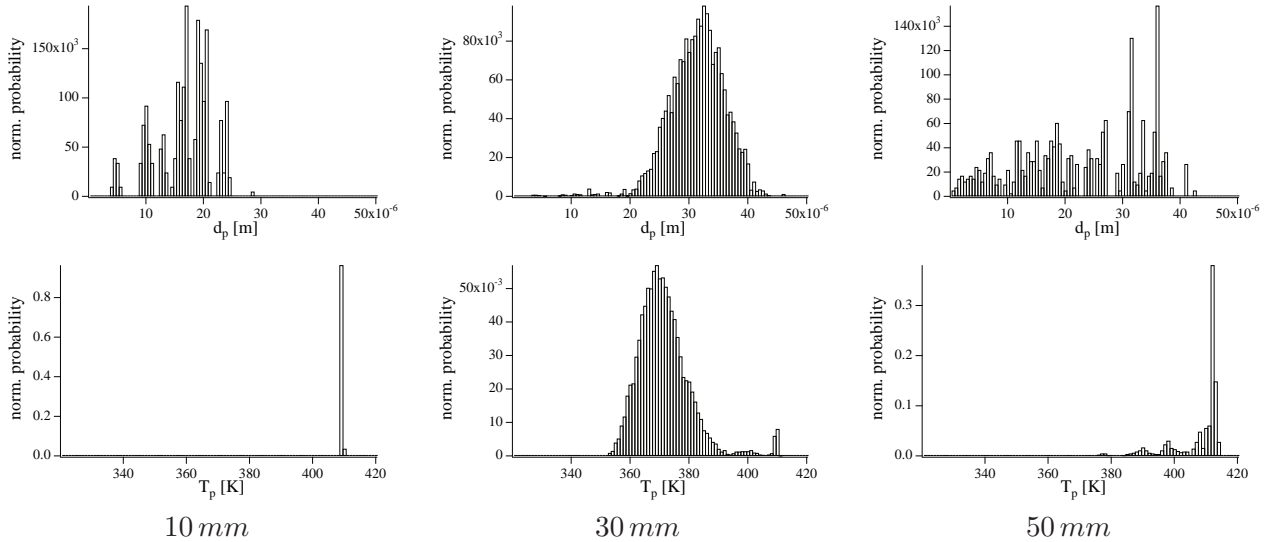


Figure 11.19: Diameter and Temperature histograms of the polydisperse EL simulation. Samples taken in a series of cubes at 15 mm downstream location and 10 mm (left), 30 mm (middle) and 50 mm (right) lateral distance from the centerline. (see figure 11.17 for the exact arrangement).

Interaction with the gaseous phase

Evaporation processes in the TLC configuration are characterized by strong inverse coupling effects. The first is mass transfer, which alters the composition of chemical species present in the chamber. Figures 11.20 and 11.22 show comparisons of fields of the source term of mass exchange, Γ , as it is received by the gas phase. Differences between the polydisperse and the monodisperse EL results are relatively small. The more random and more diffused droplet field of the polydisperse case leads to a smoother distribution of source terms. In the monodisperse case, local source term maxima are notably sharper. In the present application, these strong, localized source terms are not critical. However, in reactive simulations where evaporation source terms can be significantly stronger near a flame front, the numerical scheme for the gas phase may be destabilized.

In the case of EE (figure 11.22 left), the source terms generated by the liquid phase are comparatively smooth, in particular inside the injector, where the Lagrangian results clearly allow to distinguish between droplet streaks from individual injectors (in this plane, they are visible as dots because the streaks are swirled and cross the plane at an angle), whereas the EE field (figure 11.22 right) shows a nearly continuous distribution. The main features, i.e. strong and local source terms inside the injector, diffused and weak mass transfer where droplets begin to turn while entering the CTRZ and again stronger zones where droplets stagnate near the wall, agree quite well between both formulations.

The field of fuel vapour produced by evaporation is shown in figures 11.21 and 11.23. At the positions where source terms are strong, i.e. right after the injection, the resulting levels of fuel vapour are comparatively low and barely visible in this visualization. This is because these zones are overshadowed by the high vapour mass fraction that is found in the bulk of the chamber's volume, which is produced by steady accumulation in the central and lateral recirculation zones.

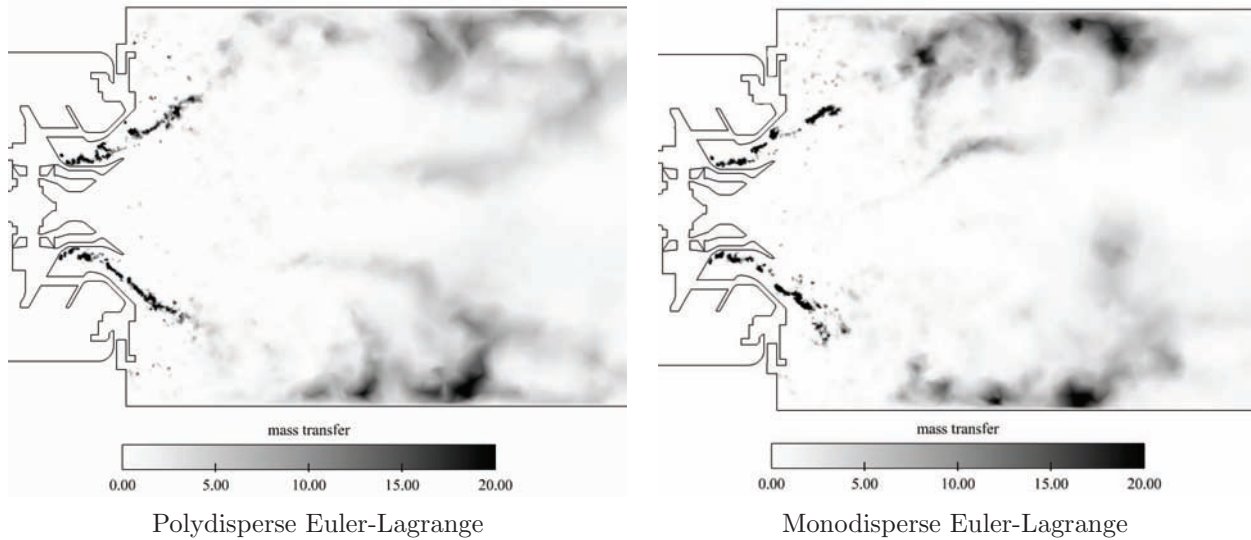


Figure 11.20: Comparison of polydisperse and monodisperse EL results. Left and right: field of the source term for mass transfer Γ [$\text{kg}/(\text{m}^3 \text{s})$] on the plane $y = 0$.

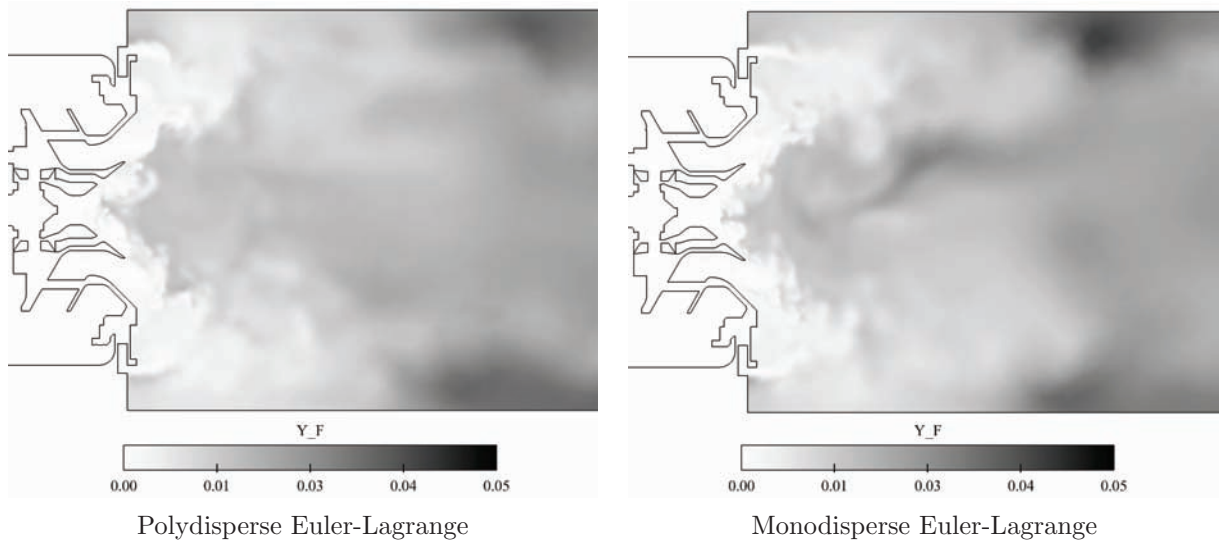


Figure 11.21: Comparison of polydisperse and monodisperse EL results. Left and right: field of the fuel species mass fraction Y_F [-] on the plane $y = 0$.

As the fuel vapour is not consumed in any way, this accumulation can be expected to continue until a state of equilibrium is reached. As this mechanism is very slow, EE and EL fuel mass fractions that have been initialized from solutions with a different state of convergence cannot be compared at this point.

The second coupling term involved in evaporation is heat transfer. A presentation can be found in figures 11.24 and 11.26. The observations on the general shape of the regions where strong source terms appear are essentially the same: strong, very sharply delimited source terms in the EL case with slightly more diffusion for the polydisperse results. On the other hand, the broadly distributed, smooth source terms originating from the spray in the EE formulation. The strongest source terms are encountered directly after the injection point, where the droplets are heated and inversely cool the gas phase, as can be seen in figures 11.25 and 11.27 on the fields of gaseous temperature that show a significant temperature drop in these zones. Unlike the mass transfer terms that show high intensity regions in proximity of the wall impact region, heat transfer values decrease constantly and do not show these near wall maxima. This is due to the

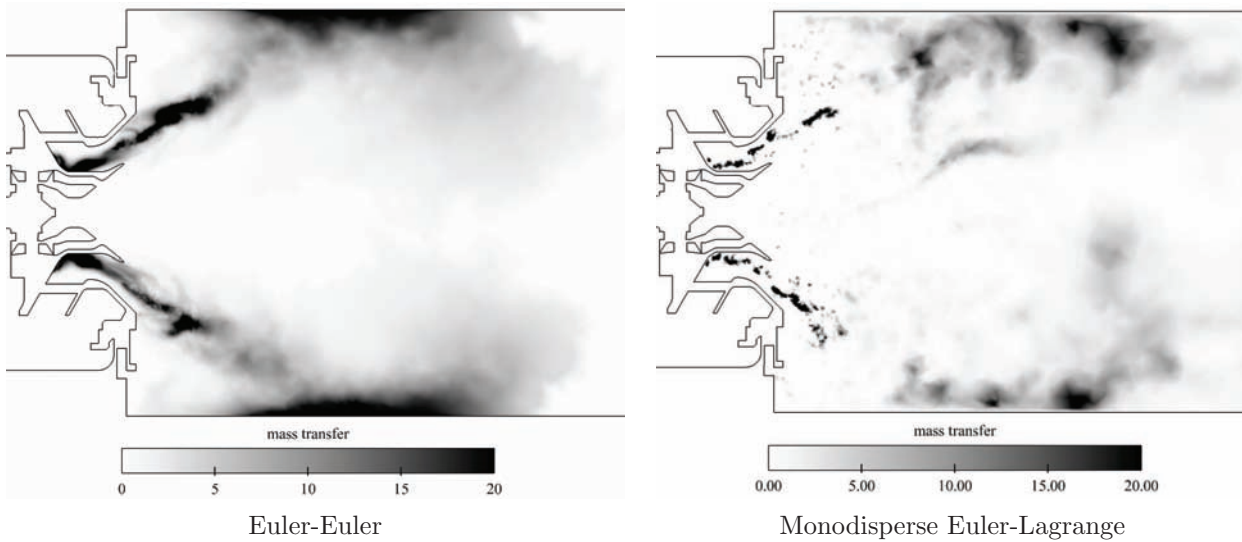


Figure 11.22: Comparison of *EE* results with monodisperse *EL* results. Left and right: field of the source term for mass transfer Γ [$\text{kg}/(\text{m}^3 \text{s})$] on the plane $y = 0$.

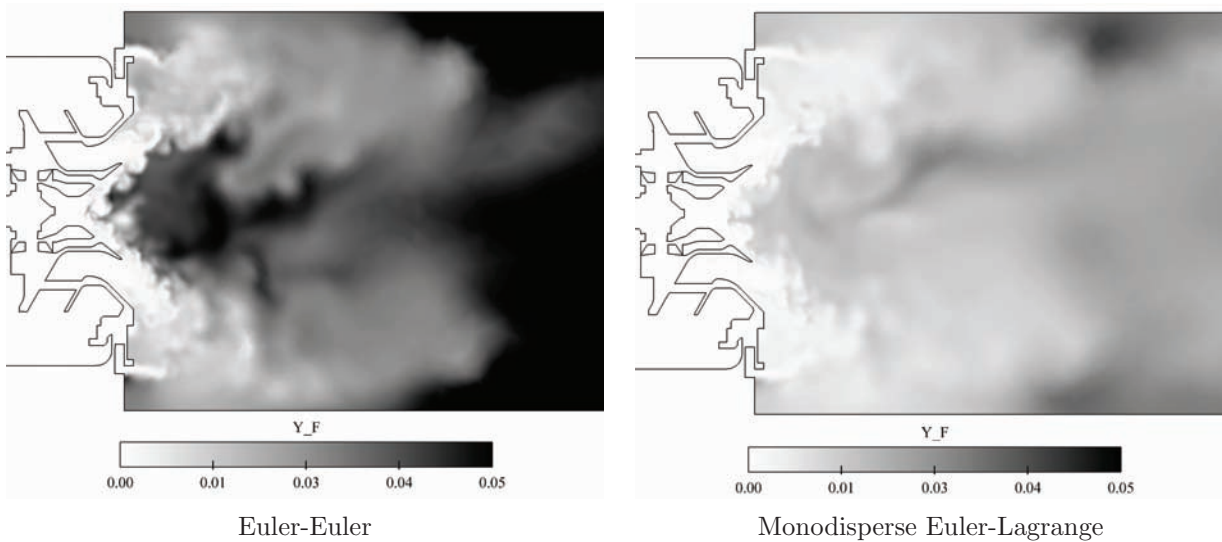


Figure 11.23: Comparison of *EE* results with monodisperse *EL* results. Left and right: field of the fuel species mass fraction Y_F [-] on the plane $y = 0$.

fact that the droplets quickly reach a state of equilibrium. Although they still evaporate rapidly and transfer enthalpy to the gaseous phase in the form of the latent heat of the evaporated mass, droplets no longer undergo the strong, purely conductive heat exchange that dominates during the initial heating phase.

Considering the resulting gaseous temperature fields (figures 11.25 and 11.27), it is quite notable that despite the visible differences in the distribution of the source terms between *EL* and *EE*, the shape and dimensions of cooled-down zones in the gaseous flow are very similar in all cases.

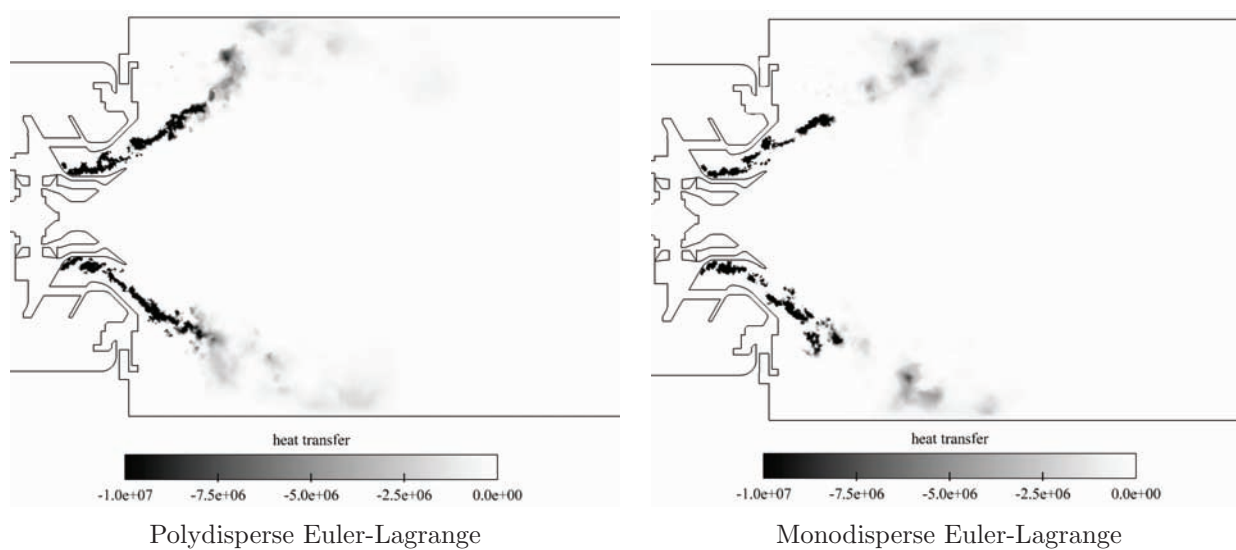


Figure 11.24: Comparison of polydisperse and monodisperse EL results. Left and right: field of the source term for mass transfer Π_g [J/(m³ s)] on the plane $y = 0$.

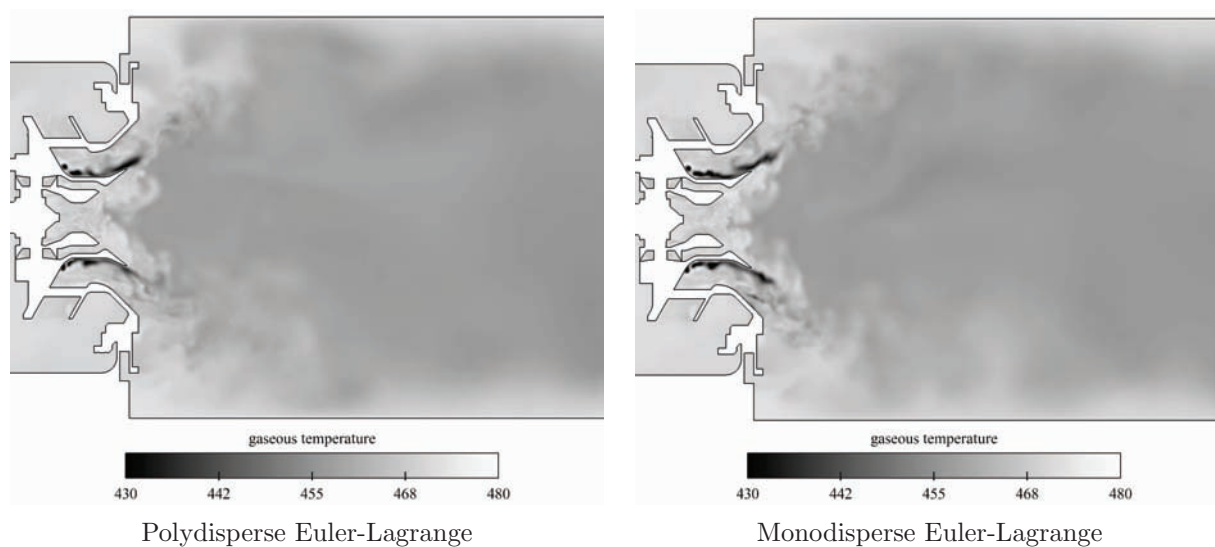


Figure 11.25: Comparison of polydisperse and monodisperse EL results. Left and right: gaseous phase temperature field T [K] on the plane $y = 0$.

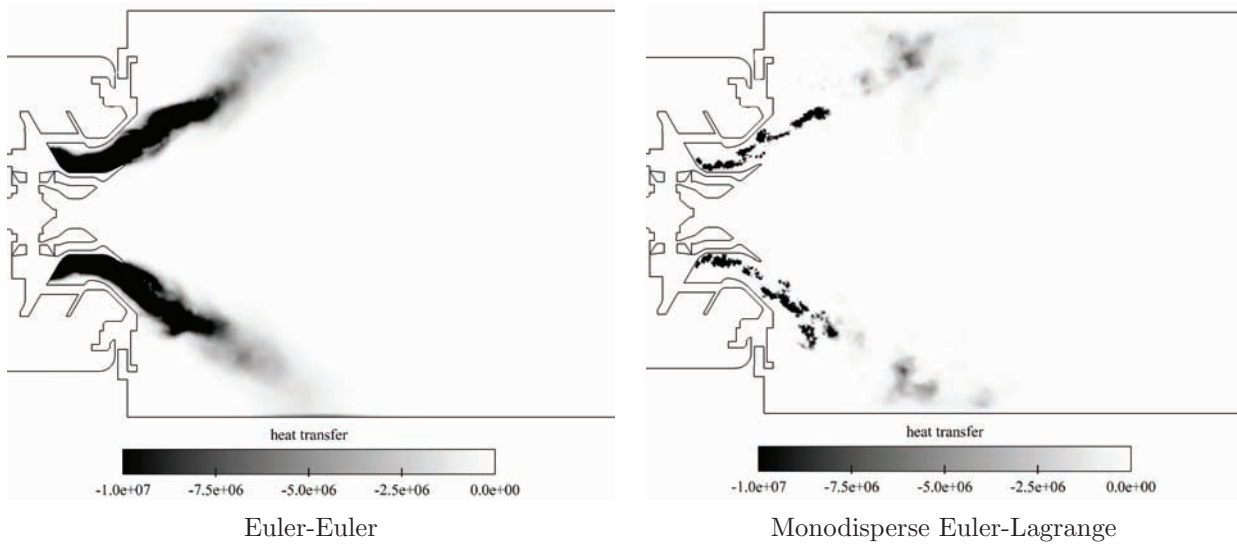


Figure 11.26: Comparison of *EE* results with monodisperse *EL* results. Left and right: field of the source term for mass transfer $\Pi_g [J/(m^3 s)]$ on the plane $y = 0$.

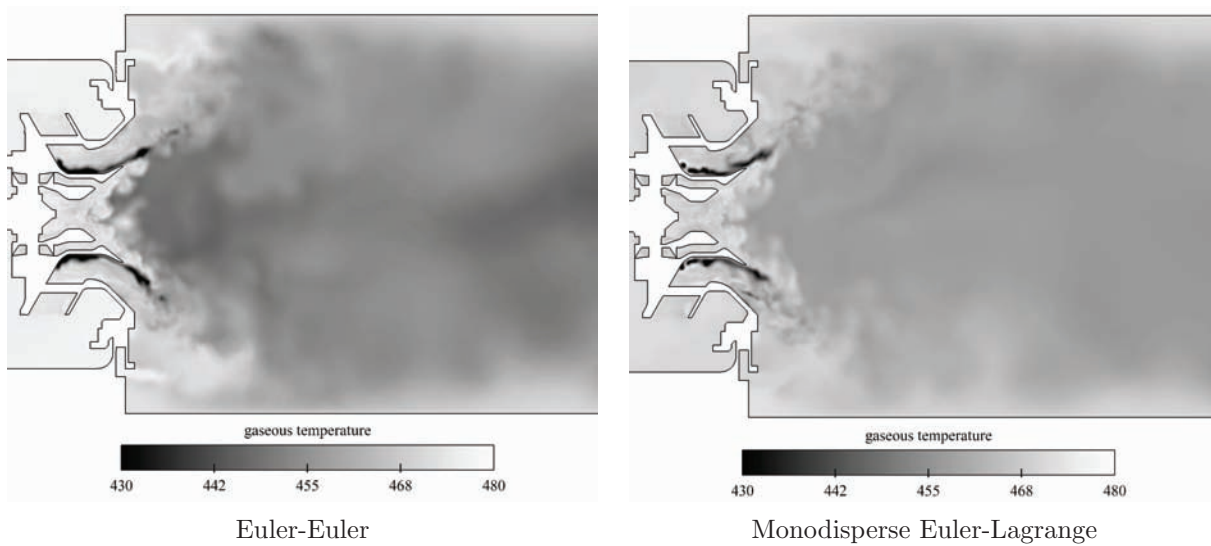


Figure 11.27: Comparison of *EE* results with monodisperse *EL* results. Left and right: gaseous phase temperature field $T [K]$ on the plane $y = 0$.

11.3.3 Time-averaged results, comparison with experimental data

After having discussed simulation results from a phenomenological point of view, the following section is dedicated to the verification by comparison to experimental data. The quantities considered are extracted along lines at distances of 10 mm and 15 mm from the swirler exit, as shown in figure 11.28. They include mean and fluctuating values for axial and tangential droplet velocities, the number density and liquid volume flux as well as representative diameters, among which the average diameter D_{10} and the Sauter mean diameter (SMD) D_{32} have been chosen.

In the EE simulations, average quantities are obtained using a classical on-the-fly averaging procedure. Average quantities of the EL calculations are obtained indirectly, using particle properties projected on the Eulerian grid with the same distribution formula as for the source terms (see section 5.9.3). The resulting pseudo-eulerian instantaneous fields are processed with the same on-the-fly averaging as the Eulerian methods. Regions without particles are attributed zero values, meaning that they are not counted into the average.

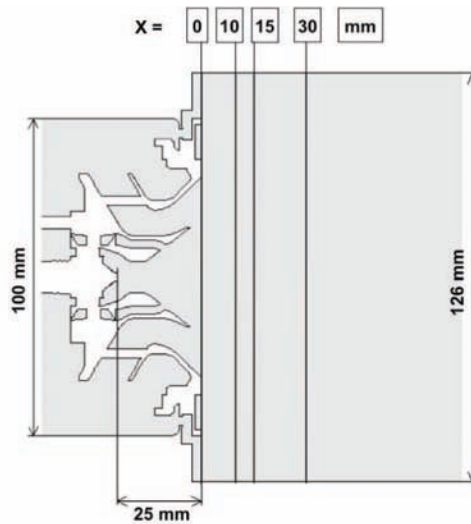


Figure 11.28: *TLC configuration - overview of the measurement lines at 10 mm, 15 mm and 30 mm.*

The profiles of time-averaged, axial droplet velocity, shown in figure 11.29, present generally good agreement between simulation and experiment. While the shape of the profiles is very well reproduced by all simulations (including the small, secondary peak created by the cooling films), there is a slight over-estimation of axial velocity in all three simulation results, which is found to be relatively constant over the entire width of the chamber. The profiles of both EL calculations coincide almost perfectly, revealing a negligible influence of polydispersion in this comparison.

A similar statement can be made in view of the mean, tangential droplet velocity profiles of figure 11.30. There is a very good agreement between all simulation results with mono- and polydisperse EL profiles being almost identical. The main peaks show a certain over-estimation of maximum tangential velocity and there is an additional reversal of tangential velocity components, located near the cooling films, that is not found in the experiment. This feature is only observed on one side of the chamber, which could hint at either a flow asymmetry that is not present in the experiment or a lack of convergence, which may over-represent the influence of large-scale motions in these regions.

Prior to the discussion of the droplet velocity fluctuation, the Stokes number (equation 4.4) of a typical particle is estimated. The droplet relaxation timescale τ_p is obtained from equation

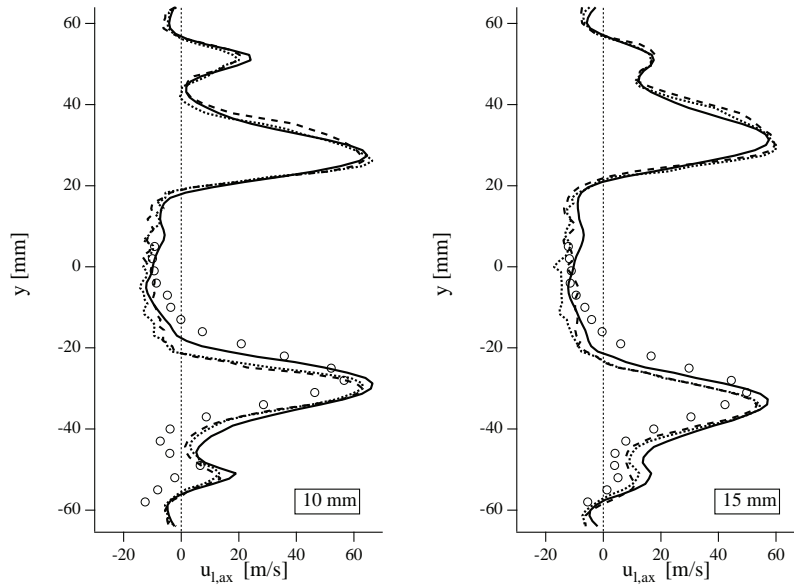


Figure 11.29: TLC configuration - axial liquid phase velocity profiles. Comparison of (inherently monodisperse) EE-results (—), monodisperse EL-results (---), polydisperse EL-results (⋯) and experimental data (○○○).

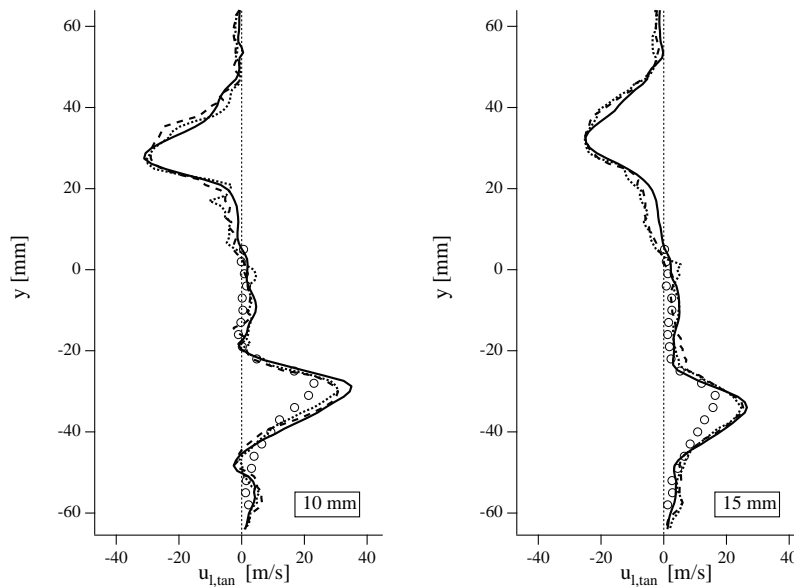


Figure 11.30: TLC configuration - tangential liquid phase velocity profiles. Comparison of (inherently monodisperse) EE-results (—), monodisperse EL-results (---), polydisperse EL-results (⋯) and experimental data (○○○).

4.2. The characteristic timescale of the gaseous flow, $\tau_L = L/u$ can be estimated from the width of the shear layer between the main flow region and the CTRZ ($L \approx 10 \text{ mm}$) and the velocity fluctuations encountered in this area ($u = u_{RMS} \approx 30 \text{ m/s}$, see figures 10.16 and 10.17). For a droplet of $d_p = 30 \mu\text{m}$, one obtains a Stokes number of $St = 4.5$. The particles can therefore be expected to have a certain inertial behaviour relative to the gas.

For the EE results, an element of post-processing has to be explained: as the governing equations of the EE approach resolve a field of mesoscopic quantities, the contribution of the Random, uncorrelated motion is neglected. While this does not affect the time-averaged results, it influences the fluctuating quantities: RMS levels of EE results can be expected to be lower than

their experimental or Lagrangian counterparts if the random uncorrelated velocity fluctuations are not taken into account. A correlation proposed by Vance et al. [149] allows to add this contribution a posteriori to the fluctuation field (see section 3.3.1 for more detail). This method has been applied successfully by Riber [124] and also by Simson in a his EE study of the TLC configuration with hollow-cone injection [138].

The results are shown in figures 11.31 and 11.32, while the influence of the Vance correction is presented in figures 11.33 and 11.34. Axial fluctuation profiles agree quite well with experimental data, but there are a few significant differences. Simulation results from all three methods have a secondary peak at about 35 mm radial distance, which is found neither in the experimental results, nor in the gaseous flow (figure 10.17). Judging from the gaseous flow topology, these peaks coincide with the shear layer created over the separated boundary layer on the outer swirler walls and stretching into the chamber. As the high velocity zones and therefore the associated shear layers are subjected to a slow, radial flapping motion (see also chapter 10), it could be argued that these peaks would be smoothed out on averages taken over longer periods. As the averages of the gaseous results are indeed taken over a longer physical time than those of the two-phase simulations, this appears to be a viable argument to be further investigated. Other than this additional peak, fluctuation levels tend to be slightly over-predicted in some locations but in view of the state of convergence, they are overall quite consistent.

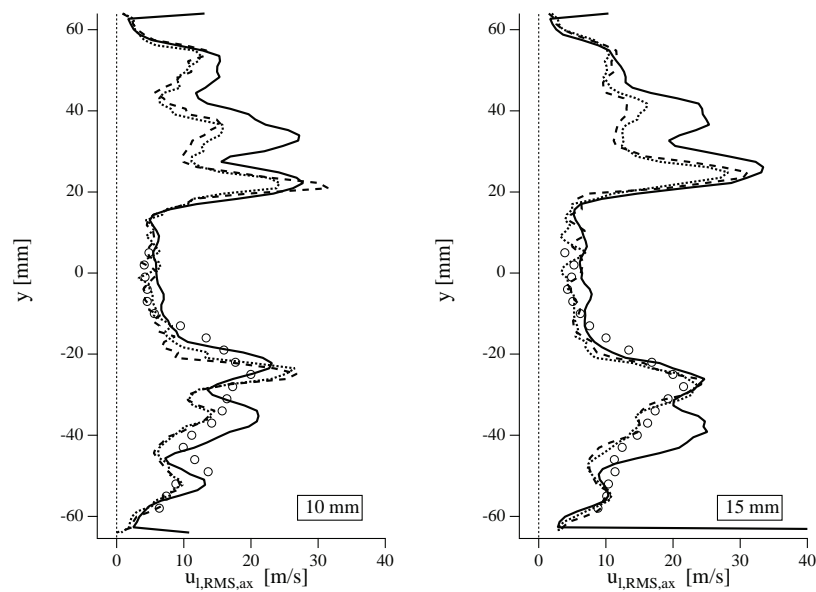


Figure 11.31: *TLC configuration - axial liquid phase velocity fluctuation profiles. Comparison of (inherently monodisperse) EE-results including the Vance correction (—), monodisperse EL-results (- - -), polydisperse EL-results (⋯) and experimental data (○ ○ ○).*

An additional remark can again be made on the very close fit of the Lagrangian results compared to each other, which shows that even for second-order statistics on velocity, the effect of polydispersion is negligible in this type of flow. This statement applies also on the profiles of tangential velocity fluctuations. Agreement between EL and EE results can be found to be good in zones of dense spray and high velocity (i.e. the main, primary droplet stream) and less accurate in less dense regions, near the wall or in the center of the chamber. This is due to the low rate of droplets to be sampled in EL, but also to the slower fluid motion, leading to insufficient convergence, which is especially critical for the use of the Vance correlation.

The influence of the correction on EE fluctuating quantities can be observed in figures 11.33

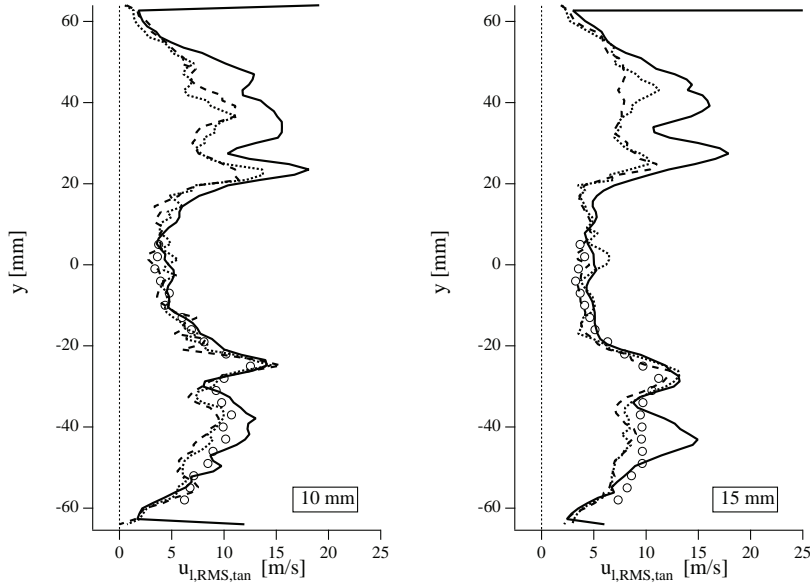


Figure 11.32: TLC configuration - tangential liquid phase velocity fluctuation profiles. Comparison of (inherently monodisperse) EE-results including the Vance correction (—), monodisperse EL-results (---), polydisperse EL-results (····) and experimental data (○ ○ ○).

and 11.34, which show corrected and uncorrected profiles alongside with experimental data and monodisperse EL results. It is clear that uncorrected fluctuations drop below the levels predicted by all other sources. Especially near the primary peak, i.e. zones of relatively well-converged statistics, the uncorrected values are under-estimated nearly by half and coincide well with the experiment and Lagrangian results after applying the correlation.

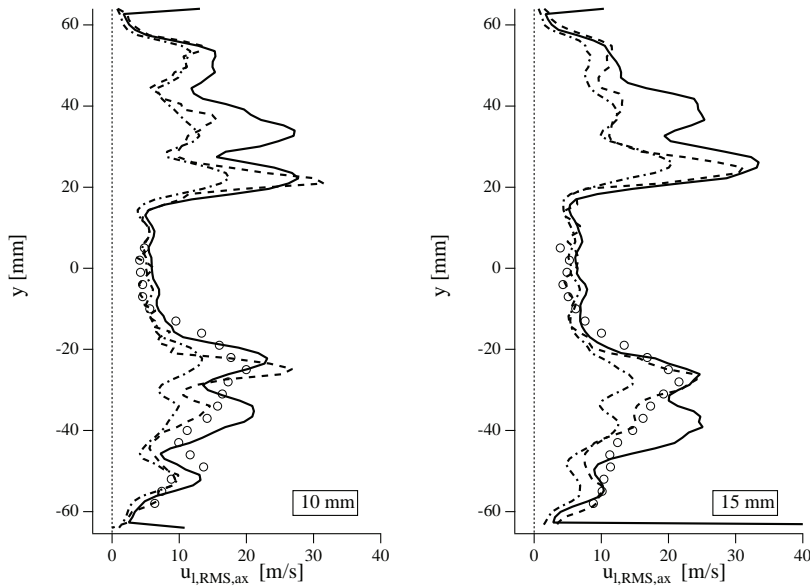


Figure 11.33: TLC configuration - axial liquid phase velocity fluctuation profiles. Comparison of (inherently monodisperse) EE-results including the Vance correction (—), EE-results without the Vance correction (---), monodisperse EL-results (····) and experimental data (○ ○ ○).

Additional experimental data is available for characteristic diameters recorded and averaged in the form of profiles at the same locations as velocity data presented before. As the most frequently used diameters, profiles of the mean diameter D_{10} as well as the Sauter mean diameter

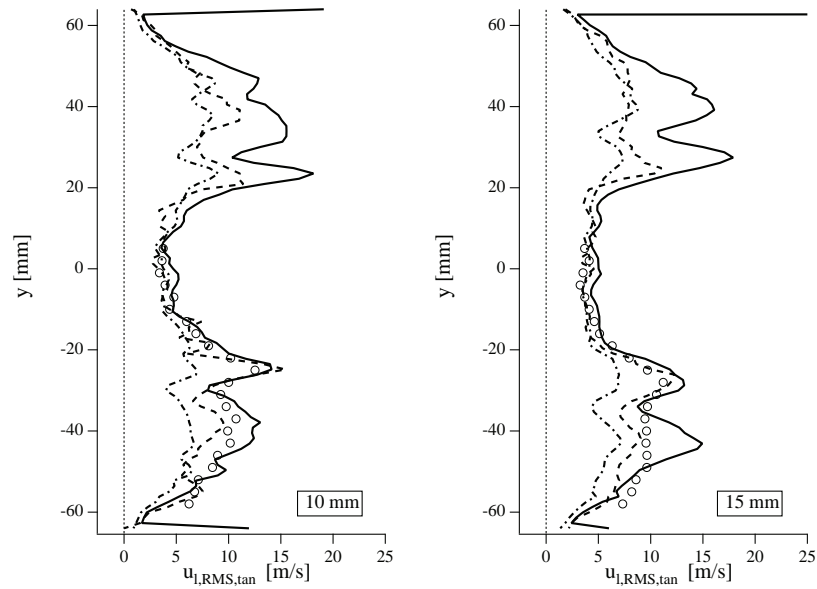


Figure 11.34: TLC configuration - tangential liquid phase velocity fluctuation profiles. Comparison of (inherently monodisperse) EE-results including the Vance correction (—), EE-results without the Vance correction (---), monodisperse EL-results (- - -) and experimental data (○ ○ ○).

(SMD) D_{32} are shown in figures 11.35 and 11.36 respectively.

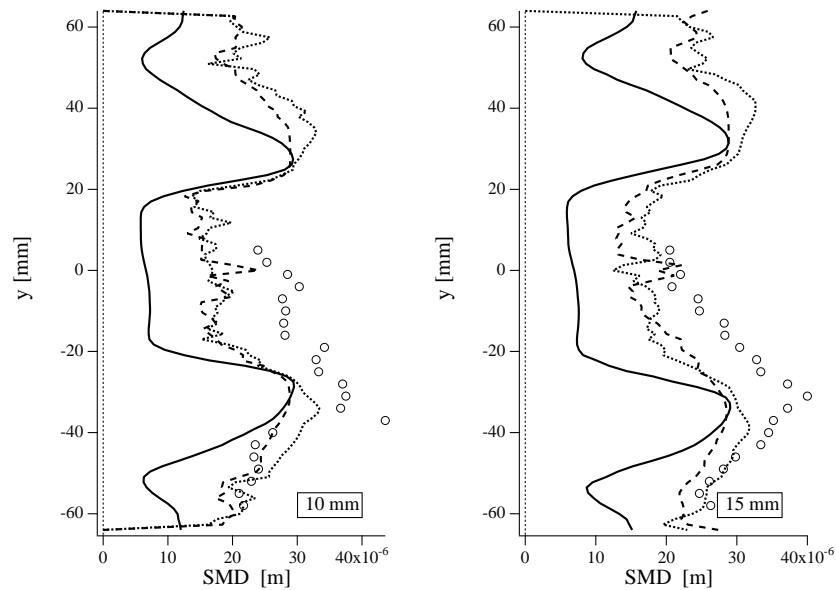


Figure 11.35: TLC configuration - profiles of the Sauter mean diameter. Comparison of (inherently monodisperse) EE-results (—), monodisperse EL-results (- - -), polydisperse EL-results (····) and experimental data (○ ○ ○).

Simulation results show a number of clear discrepancies when compared to the experiment. Generally, SMD levels from all simulations are under-estimated, while the mean diameter is over-predicted. This is a sign that the shape and/or the variance of the assumed droplet distribution at injection does not match the one of the experiment. In the monodisperse case, this is trivial as $D_{10} = D_{32}$. In the polydisperse case, these diameters are not identical but do not differ as clearly as observed in the experiment. One reason for this could lie in the low momentum flux ratio q at injection, which causes the spray to be formed very near the wall. As breakup

therefore takes place in the boundary layer, its mechanisms may differ from the ones observed in the Jet-in-crossflow testcase (chapter 8). Consequently, the correlation on which the droplet size distribution in the polydisperse case has been based (equation 11.1) could be inaccurate. Furthermore, the resulting droplet size distribution could be wider or differ in its shape from the log-normal distribution assumed here, causing the increased difference between D_{10} and SMD. Apart from this systematic discrepancy, several other points can be noted. Between the monodisperse cases (EE and EL), there is very good agreement in the area of the primary spray, roughly around 30 mm radial distance. In the outer and inner zones, the EE diameter curve drops to values near the clipping diameter of $5\ \mu\text{m}$. In the Lagrangian simulation, both characteristic diameters are significantly higher in these regions but strong oscillations show that the number of sampled particles is very low. This is consistent with histogram data in these areas (figure 11.18), which shows a large distribution of diameters in this area that also includes relatively big droplets. The differences between EE and monodisperse EL results outside the primary spray can thus clearly be attributed to polydisperse effects that appear over time in the EL formulation (despite being monodisperse at injection), whereas EE remains locally monodisperse.

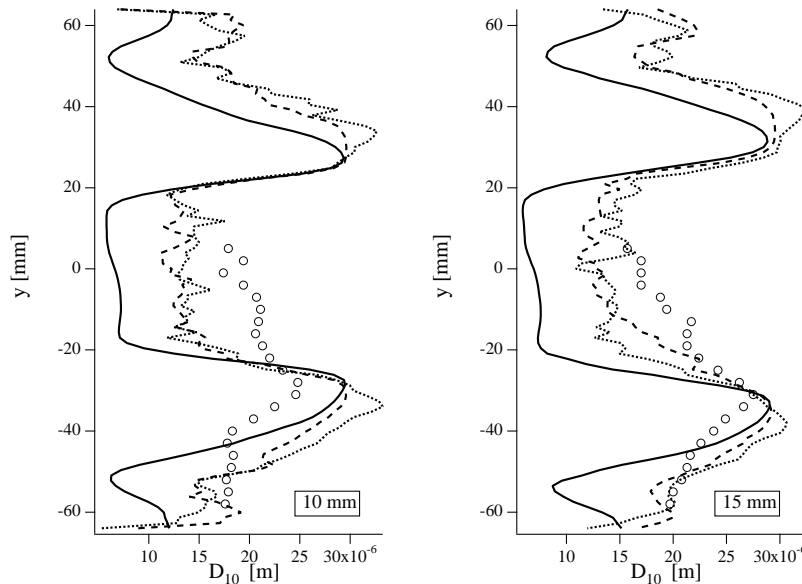


Figure 11.36: TLC configuration - profiles of the mean diameter (D_{10}). Comparison of (inherently monodisperse) EE-results (—), monodisperse EL-results (- - -), polydisperse EL-results (⋯) and experimental data (○○○).

A comparison between monodisperse and polydisperse EL results mainly reveals differences in the primary spray region. Here, the SMD tends to increase linearly from the center towards a peak in the primary spray. In the polydisperse case, this linear region extends further outwards with the maximum diameter increasing in magnitude. This behaviour can be attributed to inertial effects in the swirling flow, which force the biggest droplets farther outwards. This tendency is coherent with experimental data, where the slope and the magnitude of the diameter peak is even more pronounced. Additionally, this linear increase is not observed for the mean diameter from the experiment, which means that around 48 mm radial distance, there is a very large discrepancy between SMD and D_{10} . The local diameter distribution can therefore be expected to be very broad in this region, an effect that is not reproduced to the same extent, even by the polydisperse simulation.

The liquid volume flux, shown in figure 11.37 is an interesting quantity to consider because it provides information on the path the bulk of the liquid mass is following, but also on mass

conservation (assuming ρ_l is constant, which is the case in the present work). The comparison between simulation data and the experiment reveals major discrepancies. Both the magnitude and the location of the peaks differ by at least a factor 5 between the experiment and simulation results, while the latter agree very well between each other. Reasons for this discrepancy have been investigated in detail on the simulation side. Two scenarios are regarded as possible causes: the first is a problem of mass conservation in the simulations or the post-processing, the second is an inaccuracy of the liquid volume flux measurements using the patternator technique (see section 9.3.1). A problem of mass conservation is very improbable because the two simulation strategies differ strongly in principle and by their numerical implementation. Furthermore, they are verified by mass balance tools. Independent programming errors in both EL and EE going undetected and leading to the same results are highly unlikely. Furthermore, simulation results are consistent within themselves. Values of the liquid volume fraction, the droplet velocity and the mean diameter can, in particular for the monodisperse cases, be probed locally and compared to the flux data from the postprocessing, leading to consistent results.

Experimental data show certain elements of inconsistency. Attempts to reconstruct the liquid volume flux locally using measurement data on the droplet number density (figure 11.38), the mean diameter and liquid phase velocity did not yield the volume fluxes of the direct measurement. A comparison of experimental data obtained for different liquid mass fluxes at injection raises additional questions as the liquid volume flux for the case of 20 g/s is significantly lower than the one obtained for 10 g/s .

There is a high degree of confidence in the simulation results, but ultimately, as the cause cannot be further isolated the issue remains unclosed. The results are nevertheless presented here as a matter of completeness and for the comparison between simulation results.

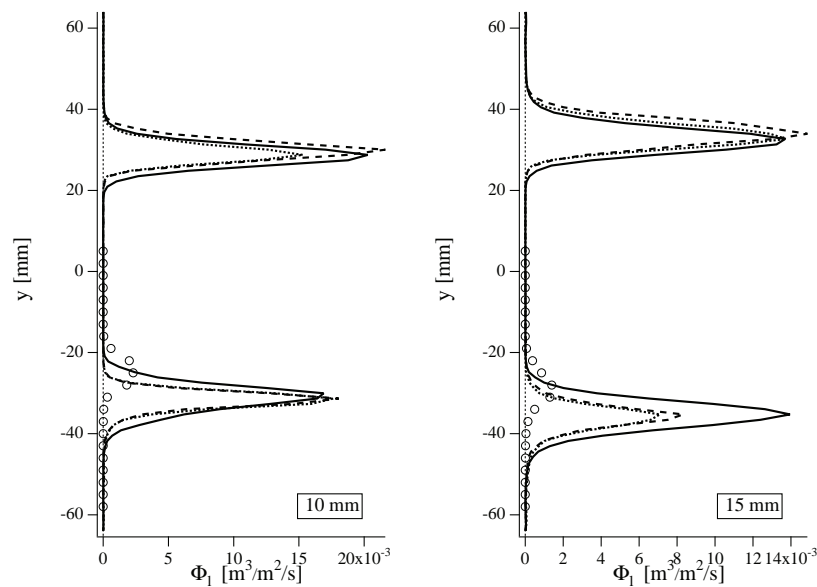


Figure 11.37: *TLC configuration - profiles of liquid volume flux. Comparison of (inherently monodisperse) EE-results (—), monodisperse EL-results (---), polydisperse EL-results (⋯) and experimental data (○○○).*

The final quantity to be considered is the droplet number density n_l (figure 11.38), which has already been commented in the preceding paragraph. An additional property that should be mentioned here is the non-zero number density encountered in all low-density regions of the EE simulation. This is a direct result of the clipping that is applied in EE for regions that are essentially devoid of droplets. As the diameter is simultaneously very low in these areas, the actual liquid volume fraction takes a value of the order of $\alpha_l \approx 3 \cdot 10^{-7}$, which can be considered a negligible value.

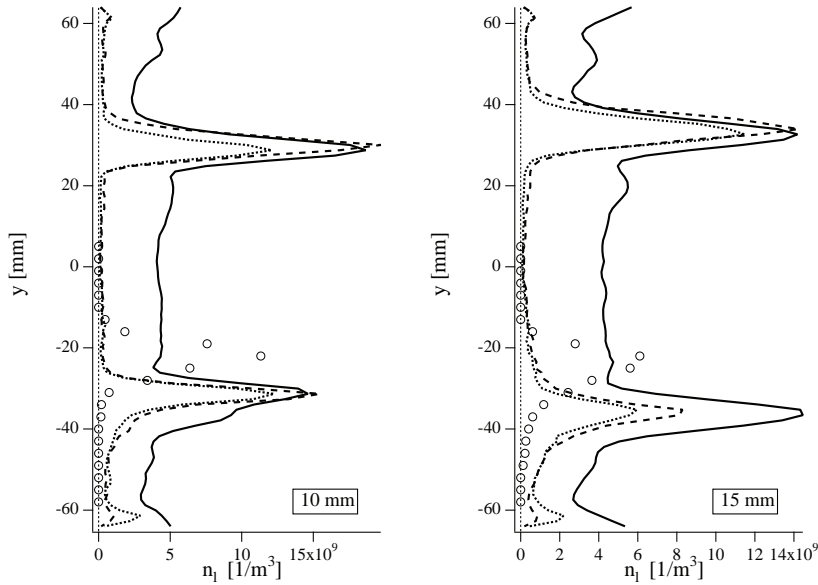


Figure 11.38: TLC configuration - profiles of the particle number density. Comparison of (inherently monodisperse) EE-results (—), monodisperse EL-results (- - -), polydisperse EL-results (⋯) and experimental data (○ ○ ○).

11.4 Computational cost

The computational cost associated with EE and EL methods is an important part of the global comparison. Table 11.1 lists the key figures of the three simulation cases. The key finding is a significantly higher cost of the EE simulation, where there is almost a factor 2 relative to the polydisperse EL case. Interestingly, the number of particles in the monodisperse EL case is slightly higher compared to its polydisperse counterpart, which leads to a slight advantage of the latter.

CPU times			
	EE	EL monodisp.	EL polydisp.
Number of numerical particles	-	1282155	1115579
Averaging time [s]	$16.1 \cdot 10^{-3}$	$43.6 \cdot 10^{-3}$	$41.5 \cdot 10^{-3}$
Av. time / residence time [-]	0.412	1.12	1.06
CPU hours / res. time [-]	473	255	247
64 processors on a SGI Altix ICE 8200 EX (Jade, CINES)			

Table 11.1: Summary of the CPU times of two-phase-flow simulations of the TLC configuration

The apparent superiority of the EL approach in terms of CPU cost must, however, be relativized. One aspect is the use of the parcel approach for EL, which considerably accelerates the method for high particle numbers. The second is the longer time that is needed to achieve a given degree of statistical convergence, especially for RMS values. The comparison of averaging time over the residence time in the chamber between EL and EE shows roughly a factor 2 in favour of the EE method although the term “degree of convergence” is somewhat arbitrary. Here, not using the parcel approach would actually accelerate the convergence of Lagrangian statistics. It depends on the computer resources and the scaling characteristics of the code if this alternative is advisable or not.

11.5 Conclusion

Three different two-phase flow simulations have been performed in an effort to compare the Euler-Euler method to a Lagrangian approach, including two Lagrangian cases to assess the influence of polydispersion on the results. The focus of the result's discussion was on droplet dynamics and evaporation effects. Phenomenological observations are backed up by the quantitative comparison to experimental data, which shows globally good agreement and leads to a good level of confidence in the results of all three simulation cases.

In terms of droplet dynamics, all results show a good level of accuracy, even in the case of the Eulerian results, where doubts remained concerning the capability of a first-order scheme to reproduce correct fluctuation levels. The use of an a-posteriori reconstruction of the random uncorrelated fluctuations that are neglected in the mesoscopic Eulerian formulation could be demonstrated to correctly raise fluctuation levels to the values seen in the experiment and the Lagrangian simulations. Additionally, the influence of polydispersion was observed to have very little influence on the first and second order statistics of droplet velocities.

In terms of prediction of characteristic diameters in the spray, even the polydisperse simulation fails to predict the correct levels, although general tendencies are quite well-reproduced. Here, the simulations mainly suffer from the lack of knowledge about the diameter distribution of the spray created by the multipoint injection. The empirical correlation used in this context shows limited accuracy at the comparison with the experiment. The development of models that are able to predict atomization processes for injection cases is therefore regarded a key priority in future efforts to ameliorate the results.

Droplet diameter and temperature evolution have been analyzed globally, along particles trajectories and in the form of histograms. A good agreement between simulation results was observed, particularly on the wet bulb temperature that takes very comparable levels by droplets in all simulation results as they reach equilibrium. The effect of a polydisperse injection influences mainly the primary spray regions. Inside the recirculation zones, polydispersion naturally develops for the Lagrangian simulation with monodisperse injection, too. In these areas, differences between EL and EE are generally quite pronounced, which is also due to the clipping method being in effect at those location, freezing the further evolution of the spray.

Coupling with the gaseous phase reveals differences between EL and EE in terms of the distribution of source terms. Owing to the nature of the EE approach, the source term field is much smoother and more widely distributed compared to the very local and sharply delimited source terms found in the EL results. However, polydispersion revealed a tendency to slightly smooth these zones due a quicker diffusion of compact droplet streams, which can help reducing the risk of destabilizing of the gaseous phase numerical scheme.

As a general conclusion of this chapter, it can be stated that both EE and EL can provide very satisfying results in terms of droplet dynamics. In this field, polydispersion did not bring notable improvement for the results. Evaporation is also globally well captured by both methods. Here, the EL method and polydispersion in particular locally leads to additional physical detail that could prove to be significant in the presence of a flame. For this type of non-reacting application, EE proves to be a very capable method, that only falls behind the EL formulation in very limited aspects. On the other hand, the overall potential of the Lagrange formulation in future applications involving more complex physics should not be under-estimated.

11.6 Tables

Plenum inlet	
Mass flux	0,365 kg/s
Temperature	473 K
Collar perforation	
Mass flux	0,012 kg/s
Temperature	473 K
Walls	
Wall temperature	473 K
Multipoint injection	
liquid mass flux	10 g/s
liquid phase temperature	300 K

Table 11.2: Boundary values, liquid and gaseous phase

Liquid phase properties	Kerosene surrogate
Boiling temperature	$T_{eb} = 489.0 K$
Density	$\rho_l = 782.03 kg/m^3$
Heat capacity	$C_{p,l} = 3.0077 \times 10^3 J/kg/K$
Evaporation heat	$L_{ev} = 323.19 \times 10^3 J/kg$

Table 11.3: Physical properties of the kerosene surrogate, at boiling point and standard pressure.

Numerical scheme (gas phase)	Lax Wendroff
Scheme spatial precision	2nd order
Scheme temporal precision	2nd order
Numerical scheme (liquid phase)	PSI
Scheme spatial precision	2nd order
Scheme temporal precision	1st order
Liquid phase coupling terms	two-way-coupling evaporation no model for the RUM
SGS model (gas)	standard Smagorinsky
SGS model (liquid)	Yoshizawa + Smagorinsky [100]
Artificial viscosity (gas)	Colin sensor [32]
2nd order coefficient	0.1
4th order coefficient	0.023
Artificial viscosity (liquide)	Colin sensor [32]
2nd order coefficient	0.05
4th order coefficient	0.005

Table 11.4: Numerical parameters used in the Euler-Euler simulations

Numerical scheme (gas phase)	Lax Wendroff
Scheme spatial precision	2nd order
Scheme temporal precision	2nd order
Liquid phase coupling	two-way-coupling evaporation
Interpolation method	Taylor
Phys. particles per parcel	10
SGS model (gas)	standard Smagorinsky
Artificial viscosity (gas)	Colin sensor [32]
2nd order coefficient	0.1
4th order coefficient	0.023

Table 11.5: Numerical parameters used in the Euler-Lagrange simulations

Eulerian injection parameters	
Number of injectors	24
Prescribed mass flux per injector	$0.4167 \cdot 10^{-3}$ kg/s
Injection velocity	2.714 m/s
Droplet temperature	300 K
Droplet diameter	monodisperse at $30.0 \cdot 10^{-6}$ m
Injection type	Disk
Disk diameter	2.5 mm (enlarged orifice diam.)
Column model	none

Table 11.6: Injection conditions of the Euler-Euler case

Monodisperse Lagrangian injection parameters	
Number of injectors	24
Prescribed mass flux per injector	$0.4167 \cdot 10^{-3}$ kg/s
Injection velocity	2.714 m/s
Droplet temperature	300 K
Droplet diameter	monodisperse at $30.0 \cdot 10^{-6}$ m
Injection type	Disk
Disk diameter	0.5 mm (original orifice diam.)
Column model	none

Table 11.7: Injection conditions of the monodisperse Euler-Lagrange case

Polydisperse Lagrangian injection parameters	
Number of injectors	24
Prescribed mass flux per injector	$0.4167 \cdot 10^{-3}$ kg/s
Injection velocity	2.714 m/s
Droplet temperature	300 K
Droplet diameter	polydisperse
particle size distribution	log-normal
Mean droplet diameter	$41.31 \cdot 10^{-6}$ m
Standard deviation	$8.3515 \cdot 10^{-6}$ m
Minimum diameter	$10.0 \cdot 10^{-6}$ m
Maximum diameter	$80.0 \cdot 10^{-6}$ m
Injection type	Disk
Disk diameter	0.5 mm (original orifice diam.)
Column model	none

Table 11.8: Injection conditions of the polydisperse Euler-Lagrange case

Bibliography

- [1] R. Abgrall. Toward the ultimate conservative scheme: following the quest. *J. Comput. Phys.*, 167(2):277–315, 2001.
- [2] B. Abramzon and W. A. Sirignano. Droplet vaporisation model for spray combustion calculations. *Int. J. Heat and Mass Transfer*, 9:1605–1618, 1989.
- [3] M. Adelberg. Breakup Rate and Penetration of a Liquid Jet in a Gas Stream. *AIAA Journal*, 6:1134–1147, 1968.
- [4] S. K. Aggarwal, A. Y. Tong, and W. A. Sirignano. A comparison of vaporization models in spray calculations. *AIAA Journal*, 22(10):1448–1457, 1984.
- [5] S. V. Apte, M. Gorokhovski, and P. Moin. LES of atomizing spray with stochastic modeling of secondary breakup. *Int. J. Multiphase Flow*, 29:1503–1522, 2003.
- [6] S. V. Apte, K. Mahesh, P. Moin, and J. C. Oefelein. Large-eddy simulation of swirling particle-laden flows in a coaxial-jet combustor. *Int. J. Multiphase Flow*, 29(8):1311–1331, 2003.
- [7] S.V. Apte, K. Mahesh, M. Gorokhovski, and P. Moin. Stochastic modeling of atomizing spray in a complex swirl injector using large eddy simulation. *Proc. Combust. Inst.*, 32(2):2257–2266, 2009.
- [8] J.S. Baggett. On the feasibility of merging LES with RANS for the near-wall region of attached turbulent flows. *CTR, Ann. Research Briefs*, pages 267–277, 1998.
- [9] JS Baggett, J. Jimenez, and AG Kravchenko. Resolution requirements in large-eddy simulations of shear flows. *CTR, Ann. Research Briefs*, pages 51–66, 1997.
- [10] GI Barenblatt. Scaling laws for fully developed turbulent shear flows. Part 1. Basic hypotheses and analysis. *J. Fluid Mech.*, 248:513–520, 2006.
- [11] J. Becker and C. Hassa. Breakup and atomization of a kerosene jet in crossflow at elevated pressure. *Atom. Sprays*, 11:49–67, 2002.
- [12] J. Bellan and M. Summerfield. Theoretical examination of assumptions commonly used for the gas phase surrounding a burning droplet. *Combust. Flame*, 33:107–122, 1978.
- [13] R. Ben Dakhli. *Combustion stationnaire et instationnaire de mélanges diphasiques*. PhD thesis, Ecole Centrale Paris, 2001.
- [14] N. Bertier, F. Dupoirieux, L. Matuszewski, and C. Guin. Simulation numérique d’une chambre de combustion multipoint. In *2nd Colloque INCA*, October 2008.
- [15] R.B. Bird, W.E. Stewart, and E.N. Lighfoot. *Transport phenomena*. John Wiley & Sons, New York, 1960.

- [16] G. Bittlinger and N. Brehm. High pressure combustion test of lean premixed prevaporized (LPP) modules in an axially staged combustor using a multisector rig. In *ISABE-International Symposium on Air Breathing Engines, 14 th, Florence, Italy, 1999*.
- [17] M. Boileau. Simulation numérique de la combustion diphasique. Rapport de stage WN/CFD/03/73, CERFACS, 2003.
- [18] M. Boileau. *Simulation aux grandes échelles de l'allumage diphasique des foyers aéronautiques*. PhD thesis, INP Toulouse, (not yet defended) 2007.
- [19] M. Boileau. *Simulation aux grandes échelles de l'allumage diphasique des foyers aéronautiques -TH/CFD/07/103*. PhD thesis, Institut National Polytechnique de Toulouse, France - Dynamique des Fluides, 2007.
- [20] M. Boileau, G. Staffelbach, B. Cuenot, T. Poinsot, and C. Bérat. LES of an ignition sequence in a gas turbine engine. *Combust. Flame*, 154(1-2):2–22, 2008.
- [21] M.H. Buschmann and M. Gad-el Hak. Debate concerning the mean-velocity profile of a turbulent boundary layer. *AIAA Journal*, 41(4):565–572, 2003.
- [22] O. Cabrit and F.. Nicoud. Direct simulations for wall modeling of multicomponent reacting compressible turbulent flows. *Phys. Fluids*, 21(055108), 2009.
- [23] M. Cazalens, S. Roux, C. Sensiau, and T. Poinsot. Combustion Instability Problems Analysis for High Pressure Jet Engine Cores. *J. Prop. Power*, 24(4):770–778, 2008.
- [24] JL Champion, P. Di Martino, and X. Coron. Influence of flow characteristics on the discharge coefficient of a multiperforated wall. *Turbo Expo*, pages 6–9, 2005.
- [25] S. Chapman and T.G. Cowling. *The Mathematical Theory of Non-Uniform Gases*. Cambridge University Press, cambridge mathematical library edition, 1939 (digital reprint 1999).
- [26] P. Chassaing. *Turbulence en mécanique des fluides, analyse du phénomène en vue de sa modélisation à l'usage de l'ingénieur*. Cépaduès-éditions, Toulouse, France, 2000.
- [27] T. H. Chen, C. R. Smith, D. G. Schommer, and A. S. Nejad. Multi-Zone Behavior of Transverse Liquid Jet in High Speed Flow. *AIAA, Aerospace Sciences Meeting and Exhibit, 31st, Reno, NV, Jan. 11-14*, 93(0453), 1993.
- [28] W.-H. Chou, L.-P. Hsiang, and G.M. Faeth. Temporal Properties of Drop Breakup in the Shear Breakup Regime. *Int. J. Multiphase Flow*, 23(4):651–669, 1997.
- [29] R. Clift, J. R. Grace, and M. E. Weber. *Bubbles, Drops, and Particles*. Academic Press, 1978.
- [30] D. Coles. The law of the wake in the turbulent boundary layer. *J. Fluid Mech.*, 1(02):191–226, 2006.
- [31] O. Colin. *Simulations aux grandes échelles de la combustion turbulente prémélangée dans les statoréacteurs*. PhD thesis, INP Toulouse, 2000.
- [32] O. Colin and M. Rudgyard. Development of high-order Taylor-Galerkin schemes for unsteady calculations. *J. Comput. Phys.*, 162(2):338–371, 2000.
- [33] E.M. Conway. *High-speed dreams: NASA and the technopolitics of supersonic transportation, 1945-1999*. Johns Hopkins Univ. Pr., 2005.

- [34] J. Deardorff. A numerical study of three-dimensional turbulent channel flow at large Reynolds numbers. *J. Fluid Mech.*, 41:453–480, 1970.
- [35] H. Deconinck, H. Paillere, R. Struijs, and P.L. Roe. Multidimensional upwind schemes based on fluctuation-splitting for systems of conservation laws. *Comput. Mech.*, 11(5-6):323–340, 1993.
- [36] P. Dellenback, D. Metzger, and G. Neitzel. Measurement in turbulent swirling flows through an abrupt axisymmetric expansion. *AIAA Journal*, 13(4):669–681, 1988.
- [37] W. Dodds. Twin annular premixing swirler twin annular premixing swirler (taps) combustor. ([url: www.techtransfer.berkeley.edu/aviation05downloads/Dodds.pdf](http://www.techtransfer.berkeley.edu/aviation05downloads/Dodds.pdf)).
- [38] F. Ducros, P. Comte, and M. Lesieur. Large-eddy simulation of transition to turbulence in a boundary layer developing spatially over a flat plate. *J. Fluid Mech.*, 326:1–36, 1996.
- [39] D. Dunn-Rankin. *Lean combustion: technology and control*. Academic Pr, 2008.
- [40] F. Durst and M. Zaré. Laser Doppler measurements in two-phase flows. In *The accuracy of flow measurements by laser Doppler methods, Proceedings of the LDA-Symposium, Copenhagen, Denmark, August 25-28, 1975.*, 1975.
- [41] P. Fede and O. Simonin. Numerical study of the subgrid fluid turbulence effects on the statistics of heavy colliding particles. *Phys. Fluids*, 18(045103), 2006.
- [42] R. Fedkiw, T. Aslam, B. Merriman, and S. Osher. A non-oscillatory Eulerian approach to interfaces in multimaterial flows (The Ghost Fluid Method). *J. Comput. Phys.*, 152:457–492, 1999.
- [43] P. Février. *Etude numérique des effets de concentration préférentielle et de corrélation spatiale entre vitesses de particules solides en turbulence homogène isotrope stationnaire*. PhD thesis, INP Toulouse, 2000.
- [44] P. Février and O. Simonin. Statistical and Continuum Modelling of Turbulent Reactive Particulate Flows. Part 2: Application of a Two-Phase Second-Moment Transport Model For Prediction of Turbulent Gas-Particle Flows. In *Theoretical and Experimental Modeling of Particulate Flows, Lecture Series 2000-06, von Karman Institute for Fluid Dynamics, Belgium*, 2000.
- [45] P. Février, O. Simonin, and K. Squires. Partitioning of Particle Velocities in Gas-Solid Turbulent Flows into a Continuous Field and a Spatially Uncorrelated Random Distribution: Theoretical Formalism and Numerical Study. *J. Fluid Mech.*, 533:1–46, 2005.
- [46] S. Freitag and C. Hassa. Spray characteristics of a kerosene jet in cross flow of air at elevated pressure. In *ILASS, paper ID A134*, Como Lake, Italy, 2008.
- [47] A. Frohn and N. Roth. *Dynamics of Droplets*. Springer-Verlag, New York, 2000.
- [48] R. P. Fuller, P.-K. Wu, and K. A. Kirkendall. Effects of Injection Angle on Atomization of Liquid Jets in Transverse Airflow. *AIAA Journal*, 38(1):64–72, 2000.
- [49] M. García. *Développement et validation du formalisme Euler-Lagrange dans un solveur parallèle et non-structuré pour la simulation aux grandes échelles - TH/CFD/09/1*. PhD thesis, Université de Toulouse - Ecole doctorale : Mécanique, Energétique, Génie civil, Procédés, 2009.
- [50] M. Germano, U. Piomelli, P. Moin, and W. Cabot. A dynamic subgrid-scale eddy viscosity model. *Phys. Fluids*, 3(7):1760–1765, 1991.

- [51] G. A. E. Godsave. Studies of the combustion of drops in a fuel spray: the burning of single drops of fuel. In *Proc. Combust. Inst.*, pages 847–864, Baltimore, 1953. The Combustion Institute.
- [52] M. Gritsch, A. Schulz, and S. Wittig. Effect of crossflows on the discharge coefficient of film cooling holes with varying angles of inclination and orientation. *J. Turbomachinery*, 123:781, 2001.
- [53] Grötzbach. Direct numerical and large eddy simulation of turbulent channel flows. In N. P. Cheremisinoff, editor, *Encyclopedia of Fluid Mechanics*, pages 1337–1391, Gulf, West Orange, NJ, 1987.
- [54] D. Gueyffier, J. Li, A. Nadim, R. Scardovelli, and S. Zaleski. Volume-of-fluid interface tracking with smoothed surface stress methods for three-dimensional flows. *J. Comput. Phys.*, 152(2):423–456, 1999.
- [55] N. Guézennec and T. Poinso. Acoustically Nonreflecting and Reflecting Boundary Conditions for Vorticity Injection in Compressible Solvers. *AIAA Journal*, 47(7), 2009.
- [56] M.G Hall. Vortex breakdown. *Ann. Rev. Fluid Mech.*, 4(1):195–218, 1972.
- [57] G. Haller. An objective definition of a vortex. *J. Fluid Mech.*, 525:1–26, 2005.
- [58] N. Hay and D. Lampard. Discharge coefficient of turbine cooling holes: a review. *J. Turbomachinery*, 120:314, 1998.
- [59] S. Hayashi and S. Kumagai. Flame propagation in fuel droplet-vapor-air mixtures. In *Fifteenth (International) Symposium on Combustion*, pages 445–452. The Combustion Institute, 1975.
- [60] M. Herrmann. Detailed Numerical Simulations of the Primary Atomization of a Turbulent Liquid Jet in Crossflow. In *American Physical Society, 61st Annual Meeting of the APS Division of Fluid Dynamics, November 23-25, 2008, abstract# GP. 001*, 2008.
- [61] M. Herrmann. Detailed Simulations of the Breakup Processes of Turbulent Liquid Jets in Subsonic Crossflows. In *11th Triennial International Conference on Liquid Atomization and Spray Systems, July 2009, paper# 188*, 2009.
- [62] E.D. Hirleman. Modeling of multiple scattering effects in Fraunhofer diffraction particle size analysis. *Part. Part. Syst. Charact.*, 5:57–65, 1988.
- [63] C. Hirsch. *Numerical Computation of internal and external flows*. John Wiley, New York, 1988.
- [64] Hirschfelder, Curtis, and Bird. *Molecular Theory of Gases and Liquids*. John Wiley & Sons, New York, 1954 edition, 1954.
- [65] G. Hoffmann and C. Benocci. Approximate wall boundary conditions for large eddy simulations. In Benzi R., editor, *Advances in turbulence V*, pages 222–228. Kluwer Academic Publishers, 1995.
- [66] S. Hoyas and J. Jiménez. Scaling of the velocity fluctuations in turbulent channels up to $Re=2003$. *Phys. Fluids*, 18:011702, 2006.
- [67] L.-P. Hsiang and G.M. Faeth. Near-Limit Drop Deformation and Secondary Breakup. *Int. J. Multiphase Flow*, 18(5):635–652, 1992.
- [68] G. L. Hubbard, V. E. Denny, and A. F. Mills. Droplet evaporation: effects of transients and variable properties. *Int. J. Heat and Mass Transfer*, 18(9):1003–1008, 1975.

- [69] JCR Hunt, AA Wray, and P. Moin. Eddies, streams, and convergence zones in turbulent flows. In *CTR, Proceedings of the 1988 Summer Program*, pages 193–208, 1988.
- [70] IE Idel’Cik. Memento des pertes de charge. *Paris*, 1969.
- [71] F. Jaegle, O. Cabrit, S. Mendez, and T. Poinso. Implementation methods of wall functions in cell-vertex numerical solvers. *Flow Turb. and Combustion*, Submitted.
- [72] A. Jameson, W. Schmidt, and E. Turkel. Numerical solution of the euler equations by finite volume methods using runge-kutta time stepping schemes. In AIAA paper 81-1259, editor, *14th Fluid and Plasma Dynamic Conference*, Palo Alto, 1981.
- [73] C. Jiménez. Personal communication.
- [74] A Kaufmann. *Vers la simulation des grandes échelles en formulation Euler/Euler des écoulements réactifs diphasiques*. PhD thesis, INP Toulouse, 2004.
- [75] W.M. Kays, M.E. Crawford, and B. Weigand. *Convective heat and mass transfer*. McGraw-Hill Science/Engineering/Math, 2004.
- [76] A. Keating and U. Piomelli. A dynamic stochastic forcing method as a wall-layer model for large-eddy simulation. *J. Turb.*, 7(1):1–24, 2006.
- [77] M. Klein, A. Sadiki, and J. Janicka. Investigation of the influence of the Reynolds number on a plane jet using direct numerical simulation. *Int. J. Heat Fluid Fl.*, 24(6):785–794, 2003.
- [78] R.H. Kraichnan. Diffusion by a random velocity field. *Phys. Fluids*, 13:22, 1970.
- [79] K.K. Kuo. *Principles of Combustion*. John Wiley, New York, 1986.
- [80] N. Lamarque. *Schémas numériques et conditions limites pour la simulation aux grandes échelles de la combustion diphasique dans les foyers d’hélicoptère - TH/CFD/07/117*. PhD thesis, Institut National Polytechnique de Toulouse, France - Dynamique des Fluides, 2007.
- [81] J. Lavedrine. *Simulations aux grandes échelles de l’écoulement diphasique dans des modèles d’injecteur de moteurs aéronautiques - TH/CFD/08/47*. PhD thesis, Institut Polytechnique National de Toulouse, France, 2008.
- [82] G. Lavergne and R. Lecourt. TLC deliverable, Task 2.2.1 Multi-point injection systems characterization. Technical report, ONERA DMAE.
- [83] CK Law. Unsteady droplet vaporization with droplet heating. *Combust. Flame*, 26:17–22, 1976.
- [84] P. D. Lax and B. Wendroff. Systems of conservation laws. *Comm. Pure Appl. Math.*, 13:217–237, 1960.
- [85] A.H. Lefebvre. *Gas Turbines Combustion*. Taylor & Francis, 1999.
- [86] S. Leibovich. Vortex Stability and Breakdown: Survey and Extension. *AIAA Journal*, 22(9):1192–1206, 1984.
- [87] D.K. Lilly. A proposed modification of the Germano subgrid scale closure method. *Phys. Fluids*, 4:633–635, 1992.
- [88] T. H. Lin, C. K. Law, and S. H. Chung. Theory of laminar flame propagation in off-stoichiometric dilute sprays. *Int. J. Heat and Mass Transfer*, 31:1023–1034, 1988.

- [89] T. H. Lin and Y. Y. Sheu. Theory of laminar flame propagation in near-stoichiometric dilute sprays. *Int. J. Heat and Mass Transfer*, 84:333–342, 1991.
- [90] M. Linkes. Evaluation of Numerical Strategies for the Simulation of Two-Phase Flows in the Eulerian-Eulerian Framework. Master's thesis, INP Toulouse ENSEEIHT, 2009.
- [91] T. Menard, S. Tanguy, and A. Berlemont. Coupling Level Set/VOF/Ghost Fluid method: Validation and applications to 3D simulations of jet primary break-up. *Int. J. Multiphase Flow*, 33:511–524, 2007.
- [92] S. Mendez. *Simulation numérique et modélisation de l'écoulement autour des parois multi-perforées - TH/CFD/07/104*. PhD thesis, Université de Montpellier II, France - Mathématiques - I2S, 2007.
- [93] S. Mendez and F. Nicoud. Adiabatic homogeneous model for flow around a multiperforated plate. *AIAA Journal*, 46(10):2623–2633, 2008.
- [94] S. Mendez and F. Nicoud. Large eddy simulation of a bi-periodic turbulent flow with effusion. *J. Fluid Mech.*, 598:27–65, 2008.
- [95] G. Mie. Beiträge zur Optik trüber Medien, speziell kolloidaler Metallösungen. *Annalen der Physik*, 4(25):377–445, 1908.
- [96] R. Miller and J. Bellan. Direct numerical simulation and subgrid analysis of a transitional droplet laden mixing layer. *Phys. Fluids*, 12(3), 1999.
- [97] R. S. Miller, K. Harstad, and J. Bellan. Evaluation of equilibrium and non-equilibrium evaporation models for many-droplet gas-liquid flow simulations. *Int. J. Multiphase Flow*, (24):1025–1055, 1998.
- [98] B. Mohammadi and G. Puigt. Wall functions in computational fluid mechanics. *Comput. Fluids*, 35(10):1108–1115, 2006.
- [99] P. Moin and SV Apte. Large-Eddy Simulation of Realistic Gas Turbine-Combustors. *AIAA Journal*, 44(4):698–708, 2006.
- [100] M. Moreau. *Modélisation numérique directe et des grandes échelles des écoulements turbulents gaz-particules dans le formalisme eulérien mésoscopique*. PhD thesis, INP Toulouse, 2006.
- [101] M. Moreau, B. Bedat, and O. Simonin. A priori testing of subgrid stress models for euler-euler two-phase LES from euler-lagrange simulations of gas-particle turbulent flow. In *18th Ann. Conf. on Liquid Atomization and Spray Systems*. ILASS Americas, 2005.
- [102] J.-B. Mossa. *Extension polydisperse pour la description euler-euler des écoulements diphasiques réactifs - TH/CFD/05/74*. PhD thesis, Institut National Polytechnique de Toulouse, France-Mécanique des fluides, 2005.
- [103] F. Nicoud, J. Baggett, P. Moin, and W. Cabot. Les wall-modeling based on optimal control theory. *Phys. Fluids*, 13(10):1629–1632, 2001.
- [104] F. Nicoud and F. Ducros. Subgrid-scale stress modelling based on the square of the velocity gradient. *Flow Turb. and Combustion*, 62(3):183–200, 1999.
- [105] M. Orain, F. Grisch, E. Jourdanneau, B. Rossow, C. Guin, and B. Trétout. Simultaneous measurements of equivalence ratio and flame structure in multipoint injectors using PLIF. *C. R. Mécanique*, 337(6-7):373–384, 2009.

- [106] P.J. O'Rourke and A.A. Amsden. The TAB method for numerical calculation of spray droplet breakup. In *International fuels and lubricants meeting and exposition*, volume 2, 1987.
- [107] N. Peters. The turbulent burning velocity for large-scale and small-scale turbulence. *J. Fluid Mech.*, 384:107 – 132, 1999.
- [108] N. Peters. *Turbulent combustion*. Cambridge University Press, 2000.
- [109] B.S. Petukhov. Heat transfer and friction in turbulent pipe flow with variable physical properties. *Adv. Heat Transfer*, 6:503–564, 1970.
- [110] U. Piomelli. Wall-Layer Models for Large-Eddy Simulations. *Progr. Aerospace Sci.*, 44:437–446, 2008.
- [111] U. Piomelli and E. Balaras. Wall-layer models for large-eddy simulations. *Ann. Rev. Fluid Mech.*, 34(1):349–374, 2002.
- [112] U. Piomelli, E. Balaras, H. Pasinato, K.D. Squires, and P.R. Spalart. The inner–outer layer interface in large-eddy simulations with wall-layer models. *Int. J. Heat Fluid Fl.*, 24(4):538–550, 2003.
- [113] U. Piomelli, J. Ferziger, P. Moin, and J. Kim. New approximate boundary conditions for large eddy simulations of wall-bounded flows. *Phys. Fluids A*, 1(6):1061–1068, June 1989.
- [114] T. Poinso and S.K. Lele. Boundary Conditions for Direct Simulation of Compressible Viscous Flows. *J. Comput. Phys.*, 101:104–129, 1992.
- [115] T. Poinso and D. Veynante. *Theoretical and numerical combustion*. R.T. Edwards, 2nd edition., 2005.
- [116] S.B. Pope. *Turbulent Flows*. Cambridge University Press, 2000.
- [117] L. Prandtl. Bericht über untersuchungen zur ausgebildeten turbulenz. *Zeitschrift für angewandte Mathematik und Mechanik*, 5:136 – 139, 1925.
- [118] M. Rachner, J. Becker, C. Hassa, and T. Doerr. Modelling of the atomization of a plain liquid fuel jet in crossflow at gas turbine conditions. *Aerospace Science and Technology*, 6:495–506, 2002.
- [119] S. Rajagopalan and R.A. Antonia. Some properties of the large structure in a fully developed turbulent duct flow. *Phys. Fluids*, 22:614, 1979.
- [120] A. A. Ranger and J. A. Nicholls. Aerodynamic Shattering of Liquid Drops. *AIAA Journal*, 7(2):285–290, February 1969.
- [121] W.E. Ranz and W.R. Marshall. Evaporation from drops. *Chem. Eng. Prog.*, 48(4):173, 1952.
- [122] R.D. Reitz. Modeling atomization processes in high-pressure vaporizing sprays. *Atom. Spray Technol.*, 3:309–337, 1987.
- [123] J. Réveillon and L. Vervisch. Analysis of weakly turbulent diluted-spray flames and spray combustion regimes. *J. Fluid Mech.*, 537:317–347, 2005.
- [124] E. Riber. *Développement de la méthode de simulation aux grandes échelles pour les écoulements diphasiques turbulents - TH/CFD/07/41*. PhD thesis, Institut National Polytechnique de Toulouse, France -Dynamique des Fluides, 2007.

- [125] E. Riber, M. Moreau, O. Simonin, and B. Cuenot. Towards Large Eddy Simulation of Non-Homogeneous Particle Laden Turbulent Gas Flows Using Euler-Euler Approach. In *11th Workshop on Two-Phase Flow Predictions*, Merseburg, Germany, 2005.
- [126] A. Roux. *Simulation aux Grandes Échelles d'un Statoréacteur - TH/CFD/09/65*. PhD thesis, Université de Toulouse - MEGeP (Dynamique des Fluides), 2009.
- [127] S. Roux, G. Lartigue, T. Poinso, U. Meier, and C. Bérat. Studies of mean and unsteady flow in a swirled combustor using experiments, acoustic analysis and Large Eddy Simulations. *Combust. Flame*, 141:40–54, 2005.
- [128] P. Sagaut. *Large eddy simulation for incompressible flows*. Springer, 2002.
- [129] M. Sanjosé. *Évaluation de la Méthode Euler-Euler pour la Simulation aux Grandes Échelles des Chambres à Carburants liquides*. PhD thesis, Université de Toulouse - Ecole doctorale : Mécanique, Énergétique, Génie civil, Procédés, 2009.
- [130] C. Saulnier. Analyse théorique et simulation numérique d'une flamme monodimensionnelle laminaire diphasique. Rapport de stage - Institut National Polytechnique WN/CFD/02/64, CERFACS, 2002.
- [131] SS Sazhin, T. Kristyadi, WA Abdelghaffar, and MR Heikal. Models for fuel droplet heating and evaporation: comparative analysis. *Fuel*, 85(12-13):1613–1630, 2006.
- [132] L. Schiller and A. Nauman. A drag coefficient correlation. *VDI Zeitung*, 77:318–320, 1935.
- [133] U. Schumann. Subgrid scale model for finite difference simulations of turbulent flows in plane channels and annuli. *J. Comput. Phys.*, 18:376–404, 1975.
- [134] L. Selle. *Simulation aux grandes échelles des interactions flamme-acoustique dans un écoulement vrillé - TH/CFD/04/35*. PhD thesis, Institut National Polytechnique de Toulouse, France - Dynamique des Fluides, 2004.
- [135] J.-M. Senoner. *Large Eddy Simulation of Two-Phase-Flows using a Euler-Lagrange Approach with secondary Breakup*. PhD thesis, Université de Toulouse - Ecole doctorale : Mécanique, Énergétique, Génie civil, Procédés, 2010.
- [136] J. M. Senoner, M. Sanjosé, B. Cuenot, and T. Poinso. A methodology to model fuel injection by pressure-swirl atomizer for large eddy simulation of real combustion chamber. *To be submitted to AIAA Journal*, 2009.
- [137] J.-M. Senoner, M. Sanjosé, T. Lederlin, F. Jaegle, M. García, E. Riber, B. Cuenot, L.Y.M. Gicquel, H. Pitsch, and T. Poinso. Eulerian and Lagrangian Large-Eddy Simulations of an evaporating two-phase flow. *C. R. Mécanique*, 337:458–468, 2009.
- [138] Y. Simeont. Simulation numérique d'un injecteur multipoint. Rapport de Projet de fin d'études CR/CFD/08/92, CERFACS, Septembre, 9 2008.
- [139] W. A. Sirignano. *Fluid dynamics and transport of droplets and sprays*. Cambridge University Press, 1999.
- [140] J. Smagorinsky. General circulation experiments with the primitive equations. i: The basic experiment. *Monthly Weather Review*, 91(3):99–165, 1963.
- [141] PR Spalart, WH Jou, M. Strelets, and SR Allmaras. Comments on the feasibility of LES for wings, and on a hybrid RANS/LES approach. *Advances in DNS/LES*, 1, 1997.

- [142] D. B. Spalding. The combustion of liquid fuels. In *Proceedings of the Fourth Symposium (international) on Combustion*, pages 847–864, Baltimore, 1953. The Combustion Institute.
- [143] G. Staffelbach, L.Y.M. Gicquel, and T. Poinso. Highly parallel large eddy simulation of multiburner configurations in industrial gas turbines. *The Cyprus International Symposium on Complex Effects in Large Eddy Simulation*, 2005.
- [144] G. Staffelbach and T. Poinso. High performance computing for combustion applications. In *Super Computing 2006*, Tampa, Florida, USA, 2006.
- [145] G. G. Stokes. On the effect of the inertial friction of fluids on the motion of pendulums, *Cambr. Phil. Trans. IX*, 8:1–141, 1851.
- [146] R. Struijs. Multi-dimensional upwind discretization method for the Euler equations on unstructured grids. *Ph. D. Thesis Technische Univ., Delft (Netherlands)*, 1994.
- [147] M. Sussman, P. Smereka, and S. Osher. A level set method for computing solutions to incompressible two-phase flow. *J. Comput. Phys.*, 114(1):146–159, 1994.
- [148] J.C. Tannehill, D.A. Anderson, and R.H. Pletcher. *Computational fluid mechanics and heat transfer*. Hemisphere Publishing Corporation, 1997.
- [149] M.W. Vance, K.D. Squires, and O. Simonin. Properties of the particle velocity field in gas-solid turbulent channel flow. *Phys. Fluids*, 18(063302), 2006.
- [150] A. Vié, L. Martinez, S. Jay, A. Benkenida, and B. Cuenot. Validation of the Eulerian Mesoscopic Approach in Particle-Charged Homogeneous Isotropic Decaying Turbulence in the scope of Large Eddy Simulation of Fuel Sprays. In *11th Triennial International Conference on Liquid Atomization and Spray Systems, July 2009, paper# 188*, 2009.
- [151] T. von Kármán. Mechanische aehnlichkeit und turbulenz. *Nach. Ges. Wiss. Göttingen, Math. Phys. Klasse*, 1:58–76, 1930.
- [152] Lian-Ping Wang and Martin R. Maxey. Settling velocity and concentration distribution of heavy particles in homogeneous isotropic turbulence. *J. Fluid Mech.*, 256:27–68, 1993.
- [153] T. Wei and WW Willmarth. Reynolds-number effects on the structure of a turbulent channel flow. *J. Fluid Mech.*, 204:57–95, 2006.
- [154] H. Werner and H. Wengle. Large-eddy simulation of turbulent flow over and around a cube in a plate channel. In *Eighth symposium on turbulent shear flows*, pages 155–68. Springer Verlag, Berlin, 1993.
- [155] F. M. White. *Fluid Mechanics*. McGraw-Hill, 4th edition, 1999.
- [156] P.-K. Wu, K. A. Kirkendall, and R. P. Fuller. Breakup Processes of Liquid Jets in Subsonic Crossflows. *J. Prop. Power*, 13(1):64–73, 1997.
- [157] A. Yoshizawa. Statistical theory for compressible turbulent shear flows, with the application to subgrid modeling. *Phys. Fluids*, 29(7):2152–2164, 1986.

Part V

Appendices

Appendix A

Validation of the evaporation model

A.1 Introduction

A validation of the evaporation model described in the preceding sections has been performed to ensure the proper integration into the numerical framework. Here, a validation against experiments is not the intent as models of this type are evaluated in literature [97] [131]. Instead, an analytical solution for simple testcases is considered and taken as a reference. Among the different options for Φ_g^c , only the most detailed one, which includes the effect of the Stefan flux is retained.

A.1.1 One-dimensional evaporation of a monodisperse droplet stream

A one-dimensional problem is considered. A uniform, laminar flow of heated air is superposed with a homogeneous n-heptane droplet spray that starts to evaporate right at the location where it is introduced into the domain. This testcase allows to analyze heat- and mass transfer in a convective environment, which means that gaseous and liquid properties vary spatially and effects of the numerical methods for liquid and gaseous phase and of the coupling between them are not negligible. Yet, the configuration is simple enough to have an analytical solution to which simulation results can be compared (depending on the case under certain additional assumptions). Simulations are presented and compared for both, the EE and the EL approach. Figure A.1 shows the generic configuration of this testcase. The mesh consists of a single, uniform stretch of quadrilateral cells with the inlet located on the left and the outlet located on the right hand side.

Top and bottom boundaries form a pair of periodic boundary conditions. Droplets are introduced into the domain at the same velocity as the gas. The exact injection procedure is different between the EE and EL case, but both methods will lead to an equivalent spray where evaporation takes place.

In the EL framework, droplets are injected well downstream of the gaseous injection to avoid interference between source terms and the inlet condition. The y-position of the injection point is placed on the centre line which guarantees a symmetric distribution (relative to the x -axis) of all source terms, thus resulting in a purely one-dimensional behaviour of the solution.

Because the mesh dimensions in y and z directions are unity, cell volumes are relatively high. If a homogeneous spray with a certain droplet number density n_l is to be produced, very high droplet numbers would have to be injected. To avoid this unnecessary computational cost, droplets are grouped in parcels (or numerical particles) in a way that results in approximately 30 parcels per cell. The spray then can still be considered homogeneous in x as fluctuations of coupling source

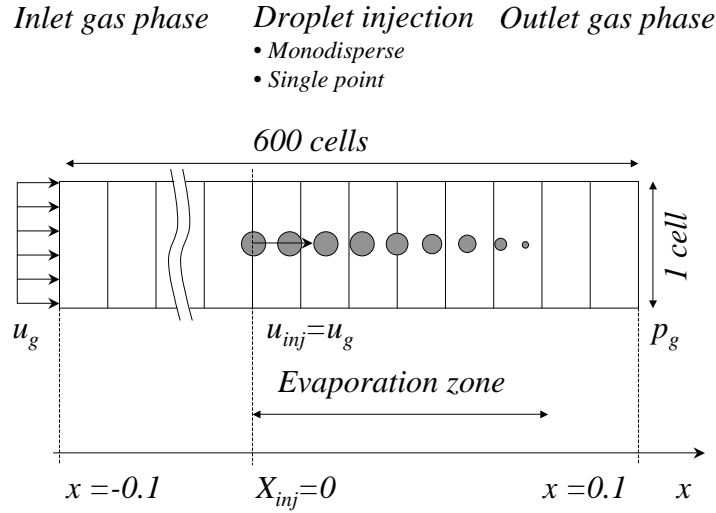


Figure A.1: 1D-configuration used for the evaluation of evaporation models in Euler-Lagrange formulation (droplet and mesh cell dimensions and numbers not to scale)

terms that are due to varying number of particles per cell are negligible.

In the EE framework, the mesh begins at $x = 0$ with both, gaseous and liquid injection conditions situated at the left-hand side boundary. Evaporation starts right at the inlet.

A.1.2 Simulation parameters

The simulation parameters, such as boundary conditions and Lagrangian injection parameters, are summarized in table A.2. The liquid phase species is n-heptane, for which liquid phase properties are listed in figure A.1.

Liquid phase properties	n-heptane
Boiling temperature	$T_{eb} = 371.52 \text{ K}$
Density	$\rho_l = 688.0 \text{ kg/m}^3$
Heat capacity	$C_{p,l} = 2.558 \times 10^3 \text{ J/kg/K}$
Evaporation heat	$L_{ev} = 316.35 \times 10^3 \text{ J/kg}$

Table A.1: Physical properties of n-heptane, at boiling point and standard pressure.

A.1.3 The analytical solution

The analytical solution is derived in detail in [130], presented in slightly different form in [18] and will briefly be described in the following. The assumptions are:

- the flow is laminar, stationary and one-dimensional,
- the thermal conductivity in the liquid phase is infinite,
- the particles are tracers ($St = 0$), i.e. the liquid and gaseous phases have the same velocity in the whole domain ($u_l = u_g = u$),

Inlet conditions	
Gas velocity	$u_g = 2.2 \text{ m/s}$
Gas temperature	$T_g = 380 \text{ K}$
Gaseous ethanol mass fraction	$Y_F = 3.85 \times 10^{-7}$
Oxygen mass fraction	$Y_O = 2.33 \times 10^{-1}$
Carbon dioxide mass fraction	$Y_{CO_2} = 0$
Water mass fraction	$Y_{H_2O} = 0$
Nitrogen mass fraction	$Y_{N_2} = 7.670 \times 10^{-1}$
Outlet conditions	
Pressure	$P_g = 1.01325 \times 10^5 \text{ Pa}$
Liquid phase parameters	
Particle velocity	$u_l = 2.2 \text{ m/s}$
Mass flux	$\dot{m} = 1.515 \cdot 10^{-3} \text{ kg/s}$
Droplets diameter	$d_l = 30 \text{ }\mu\text{m}$
Liquid temperature	$T_l = 324.285 \text{ K}$

Table A.2: Calculation parameters for the 1D evaporation

- the pressure is constant,
- the product $[\rho D_F]$, the Spalding number $B = B_M = B_T$, the gas thermal conductivity λ_g and heat capacity C_{pg} are constant.
- the temperature of the liquid phase is constant and equal to the equilibrium temperature ($T_l = T_{wb}$).

We suppose also that the mass loading is low and thus $\alpha_g \sim 1$. Under these assumptions, the equations to be solved are

$$\frac{d}{dx}(\rho_g u) = \Gamma \quad (\text{A.1})$$

$$\frac{d}{dx}(\rho_g u Y_k) - [\rho D_F] \frac{d^2}{dx^2}(Y_k) = \delta_{kF} \Gamma \quad (\text{A.2})$$

$$\frac{d}{dx}(\rho_g u C_{pg} T_g) - \lambda_g \frac{d^2}{dx^2}(T_g) = h_l(T_l) \Gamma_g \quad (\text{A.3})$$

The mixture density is defined as:

$$\rho_m = \rho = \alpha_g \rho_g + \alpha_l \rho_l \quad (\text{A.4})$$

The mixture mass conservation equation allows to write:

$$\rho u = F = \text{cste} = \rho_{in} u_{in} \quad (\text{A.5})$$

Introducing the variable $Z = \frac{\rho_g}{\rho}$, equations A.1, A.2 and A.3 become:

$$Z \frac{dZ}{dx} = \mathcal{A} \frac{1}{T_g} (1 - Z_{in})^{2/3} (1 - Z)^{1/3} \quad (\text{A.6})$$

$$\frac{d}{dx}(ZY_F) - \frac{[\rho D_F]}{F} \frac{d^2 Y_F}{dx^2} = \frac{dZ}{dx} \quad (\text{A.7})$$

$$\frac{d}{dx}(ZT_g) - \frac{\lambda_g}{C_{pg}F} \frac{d^2 T_g}{dx^2} = \frac{C_{pl}T_{wb}}{C_{pg}} \frac{dZ}{dx} \quad (\text{A.8})$$

$$\text{with } \mathcal{A} = \frac{3Sh[\rho\lambda]_\zeta \ln(1+B)p\bar{W}}{2\rho_l Rr_{in}^2 F} \quad (\text{A.9})$$

The variable change $\beta = \frac{1-Z}{1-Z_{in}}$ leads to the following equations:

$$-\frac{d\beta}{dx} + (1-Z_{in})\beta \frac{d\beta}{dx} = \frac{\mathcal{A}}{T_g} \beta^{1/3} \quad (\text{A.10})$$

$$\frac{dY_F}{dx} - (1-Z_{in}) \frac{d}{dx}(\beta Y_F) - \frac{[\rho D_F]}{F} \frac{d^2 Y_F}{dx^2} = -(1-Z_{in}) \frac{d\beta}{dx} \quad (\text{A.11})$$

$$\frac{dT_g}{dx} - (1-Z_{in}) \frac{d}{dx}(\beta T_g) - \frac{\lambda_g}{C_{pg}F} \frac{d^2 T_g}{dx^2} = \frac{C_{pl}T_{wb}}{C_{pg}} - (1-Z_{in}) \frac{d\beta}{dx} \quad (\text{A.12})$$

The following boundary conditions are used:

$$\begin{cases} \beta(x=0) = 1 & ; \quad \beta(x=x_{ev}) = 0 \\ Y_F(x=0) = Y_{F,in} & ; \quad \frac{d}{dx}(Y_F)(x=x_{ev}) = 0 \\ T_g(x=0) = T_{g,in} & ; \quad \frac{d}{dx}(T_g)(x=x_{ev}) = 0 \end{cases}$$

The fact that the spray is very dilute allows to consider that Z_{in} is close to 1. One can then write $Z_{in} = 1 - \epsilon$ with $\epsilon \ll 1$. Equation A.10 is developed to the 0th order in ϵ .

$$\frac{d\beta_0}{dx} + \frac{\mathcal{A}}{T_{g,0}} \beta_0^{1/3} + \mathcal{O}(\epsilon) = 0 \quad (\text{A.13})$$

An integration between $x=0$ and x gives:

$$\beta_0(x) = \left(1 - \frac{2\mathcal{A}}{3T_{g,in}} x\right)^{3/2} \quad (\text{A.14})$$

and in terms of Z :

$$Z(x) = 1 - (1 - Z_{in}) \left(1 - \frac{2\mathcal{A}}{3T_{g,in}} x\right)^{3/2} \quad (\text{A.15})$$

Equations A.11 and A.12 are developed to the first order in ϵ .

$$\left[\frac{dY_{F,0}}{dx} - \frac{[\rho D_F]}{F} \frac{d^2 Y_{F,0}}{dx^2} \right] + \epsilon \left[\frac{dY_{F,1}}{dx} - \frac{d(\beta_0 Y_{F,0})}{dx} - \frac{[\rho D_F]}{F} \frac{d^2 Y_{F,1}}{dx^2} + \frac{d\beta_0}{dx} \right] + \mathcal{O}(\epsilon^2) = 0 \quad (\text{A.16})$$

$$\left[\frac{dT_{g,0}}{dx} - \frac{\lambda}{C_{pg}F} \frac{d^2 T_{g,0}}{dx^2} \right] + \epsilon \left[\frac{dT_{g,1}}{dx} - \frac{d(\beta_0 T_{g,0})}{dx} - \frac{\lambda}{C_{pg}F} \frac{d^2 T_{g,1}}{dx^2} + \frac{C_{pl}T_{wb}}{C_{pg}} \frac{d\beta_0}{dx} \right] + \mathcal{O}(\epsilon^2) = 0 \quad (\text{A.17})$$

Equations A.16 and A.17 are resolved at the 0th order, then at the first order. The solution is then composed of both contributions:

$$Y_F(x) = Y_{F,0} + \epsilon Y_{F,1} = Y_{F,0} + (1 - Z_{in})Y_{F,1} \quad (\text{A.18})$$

$$T_g(x) = T_{g,0} + \epsilon T_{g,1} = T_{g,0} + (1 - Z_{in})T_{g,1} \quad (\text{A.19})$$

The integrations which are necessary to solve equations A.18 and A.19 are performed numerically in a program that runs independently of the AVBP code.

A.1.4 Results

The comparison of Euler-Lagrange results to results of Euler-Euler simulations necessitates the calculation of the variables that are not explicitly present in a Lagrangian approach. These are, for example, the liquid volume fraction α_l and the droplet number density n_l . These quantities are calculated inside AVBP before writing out a solution and distributed to the grid nodes with the same scheme as for the source terms. The same procedure is applied to variables such as the droplet diameter in order to facilitate post-processing. The Lagrangian results are therefore averaged quantities inside a grid cell. It is important to note that all variables are assigned the default value of zero in cells where no Lagrangian droplets are present. This makes a certain physical sense for instance in the case of the droplet diameter or the source terms Γ_g and Π_g . In the case of the droplet temperature, however, the drop to zero Kelvin downstream of the evaporation zone has no physical significance and is not taken into account for averaging procedures.

The solutions represent a classical evaporation case: The gas temperature decreases because of the heat transfer between the two phases. As a result, and because the composition of the mixture is modified, the gas density is increasing. This causes the gas (and liquid-) velocity to decrease as a result of momentum conservation.

On the liquid side, the droplet number density is increasing because velocity decreases, reducing the distance between droplets. At the same time, the liquid volume fraction decreases as a result of a diminishing diameter of each droplet.

Figures A.2 and A.3 show the comparison between EE, EL as well as the analytical solution. As a general statement, the computed solution fits very well to the analytical one, except for the liquid temperature which increases at first, then reaches a maximum and converges towards a final value that is close to the constant temperature of the analytical solution. This means that the fragile equilibrium between conductive heat exchange and heat loss due to evaporation that determines the droplet temperature is not exactly balanced at the onset of the evaporation process. The difference is due to the assumption of zero conductive heat transfer ($\Phi_l^c = 0$) in the liquid phase of the analytical solution in section A.1.3 which is not the case in AVBP.

The comparison to the Euler-Euler simulations reveals overall very well corresponding results. As a consequence, all the differences between Euler-Lagrange and the analytical solution are also found in the Euler-Euler case and are explained by the same mechanisms.

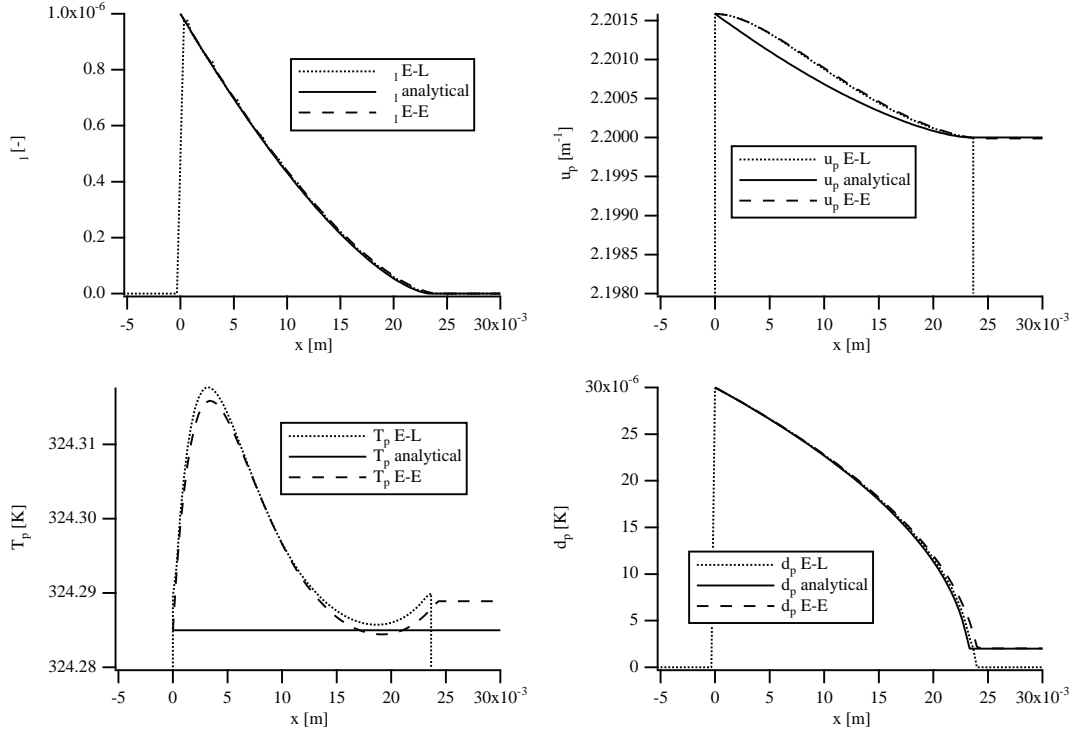


Figure A.2: Results of case A (E-L: Euler-Lagrange, E-E: Euler-Euler).

The diagrams of the mass exchange rate, Γ_g , and the heat exchange rate, Π_g , show both significant wiggles, especially in the early stages of evaporation. This is an effect related to the relatively low number of particles inside each cell. As the injection has to satisfy both a mass flux and a fixed droplet diameter, the time intervals between two subsequent droplet injections may not be constant over time. In a given timestep, several droplets are injected; the amount of liquid mass per timestep can in general not be divided into droplets of constant diameter without a remainder. Therefore, the last droplet is postponed to the next timestep which creates a "gap" in a supposedly equidistant stream of droplets. The result is a series of droplet "trains" instead of a perfectly equidistant lineup. As a result, evaporation source-terms are subject to certain variations between cells.

This effect is relatively pronounced as particles are grouped into parcels. It has to be pointed out that it is possible to totally smooth out the fluctuations by choosing a sufficiently low number of droplets per parcel (increasing the number of droplets per cell). Note that the variations are not conveyed to the gas variables which show very smooth curves except for some very minor oscillations of the pressure.

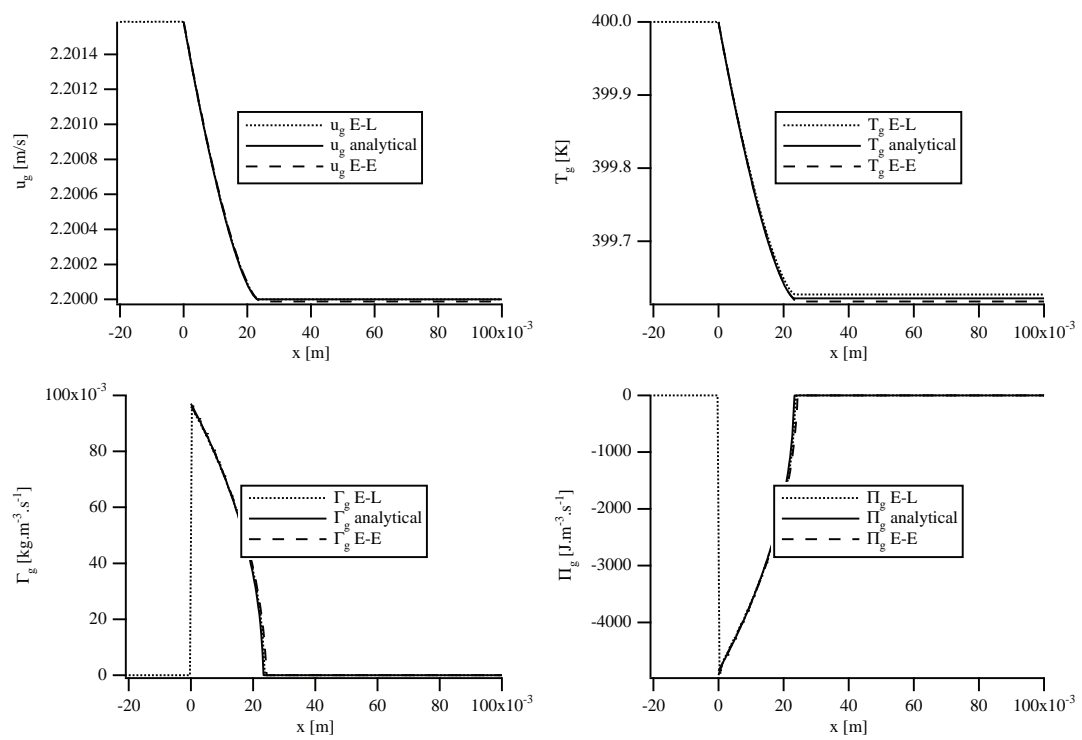


Figure A.3: Results of case A (E-L: Euler-Lagrange, E-E: Euler-Euler).

Appendix B

One-dimensional spray flames

B.1 Introduction

This appendix presents results of one-dimensional spray flames. They correspond to different degrees of complexity in the coupling between droplet dynamics and chemical reactions. A schematic of both flames is shown in figure B.1.

The first is a so-called homogeneous flame (or “anchored” spray flame [13]). It consists in a spray that is introduced in a gaseous flow at the same speed and immediately undergoes evaporation. This zone is followed by the reaction zone after a short distance. Here, evaporation and reaction mechanisms are only weakly coupled, the case can also be regarded on a gaseous flame with boundary conditions on the side of the fresh gases imposed by evaporation.

The second is a saturated spray flame as it is studied by Ben-Dakhli [13] and Boileau [19]. Here, the upstream boundary conditions correspond to a saturated spray, i.e. with a mass fraction of evaporated fuel sufficiently high to halt evaporation, creating a non-evolving gas-spray mixture. Evaporation is only re-activated when the droplets enter the flame front due to increasing temperature. The additional gaseous fuel is consumed by the reaction at the same

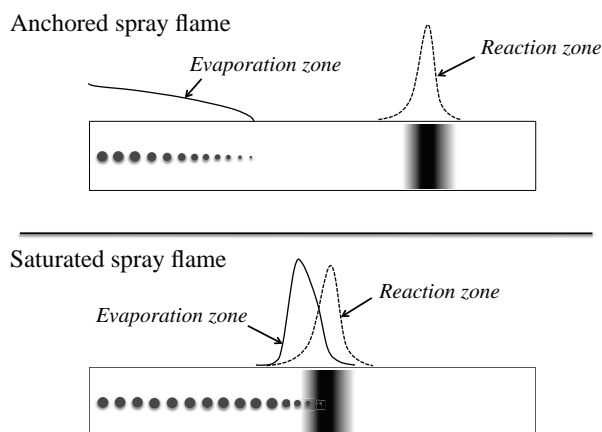


Figure B.1: Schematic of the anchored and the saturated 1D spray flames.

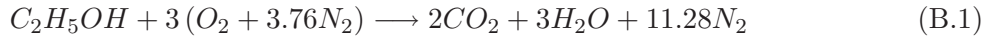
time it is created by evaporation, creating a very strong coupling between both processes. In addition to the physical complexity, the saturated flame is also the more challenging case from

the numerical point of view. As evaporation is more confined to a narrow zone and consequently creates stronger source terms, this flame is at the same time a testcase for the stability of the numerical approach.

B.2 Anchored spray flame

B.2.1 Chemistry

The chemistry used for this flame is a single-step reduced scheme for ethanol that has been obtained by Boileau [17] to fit the experimental data of [59]. It can be written as (Eq.B.2).



The species reaction rates can be linked to the fuel reaction rate.

$$\dot{\omega}_F = 2 W_F \left(\frac{\rho Y_F}{W_F} \right)^{n_F} \left(\frac{\rho Y_{O_2}}{W_{O_2}} \right)^{n_{O_2}} A T^\beta \exp \left(\frac{-E_a}{RT} \right) \quad (B.2)$$

The parameters of the chemistry kinetic scheme are summarized in table B.1.

n_F	n_{O_2}	β	A (cgs)	E_a (cal/mol)
1.30	0.55	0.0	2.17×10^{12}	20 000

Table B.1: Fitted coefficients of the reduced Ethanol/Air combustion scheme

B.2.2 Spray properties

The physical properties for liquid ethanol are gathered in table B.2.

Liquid phase properties	Ethanol
Boiling temperature	$T_{eb} = 351.45 K$
Density	$\rho_l = 783 kg/m^3$
Heat capacity	$C_{p,l} = 2.434 \times 10^3 J/kg/K$
Evaporation heat	$L_{ev} = 841.12 \times 10^3 J/kg$

Table B.2: Physical properties of liquid ethanol, at boiling point and standard pressure.

B.2.3 Analytical solution

A laminar *homogenous* premixed flame in dilute spray is a particular but frequently encountered combustion regime where the liquid phase is completely evaporated before the flame zone. This mono-dimensional configuration is an interesting test case as the physical processes of evaporation and combustion are totally *uncoupled*, as schematized on figure B.1. For such a problem, an analytical solution has been derived in [88],[89], by solving successively two problems and connecting the common limit condition at the end of evaporation. A short description of the analytical solution can be found in [18]. The resolution of both problems as well as their connection is performed numerically in a code that is independant from AVBP.

B.2.4 Simulation parameters

The boundary and/or injection conditions used in the simulations are gathered in table B.3. The EE simulation is initialized from the analytical solution, which is formulated in Eulerian variables. It can, however, not be translated directly in a Lagrangian droplet field. Therefore, the EL simulation is started as a pure evaporation case, with the flame being subsequently initialized by imposing a species composition that corresponds to the reaction products as well as the adiabatic flame temperature downstream of the intended flame coordinate.

Inlet conditions	
Gas velocity	$u_g = 0.469 \text{ m/s}$
Gas temperature	$T_g = 480 \text{ K}$
Gaseous ethanol mass fraction	$Y_F = 1.231 \times 10^{-3}$
Oxygen mass fraction	$Y_O = 2.327 \times 10^{-1}$
Carbon dioxide mass fraction	$Y_{CO_2} = 0$
Water mass fraction	$Y_{H_2O} = 0$
Nitrogen mass fraction	$Y_{N_2} = 7.660 \times 10^{-1}$
Outlet conditions	
Pressure	$P_g = 1.01325 \times 10^5 \text{ Pa}$
Liquid phase parameters	
Particle velocity	$u_l = 0.469 \text{ m/s}$
Mass flux	$\dot{m} = 53.8 \cdot 10^{-3} \text{ kg/s}$
Droplets diameter	$d_l = 30 \text{ }\mu\text{m}$
Liquid temperature	$T_l = 310 \text{ K}$
Global equivalence ratio	$\Phi_t = 0.7$

Table B.3: Calculation parameters for the anchored spray flame

B.2.5 Results

As a general observation on the simulation results presented in this section, a notable shift in the position of the flame front of all different cases can be noted. This discrepancy is due to the different ways of initializing the simulations, which leads to a brief movement of the flamefront before reaching a steady state (characterized by virtually identical flamespeeds in both simulation cases). As the spray injection is anchored at the same position in all three cases, the results are presented as they are without a-posteriori alignments. All results are physically equivalent as evaporation- and reaction zones are completely uncoupled.

Figures B.2 and B.3 show the evolution of gaseous variables. The position of the flame can be distinguished on the gaseous temperature that sees a sharp rise to approximately 1900 K . The final temperatures of the simulation results agree very well but are slightly higher in comparison to the analytical solution. This can be linked to a small discrepancy in fuel mass fraction between simulation results and the analytical solution after complete evaporation (figure B.6). The gaseous flow is accelerated when crossing the flame front, which is due to mass-conservation in the expanding one-dimensional flow. It can be noted that in the EE results, a liquid phase velocity is still present in areas downstream of the point of completed evaporation, while the Lagrangian velocity is no longer defined. Eulerian quantities in these zones are artificial as they transport near-zero volume fractions and should not be considered from a physical standpoint.

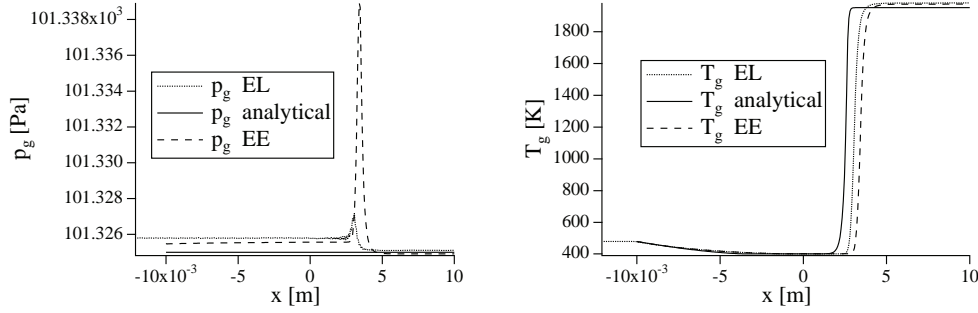


Figure B.2: Gaseous phase pressure and temperature from Euler-Lagrange- (EL) and Euler-Euler- (EE) results as well as the analytical solution.

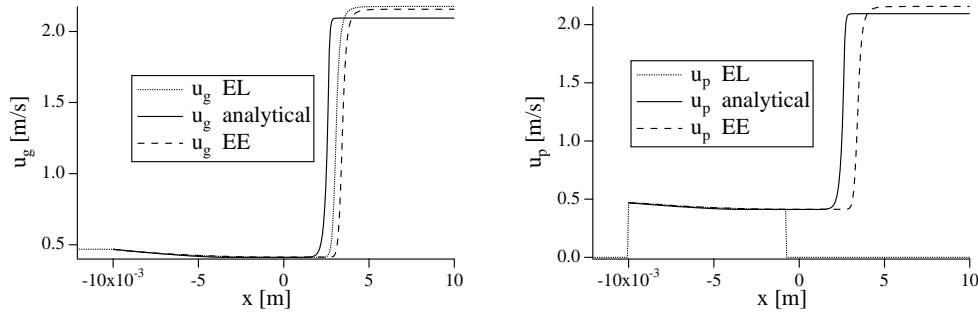


Figure B.3: Evaporation fluxes towards the gaseous phase from Euler-Lagrange- (EL) and Euler-Euler- (EE) results as well as the analytical solution.

The pressure field is assumed constant in the analytical solution, but the pressure through a stationary premixed flame undergoes a drop which depends on flame speed and temperature drop.

$$\Delta P = p_b - p_f = \rho_f s_L^2 \left(1 - \frac{T_b}{T_f} \right) \quad (\text{B.3})$$

The physical gas properties leads to a theoretical pressure drop of $\Delta P = -0.60 Pa$, which corresponds to the pressure drop observed in the simulation results. EL and EE reveal the same magnitude but are slightly shifted relative to each other, which is related to the slightly incomplete convergence process towards a steady solution. There is a pronounced peak at the position of the flame, which is a numerical artifact of the scheme for the gaseous phase. This peak is clearly less pronounced in the Lagrangian solution.

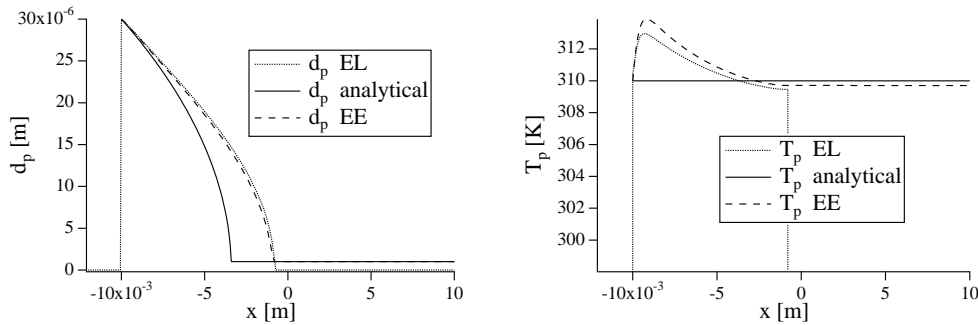


Figure B.4: Evaporation fluxes towards the gaseous phase from Euler-Lagrange- (EL) and Euler-Euler- (EE) results as well as the analytical solution.

Figure B.4 shows the evolution of the droplet diameter and temperature. Between the locations of complete evaporation in the analytical solution and the numerical results, a slight difference

of about 2.5 mm can be observed. This is typically due to effects of heat transfer which are neglected in the analytical solution but not in the simulation. This tends to lower the evaporation rate as evidenced by the evolution of mass transfer, shown in figure B.5. Differences between Euler-Lagrange and Euler-Euler are relatively in comparison. This indicates that the discrepancies between simulation results and the analytical solution are mainly due to the approximations made in the analytical solution and not to the numerical approach.

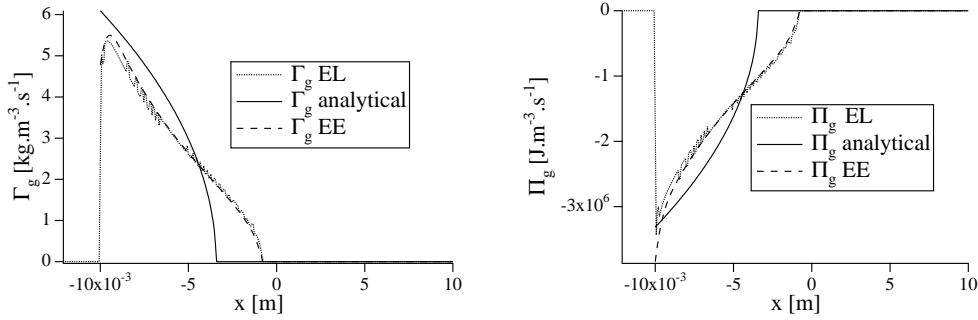


Figure B.5: Evaporation fluxes towards the gaseous phase from Euler-Lagrange- (EL) and Euler-Euler- (EE) results as well as the analytical solution.

The temperature evolution shows an initial droplet heating phase, leading to a temperature increase of approximately 4 K , followed by a decrease to a value near the initial temperature. This is evidence that the approximation of a constant temperature in the analytical solution is not very well satisfied. The resulting differences can also be observed on the heat transfer curve in figure B.5. Agreement between EL and EE is relatively accurate, the most marked difference is observed on the droplet temperature and amounts to about 1 K . The evolution of heat and mass transfer curves of the Lagrangian case show a certain oscillatory behaviour, which is due to an uneven distribution of particles over the grid, as described in more detail in appendix A.

Figure B.6 shows the evolution of mass fractions. It presents the classical structure of changes in composition between fresh and burned gases. The difference to a gaseous flame is the fuel mass fraction that is equal to zero at the inlet and rises to its maximum level in the evaporation region.

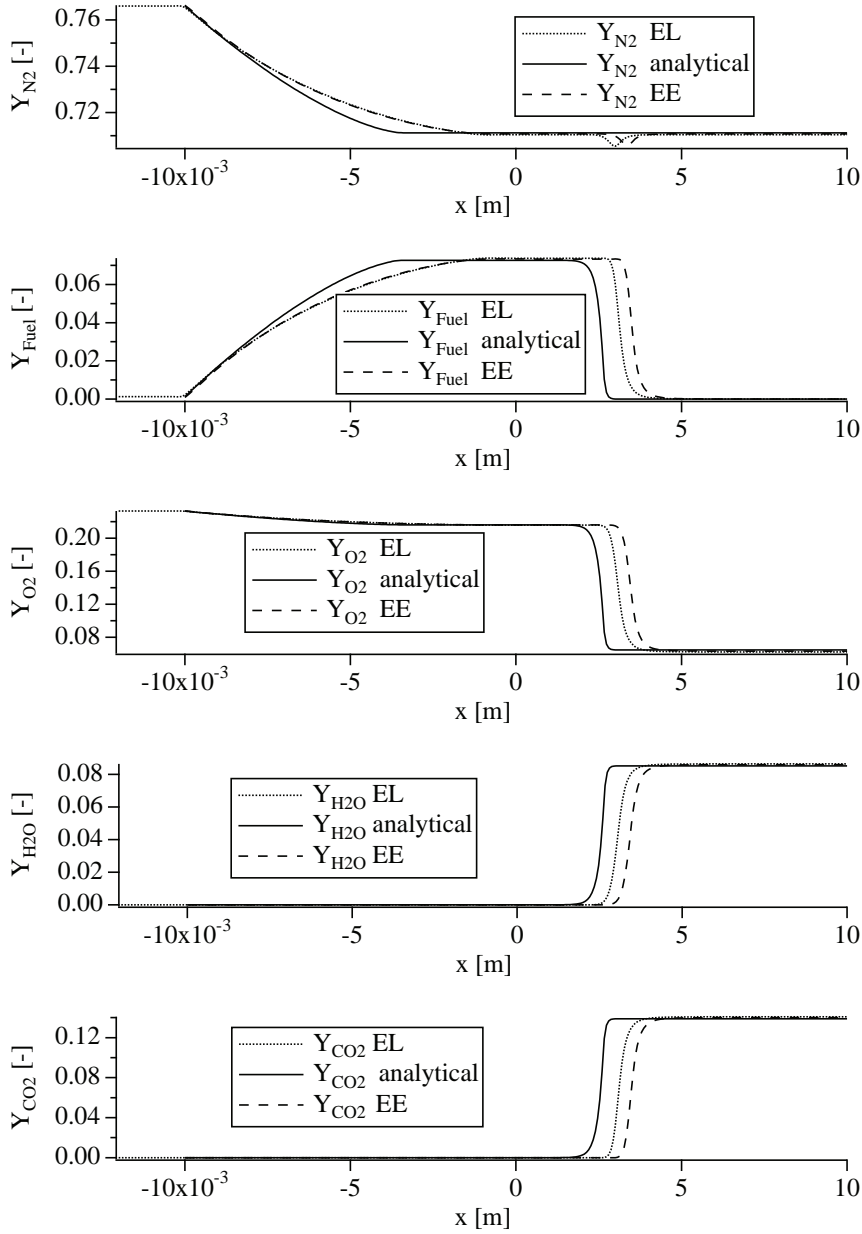


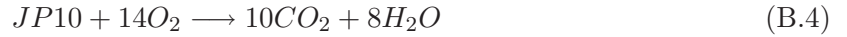
Figure B.6: Species mass fraction evolutions from Euler-Lagrange- (EL) and Euler-Euler- (EE) results as well as the analytical solution.

B.3 Saturated spray flame

The saturated case is based on the work of Boileau [19], who studied this flame using the EE approach, including a detailed analysis of the flame structure. Here, this testcase is recreated in a Lagrangian representation and compared to the EE results. There is no analytical solution available. In this context, it serves as an advanced verification of the equivalence of both approaches as well as a test for the numerical scheme of the gas phase confronted with strong, local source terms generated by the Lagrangian solver.

B.3.1 Chemistry

The chemistry used for this flame is a single-step reduced scheme for JP10. It can be written as (Eq.B.5).



The species reaction rates can be linked to the fuel reaction rate.

$$\dot{\omega}_F = 2W_F \left(\frac{\rho Y_F}{W_F} \right)^{n_F} \left(\frac{\rho Y_{O_2}}{W_{O_2}} \right)^{n_{O_2}} A T^\beta \exp\left(\frac{-E_a}{RT}\right) \quad (\text{B.5})$$

The parameters of the chemistry kinetic scheme are summarized in table B.1.

n_F	n_{O_2}	β	A (cgs)	E_a (cal/mol)
1.154	0.738	0.0	6.454×10^{13}	29 188.8

Table B.4: Fitted coefficients of the reduced Ethanol/Air combustion scheme

B.3.2 Spray properties

The physical properties for liquid ethanol are gathered in table B.5.

Liquid phase properties	JP10
Boiling temperature	$T_{eb} = 461.23 \text{ K}$
Density	$\rho_l = 796 \text{ kg/m}^3$
Heat capacity	$C_{p,l} = 2.1 \times 10^3 \text{ J/kg/K}$
Evaporation heat	$L_{ev} = 305.0 \times 10^3 \text{ J/kg}$

Table B.5: Physical properties of liquid ethanol, at boiling point and standard pressure.

B.3.3 Simulation parameters

The boundary and/or injection conditions used in the simulation are summarized in table B.6. These values are obtained by a separate 0D evaporation calculation at the global equivalence ratio of $\Phi_t = 0.25$ that is run until the saturated state is reached. The inlet conditions of the 1D flame are obtained from the 0D results and translated into boundary conditions suitable for EE and EL. The flame is initialized by imposing the species composition corresponding to reaction products as well as the adiabatic flame temperature downstream of the intended flame position.

Inlet conditions	
Gas velocity	$u_g = 0.34 \text{ m/s}$
Gas temperature	$T_g = 272.1 \text{ K}$
Gaseous ethanol mass fraction	$Y_F = 2.175 \times 10^{-3}$
Oxygen mass fraction	$Y_O = 2.325 \times 10^{-1}$
Carbon dioxide mass fraction	$Y_{CO_2} = 0$
Water mass fraction	$Y_{H_2O} = 0$
Nitrogen mass fraction	$Y_{N_2} = 7.653 \times 10^{-1}$
Outlet conditions	
Pressure	$P_g = 1.17665 \times 10^5 \text{ Pa}$
Liquid phase parameters	
Particle velocity	$u_l = 0.34 \text{ m/s}$
Mass flux	$\dot{m} = 0.035 \text{ kg/s}$
Droplets diameter	$d_l = 24.86 \text{ }\mu\text{m}$
Liquid temperature	$T_l = 272.1 \text{ K}$
Global equivalence ratio	$\Phi_t = 0.25$

Table B.6: Calculation parameters for the saturated spray flame

B.3.4 Results

To make results presented for the saturated flame more readable, all curves have been shifted by the relative distance of the maximum reaction rates in EE and EL results. Unlike the anchored flame, which is fixed (or anchored...) at the coordinate of spray injection, upstream and downstream conditions of the saturated flame are constant along the spatial coordinate. This practical property allows to exactly superpose the combined evaporation/reaction region.

Gaseous quantities from the simulation results are shown in figures B.7 and B.8. There is excellent agreement between EE and EL simulations for the gaseous temperature and velocity. Differences can be observed on the pressure, where the EE results reveal a certain degree of spurious oscillations in the regions of strong evaporation terms that are observed to a much lesser extent in the EL formulation. There is a slight shift of the entire pressure level, which is due to the slow convergence of this variable, which is not complete in the shown result.

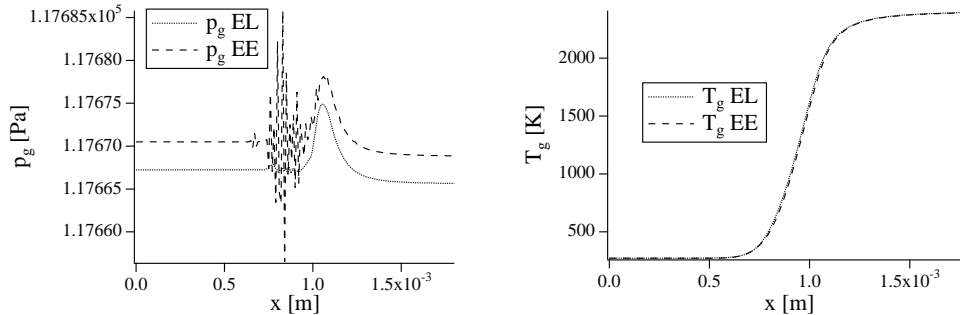


Figure B.7: Gaseous phase pressure and temperature from Euler-Lagrange- (EL) and Euler-Euler- (EE) results.

As it has to be noted generally for the EE approach, quantities after the end of evaporation, like the liquid phase velocity shown in figure B.8 is not physical in these zones. Agreement between EE and EL in the regions of accelerating and evaporating droplets upstream of this point is very

good.

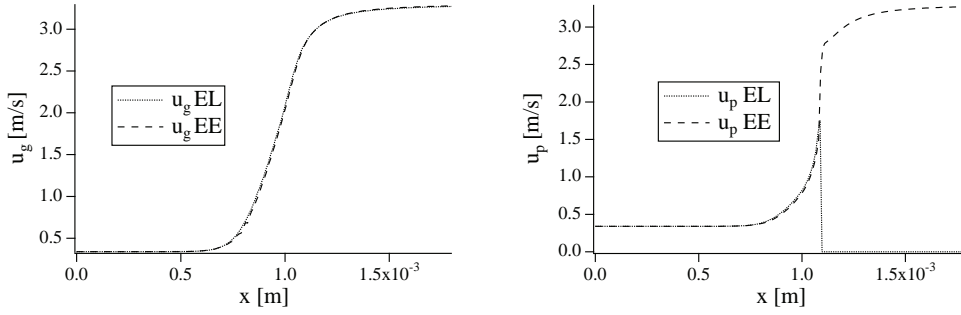


Figure B.8: Gaseous and liquid phase velocities from Euler-Lagrange- (EL) and Euler-Euler- (EE) results.

The rapid evaporation process as droplets enter the reaction zone and consequently meet increasing temperature levels is visualized in figure B.9, which shows the dimensionless square of the diameter. After a short initial phase, the bulk of the droplet evolution is essentially linear, which corresponds to evaporation following the d^2 -law at constant temperature. As the evolution of dimensionless droplet temperature shows, there is indeed a rapid heatup phase followed by a zone of constant temperature, which corresponds in this case to the boiling temperature. In the evaporation model, droplet boiling is detected and results in a changed procedure in the program flow (see section 4.3.5). The discrepancies between EE and EL are due to slight differences in implementation between both methods.

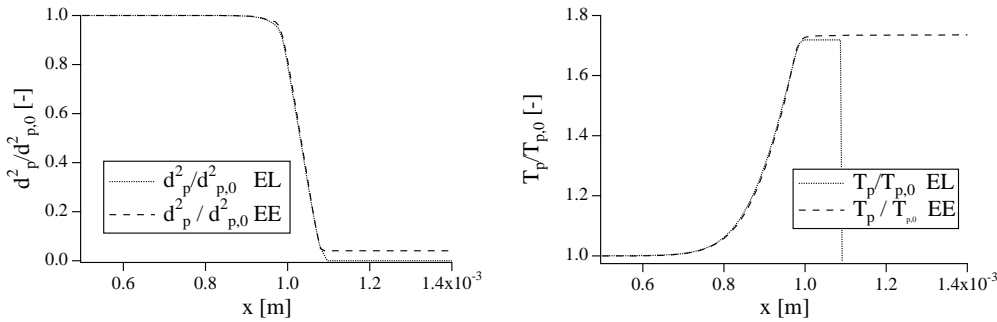


Figure B.9: Dimensionless square of the droplet diameter and dimensionless droplet temperature from Euler-Lagrange- (EL) and Euler-Euler- (EE) results.

Effects of droplet boiling are also observed on the evaporation source terms that are passed to the gaseous solver. Notably, the heat transfer term Π_g changes its sign near the onset of boiling. The reason for this can be found in the droplet enthalpy balance (equation 4.30). As the constant temperature means that $\Phi_l^c = 0$, the source term $\Pi_g = \Phi_g^c + \Phi_g^{ev}$ takes the form $\Pi_g = \Phi_l^{ev} = -\dot{m}_F h_{s,p}(T_\zeta)$. This means that heat transfer during droplet boiling is reduced to the transport of liquid phase enthalpy contained in the evaporated mass.

The evolution of species mass fractions is shown in figure B.11. The most notable change relative to a gaseous flame or the anchored spray flame is the evolution of the fuel mass fraction. The constant level of non-zero mass fraction upstream of the flame is followed by a brief increase inside the flame front that is followed by a drop to $Y_F = 0$ downstream of the flame. This shows how the evaporation zone blends with the reaction zone, where the gaseous fuel mass fraction is reduced by chemistry while being simultaneously produced by the liquid phase source terms. A detailed breakdown of the terms contributing to this process can be found in the thesis of Boileau [19].

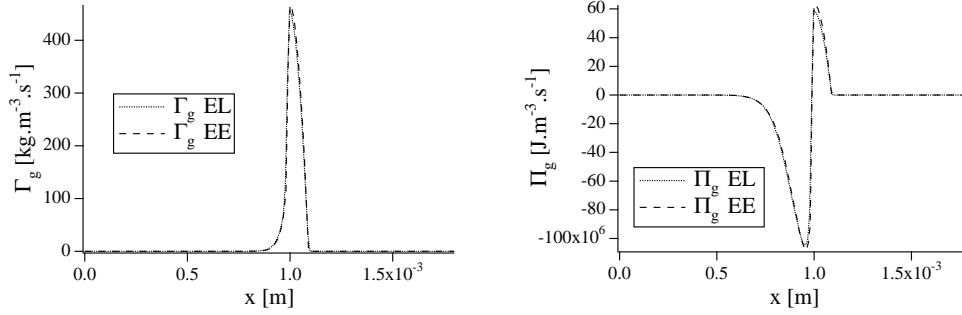


Figure B.10: Evaporation fluxes towards the gaseous phase from Euler-Lagrange- (EL) and Euler-Euler- (EE) results.

B.4 Conclusion of the one-dimensional test cases

Three one-dimensional tests have been conducted with the primary goal of validating the Lagrangian implementation of the evaporation model. Another objective has been the demonstration of reactive cases involving Lagrangian, evaporating droplets as these applications are considered the most critical in terms of stability issues of the numerical scheme. Comparisons are made between the well-proven EE approach and the more recently developed EL approach. Where possible, an analytical solution has been included into the comparisons to raise the degree of confidence in the results.

The main finding is a successful Lagrangian implementation, with the additional insight that both formulations, despite their different nature, yield results that agree with very little error. This is an important piece of information if larger-scale comparisons are to be undertaken, as it is the case in the present work.

In terms of stability, the Lagrangian simulations perform very soundly, in cases even reducing the level of pressure oscillations relative to the EE results. As a general note, experience shows that this increased robustness of EL with respect to EE simulations is also encountered on three-dimensional cases and can lead to a much more straightforward setup and initialization of such simulations.

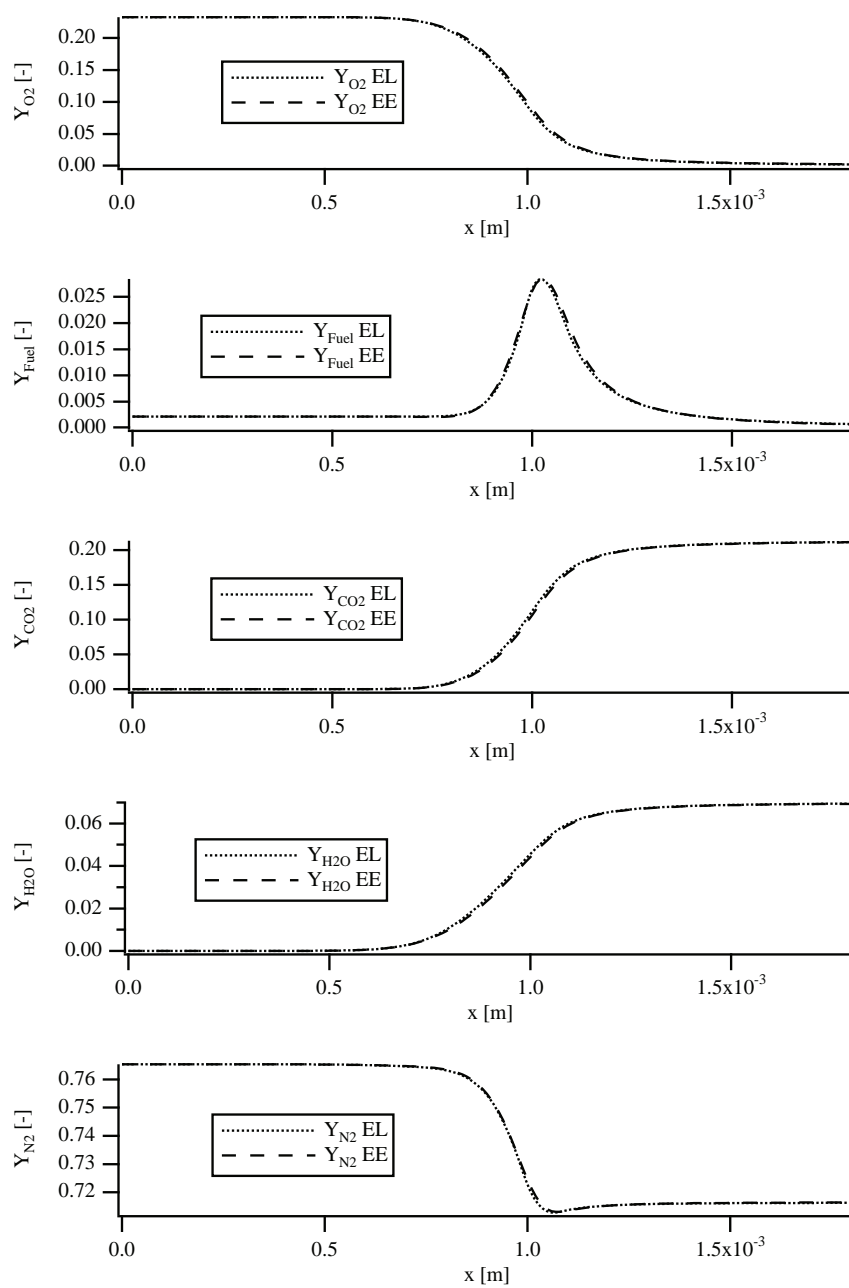


Figure B.11: Species mass fraction evolutions for Euler-Lagrange- (E-L), Euler-Euler- (E-E) and analytical solution.